

2013

Damage Characterization and Analytical Modeling of Quasi-statically Indented Graphite/Epoxy- Honeycomb Core Composite Sandwich Stru

Abhendra K. Singh

Follow this and additional works at: http://surface.syr.edu/mae_etd

 Part of the [Aerospace Engineering Commons](#)

Recommended Citation

Singh, Abhendra K., "Damage Characterization and Analytical Modeling of Quasi-statically Indented Graphite/Epoxy-Honeycomb Core Composite Sandwich Stru" (2013). *Mechanical and Aerospace Engineering - Dissertations*. Paper 77.

This Dissertation is brought to you for free and open access by the College of Engineering and Computer Science at SURFACE. It has been accepted for inclusion in Mechanical and Aerospace Engineering - Dissertations by an authorized administrator of SURFACE. For more information, please contact surface@syr.edu.

ABSTRACT

The research conducted for this dissertation focused on understanding the nature and extent of barely visible impact damage (BVID) in composite sandwich structures. This was part of a larger research effort that included studies on the influence of BVID on the compressive strengths and failure modes of composite sandwich structures. In this dissertation, the nature and extent of BVID is studied in aluminum honeycomb core sandwich panels with eight and sixteen ply, quasi-isotropic, graphite/epoxy face sheets. The damage in the sandwich structure is created quasi-statically using spherical indentors of two different sizes. Apart from the face sheet thickness and indenter size, other parameters that are varied in the experimental investigations include the core thickness, core density and face sheet layup. The effects of these parameters on the nature and extent of damage in the sandwich structure is evaluated. The different damage metrics of dent diameter, dent depth and planar area of delamination are used for damage characterization and these damage metrics are evaluated non-destructively. The damage resistance of the different sandwich configurations based on these damage metrics is then assessed. It is shown that when the extent of damage in a sandwich structure is determined based on the dent depth or the dent diameter, the sandwich structure that uses a higher density core is the most damage resistant. However, when the extent of damage is based on the planar area of delamination, the parameters that govern the damage size differ for the different face sheet thicknesses. An analytical model is developed in this dissertation to predict the quasi-static load versus displacement response of the sandwich structure during loading, including the onset of damage and the subsequent unloading behavior. It is shown that the analytical model is capable of predicting the residual dent depth and the residual dent diameter of the sandwich structure for damage within the vicinity of BVID.

**Damage Characterization and Analytical Modeling of Quasi-
Statically Indented Graphite/Epoxy-Honeycomb Core Composite
Sandwich Structures**

by

Abhendra K. Singh

B.Tech. Indian Institute of Technology (IIT), Roorkee, India, 2002

M.S. Syracuse University, Syracuse, New York, USA, 2009

Dissertation

Submitted in partial fulfillment of the requirements for the degree of Doctor of
Philosophy in Mechanical and Aerospace Engineering in the Graduate School of
Syracuse University

June 2013

Copyright © Abhendra K. Singh 2013

All rights reserved

ACKNOWLEDGEMENTS

First and foremost, I would like to thank God for giving me this opportunity to come to the United States of America and pursue my Doctor of Philosophy in this great institution of Syracuse University. Without His grace and strength, it would have been impossible for me to complete this degree.

I am forever indebted to my advisor and mentor, Dr. Barry D. Davidson, for taking me under his wings these past few years and teaching me the art of scientific research. Without his unwavering support, motivation and commitment towards my entire course, I would not have been able to come this far. I am also deeply thankful to NASA Constellation University Institutes Project, the co-sponsors of this research under grant NCC3-989 with Claudia Meyer as the Project Manager. Without the financial support provided by NASA, this research would not have been possible. I would also like to thank the many faculty members and staff of Syracuse University for their valuable insights in my research problems or any help rendered to me otherwise. My deepest gratitude also extends to my family and friends all over the world for their continued good wishes, prayers and support during my entire course.

This work is dedicated to my parents, Mrs. Satya W. Singh and late Mr. Kanta B. Singh, for every sacrifice they made towards my education from my childhood days in the Republic of the Fiji Islands.

Abhendra K. Singh

Syracuse University, New York, USA.

Table of Contents

1.INTRODUCTION.....	1
2.LITERATURE REVIEW	6
2.1 Impact Types	7
2.2 Low Velocity Impact (LVI) vs. Quasi-Static Indentation (QSI).....	10
2.3 Damage Modes and Damage Evaluation Techniques.....	11
2.3.1 Damage Modes	12
2.3.2 Parametric Effects on the Sandwich Damage Modes.....	15
2.3.3 Damage Evaluation Techniques	19
2.4 Compression-After-Impact (CAI) Studies	20
2.5 Modeling of Sandwich Response Due to Impact	22
2.5.1 Spring-Mass Models.....	23
2.5.2 Energy Balance Models.....	25
2.5.3 Direct Plate Theory Model	27
2.5.4 Unloading Models	29
2.5.5 Finite Element Models.....	30
2.5.6 Modeling Summary	31
2.6 Summary	32
3.APPROACH.....	35
3.1 Research Objectives	35
3.2 Choice of Methodologies	37
3.3 Materials and Manufacturing	38
3.4 Test Matrix	44
3.5 Quasi-Static Indentation (QSI) Testing.....	46
3.6 Dent Measurements.....	49
3.6.1 Method Development	49
3.6.2 Validation of Method.....	51
3.6.3 Application of Method to Full-Sized Specimens	52
3.7 Delamination Measurements.....	56

4.LOAD-DISPLACEMENT RESULTS	57
4.1 8 Ply Results.....	59
4.1.1 QSI Tests with 25.4 mm Diameter Indentor.....	59
4.1.2 QSI Tests with 76.2 mm Diameter Indentor.....	65
4.2 16 Ply Results.....	71
4.2.1 QSI Tests with 25.4 mm Diameter Indentor.....	71
4.2.2 QSI Tests with 76.2 mm Diameter Indentor.....	76
4.3 Summary	81
5.DELAMINATION ASSESSMENTS	84
5.1 Delamination Measurements.....	85
5.2 8 Ply QSI Delamination Assessments.....	95
5.3 16 Ply QSI Delamination Assessments.....	103
5.4 Summary	119
6.DAMAGE RESISTANCE EVALUATIONS	121
6.1 8 Ply Damage Resistance Evaluations	122
6.1.1 Parametric Effects.....	124
6.1.2 Damage Resistance Metrics.....	131
6.2 16 Ply Damage Resistance Evaluations	136
6.2.1 Parametric Effects.....	138
6.2.2 Damage Resistance Metrics.....	146
6.3 Comparison of Results – 8 versus 16 Ply.....	150
6.4 Summary	152
7.EXPERIMENTAL DETERMINATION OF MODEL PARAMETERS	153
7.1 Experimental Determination of Face Sheet Properties	153
8.EXPERIMENTAL MASTER PLOTS.....	167
8.1 Experimental Master Plots	168
9.MODEL FORMULATION.....	179
9.1 Existing Models.....	180
9.2 Preliminary Assessments.....	182
9.3 Modeling Loading Regime 1: Zero Load to Core Crushing Onset Load.....	189
9.3.1 The Local Hertzian Indentation, w_h	189

9.3.2 Bending Deflection of the Face Sheet, w_0	191
9.4 Governing Equations – Rayleigh-Ritz Method of Energy Minimization	193
9.4.1 Assumed Displacement Field	197
9.4.2 Determination of the Equivalent Flat-nosed Indentor Radius, b	199
9.4.3 Effective Face Sheet Properties	200
9.5 Method of Solution.....	202
9.6 Modeling Loading Regime II: Core Crushing Onset Load to Delamination Onset Load	203
9.7. Property Degradation Due to Matrix Cracking and Delaminations	208
9.7.1 Degraded Lamina Properties Due to Matrix Cracking	208
9.7.2 Assumed Delaminating Interfaces	208
9.7.3 Reduced Equivalent Bending Stiffness, D_{res}	210
9.7.4 Reduced In-plane Radial Modulus, E_{res}	211
9.7.5 Residual In-plane Poisson’s Ratio, ν_{res}	212
9.8 Prediction of Delamination Onset Load.....	213
9.9 Loading Regime III: Delamination Onset Load to Peak Load Model	218
9.9.1 Correction of Peak Displacement	224
9.9.2 Linear Degradation of Face Sheet Properties	227
9.10 The Unloading Regime	233
9.11 Summary	238
10.MODELING RESULTS.....	239
10. 1 Dent Diameter and Dent Depth Results	239
10.2 Load versus Displacement Comparisons	246
10.2.1 8 Ply Specimens Indented with the 25.4 mm Diameter Indentor	246
10.2.2 8 Ply Specimens Indented with the 76.2 mm Diameter Indentor	251
10.2.3 16 Ply Specimens Indented with the 25.4 mm Diameter Indentor	258
10.2.4 16 Ply Specimens Indented with the 76.2 mm Diameter Indentor	265
10.3 Summary	272
11.CONCLUSIONS	274
12.FUTURE WORK.....	276
12.1 Damage Evaluation in the Transition Region	276

12.2 The Two-region Plate Model	277
APPENDIX A	281
APPENDIX B	282
APPENDIX C	284
APPENDIX D	287
APPENDIX E	288
APPENDIX F	289
APPENDIX G	290
APPENDIX H	292
APPENDIX I	301
APPENDIX J	313
References	317
VITA	328

List of Figures

Figure 2.1. Types of response during impact on plates. Source: Olsson [3].....	9
Figure 3.1. Schematic of a honeycomb core showing the core thickness, cell size and the ribbon direction.....	41
Figure 3.2. Typical panel dimensions after manufacturing and edge trimming (all dimensions in mm). ..	43
Figure 3.3. QSI test set-up, 8 ply sandwich specimen with the 76.2 mm diameter indenter.....	47
Figure 3.4. Ultrasonic dent measurement validation for an 8 ply small QSI specimen using the dial gauge indicator.	52
Figure 3.5. Typical dent profiles for the eight ply case using 25.4 mm (a) and 76.2 mm (b) diameter indentors.....	54
Figure 3.6. Typical dent profiles for the 16 ply case using 25.4 mm (a) and 76.2 mm (b) diameter indentors.....	55
Figure 3.7. Representative x-z and y-z surface profile for a 16 ply specimen indented with the 25.4 mm diameter indenter.	56
Figure 4.1. Schematic representing the general P-d plot for all specimens.	58
Figure 4.2. Representative P-d plots for the 8 ply specimens indented with the 25.4 mm diameter indenter.	59
Figure 4.3. Representative P-d plots for Q1-C1 and Q1-C2 8 ply specimens indented with the 25.4 mm diameter indenter.	61
Figure 4.4. Representative P-d plots for Q1-C1 and Q2-C1 8 ply specimens indented with the 25.4 mm diameter indenter.	63
Figure 4.5. Representative P-d plots for Q1-C2 and Q4-C2 8 ply specimens indented with the 25.4 mm diameter indenter.	64
Figure 4.6. Representative P-d plots for Q1-C3 and Q4-C3 8 ply specimens indented with the 25.4 mm diameter indenter.	64
Figure 4.7. Representative P-d plots for the 8 ply specimens indented with 76.2 mm diameter indenter..	66
Figure 4.8. Representative P-d plots for Q1-C1 and Q1-C2 8 ply specimens indented with 76.2 mm diameter indenter.	67
Figure 4.9. Representative P-d plots for Q1-C1 and Q2-C1 8 ply specimens indented with 76.2 mm diameter indenter.	69
Figure 4.10. Representative P-d plots for Q1-C2 and Q4-C2 8 ply specimens indented with 76.2 mm diameter indenter.	70
Figure 4.11. Representative P-d plots for Q1-C3 and Q4-C3 8 ply specimens indented with 76.2 mm diameter indenter.	71
Figure 4.12. Representative P-d plots for the 16 ply specimens indented with the 25.4 mm diameter indenter.	72
Figure 4.13. P-d plots for Q1-C1, Q1-C2 and Q1-C3 16 ply specimens indented with the 25.4 mm diameter indenter.	73

Figure 4.14. P-d plots for different face sheet layups with C1 core for the 16 ply specimens indented with the 25.4 mm diameter indenter.	75
Figure 4.15. P-d plots for Q1-C3 and Q4-C3 sandwich geometries for the 16 ply specimens indented with the 25.4 mm diameter indenter.	76
Figure 4.16. Representative P-d plots for 16 ply specimens indented with the 76.2 mm diameter indenter	77
Figure 4.17. P-d plots for Q1-C1, Q1-C2 and Q1-C3 16 ply specimens indented with the 76.2 mm diameter indenter.	78
Figure 4.18. P-d plots for different face sheet layups with C1 core for the 16 ply specimens indented with the 76.2 mm diameter indenter.	80
Figure 4.19. P-d plots for Q1-C3 and Q4-C3 sandwich geometries for the 16 ply specimens indented with the 76.2 mm diameter indenter.	81
Figure 5.1. C-Scan image, destructively obtained cross-sectional view, and corresponding 2D damage map in the 0° cut direction for a 8 ply Q1-C1 sandwich specimen indented with the 25.4 mm diameter indenter.	89
Figure 5.2. 3D damage map for the Q1-C1 specimen of Figure 5.1. Squares in the grids measure 5.00 mm x 5.00 mm.	91
Figure 5.3. C-Scan image, destructively obtained cross-sectional view, and corresponding 2D damage map in the 0° cut direction for a 16 ply Q4-C1 sandwich specimen indented with the 25.4 mm diameter indenter.	93
Figure 5.4. 3D damage map for the Q4-C1 specimen of Figure 5.3. Squares in the grids measure 6.35 mm x 6.35 mm.	94
Figure 5.5. Representative c-scan images and the interface by interface details for the four different 8 ply face sheet layups indented with the 25.4 mm diameter indenter.	97
Figure 5.6. Representative c-scan images of the Q1-C1 and Q2-C1 sandwich configurations for the 8 ply specimens indented with the 25.4mm diameter indenter at BVID load.	99
Figure 5.7. Representative c-scan images of the Q1-C1, Q1-C2 and Q1-C3 sandwich configurations for the 8 ply specimens indented with the 25.4mm diameter indenter at BVID load.	100
Figure 5.8. Representative c-scan images of the Q1-C1 and Q1-C2 sandwich configurations for the 8 ply specimens indented with the 25.4mm diameter indenter at BVID load.	102
Figure 5.9. Representative c-scan images of the Q2-C1 and Q3-C1 sandwich configurations for the 8 ply specimens indented with the 25.4mm diameter indenter at BVID load.	103
Figure 5.10. Representative c-scan images for the five different 16 ply face sheet layups indented with the 25.4 mm diameter indenter.	105
Figure 5.11. Interface by interface layups for the representative c-scan images for the 16 ply face sheet layups presented in Figure 5.10.	106
Figure 5.12. Representative c-scan images of the Q1-C1 and Q2-C1 sandwich configurations for the 16 ply specimens indented with the 25.4mm diameter indenter at BVID load.	108
Figure 5.13. Representative c-scan images of the Q1-C1, Q1-C2 and Q1-C3 sandwich configurations for the 16 ply specimens indented with the 25.4mm diameter indenter at BVID load.	110
Figure 5.14. Representative c-scan images for the five different 16 ply face sheet layups indented with the 76.2 mm diameter indenter.	112

Figure 5.15. Representative c-scan gate settings for the 16 ply delamination assessments.	113
Figure 5.16. Interface by interface layups for the representative c-scan images for the 16 ply face sheet layups presented in Figure 5.14.	114
Figure 5.17. Representative c-scan images of the Q1-C1, Q1-C2 and Q1-C3 sandwich configurations for the 8 ply specimens indented with the 76.2 mm diameter indenter at BVID load.	117
Figure 5.18. Representative c-scan images of the Q1-C1 and Q2-C1 sandwich configurations for the 16 ply specimens indented with the 76.2 mm diameter indenter at BVID load.	118
Figure 6.1. Results for average QSI force versus average dent depth for the 8 ply specimens.	126
Figure 6.2. Results for average QSI force versus average dent diameter for the 8 ply specimens.	126
Figure 6.3. Dent diameter versus dent depth for all the 8 ply specimen types.	128
Figure 6.4. Ratio of dent diameter to dent depth by specimen type for the 8 ply specimens.	129
Figure 6.5. Ratio of dent diameter to local chord length of the indenter for the 8 ply specimens.	130
Figure 6.6. Sketch illustrating local chord length definition.	131
Figure 6.7. QSI force vs planar area of delamination for the 8 ply specimens indented with the 25.4 mm diameter indenter.	132
Figure 6.8. Dent depth versus planar area of delamination for the 8 ply specimens indented with the 25.4 mm diameter indenter.	134
Figure 6.9. Ratio of planar area of delamination to dent area for the 8 ply specimens indented with the 25.4 mm diameter indenter.	136
Figure 6.10. Results for average QSI force versus average dent depth for the 16 ply specimens.	139
Figure 6.11. Results for average QSI force versus average dent diameter for the 16 ply specimens.	140
Figure 6.12. Dent diameter versus dent depth for all the 16 ply specimen types.	141
Figure 6.13. Ratio of dent diameter to dent depth by specimen type for the 16 ply specimens.	145
Figure 6.14. Ratio of dent diameter to local chord length of the indenter for the 16 ply specimens.	146
Figure 6.15. QSI force vs planar area of delamination for the 16 ply specimens.	147
Figure 6.16. Dent depth versus planar area of delamination for the 16 ply specimens.	149
Figure 6.17. Ratio of planar area of delamination to dent area for the 16 ply specimens.	150
Figure 7.1. Schematic showing honeycomb core stress-strain idealized behavior proposed by Minakuchi et al. [65] for loading-unloading of the core in the transverse direction.	159
Figure 7.2. Stress-strain behavior of C1 core for transverse compressive-tensile loading.	161
Figure 7.3. Stress-strain behavior of C2 core for transverse compressive-tensile loading.	162
Figure 7.4. Stress-strain behavior of C3 core for transverse compressive-tensile loading.	162
Figure 7.5. C1 core experimental stress vs. strain data for the compression and tensile tests for the determination of E_{zc} and E_{zt} respectively.	163
Figure 7.6. C2 core experimental stress vs. strain data for the compression and tensile tests for the determination of E_{zc} and E_{zt} respectively.	164
Figure 7.7. C3 core experimental stress vs. strain data for the compression and tensile tests for the determination of E_{zc} and E_{zt} respectively.	165

Figure 8.1. Plot of dent depths for the different 8 ply specimens using both the MTS machine data and the ultrasonic measurements.	170
Figure 8.2. Comparison of master plot with individual specimen data for 8 ply Q1-C1 specimens indented with the 25.4 mm diameter indenter.	171
Figure 8.3. Comparison of master plot with individual specimen data for 8 ply Q1-C1 specimens indented with the 76.2 mm diameter indenter.	172
Figure 8.4. Comparison of master plot with individual specimen data for 16 ply Q1-C1 specimens indented with the 25.4 mm diameter indenter.	173
Figure 8.5. Comparison of master plot with individual specimen data for 16 ply Q1-C1 specimens indented with the 76.2 mm diameter indenter.	174
Figure 9.1. Comparison of experimental 8 ply Q1-C1, 25.4 mm indenter diameter test results with Olsson's and Turk and Hoo Fatt's models.	185
Figure 9.2. Comparison of experimental 8 ply Q1-C1, 76.2 mm indenter diameter test results with Olsson's and Turk and Hoo Fatt's models.	186
Figure 9.3. Schematic defining the dent radius, equivalent flat-nosed indenter radius and the maximum dent depth during the indentation process.....	197
Figure 9.4. Schematic representing the variation of contact radius, b , with increasing load, P	200
Figure 9.5. Results for the modeling regimes described in Sections 9.3 and 9.6 for the 8 ply Q1-C1 specimens indented with the 25.4 mm diameter indenter.....	204
Figure 9.6. Results for the modeling regimes described in Sections 9.3 and 9.6 for the 8 ply Q1-C1 specimens indented with the 76.2 mm diameter indenter.....	205
Figure 9.7. Results for the modeling regimes described in Sections 9.3 and 9.6 for the 16 ply Q1-C1 specimens indented with the 25.4 mm diameter indenter.....	206
Figure 9.8. Results for the modeling regimes described in Sections 9.3 and 9.6 for the 16 ply Q1-C1 specimens indented with the 76.2 mm diameter indenter.....	207
Figure 9.9. Plot showing the loading regime model versus experimental results for the 8 ply Q1-C1 sandwich configuration indented with the 25.4 mm diameter indenter.....	220
Figure 9.10. Plot showing the loading regime model versus experimental results for the 8 ply Q1-C1 sandwich configuration indented with the 76.2 mm diameter indenter.....	221
Figure 9.11. Plot showing the loading regime model versus experimental results for the 16 ply Q1-C1 sandwich configuration indented with the 25.4 mm diameter indenter.....	222
Figure 9.12. Plot showing the loading regime model versus experimental results for the 16 ply Q1-C1 sandwich configuration indented with the 76.2 mm diameter indenter.....	223
Figure 9.13. Load versus dent radius plot for the different regimes in the loading phase of the model for the 8 ply Q1-C1 sandwich configuration indented with the 25.4 mm diameter indenter.....	224
Figure 9.14. Model versus the experimental results for the different A_d and A_i ratios, as defined by equation 9.30, for the 8 ply sandwich configuration indented with the 25.4 mm diameter indenter.....	227
Figure 9.15. Improved (linear degradation) post delamination onset regime model for the 8 ply Q1-C1 sandwich configuration indented with the 25.4 mm diameter indenter.....	229
Figure 9.16. Improved (linear degradation) post delamination onset regime model for the 8 ply Q1-C1 sandwich configuration indented with the 76.2 mm diameter indenter.....	230

Figure 9.17. Improved (linear degradation) post delamination onset regime model for the 16 ply Q1-C1 sandwich configuration indented with the 25.4 mm diameter indenter.	231
Figure 9.18. Improved (linear degradation) post delamination onset regime model for the 16 ply Q1-C1 sandwich configuration indented with the 76.2 mm diameter indenter.	232
Figure 9.20. Schematic showing core behavior during the unloading regime.	234
Figure 9.21. Model versus experimental unloading regime results for the 8 ply, Q1-C1 sandwich configuration indented with the 25.4 mm diameter indenter assuming uncrushing of the entire crush zone at every load.	237
Figure 9.22. Model versus experimental unloading regime results for the 8 ply Q1-C1 sandwich configuration indented with the 25.4 mm diameter indenter assuming linear increase in crush zone radius getting uncrushed from the peak load to zero load.	237
Figure 10.1. Q1-C1 8 ply model versus experimental P-d plot comparisons for specimens indented with the 25.4 mm diameter indenter.	248
Figure 10.2. Q1-C2 8 ply model versus experimental P-d plot comparisons for specimens indented with the 25.4 mm diameter indenter.	248
Figure 10.3. Q1-C3 8 ply model versus experimental P-d plot comparisons for specimens indented with the 25.4 mm diameter indenter.	249
Figure 10.4. Q2-C1 8 ply model versus experimental P-d plot comparisons for specimens indented with the 25.4 mm diameter indenter.	249
Figure 10.5. Q3-C1 8 ply model versus experimental P-d plot comparisons for specimens indented with the 25.4 mm diameter indenter.	250
Figure 10.6. Q4-C2 8 ply model versus experimental P-d plot comparisons for specimens indented with the 25.4 mm diameter indenter.	250
Figure 10.7. Q4-C3 8 ply model versus experimental P-d plot comparisons for specimens indented with the 25.4 mm diameter indenter.	251
Figure 10.8. Q1-C1 8 ply model versus experimental P-d plot comparisons for specimens indented with the 76.2 mm diameter indenter.	252
Figure 10.9. Q1-C2 8 ply model versus experimental P-d plot comparisons for specimens indented with the 76.2 mm diameter indenter.	253
Figure 10.10. Q1-C3 8 ply model versus experimental P-d plot comparisons for specimens indented with the 76.2 mm diameter indenter.	254
Figure 10.11. Q2-C1 8 ply model versus experimental P-d plot comparisons for specimens indented with the 76.2 mm diameter indenter.	255
Figure 10.12. Q3-C1 8 ply model versus experimental P-d plot comparisons for specimens indented with the 76.2 mm diameter indenter.	256
Figure 10.13. Q4-C2 8 ply model versus experimental P-d plot comparisons for specimens indented with the 76.2 mm diameter indenter.	257
Figure 10.14. Q4-C3 8 ply model versus experimental P-d plot comparisons for specimens indented with the 76.2 mm diameter indenter.	258
Figure 10.15. Q1-C1 16 ply model versus experimental P-d plot comparisons for specimens indented with the 25.4 mm diameter indenter.	259

Figure 10.16. Q1-C2 16 ply model versus experimental P-d plot comparisons for specimens indented with the 25.4 mm diameter indenter.	260
Figure 10.17. Q1-C3 16 ply model versus experimental P-d plot comparisons for specimens indented with the 25.4 mm diameter indenter.	261
Figure 10.18. Q2-C1 16 ply model versus experimental P-d plot comparisons for specimens indented with the 25.4 mm diameter indenter.	262
Figure 10.20. Q4-C1 16 ply model versus experimental P-d plot comparisons for specimens indented with the 25.4 mm diameter indenter.	264
Figure 10.21. Q5-C1 16 ply model versus experimental P-d plot comparisons for specimens indented with the 25.4 mm diameter indenter.	265
Figure 10.22. Q1-C1 16 ply model versus experimental P-d plot comparisons for specimens indented with the 76.2 mm diameter indenter.	267
Figure 10.23. Q1-C2 16 ply model versus experimental P-d plot comparisons for specimens indented with the 76.2 mm diameter indenter.	268
Figure 10.24. Q1-C3 16 ply model versus experimental P-d plot comparisons for specimens indented with the 76.2 mm diameter indenter.	269
Figure 10.25. Q2-C1 16 ply model versus experimental P-d plot comparisons for specimens indented with the 76.2 mm diameter indenter.	270
Figure 10.26. Q3-C1 16 ply model versus experimental P-d plot comparisons for specimens indented with the 76.2 mm diameter indenter.	271
Figure 10.27. Q5-C1 16 ply model versus experimental P-d plot comparisons for specimens indented with the 76.2 mm diameter indenter.	272
Figure 12.1. Schematic showing the proposed unloading path for further tests to investigate the damage modes in the transition region.	277
Figure A.1. Autoclave cycle used for sandwich panel curing.	281
Figure D.1. The edgewise compression test set-up used for the determination of the in-plane compliance, α_{11}	287
Figure E.1. The four point bend test set-up used for the determination of the flexural compliances, δ_{11} and δ_{12}	288
Figure F.1. Flat-wise compression test set-up for the core property determination.	289
Table AH.1. Values of k_1 for the different cases presented in Figure AH.1. Source [88]	293
Figure AH.2. Displacement ratio plots for the comparison of the bending energy solution to the exact small deflection plate solution with $poc=0$	295
Figure AH.3. Displacement ratio plots for the comparison of the bending energy solution to the exact small deflection solution for $P=0$	297
Figure AH.4. Displacement ratio plots for the comparison of bending and membrane energy combined solution to the exact large deflection plate solution with $poc=0$	299
Figure AH.5. Displacement ratio plots for the comparison of bending and membrane energy combined solution to the exact large deflection plate solution with $P=0$	300
Figure AI.4. Plot of equivalent Poisson's ratio values for the delaminated 8 ply Q1 laminate in the different angular directions.	310

List of Tables

Table 3.1. 8 ply face sheet layup information.....	40
Table 3.2. 16 ply face sheet layup information.....	40
Table 3.3. Thickness and density details of the different aluminum honeycomb cores used.	41
Table 3.4. Test matrix for the 8 Ply specimens tested with both the 25.4 mm and 76.2 mm diameter indentors.....	45
Table 3.5. Test matrix for the 16 ply specimens tested with both the 25.4 mm and 76.2 mm diameter indentors.....	46
Table 6.1.a Dent depth, dent diameter and planar area of delamination data for the 8 ply specimens indented with the 25.4 mm diameter indenter.	123
Table 6.1.b. Dent depth, dent diameter and planar area of delamination data for the 8 ply specimens indented with the 76.2 mm diameter indenter.	124
Table 6.2.a. Dent depth, dent diameter and planar area of delamination data for 16 ply specimens indented with 25.4 mm diameter indenter.	137
Table 6.2.b. Dent depth, dent diameter and planar area of delamination data for 16 ply specimens indented with 76.2 mm diameter indenter.	138
Table 7.1. The in-plane and flexural compliance values for the 8 ply Q1 face sheet layup.	157
Table 7.2 Published and adjusted IM7/8552 lamina properties.....	157
Table 7.3. Summary of honeycomb core properties.	166
Table 8.1. Comparison of the number of experimental specimen data available to the number of resulting master plots for the 8 ply specimens indented with the 25.4 mm diameter indenter.....	175
Table 8.2. Comparison of the number of experimental specimen data available to the number of resulting master plots for the 8 ply specimens indented with the 76.2 mm diameter indenter.....	176
Table 8.3. Comparison of the number of experimental specimen data available to the number of resulting master plots for the 16 ply specimens indented with the 25.4 mm diameter indenter.....	177
Table 8.4. Comparison of the number of experimental specimen data available to the number of resulting master plots for the 16 ply specimens indented with the 76.2 mm diameter indenter.....	178
Table 8.5. Summary of the original number of experimental P-d plots versus the reduced number of plots due to the development of the master plots.....	178
Table 9.1. Core foundational stiffness, kF, values for the different cores.	192
Table 9.2. Table of resulting sublaminates due to the assumed delaminations at the different interfaces for the 8 ply case.....	209
Table 9.3. Table of resulting sublaminates due to the assumed delaminations at the different interfaces for the 16 ply case.....	210
Table 9.4. Table of intact and residual bending stiffness values for both the 8 and 16 ply face sheets....	211
Table 9.5. Table of reduced in-plane bending modulus for the fully delaminated 8 ply face sheet laminates.	212
Table 9.6. Table of reduced in-plane bending modulus for the fully delaminated 16 ply face sheet laminates.	212

Table 9.7. Table of reduced in-plane Poisson's ratio for the fully delaminated 8 ply face sheet laminates.	213
Table 9.8. Table of reduced in-plane bending modulus for the fully delaminated 16 ply face sheet laminates.	213
Table 9.9. Predicted delamination onset loads, 8 ply specimens.	217
Table 9.10. Predicted delamination onset loads, 16 ply specimens.	218
Table 10.1. Comparison of the experimental versus predicted dent depths for the 8 ply case.	241
Table 10.2. Comparison of the experimental versus predicted dent depths for the 16 ply case.	242
Table 10.3. Comparison of the experimental versus predicted dent diameters for the 8 ply case.	243
Table 10.4. Comparison of the experimental versus predicted dent diameters for the 16 ply case.	244
Table 10.5. Summary of the percentage range of error for the dent depth and dent diameter predictions under the different test conditions.	245
Table 10.6. Summary of the average percentage error for the dent depth and dent diameter predictions under the different test conditions.	245
Table B.1. Damage and residual compressive strength data for preliminary tests of certain full-sized specimens tested with 12.7 mm and 25.4 mm diameter indentors.	283
Table C.1. Test results for the preliminary tests for the 8 ply small QSI specimens indented with the 25.4 mm diameter indenter.	284
Table C.2. Test results for the preliminary tests for the 8 ply small QSI specimens indented with the 76.2 mm diameter indenter.	285
Table C.3. Test results for the preliminary tests for the 16 ply small QSI specimens indented with the 25.4 mm diameter indenter.	285
Table C.4. Test results for the preliminary tests for the 16 ply small QSI specimens indented with the 76.2 mm diameter indenter.	286
Table AH.1. Values of k_1 for the different cases presented in Figure AH.1. Source [88]	293

Chapter 1

INTRODUCTION

Sandwich composites are stiff, light-weight structures that offer high resistance to compressive stresses and bending moments. Because of their high stiffness to weight ratio, sandwich composites are finding increasing use in both aerospace and marine applications. Sandwich composites usually consist of two thin but stiff face sheets and a relatively thick but light core. Commonly used sandwich composite constituents are laminates of glass and/or carbon fiber/epoxy face sheet, while core materials usually consist of polyvinylchloride, polyurethane, polyethylene and syntactic foams as well as nomex and aluminum honeycomb. In sandwich composites, the face sheets are typically bonded to the core by the use of an adhesive.

One of the major concerns with sandwich composite structures is impact damage. Impact damage is not considered so much of a threat in metallic structures because of the ductile nature of the metals which allows absorption of large amounts of energy. In contrast to metals, impact damage in sandwich composite structures are considered a great threat since most composites are brittle and can only absorb energy through elastic deformation and/or damage mechanisms and not through plastic deformation. Thus, the event of impact in sandwich composite structures results in different damage modes that seriously compromise the structural integrity of the structure. Some of these damage modes are matrix cracking, delamination, core crushing and fiber breakage. Common causes of impact damage in sandwich structures are accidental tool drop during service of the structure, hail, bird strike and debris strikes. These are usually impacts that are non-ballistic in nature and thus occur at a low velocity. Low velocity impact (LVI) in sandwich structures may result in external damage that evades the naked eye and thus may

remain undetected. The upper threshold of such undetected external damage is commonly known as “barely visible impact damage” (BVID). In other words, BVID is indicative of the maximum amount of damage that may exist undetected in practical structures. Undetected external damage in composite structures is generally accompanied by internal damage with potentially serious strength and stiffness reduction consequences. This can be catastrophic particularly in cases where the structure predominantly undergoes compressive loading. Thus, it is of great importance to understand the nature and extent of external and internal damage in composite structures with BVID and the strength reduction consequences of such impact damage.

The study conducted for this dissertation was part of a larger research effort in collaboration with Cornell University which focused on understanding the parametric effects of core density, core thickness, face sheet stacking sequence, face sheet thickness and indenter diameter on the damage and residual compressive strength of graphite/epoxy-aluminum honeycomb core sandwich structures subjected to conditions that produced BVID. The damage characterization studies, which is a major part of this dissertation and which involved evaluation of important damage modes that result due to LVI, was done in-house at Syracuse University. The compression-after-impact (CAI) studies, which involved experimental and numerical evaluation of post impact residual strength and failure modes of the sandwich structures, were done by fellow researchers, Dr. Michael M. Czabaj and Mr. Benjamin P. J. Hasseldine, as part of their dissertation at Cornell University.

The specific research conducted for this dissertation and presented in this thesis focuses on two major areas. Firstly, it focuses on the characterization of external and internal damage in graphite/epoxy-honeycomb core sandwich structures with BVID. The primary damage metrics that were of interest were the size of the external “dent”, characterized by the damage metrics of

dent diameter and dent depth, as well as the extent of delamination in the face sheet. The effects of the different parameters of core density, core thickness, face sheet stacking sequence, face sheet thickness and indenter diameter on the resultant damage, as defined by these damage metrics, were also studied. These parameters were of interest both in understanding their influence on the extent of damage as well as on the post-impact compressive strength and damage failure modes. The experimental findings presented in this dissertation are expected to guide the development and refining of models for post-impact compressive strength study carried out by fellow researchers at Cornell University, with the overall goal of developing a clear mechanistic and parametric understanding of the effects of different variables on impact damage and compression-after-impact (CAI) strength.

Secondly, the dissertation focuses on the development of an analytical model that could correctly capture the deformation response of the sandwich structure for indentation loading up to the BVID load threshold as well as subsequent unloading. The knowledge on damage attained from the experimental evaluations was used for the development of this model. An analytical model is chosen over a numerical model because of the complexity in the development of numerical models. Through a reproduction of the load versus displacement response of the sandwich structure due to indentation loading and subsequent unloading, the model is able to predict the permanent dent depth of the sandwich structure loaded up to the BVID threshold load. In making the dent predictions, the model is also able to provide additional information on the diameter of the external dent of the sandwich structure. Based on the damage metrics of dent diameter and dent depth, the model is expected to help determine the most damage resistant sandwich configuration for impact damage. Here, damage resistance of a structure refers to the ability of the structure to minimize the extent of damage due to an external event like impact.

These damage metrics of dent diameter and dent depth are also of interest to the CAI study to see if there is any correlation between these damage metrics and the most damage tolerant structure. Here, damage tolerance refers to the ability of a damaged structure to remain in service without undergoing catastrophic failure.

A literature review on the response and damage of both monolithic laminates and sandwich composites due to LVI was conducted in order to understand the various research findings already known in this field and, in doing so, help define a clear path for this research. Chapter 2 of this dissertation presents this literature review. The primary focus are on the different types of impact, comparisons between LVI and QSI, the different damage modes and the influence of different parameters on these damage modes, the damage evaluation techniques, and CAI studies and modeling of sandwich response due to impact or indentation. The findings in the review are used to guide both the experimental and modeling approaches used in this study. Details of the experimental approach are presented and discussed in Chapter 3, where the procedure for determining the dent depths and dent diameters is also described. Chapter 4 discusses the influence of the different parameters on the sandwich response, which is determined by the experimentally measured load and displacement results during indentation load. The load versus displacement results of the different sandwich configurations are compared and discussed in this chapter. Chapter 5 presents and discusses the delamination assessment results obtained through non-destructive and destructive evaluation techniques with primary focus on the shape, size, distribution and extent of delamination in the different sandwich configurations. The procedure for the measurement of planar area of delamination is also described in Chapter 5. The ability of the different sandwich configurations to resist damage based on the different damage metrics of dent depth, dent diameter and planar area of

delamination is discussed in Chapter 6. Chapter 7 presents the experimental determination of certain parameters that were needed for the development of the analytical model. The procedure for obtaining the “experimental master plots” is described in Chapter 8. Here, experimental master plots are single representative plots of several different test specimens from the same sandwich configuration that were tested at the same load level, and which are used for assessment of the models predictions. Chapter 9 presents the derivation of the analytical model, and Chapter 10 presents model predictions for the different sandwich configurations. The major conclusions of this research as well as proposals for future work are addressed in Chapter 11 and Chapter 12 respectively.

Chapter 2

LITERATURE REVIEW

Introduction

A significant number of papers have published in the literature on the response and damage of both monolithic laminates and sandwich structures due to impact. Early works in this area were primarily on monolithic laminates, but recent years have seen an increase in the number of works published on the impact of sandwich structures. These publications include experimental and computational evaluations on the response and damage of sandwich structures for both high and low-velocity impacts.

The state of knowledge already available in this field is presented through this review which in turn is expected to clearly define the path for this dissertation and the overall contribution the research outcomes being reported in this dissertation is expected to make to the advancement of knowledge in this field. The review presented in this chapter therefore discusses the different topics of interest that have a direct relation to low velocity impact (LVI) damage. These topics of interest, presented through various sub-sections in the chapter, include types of impact, comparisons between LVI and quasi-static indentation (QSI), the different damage modes that have been observed in composite structures due to impact, the effects of different parameters on these damage modes and the damage evaluation techniques that are prominently used for damage characterization of impacted composite structures. A review of the compression-after-impact (CAI) studies is also presented that discusses the effect of different parameters on the post-impact residual strength and failure modes of damaged structures. This is followed by a review on the models developed and published in the literature for modeling the

deformation response of sandwich structures due to impact. At the end of the chapter, a brief summary of review findings is presented that both establishes the need for further research in this field as well as guides the approach for the research conducted for this dissertation.

2.1 Impact Types

Impact of composites can be defined as the physical encounter a foreign object travelling with a certain velocity makes with the external surface of a composite structure. Impact types are usually classified as high velocity (ballistic) or low velocity. Both types are dynamic in nature; however, as will be discussed later, low velocity impacts can also be reasonably approximated as quasi-static since they manifest response characteristics that are similar to what would be seen if the structure is statically loaded. Examples of high velocity impact by foreign objects are fragments from blast debris or bullets in a military scenario; alternatively, accidentally dropping a tool during normal service use, hail, bird strike, debris and various other strikes can be considered as LVI. There is no consensus in the literature using the different parameters of velocity, impact force or energy as the distinguishing criteria between high and low velocity impacts. That is, the differentiation is somewhat subjective and different researchers have put forward different suggestions. Both impact velocity^{1,2} as well as extent of damage³ are used to categorize between high and low velocity impacts.

Davies and Zhang [1] suggest that velocities higher than 20m/s can be considered ballistic, while Schoeppner and Abrate [2] consider low velocity impact events to be having velocity lower than 40m/s. Olsson [3] uses damage extent as the guiding criteria in distinguishing high velocity impacts from low velocity impacts. According to Olsson, impacts that cause penetration could be considered high velocity impacts while those that do not cause penetration could be considered low velocity impacts. The impact event produces elastic waves

that propagate from the point of impact in the material and Olsson [3] discusses these various theories of wave propagation in detail. He suggests that for impact times on the order of the time needed for the waves to travel through the specimen's thickness, the laminate response is dictated by three dimensional wave propagation. A schematic of this is shown in Figure 1a. These dilational wave propagations occur where impact times are very short and as such, are usually synonymous with high velocity impacts. According to Olsson, in most cases these three dimensional waves result in detectable and extensive (penetrating) damage. For impact times which are slightly longer, the response according to Olsson is initially governed by flexural and shear waves. This wave propagation is presented by the schematic in Figure 1b and are synonymous with intermediate velocity impacts. This results in damage that is not as excessive as that caused by high velocity impacts. For impact times that are much longer than that needed by the waves to reach the plate boundaries, the lowest vibration mode of the impactor-plate system governs the response. This third type of response is called quasi-static [3] since the plate deflections exhibit the same kind of behavior as would be seen in a purely static case. The schematic in Figure 1c shows the wave propagation in this quasi-static response. Barely visible impact damage (BVID) is usually associated with the types of responses shown in Figure 1c. Olsson [3] also introduces impactor-laminate mass ratios as a way of defining impact events. It is shown that in the case of "small mass impactors", defined by the impactor mass being less than one-fifth of the mass of the impact affected plate area, impact response is dominated by flexural waves as in the case of intermediate velocity impacts. Likewise, it is shown that quasi-static impact response occurs when the impactor mass is at least twice as large as the impact affected plate area. Consistent with Olsson, Swanson [4] also shows that an impactor-laminate mass ratio greater than 2 is a sufficient condition for quasi-static response.

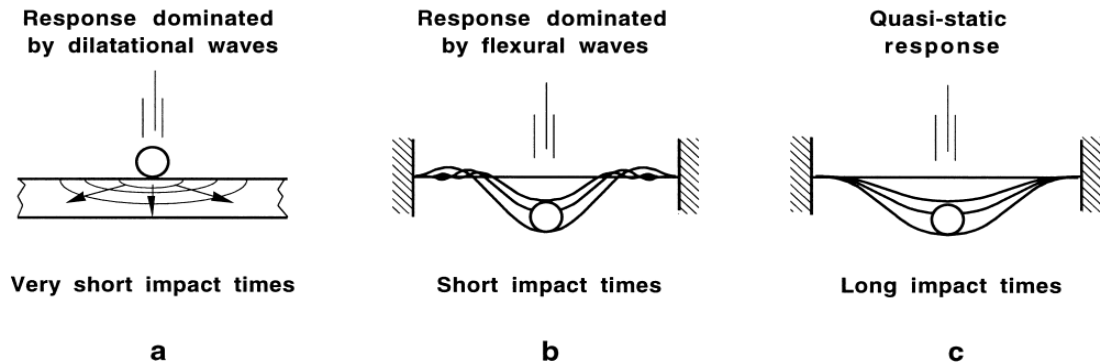


Figure 2.1. Types of response during impact on plates. *Source:* Olsson [3]

The classification of impact based on the different types of impact responses is directly related to the level of damage that is created in an impacted structure. . The level of damage required for this research is damage that is barely visible to the naked eye. As explained in chapter 1, BVID is an indirect measure of the maximum amount of damage that may exist undetected in practical structures. A ballistic impact with very short impact times causes extensive damage which clearly exceeds the damage requirements for this research. An intermediate velocity impact, as demonstrated by Figure 1b, results in damage not as extensive as high velocity but can be in excess of the damage required for this research. A quasi-static response, which has longer impact times, results in lesser amount of damage and is therefore the suitable plate response to external loading that would help create the level of damage required for this research.

2.2 Low Velocity Impact (LVI) vs. Quasi-Static Indentation (QSI)

In practical structures, damage that is barely visible is usually caused by impacts with a relatively low velocity. Different researchers have shown that for BVID, QSI tests essentially show the same response and damage of the sandwich structure as LVI tests.⁵⁻⁸ Therefore QSI tests have been used as a convenient substitute for LVI tests when creating damage in a sandwich structure in the vicinity of BVID. QSI tests are also advantageous over LVI tests in that they are easily implementable, allow for controllable and consistent levels of damage to be created and can be more readily used to identify the sequence of damage progression as compared to LVI tests.

Williamson and Lagace [5] show that the static indentation and impact tests produce the same deformation response and damage characteristics with maximum contact force as the key parameter in the event. This outcome, according to them is independent of the support condition. The similarity in damage produced by LVI when compared to QSI is also reported by Herup and Palazotto [6]. However, they do point out that static and dynamic tests compare better for thinner face sheets than thicker face sheets. Their results suggest that the dynamics of the impact becomes more important with increasing face sheet thickness. This is expected as the additional mass of a thicker face sheet increases the inertia of the specimens. Li et al. [7] show that damage areas compare well between QSI and LVI tests for low energy levels when the comparison is made at the maximum force, but tend to differ for higher energy levels. Ferri and Sankar [8] report that LVI and QSI tests show similar trends in how the sandwich responds to external loading, except they do differ slightly due to the viscoelastic nature of the foam core which they use in their experimental work.

The literature iterates that the deformation response of the sandwich structure as well as the damage created is similar for LVI and QSI tests when damage is considered at BVID level. Since the damage required for this research is in the vicinity of BVID, the affirmation by multiple studies creates the premise for considering QSI tests as an equivalent and reasonable substitute for LVI tests in this research. The level of damage is also easily controllable in QSI tests as compared to LVI which is vital for preventing excessive damage that would be contrary to the interests of this research. From the viewpoint of modeling, QSI tests are again advantageous as they more readily help understand the fundamental progression of damage, as conveyed by the load-displacement results, when compared to LVI tests.

2.3 Damage Modes and Damage Evaluation Techniques

Damage in sandwich structures undergoing LVI or QSI exist in different modes and have direct strength reduction consequences on the structure.⁹⁻¹¹ The knowledge of different damage modes that exist in sandwich structures is imperative to this research both from the viewpoint of characterization of damage as well as their relationship, if any, to the post-impact strength reduction and failure modes. This section presents a review of the different damage modes that have been observed and reported in the literature for both monolithic laminates and sandwich structures undergoing low velocity impact. The effects of the different parameters of indenter shape and size, face sheet thickness, face sheet layup, core density and core thickness on the nature and extent of damage is also reviewed since these parameters are of great interest to the post-impact strength studies. A brief review of the prominent damage evaluation techniques, both destructive and non-destructive, is also presented.

2.3.1 Damage Modes

For damage in the vicinity of BVID, the common damage modes that have been reported in monolithic laminates are matrix cracks and delaminations. In addition to these damage modes, sandwich composites also show core crushing for damage within the vicinity of BVID. Fiber breakage in the case of both monolithic laminates and sandwich structures, and face-sheet-to-core debonding only in the case of sandwich structures are two other composite damage modes that exist. However, these damage modes are synonymous with high or intermediate velocity impacts and may not exist when external damage is within the vicinity of BVID.

Matrix cracks are usually the first damage modes that occur in composites undergoing low velocity impacts. These matrix cracks also serve as starting points for delamination initiation and growth.^{2,12-15} Matrix cracks in monolithic laminates are generally divided into two categories – shear cracks and bending cracks.¹⁵ Shear cracks originate near the indenter-face sheet contact periphery at the top-most plies and grow increasingly away from the impacted area as one goes deeper down into the laminate (i.e. further from the impacted surface). Bending cracks generally occur directly beneath the indenter but at plies that are further away (laminate depth wise) from the indenter end of the face sheet. A number of studies have attempted to address the complex issue of the interactions between matrix cracks and delaminations, explaining the phenomena that govern the formation of delaminations from the matrix cracks.¹⁵⁻¹⁷

Delamination is a major damage mode in both monolithic laminates and sandwich structures and they directly affect the strength and life of the structure. Delaminations usually are lemniscates (“peanut shaped”) or oblong with their major axis oriented in the direction of the back surface ply (i.e., the ply a delaminating interface that is further away from the impacted end) in both monolithic laminates and sandwich composites.^{12,14,18-21} Delaminations may occur at

many interfaces, but apparently never between two plies with the same fiber orientation.¹⁴ Delaminations between consecutive interfaces are generally connected via matrix cracks.¹⁴⁻¹⁵ Delamination size in monolithic laminates have been observed to increase with increasing through-the-thickness distance from the impacted surface, with the largest delaminations at or near the back surface of the laminate.^{12,19-20} However in sandwich composites, as one progresses in the through-thickness direction from the impacted surface, there is a tendency for the delaminated area to initially increase up to some maximum value, and then decrease as the core is approached.¹²⁻¹³ It is unclear however whether this observation is a function of face sheet thickness or loading force.

Core crushing is another major failure mode due to the impact or indentation of sandwich composites. Core crushing is usually local to the impact region. During crushing, the core dissipates a significant portion of the transferred energy.²²⁻²³ Core crushing is a permanent damage mode that cannot be reversed. Not much work has been reported on the mechanism leading to core crushing in sandwich structures. Gibson and Ashby [24] discuss the deformation mechanisms in both foam and honeycomb cellular structures undergoing transverse compressive loading. For foam cellular structures undergoing transverse compressive loading, they show linear elastic behavior at low loads followed by a long “collapse plateau” as the load increases. This collapse plateau is by elastic buckling in elastomeric foams such as rubber, by the formation of plastic hinges in foam which yields such as metallic foam, or by brittle crushing in brittle foam such as a ceramic. The behavior in honeycomb cellular structures according to Gibson and Ashby [24] differ slightly from foam core. In honeycomb cellular structures, plastic buckling kind of behavior of the cell walls happen with increasing load leading to the final failure mode of tearing or crushing.

Two other sandwich damage modes that exist but are not commonly seen with low velocity impacts or when external damage is in the vicinity of BVID are face sheet-to-core debonding and fiber breakages. These damage modes are more synonymous with intermediate or high velocity impacts. Face sheet-to-core debonding may occur due to manufacturing defects which result in pre-existing debonded sites, or due to brittle fracture of the adhesive during service which subsequently initiates debonding.²⁵ Debonding causes the face sheet to start losing its lateral support from the core, and further debond propagation with increasing load may result in the structure completely losing its structural integrity and failing catastrophically. Damage events like impact enhance face sheet to core debonding.²⁵⁻²⁶ Fiber breakage is a dominant failure mode in high velocity impacts where impactor penetration in the face sheet enhances it.^{8,14} Fiber breakages usually occur directly under the impactor contact point and depend on the mass, velocity or energy of the impactor.

The key damage modes that have been reported in literature for damaged sandwich structures are matrix cracking, face sheet delamination, core crushing, face sheet-to-core debonding, and fiber breakage. Of these damage modes, those that likely exist in sandwich structures that have external damage in the vicinity of BVID are matrix cracking, face sheet delamination and core crushing. Pre-existing damage in sandwich structures influence the strength of the sandwich structure and drive the post-impact failure modes. Say for instance, the common post-impact compressive failure mode of delamination buckling is clearly driven by pre-existing delaminations in the sandwich structure. Likewise, pre-existing dent may result in unstable dent growth upon compressive loading and eventually lead to catastrophic failure of the structure. These are crucial damage modes that need to be characterized in the damage study, both to provide a metric for damage as well as to understand their influence on the post-impact

compressive strength and failure modes. Eventually, these crucial damage modes need to be incorporated in a CAI model where the competing failure modes driven by the pre-existing damage is expected to help correctly predict the residual compressive strength of the sandwich structure. Different parameters affect the extent of damage in the sandwich structure and the effects of various parameters on these damage modes are discussed in Section 2.3.2. Section 2.3.3 reviews the common damage evaluation techniques that have been used in literature for the evaluation of damage in the composite structures. The discussion on damage is closed by a review of the CAI study presented in Section 2.4. The section sheds light on the importance of the damage study to the CAI study through a review of the prominent post-impact failure modes which are clearly driven by pre-existing damage in the sandwich structure. A brief discussion on the influence of the different parameters on the post-impact failure modes is also presented in this section.

2.3.2 Parametric Effects on the Sandwich Damage Modes

Different parameters have an effect on the nature and extent of external and internal damage in the sandwich structures. The effect of different parameters on the damage as well as post-impact strength reduction of the sandwich structure is of interest to this research so that the combination of the different parameters that govern the most damage resistant and damage tolerant structures can be evaluated. The different parameters that are reviewed in this section are the indenter shape and size, face sheet layup, face sheet thickness, core density, core thickness and the support (boundary) condition of the specimens undergoing impact.

Indenter shapes and sizes have a significant effect on the extent of both external dent as well as internal damage.^{5,27-30} Different impactor shapes simulate different kinds of impacting objects in real life. Based on their shapes, impactors can be broadly classified as blunt or sharp

impactors. Likewise, based on their sizes, impactors can also be broadly classified as small or large. The common indenter shapes are flat ended²⁷⁻²⁸, conical²⁸, spherical^{8,34-36} or hemispherical^{12,31}. The differences in external dent size due to different indenter sizes and shapes result from the different contact areas and associated pressure distributions. Flat-ended indentors produce large external dents with usually the onset of delaminations at the indenter edges, while hemispherical indentors show smaller sized external dents with the onset of delaminations at the indenter apex.^{27,29} Conical indentors with a sharp tip also show smaller external dents and a smaller area of core crushing compared to both flat-ended and hemi-spherical indentors.²⁸ For the same load applied via hemispherical indentors of different sizes, smaller indentors result in larger dent depths and more face sheet and core damage than larger indentors.⁵

Increasing the face sheet thickness increases both the flexural rigidity as well as the local contact resistance of a sandwich panel. For a fixed impact event and core, it has been shown that an increase in face sheet thickness results in a decrease in externally visible dent area.³¹ This has been attributed to the greater stiffness and hence “spring back” of thicker face sheets. Herup and Palazotto [6] used face sheet thicknesses varying from 4 ply to 48 ply for their indentation and impact tests on sandwich structures. For the thickness of nomex honeycomb core used, which was 12.7 mm, they found that incipient damage was due to the crushing of the core, irrespective of face sheet thickness. However, the load at which core crushing began increased with increasing face sheet thickness. Tsotsis and Lee [32], also showed that increasing the face sheet thickness increased the threshold load for core crushing. Anderson and Madenci [33] also examined the low velocity impact response of simply supported sandwich panels with varying face sheet thicknesses. They showed that the peak impact force increased with increasing face sheet thickness. Hoo Fatt and Park [34] also showed that for different boundary conditions of

clamping, simply supported or a rigid substrate, increasing the face sheet thickness increased the failure load threshold of the sandwich panels. Zhou et. al [27] investigated the effect of thicker face sheets in load transfer between the top face sheet and the core, and thus identifying the influence of face sheet thickness on the evolution of damage. They showed that increasing the face sheet thickness increased the load level at which the first load drop occurred, as well as the ultimate damage load. It was also reported by their investigation that the amount by which the load dropped at the onset of damage became smaller with the thinner face sheets.

Several researchers have attempted to study the effects of face sheet layup on the extent of delamination damage in composite laminates. Nothing has been reported on the trends being any different in sandwich composites. It has been commonly reported that delamination area increases with increase in ply angle change between consecutive plies at a delaminating interface.^{12,35} It is however not clear if this is restricted to some range of face sheet thicknesses or the number of plies. The increase in delamination size due to an increase in ply angle change is governed by an increase in bending stiffness mismatch. Finn et al. [36] also studied the effect of the thickness of the “back ply group” on the extent of delamination on composite laminates. Here, back ply group refers to the group of unidirectional plies on the bottom side of the laminate opposite to the impacted end. In this investigation, 16 ply laminates of layup $[0_n/90_{(8-n)}]_s$, where n is allowed to vary from 1 to 7 in order to increase the thickness of the “back ply group” (the group of 90° plies in this specific case), were subjected to transverse impact loads. It was observed that the delamination size at the interface between the 0° and 90° ply groups increased with the increase in the thickness of the back ply group. The effects of core density and thickness on sandwich damage for the different boundary conditions have been reported much in literature. Regardless of the boundary condition and for a constant face sheet and core thickness, it has

been shown that an increase in core density increases the core crushing threshold load³²⁻³³ and results in an overall smaller external dent area.^{11,27,37} The planar area of delamination has been observed to decrease for increasing core density for simply supported boundary conditions^{12,38} and increase with increasing core density when the sandwich is supported on a flat rigid substrate³⁷. Here and subsequently, the term “planar area of delamination” is used to denote the two-dimensional area required to encapsulate the delaminated area of the “stack of delaminations” as viewed from the impacted surface. This result is typically obtained by c-scanning. When the impact event, face sheet type and core density are held constant, it has been reported that – for clamped boundary conditions – the external dent area decreases with increasing core thickness.^{31,39} For simply supported boundary conditions, sandwich specimens with thicker cores have been observed to have a greater planar area of delamination than those with thinner cores.⁴⁰

It is evident from the literature that the variation of different parameters has a significant effect on sandwich damage. Flat-ended indentors show large external dents and core crush area compared to sharp tip indentors. For the same load applied, smaller indentors result in larger dent depths as well as face sheet and core damage as compared to larger indentors. The load at which the core crushes also increases with increasing face sheet thickness and core density. For any delaminating interface, the larger the ply angle change, the more the planar area of delamination. The extent of planar area of delamination is also dependent upon the boundary condition of the sandwich structure where it is shown that the delamination area decreases with increasing core density for simply supported boundary condition while increases with increasing core density for clamped boundary condition. The influence of the different parameters on the level of damage created is of interest to this research both from the viewpoint of damage itself as well as the post-

impact residual strength of the sandwich structure. With the background laid by the review presented in this section, an independent investigation on the effect of these parameters on damage that is characterized by dent diameter, dent depth and planar area of delamination is presented in this dissertation.

2.3.3 Damage Evaluation Techniques

The damage metrics that are of interest to this research and that need to be evaluated are the size of the external dent, both diameter and depth-wise, as well as the planar area of delamination. Evaluation of these damage metrics present a measure for damage as well as provide the necessary damage information that can be incorporated in a CAI model for the prediction of residual compressive strength of the sandwich structure. Both destructive and non-destructive techniques have been used in the literature for qualitative and quantitative analysis of internal and external damage. While non-destructive techniques preserve the specimen from permanent destruction, it is limited in many instances with respect to capturing information on the full extent of internal damage. Non-destructive techniques are also more expensive than destructive techniques. Destructive techniques are useful for obtaining a more complete picture of internal defects and delaminations in a composite structure except that they come at the cost of the loss of the structure. Also, errors made while destroying the specimen are non-reversible and can affect data interpretation.

Some of the established non-destructive techniques include X-radiography,^{8,40-41} ultrasonic scan^{20,42-44}, neutron radiography,⁴⁴ eddy currents,⁴⁴ optical holography,⁴⁴ acoustic holography⁴⁴ and thermography.⁴⁴⁻⁴⁵ Out of these, ultrasonic scans are probably the most widely used for the characterization of internal damage that exist in the form of delaminations.

Ultrasonic scans use high frequency sound waves for flaw detection in composite structures.

Three of the common ultrasonic scan techniques are the A-, B- and C- scans,^{20,42-44} of which the C-scan is the most popular especially for delamination detection. Some of the common destructive techniques used in literature for composite damage characterization are section microscopy^{27,40,42} and the deply technique⁸. Section microscopy involves cutting through the damage section and characterizing matrix cracks, delaminations and/or core crushing using a microscope. Deply technique involves careful removal of the plies one after the other in order to see the extent of delamination or other observable damage in the inner plies of a composite structure.

While dent diameters and dent depths can be determined non-destructively, the full extent of delamination determination requires a combination of both destructive and non-destructive damage evaluation techniques. The c-scan, which is one of the most popular delamination evaluation techniques, is insufficient in providing information on the full extent of delamination due to shielding (blocking) of deep interface delaminations by shallow interface delaminations. One constraint of the research presented in this dissertation is that the damaged specimens cannot be destroyed as they are required for the CAI study. This brings to the fore the heavy reliance on non-destructive damage evaluation techniques for the evaluation of damage in this research. However, limited destructive evaluations on a few specimens are needed and useful in order to get a fuller picture of delamination damage in the sandwich structures.

2.4 Compression-After-Impact (CAI) Studies

The effect of damage created by LVI on the strength of a sandwich structure is well known.⁹⁻¹¹ Presence of BVID in a sandwich structure can lead to failure of the structure at a fraction of design load through a combination of different failure modes that are driven in large by the pre-existing damage in the sandwich structure. The prominent failure modes by which

sandwich structures fail under post-impact compressive loading are unstable dent growth, face-sheet kink band formation and propagation, delamination buckling and growth as well as compressive fiber failure.^{9-11,46-49} From the viewpoint of CAI modeling, implementation of pre-existing damage in the model is instrumental in predicting the post impact residual compressive strength of the sandwich structure.

The residual compressive strength as well as the type of failure mode in a damaged sandwich structure is also influenced by different parameters. Sandwich structures with thin face sheets may fail by progressive core crushing followed by unstable dent growth, kink-band formation and propagation or face sheet fracture.^{10,46-49} while specimens with thicker face sheet likely fail due to unstable dent growth leading to fiber fracture.^{10,46} Sandwich specimens with relatively thin face sheet also show increasing compressive strength with increasing core density and thickness.^{10,46} Unstable dent growth is especially common in panels with relatively low damage⁴⁶. While indenter geometry has a clear effect on both the extent of damage and the post-impact compressive strength,²⁷⁻²⁹ the effect of indenter diameter on compressive strength is said to be small or insignificant for low level of damage.^{10,45} However with increasing level of damage, the compressive strength is said to increase with increasing indenter diameter.^{10,45-46}

The different types of compressive failure modes of damaged sandwich structures as well as the effect of the different parameters on the post-impact compressive residual strength and failure modes of the sandwich structure guided most of the choices that were made with regards to the overall approach of this research. The damage metrics of dent diameter, dent depth and planar area of delamination were equally important to the CAI study as they were to the damage study since they directly influenced the prominent post-impact failure modes. Different parameters have an effect on the residual compressive strength and failure modes of damaged

sandwich structures. Therefore, as much as understanding the effect of different parameters on the nature and extent of damage was vital to the damage study, understanding their effects on the post-impact compressive strength and failure modes was vital to the CAI study.

2.5 Modeling of Sandwich Response Due to Impact

Experimental work is usually time consuming, expensive and destructive. Thus, there is an increasing need for models that convey essential information that is otherwise determined experimentally. Dent diameter, dent depth and planar area of delamination information are damage metrics of interest. Predictions of these damage parameters are important both as a measure for damage as well as in the CAI modeling work. The model for delamination prediction is not presented in this dissertation but rather is left as a future proposal in what has been called a “two-region plate model” in Chapter 12. The model that is proposed in this dissertation predicts the other two damage metrics of dent depth and dent diameter through a reproduction of the load versus displacement response of the sandwich structure undergoing indentation loading that creates damage within the vicinity of BVID. The dent depth results are predicted directly from the load versus displacement results and since dent diameter is an implicit function of dent depth, this information is also provided by the model.

Before the model was developed in this dissertation, a literature review was first carried out. The purpose of the review was to explore the various methods that already exist in literature for modeling the response of sandwich structures to indentation or impact loading. The knowledge attained on the existing models therefore guided the development of an improved model in this dissertation. This literature review is presented and discussed in this section.

While a lot of work has been published in literature on modeling impact of monolithic laminates, most of it is presented in the review by Abrate [50], recent years have also shown a steady increase in publications related to modeling of impact in sandwich composites. The obvious difference between a monolithic laminate and a sandwich is the presence of the core which has a significant effect on the impact response of sandwich composites. Some of the popular models that are presented in literature that model the response of sandwich composites to LVI are spring-mass- and/or damper models, energy balance models, mechanics based engineering methods and finite element models. Each of these modeling techniques has their own advantages and disadvantages that are discussed in this section on modeling. There continues to remain much room however for further improvement with regards to developing more appropriate models for sandwich response to LVI/QSI.

2.5.1 Spring-Mass Models

Spring–mass models have been used in the past for the analysis of impact response of composite materials. In the spring-mass models, springs are used for the representation of effective structural stiffness of the impactor-plate system. Most of the spring-mass models are either single degree of freedom⁵¹⁻⁵³ or two degree of freedom models.⁵³⁻⁵⁵ The spring-mass models proposed in literature are solved both numerically and analytically (in closed form).

Shivakumar et al. [54] propose a two-degree-of-freedom model that is solved numerically by the Newton-Raphson method. The model has four springs that respectively represent bending, shear, membrane, and contact rigidities for a circular plate undergoing impact. Gong and Lam [55] propose an analytical, closed form solution based on the two-degree-of-freedom spring-mass model for the impact of a composite laminate that attempts to determine the history of contact force produced during impact. Feraboli [52] proposes a modified single degree-of-

freedom spring-mass model for damage development in sandwich structures which is empirical in nature as the model is heavily dependent upon unknowns that have to be determined experimentally. Anderson [53] proposes a single-degree-of-freedom model for large mass impact on composite sandwich laminates. Stiffness parameters needed for the working of this model were solved numerically through three-dimensional quasi-static contact analysis of indentation of a rigid sphere on a sandwich laminate. A damper was included in their model as a representation for the viscoelastic behavior of the core. All these spring-mass models mostly exclude the transverse flexibility and the structural damping of the core in the sandwich panels during impact and cease to be valid after damage initiation. Thus, they fail to more accurately capture sandwich response post damage initiation. To include the effects of the core, Malekzadeh et al. [56] proposed a new equivalent three degree-of-freedom spring-mass-damper model for the prediction of low velocity impact response of composite sandwich panels with transversely flexible core. In this, they attempted to include the transverse flexibility and structural damping of the core and eventually proposed a numerical solution that models the contact behavior of the impactor with the panel. Their model results compared well with the experimental results.

One of the major limitations of spring-mass models is correctly accounting for the inelastic processes when damage is created since the spring-mass models are highly dependent upon the elastic material behavior. While in the initial low load regime these models give good results, the model accuracy is compromised post the onset of inelastic events both in the core and the face sheet. For instance, the core for a small strain range behaves elastically and then undergoes plastic deformation upon crushing. This has to be properly accounted for in the model. Also, it is difficult to implement the change in face sheet laminate properties due to increasing non-linearity with face sheet damage. While improved results have been obtained through the

addition of a damper in the models that represent viscoelastic core behavior,⁵³ correctly implementing the inelastic effects in the face sheet continues to remain an issue. Because of the increasingly non-linear behavior of the sandwich structure due to the onset and progression of damage, the spring-mass model was considered unsuitable for modeling the sandwich response.

2.5.2 Energy Balance Models

Energy balance models for the impact response of sandwich composites are also very popular and have been explored much in literature. Energy balance models involve conservation of total energy of the system. The components of total energy in the system are associated with the face sheet bending and stretching, the external work done and the elastic-plastic behavior of the core. Typically in energy balance models, the total energy is minimized with respect to the parameters of interest like the maximum dent depth and dent radius and the resulting equations are solved either numerically or in closed form.

Turk and Hoo Fatt [57] use total potential energy minimization to derive a closed-form solution for the deformation response of a sandwich structure. The composite sandwich is modeled as an infinite, orthotropic, elastic plate resting on a rigid plastic foundation subjected to indentation loading using a hemispherical nose indenter. In their model, they consider only the membrane strain energy as part of the contribution of the face sheet in the overall energy balance. Bending stiffness is completely neglected in the model they present. This approach however is only suitable for modeling large deflections which are at least greater than the thickness of the face sheet.

Two of the energy based models that are solved by potential energy minimization and which do consider the combined effects of both face sheet bending and stretching are the models by Zhou and Stronge [58] and by Hoo Fatt and Park [34]. Zhou and Stronge [58] consider

minimum potential energy that incorporates both face sheet bending and membrane energy but without any property degradation due to matrix cracking and delaminations. This results in an overestimate of the bending stiffness post delamination onset which affects prediction of results. The model proposed by Hoo Fatt and Park [34] combine both the face sheet small deflection bending and large deflection membrane effects under certain deflection criterion. For very small deflections, they find the local indentation response by treating the face sheet as a plate sitting on an elastic core foundation. As the face sheet indentation becomes larger but still less than half the face sheet thickness, the local indentation response is found by treating the face sheet as a plate sitting on a rigid-plastic foundation. Once the face sheet indentation becomes larger than the face sheet thickness, the local indentation is found by considering the face sheet as a thin membrane resting on a rigid-plastic foundation. Large deflections usually dominate post delamination onset but no face sheet damage information is implemented in their model.

Foo et al. [59] presented a modified energy balance model to predict low-velocity impact response of sandwich structures. In their model they derive closed form solutions for the plate's elastic structural stiffness and the critical load for the onset of core crushing. Subsequent degradation in the stiffness of the plate post damage is then obtained experimentally and the degraded plate stiffness together with core crushing threshold load were included in the modified energy balance model to predict load and deflection response for the sandwich plate due to impact. Huang et al. [60] produced an energy balance model with simple closed-form analytical solutions that predicted impact resistance characteristics and damage tolerance of laminated fiber reinforced composite plates. The energy balance for damage development during impact was obtained using a localized deformation field wherein the various effects of sublaminates anisotropy, elastic property degradation due to matrix cracking, multiple delaminations and

membrane type deformation within the damage zone were considered analytically and therefore appropriately implemented in the model. The analytical solution provided highly accurate results when validated with certain experimental results. The method of solution by Huang et al. [60] however is for a monolithic laminate and needs proper inclusion of core effects if implemented in a modified form for a sandwich composite.

The different models presented in literature show varying degrees of accuracy and most of them ignore either aspects of face sheet bending, face sheet stretching, degradation of face sheet properties due to damage onset and progression or the changing core response in the different phases of the loading regime. Despite these limitations, the existing energy based models show great promise should these details be properly implemented, and thereby, the models rectified. The result would be more robust models with higher accuracy in predictions. The simplistic nature of the energy based models make them quite favorable for modeling the sandwich response due to impact or indentation.

2.5.3 Direct Plate Theory Model

The direct plate theory model proposed by Olsson [61] is a very common and popular mechanics based engineering method model. The model is based on engineering mechanics evaluations for different regimes in the loading process and is overall governed by the small and large deflection this plate theory. The model treats the face sheet as a thin isotropic plate and assumes that impact damage is local enough to neglect its influence on the global panel behavior.

Olsson's plate theory model is divided in three regimes. Prior to core crushing, the face sheet is modeled through a combination of the Hertzian indentation contact theory and the small deflection theory of a plate on an elastic foundation. Subsequent to core crushing to but prior to delamination onset, the small deflection plate theory is used where the face sheet is treated as a

plate resting on a perfectly plastic foundation. Subsequent to delamination onset, large deflection membrane theory is used where the face sheet is treated as a membrane resting on a perfectly plastic foundation. Different model parameters are suggested by Olsson depending upon the impactor mass being larger or significantly smaller than the mass of the impacted panel.

Olsson's model, though simple in nature and easily implementable, has a number of problems. Olsson's plate theory model does not show a dependence on indenter diameter in the linear regime, an aspect that is important to this dissertation. Olsson considers the delaminated region as a pure membrane where the total applied load, F , gets divided into contributions due to the membrane forces, F_m , and the critical out-of-plane shear load, F_d . However in his formulation for the membrane deformation, only the membrane forces are included, i.e., the out-of-plane shear load is ignored. Rather, the shear load is taken to the edges of the delaminated region where it is believed to propagate delaminations. This is incorrect as the entire applied load must be carried by the membrane, i.e., the membrane cannot carry a portion of the applied load, namely F_d , out to its edges.

There are certain positive aspects of Olsson's model that were adopted for the model development in this dissertation. Olsson's model of a plate on an elastic foundation for the initial low load elastic regime prior to core crushing was seen as an effective way of modeling this regime. Also, Olsson's idea of simplifying things to an equivalent circular isotropic plate with homogenized properties, and thereby using the isotropic equations, is a tremendous help in eliminating many of the complexities that would otherwise appear with regards to large deflections of an orthotropic or an anisotropic plate subjected to transverse loading.

2.5.4 Unloading Models

The unloading models are extremely useful in predicting residual dent depth which is a parameter of interest both from the view point of quantifying damage as well in the CAI modeling. While most of the research on modeling the response of sandwich structures due to impact or indentation has focused on the loading phase, very limited amount of work has been published in literature that models the unloading behavior.

Sun and Wu [62] developed a power-law relation that uses empirical parameters, but shows good correlation with experimental results. Because of its empirical nature, it falls short in its prediction capabilities and therefore is not of much use. Olsson [63] proposes a model that uses the freed strain energy in order to model load-deflection behavior upon unloading. The freed strain energy according to Olsson equals the external work minus the plastic work. Olsson also states that a more accurate prediction would require knowledge of the core's "unwrinkling stress", which is the reaction of the core under tensile loading. According to Olsson, inclusion of this additional stress may further complicate analysis. One problem with Olsson's model is that he approximates the unloading behavior as linear even though he recognizes the actual unloading behavior to be non-linear. Also, he presents the unloading behavior between an upper and lower bound of residual dent depth and does not capture the actual profile of the unloading curve. However, the "average unloading behavior", i.e. within the bounds of the upper and lower residual dent depths, as modeled by Olsson shows good correlation with experimental results without inclusion of the unwrinkling stress. Zenkert et al. [64] presents an energy based model for the unloading phase of a sandwich composite. They divide the core into the crushed and the uncrushed regions and their total residual strain energy formulation considers the face sheet and the two core regions. Through minimization of the stored energy, a closed form analytical

solution for residual dent is obtained. The correspondence between the predicted and the experimental results was good. The model by Zenkert et al. [64] assumed the core to be behaving elastically during unloading which is not true. A recent work by Minakuchi et al. [65] showed that elastic behavior is only for a very small strain range after which the core behaves plastically.

The lack of unloading models as well as the insufficiency of the existing models proposed by Olsson [63] and Zenkert et al. [64] calls for an improved and more accurate approach to model the unloading behavior of a sandwich structure. This is because of the important residual dent depth information an accurate unloading model can provide. The model should correctly implement the non-linear face sheet and core behavior during unloading and thereby correctly predict the overall unloading response as well as the residual dent depth of the sandwich structure.

2.5.5 Finite Element Models

Recent advancement in finite element computations has seen increased amount of attempts in using this computational tool in predicting the low velocity impact or indentation response of composite structures. Despite its limitations, the finite element method continues to be the most accurate method for modeling. While more success has been achieved in the finite element computations for the impact of monolithic laminates,⁶⁶⁻⁶⁹ the presence of the core in the sandwich composites has consistently posed a hurdle in accurate computations for sandwich composites. This is due to the nature, shape and distribution of the core cells.

Computational efficiency has been shown to increase by meshing the core with a 3D element,⁷⁰⁻⁷⁴ and using the 2D shell or plate element for the face sheet.^{70,74} 2D elements however prove insufficient when transverse loads are required for failure analysis since the contact load distribution is usually a 3D problem. In the transverse direction, the core is usually treated as

homogeneous, isotropic and elastic-perfectly plastic.^{70,72,79} Approximate effective properties of the core are usually used for analysis which are either determined experimentally or through analytical approximations and various techniques have been proposed to predict effective continuum properties of the core in terms of its geometric and material characteristics.^{24,75-79} One problem in treating the core as a continuum meshed with solid elements is that it does not correctly simulate damage progression in the core since in real life, it may be highly sensitive to the distribution of local damage in the different cells. The local stress field and damage may be misrepresented in the core, as in the continuum model damage is assumed to progress evenly while in reality, they may at least be a cell width apart.⁸⁰ One possible solution to this problem that has been explored is to treat the core at the micromechanical level i.e. at the hexagonal cellular level.^{73,81} This has shown improved correlation with experimental results. Here, each cell is treated with a shell element with an attempt to produce the final geometry as close to the real core structure as possible.

Finite element models are advantageous by the fact they are capable of higher level of accuracy and can include more physical details. However, the complexity of these models in their development makes it not to be the best modeling technique to pursue. In comparison, simpler analytical models are more easily developed and parameters may be more easily varied in order to study parametric effects, though they may not be able to produce the same level of accuracy or richness of information as a finite element model.

2.5.6 Modeling Summary

The different models that have been proposed in literature for modeling sandwich response to indentation or impact loading are the spring-mass models, energy balance models, mechanics based engineering method models and the finite element models. The spring-mass

model is limited with respect to damage onset and progression since it is highly dependent on the elastic material behavior. Highly non-linear behavior, as in the case of damaged core and face sheet, is difficult to correctly implement in a spring-mass model. The direct plate theory model proposed by Olsson relies on certain inconsistent assumptions that are not easy to fix in his model without completely changing the model. Finite element models which are generally capable of higher accuracy involve a lot of complexity in their development. Therefore, it is considered not as the best option for the modeling work in this dissertation. The energy based model is relatively easier and simpler to develop and implement as compared to the finite element models. Also, accounting for increasing non-linear material behavior due to the onset and progression of damage can be more readily implemented in an energy based model as compared to other analytical models like the spring-mass models. For these reasons, it is considered the best modeling technique to pursue for this dissertation.

2.6 Summary

The focus of this dissertation is on damage characterization and analytical modeling of sandwich structures with external damage in the vicinity of BVID. This is part of a larger study where the post-impact residual compressive strength and failure modes are experimentally evaluated, with the ultimate goal of developing a numerical model that can predict residual compressive strength of sandwich structures on the basis of pre-existing damage. The literature review presented in this chapter reviewed the damage creation methods of LVI versus QSI, the prominent damage modes that exist in composite structures especially when external damage is in the vicinity of BVID, the effects of different parameters on these damage modes, the damage evaluation techniques, the influence of pre-existing damage and different parameters on post-impact residual strength and failure modes as well as the different modeling techniques to model

the sandwich response to indentation or impact loading and subsequent unloading. In real structures, BVID is usually created by LVI. The literature review showed that the deformation response of the sandwich structure as well as damage created is similar for both LVI and QSI tests when damage is considered at BVID. This finding fundamentally guides the choice of QSI over LVI as the damage creation method in this research. QSI testing is also relatively easier to implement and carry out with a greater control over the extent of damage as compared to LVI.

The key damage modes that exist in sandwich structures that have external damage in the vicinity of BVID are matrix cracking, face sheet delamination and core crushing.

Characterization of the prominent damage modes is vital both as a measure for damage itself as well as the post-impact damage study where the nature and extent of pre-existing damage drive the post-impact failure modes and influence the residual strength of the structure. A number of destructive and non-destructive damage evaluation techniques have been proposed in literature. While external damage is more easily determined non-destructively, a combination of both destructive and non-destructive techniques is needed to know the full extent of internal damage in the sandwich structure. Different parameters of face sheet thickness, face sheet layup, core density, core thickness and the size of the impactor have an influence on the nature and extent of damage as well as on the post-impact residual compressive strength and failure modes.

The prominent models proposed in literature for modeling sandwich response to indentation or impact loading are the spring-mass models, energy balance models, the mechanics based engineering method models and the finite element models. The energy based models appear to be the best choice for the modeling objective of this dissertation. They are preferred even above the more accurate finite element models because of their relatively easier and simpler

development. The inclusion of damage is also more readily implemented in energy based models as compared to other analytical models.

Chapter 3

APPROACH

Introduction

This chapter presents the details of the experimental approach for the damage study that was carried out for this dissertation. The approach for the analytical modeling is discussed separately from Chapter 7 to Chapter 9 and is not presented here. The approach for the experimental investigation was guided by the overall goals of the research which focused on characterization of damage within the vicinity of barely visible impact damage (BVID), and the effect of BVID on the post-impact strength and failure modes of the sandwich structure. The literature review was used to help define the different methodologies to achieve the overall goals of the research.

The details on the materials used for the sandwich structure, the panel manufacture and cutting information, as well as the overall test matrix are presented in this chapter. Also presented in this chapter are the methods for damage creation within the vicinity of BVID and the evaluation of damage through the important damage metrics of dent diameter and dent depth. The approach for delamination assessments including the determination of the planar areas of delamination is presented separately in Chapter 5.

3.1 Research Objectives

The experimental investigation carried out for this dissertation involves characterization of damage within the vicinity of BVID. This information is useful as a measure for damage between the different sandwich configurations to help determine the most damage resistant sandwich structures, as well as for the development of a model for the impact or indentation

event. The damage information is also expected to be implemented in the compression-after-impact (CAI) model for the prediction of the post-impact residual strength of the sandwich structure.

The important damage metrics that drive the post-impact failure modes are the size of the external dent, characterized by the dent diameters and depths, as well as the size of the delaminations. From the literature review of Chapter 2, these are the damage metrics that rise in significance both as a measure for damage as well as on their influence on the post-impact residual strength through the different failure modes. The literature review showed that different parameters have an effect on the nature and extent of damage as well as on the post-impact strength and failure modes of the sandwich structure. These parameters include the core density, the core thickness, face-sheet stacking sequence, face sheet thickness and the impactor shape and size. The parametric effects on the nature and extent of damage need to be understood as well as their influence on the post-impact residual strengths and failure modes. Finally, experimental investigations are always expensive and it is usually desired that the knowledge gained through experimental investigations be used in the development of suitable models that can provide the same information that will otherwise be determined experimentally. To this end, a model is desired that can provide the same damage information for sandwich structures with damage within the vicinity of BVID that that has otherwise been determined experimentally in this research.

The primary objectives of the research conducted for this dissertation can therefore be summarized as

- i. the characterization of damage in sandwich structures through a measure of the different damage metrics of dent diameter, dent depth and planar area of delamination;
- ii. understanding the effects of the different parameters of core thickness, core density, face sheet stacking sequence, face sheet thickness and indenter diameter on sandwich damage when the external damage is within the vicinity of BVID;
- iii. the development of a model that can provide quantitative damage information through the different damage metrics for damage within the vicinity of BVID.

3.2 Choice of Methodologies

The choices of methodologies, guided by the review findings of Chapter 2, were largely influenced by specific needs of this research and the primary objectives of the CAI study. The sandwich specimens consisted of graphite/epoxy face sheets and aluminum honeycomb cores. A secondary adhesive bond was used at the interface between the face sheets and the core. The choice of the face sheet and core materials was driven by NASA's interest in this combination for the development of their prototype composite crew module (NASA co-sponsored this research). Different combinations of face sheet layups and thicknesses and core densities and thicknesses were used to understand the effects of these parameters on sandwich damage. One small and one large spherical indenter was used for damage creation where the small indenter broadly simulated damage due to localized loading while the large indenter broadly simulated damage due to distributed loading.

The level of damage required for this research was BVID. The literature review showed that for BVID, both LVI and QSI show similar sandwich response and overall damage. This

finding from the review formed the premise for choosing QSI as the preferred method of damage creation over LVI. QSI tests also provided the added advantage of having greater control over the extent of desired damage and allowing similar amount of damage to be created between test specimens. The load and displacement data were recorded during testing, details of which are presented in Chapter 4. The load and displacement data from QSI testing is particularly useful in identifying the progression of damage in the sandwich structures. The damage metrics of dent depth, dent diameter and planar area of delamination were evaluated non-destructively.

Additional destructive evaluations were performed to determine the full extent of delamination damage in the sandwich structures as this information was not fully known ultrasonically. The details on dent diameter and dent depth determination are presented in this chapter while the details on delamination assessments are presented separately in Chapter 5. As discussed in Section 3.1, these damage metrics are of interest both as a measure for damage as well as the influence they have on the post-impact residual strength and failure modes. The knowledge attained from the experimental evaluations was then used for the development of a model with the primary objective of reproducing the loading-unloading response of the QSI testing for damage in the vicinity of BVID. A combination of the direct plate theory and the Rayleigh-Ritz method of energy minimization is used for the development of this model, the specific details of which are presented in Chapter 9.

3.3 Materials and Manufacturing

All sandwich panels used quasi-isotropic IM7/8552 graphite/epoxy face sheets. IM7/8552 is an amine cured toughened epoxy resin system supplied with carbon fibers with excellent mechanical properties and good elevated temperature performance. The thickness of IM7/8552 material used was 0.127 mm per ply. Sandwich composites used for the experimental evaluations

consisted of both 8 and 16 ply face sheets, resulting in face sheet thicknesses of 1.02 mm and 2.03 mm respectively. The four different 8 ply face sheet layups that were used are referred to as Q1, Q2, Q3 and Q4. Table 3.1 presents the layup information for the different 8 ply face sheet layups. The Q1 and Q4 layups in this table have 45° ply angle changes at most of these interfaces, while the Q2 and Q3 layups have 90° ply angle change at most interfaces. Q2 is a standard layup for design uses where the grouping together of $\pm 45^\circ$ plies on the outside reduces the effects of bending-twisting coupling, D_{16} and D_{26} . Larger bending-twisting coupling can result in unwanted structural responses in both indentation loading as well as in the post-impact compression tests. The Q1 layup minimized the angle changes and were used to study the effect of smaller ply angle change on the extent of delamination. The five different 16 ply face sheet layups that were used were referred to as Q1, Q2, Q3, Q4 and Q5. Table 3.2 presents the layup information for the different 16 ply face sheet layups. The same use of names for the Q1, Q2, Q3 and Q4 layups for the 16 ply case as in the 8 ply case is because of the same rationale behind the ply arrangements. For the 16 ply face sheets, the Q1 and Q4 layups have 45 ° angle changes like the 8 ply case. The Q2 and Q3 layups for the 16 ply case have ply angle changes of 90° at most of the interfaces with the grouping together of the 45° and -45° plies on the outside. These characteristics are common with the Q2 and Q3 layups for the 8 ply case.

Table 3.1. 8 ply face sheet layup information.

Designated Name	Layup
Q1	[45/0/-45/90] _s
Q2	[45/-45/0/90] _s
Q3	[-45/45/90/0] _s
Q4	[45/90/-45/0] _s

Table 3.2. 16 ply face sheet layup information.

Designated Name	Layup
Q1	[45/0/-45/90/-45/0/45/90] _s
Q2	[45/-45/0/90] _{2s}
Q3	[45/-45/90/0] _{2s}
Q4	[45/90/-45/0/-45/90/45/0] _s
Q5	[45/0/-45/90/90/-45/0/45] _s

The core type used for sandwich manufacture was 5052 aluminum honeycomb core. Figure 3.1 presents a schematic of the aluminum honeycomb core with the different geometrical characteristics defined. Aluminum honeycomb cores are one of the most readily available and widely used honeycomb cores. They are considered advantageous over other honeycomb core types from the viewpoint of cost, strength, machinability and energy absorption. Three different types of 5052 aluminum honeycomb cores with varying density and thickness combinations were used. The different core density and thicknesses were chosen to study effects of these parameters on the sandwich damage as well as the post-impact strength of the sandwich structure. Each of the cores had a constant cell size (as defined in Figure 3.1) of 3.175 mm. The cores were

designated as C1, C2 and C3. Details of the different core densities and thicknesses are presented in Table 3.3. Strength properties of the different cores are presented in Chapter 7.

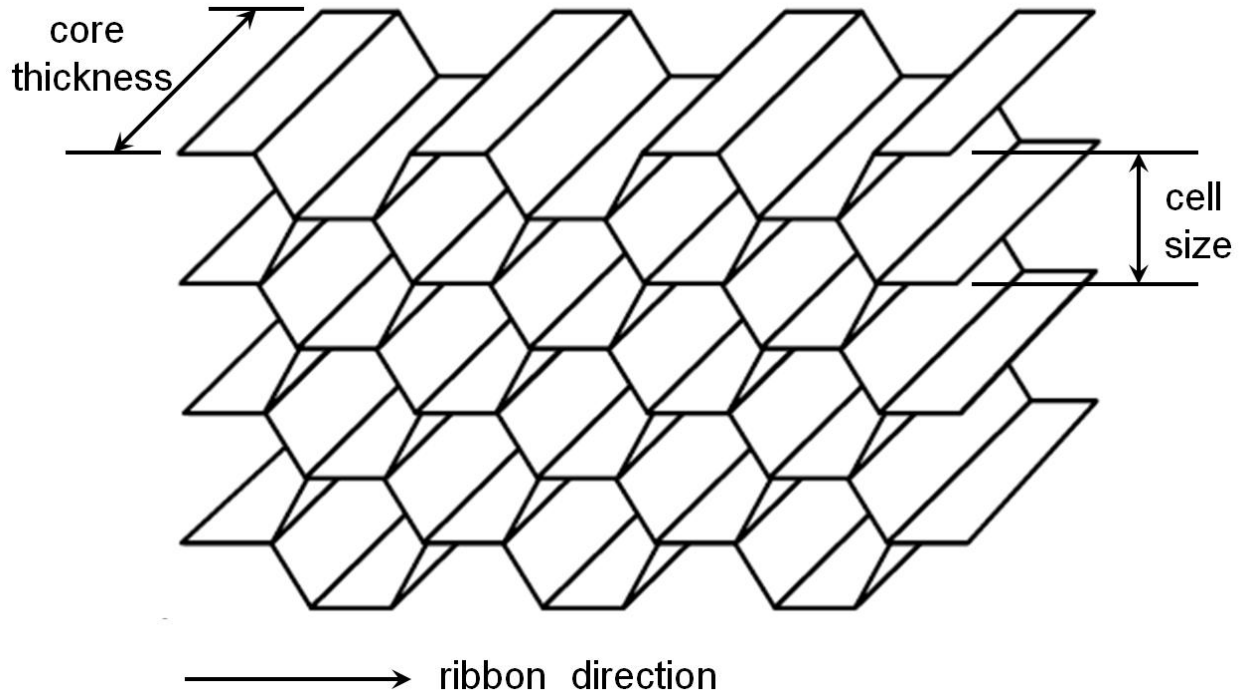


Figure 3.1. Schematic of a honeycomb core showing the core thickness, cell size and the ribbon direction.

Table 3.3. Thickness and density details of the different aluminum honeycomb cores used.

Core Type	Thickness, mm	Density, kg/m ³
C1	25.4	49.7
C2	12.7	49.7
C3	25.4	72.1

All specimens were manufactured in the Syracuse University Composite Materials Laboratory (SU-CML). The ribbon direction, as defined by Figure 3.1, of the core was always placed to coincide with the 0° direction of the face sheet layup. Prior to placing the face sheets in place, 3M EC 3524 void filling compound was used to pot the core in a manner that, after cutting the panel into specimens and inducing the damage, an edgewise compressive load could be introduced through the potted region of the core to obtain post-indentation compression strengths.⁸² Each “line” of potting compound was originally 25.4 mm wide and spanned the full width of the panel in the 90° direction.

The original panel size that was manufactured was 381 mm x 381 mm. The limit placed on the panel size was due to space constraints in the autoclave used for the manufacture. The autoclave cycle used for the panel manufacture is presented in Appendix A. All the edge trimming and cutting of the panel was done using a diamond grinding blade on a milling machine. After trimming the edges, the potted region that remained was approximately 12.7 mm wide. A schematic of a manufactured panel after trimming the edges is shown in Figure 3.2. The panel was also subsequently cut through the center strip of potting compound, such that all the edges that would be loaded had a potted region of approximately the same width.

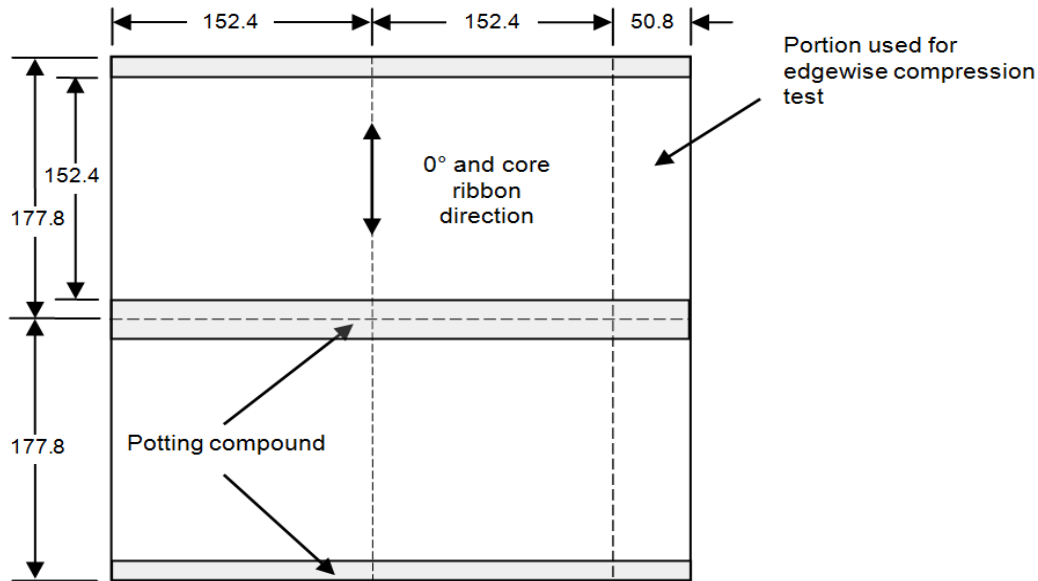


Figure 3.2. Typical panel dimensions after manufacturing and edge trimming (all dimensions in mm).

Figure 3.2 can also be used to understand how panels were cut into specimens. This figure presents the “nominal configuration,” which corresponded to each panel being cut into four “full-sized” specimens that were 177.8 mm long (0° direction and direction of subsequent compression loading) and 152.4 mm wide (90° direction), and two specimens that were 177.8 mm long x 50.8 mm wide for edgewise compression testing,⁸³ which was used to obtain undamaged compressive strengths.⁸² The full-sized specimen dimensions were influenced by the needs of the CAI test. The specimen had to be relatively large compared to the size of the dent in order to have a localized region of dent well within the specimen periphery. At the same time, the specimen had to be sufficiently small lengthwise along the direction of the application of compressive load in the CAI test so that any global buckling deformation of the specimen prior to failure from the indentation sight could be prevented. For the first several panels manufactured, “small QSI specimens”, which were generally smaller in size compared to the

“full-sized” specimens, were needed to determine the QSI load and indentation levels that would correspond to BVID. In these cases, instead of cutting the lower right quadrant of the panel into one full sized and one edgewise compression specimen, this was cut into one specimen that was approximately 100 mm square, two that were approximately 75 mm square, and two that were approximately 50 mm square. These were used for “QSI evaluation tests” using the 76.2 mm, 25.4 mm and 12.7 mm diameter indentors, respectively. In addition, in some panels, a 12.7 mm thick x 150 mm long x 25 mm wide teflon insert was placed within the plate in the location corresponding to the lower right edgewise compression specimen. These produced face sheet flexural test specimens that were used to calibrate the material properties used in finite element analyses of the post-indentation compression response.⁸³

Spherical indentors of 25.4 mm and 76.2 mm diameters were chosen with the intention to simulate different impact scenarios. The 25.4 mm diameter indenter simulated localized loading that is synonymous with sharp object impacts, while the 76.2 mm diameter indenter simulated distributed loading that is synonymous with blunt object impacts. In the exploratory tests for the determination of the appropriate indenter sizes, 12.7 mm diameter indenter was also considered. However, initial exploratory tests indicated that the post-QSI state of damage and the residual compressive strength was essentially the same for specimens that were tested with the 12.7 mm diameter indenter and the 25.4 mm diameter indenter. These exploratory test results are presented in Appendix B.

3.4 Test Matrix

Using the different combinations of face sheet layups and core types (as presented in Tables 3.1-3.3), a total of seven different sandwich geometries were considered for the 8 ply tests and eight different sandwich geometries were considered for the 16 ply tests. Tables 3.4 and 3.5

present the complete test matrix for all the full-sized specimens that were used in the experimental evaluations. The first column in these tables present the different sandwich geometries, comprised of the various face sheet (Q1-Q5) and core combinations (C1-C3). The second and third columns show the number of specimens tested using the 25.4 and 76.2 mm diameter indentors, respectively. Thus, to provide more test replicates at each condition, subsequent QSI testing utilized only the 25.4 mm and 76.2 mm diameter indentors. The final column in Tables 3.4 and 3.5 present the number of 381 mm square panels that were manufactured in order to get the required specimens. Note that more than one panel was manufactured for the first four geometries listed in both Tables 3.4 and 3.5. These sandwich geometries consisted of the face sheet layups Q1 and Q2. In these cases, at least two specimens that were tested at a given indenter diameter were taken from the same panel, and at least one specimen was taken from a different panel. In this way the effects of possible inter- and intra-panel variations in the specimens could be assessed.

Table 3.4. Test matrix for the 8 Ply specimens tested with both the 25.4 mm and 76.2 mm diameter indentors.

Sandwich Geometry	Indenter Diameter		Number of Panels Manufactured
	25.4 mm	76.2 mm	
Q1-C1	3	2	3
Q1-C2	3	3	2
Q1-C3	3	3	2
Q2-C1	5	6	3
Q3-C1	1	2	1
Q4-C2	2	1	1
Q4-C3	2	1	1
Total	19	18	13

Table 3.5. Test matrix for the 16 ply specimens tested with both the 25.4 mm and 76.2 mm diameter indentors.

Sandwich Geometry	Indenter Diameter		Number of Panels Manufactured
	25.4 mm	76.2 mm	
Q1-C1	4	4	2
Q1-C2	4	4	2
Q1-C3	4	4	2
Q2-C1	4	4	2
Q3-C1	2	1	1
Q4-C1	2	0	1
Q4-C3	2	2	1
Q5-C1	2	2	1
Total	24	21	12

3.5 Quasi-Static Indentation (QSI) Testing

All QSI testing was performed using a servo-hydraulic load frame equipped with a digital controller and data acquisition system. Figure 3.3 shows the indentation test set-up for a 8 ply sandwich specimen tested with the 76.2 mm diameter indenter. The center of the specimen was first marked using two diagonal lines on the top face sheet. Next, the sandwich specimen was placed on a circular rigid substrate and aligned so that the center of the indenter coincided with the center of the specimen. Two spring clamps were then used to hold the specimen in place. All the QSI tests were performed under displacement control with a loading and unloading ramp rate of 0.005 mm/s.

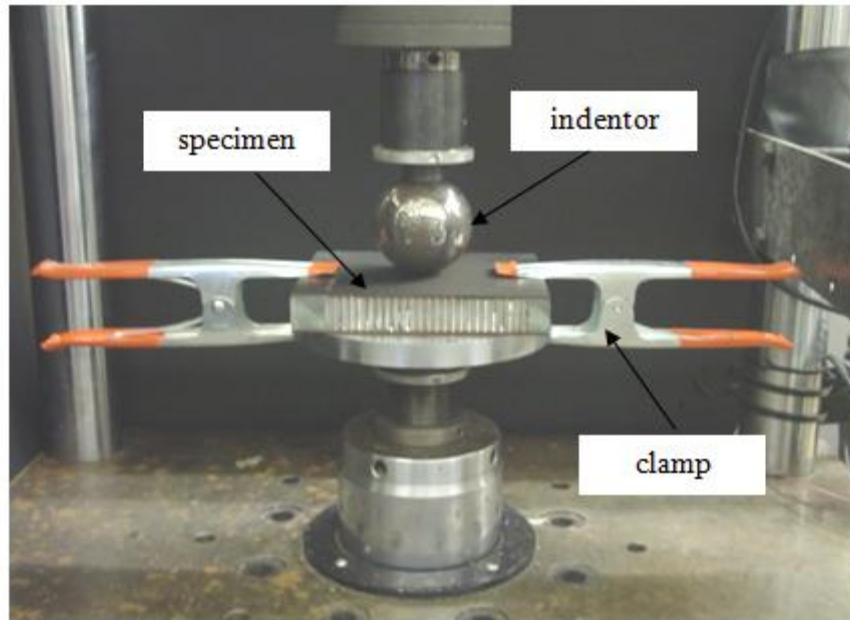


Figure 3.3. QSI test set-up, 8 ply sandwich specimen with the 76.2 mm diameter indenter.

For the 8 ply face sheet, the barely visible damage load threshold was chosen to be 1300 N and 2800 N for tests performed with 25.4 mm and 76.2 mm diameter indentors respectively. These corresponded to maximum permanent dent depths of approximately 0.5 mm and 1.0 mm for the 25.4 mm and 76.2 mm diameter indentors respectively. These load levels were determined using the “small QSI specimens” and the results are presented in Appendix C. In the load level determination, it was first ascertained that the small QSI specimens were sufficiently large that their load-deformation responses were essentially the same as those observed in the full sized panels. Small QSI specimens were then indented to varying loads and indentation levels in order to choose the QSI load and indentation levels that corresponded to the definition of barely visible impact damage (BVID). This determination was made qualitatively by consensus of the research team. Results of the BVID load determination preliminary tests using the small QSI specimens for the eight ply case are presented in Appendix C.

It was intended that the BVID permanent dent depths for the 16 ply specimens be similar to or close to the BVID dent depths for the 8 ply so that valid comparisons could be made between the 8 ply results and the 16 ply results. In this case, the 16 ply to 8 ply target dent depth ratio was 0.8. Qualitative dent assessment was done before this ratio was decided upon since a balance was important between the ideal quantitative value of dent depth and the extent of visible damage just by naked eye assessment. Therefore, based on these quantitative and qualitative assessments, the choices of load levels that approximately created the required amount of dent depths were made for the different indenter diameters for the 16 ply case. This BVID load threshold was chosen to be 2470 N and 4340 N for tests performed with 25.4 mm and 76.2 mm diameter indentors respectively for the 16 ply case. These corresponded to maximum permanent dent depths of approximately 0.4 mm and 0.8 mm for the 25.4 mm and 76.2 mm diameter indentors respectively. These load levels were again determined using the small QSI specimens from the first few manufactured panels. Results of the BVID load determination preliminary tests using the small QSI specimens for the sixteen ply case are also presented in Appendix C.

As would be expected, not all panel types responded the same. For example, for a given load level, less permanent deformation was observed in panels with the high density C3 core than in those with the C1 or C2 cores. The difference in dent depths between the C3 core and the other core types was much more in the 8 ply case than in the 16 ply case. Thus, for the 8 ply case, the specimens with the C3 core were tested to a slightly higher load level in order to obtain similar dent depths. This was not done in the 16 ply case since it would have compromised on the extent of visible damage. Thus for the 16 ply case, all the specimens from the different core types were tested to the same load level. Also, a limited number of specimens in the 8 ply case

were also tested to higher load levels than the barely visible damage threshold in order to provide additional insights into trends and mechanisms.

Even though the load-displacement plots do give a value for residual dent depth upon complete unloading, this data was not used as the specimen's final dent depth. This is because this data was deemed unreliable since the load-displacement residual dent depths are likely affected by the machine compliance and therefore does not truly represent the actual specimen permanent dent depth. The play in the machine is probably due to loose attachments in the machine and the loading fixture, as well as other mechanical inconsistencies in the test set-up that affect the measured displacement values during testing. This created the need for other methods of permanent dent depth determination which was eventually done ultrasonically.

3.6 Dent Measurements

The permanent dent in all specimens was mapped ultrasonically using the c-scan since the load-displacement data could not be used for this determination as discussed in the preceding section. This is the first time that this approach has been utilized for impact damaged laminates or sandwich panels. The data that was obtained from ultrasonic inspection was used to determine both dent diameters and dent depths of the indented specimens.

3.6.1 Method Development

In order to develop the method, a metal specimen with a known step size was initially manufactured and used to assess and refine the technique. The SU-CML c-scan unit, which employs a 500 MHz transient waveform digitizer, was utilized in pulse-echo mode for the process. The fundamental principles of the working of a c-scan are presented in Chapter 5. The c-scan's software was configured to capture the time of flight between the transducer's pulse and

the first wave reflection from the specimen's surface, and this result was used along with the wave speed in water to determine the depth of the step. This was relatively straightforward for the stepped metallic specimen, so the initial development work primarily went into defining which signal peak corresponded to the onset of the pulse and the return of the echo, as well as the evaluation of various transducers between 10 and 75 MHz. It was found that a 50 MHz transducer provided the most accurate results.

This study was then repeated with the small specimens that had been QSI tested and the dent diameter and dent depths were evaluated. The dented surface was scanned and the software associated scan software captured the time of flight between the transducer's pulse and the first wave reflection from the panel surface. This produced an array of times corresponding to the different locations on the specimen's surface. Using the wave speed of sound in water, these were then converted to distances from the transducer. The distances in the undamaged regions were averaged and all the distance data points were subtracted from this average to help find the $z=0$ plane for the undamaged region. An extra "corrective rotation" was required due to the fact that the specimens generally did not sit perfectly flat in the c-scan tank. In order to apply this corrective rotation to the data, a few different methods were evaluated. This was done because small differences in the data sampled by any approach made different methods produce slightly different results. The methods considered consisted of approaches using two perpendicular lines to correct for the specimen's orientation versus those using a plane for correction. After assessing the various methods on several specimens, the former approach was adopted. That is, data remote from the dent along the two lines that bisected the dent's center (in the x- and y-directions) were used to correct for planar misalignment of the specimen in the c-scan tank.

3.6.2 Validation of Method

The results for the dent depth versus location profiles from the ultrasonic evaluations were compared to those obtained by a mechanical surface profile measurement system. This consisted of a dial gage rigidly mounted above a precision sliding x-y scale, thereby allowing accurate depth measurements to be obtained at discrete points. In all cases, the 50 MHz transducer was again found to be the most accurate and provided results that agreed with those obtained by the mechanical measurement system. Figure 3.4 shows a representative dent profile verification result for an 8 ply small QSI specimen as an outcome of comparing measurements retrieved from the ultrasonic inspection and the mechanical system. This was performed on a small specimen along the 0° direction right through the dent center. As can be seen, the profile from the mechanical system very closely matches that which was obtained ultrasonically. These tests were repeated on a few other specimens and the results obtained using the mechanical system very closely matched that which was obtained ultrasonically, thus validating the ultrasonic technique of dent diameter and dent depth measurements.

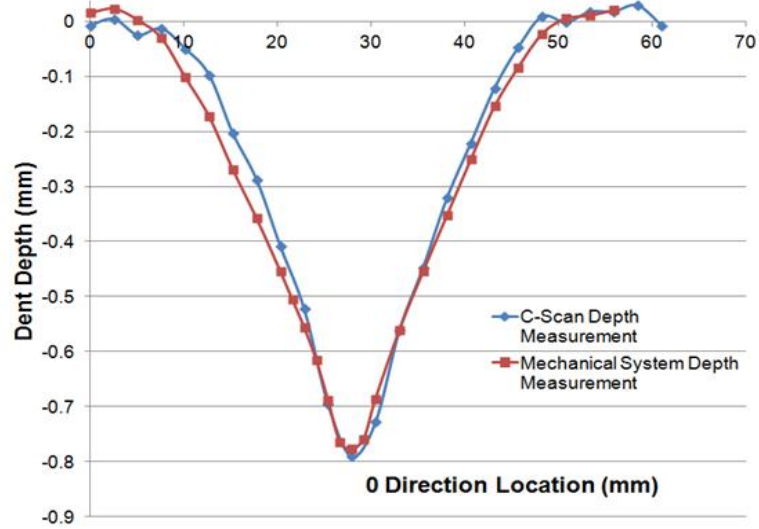


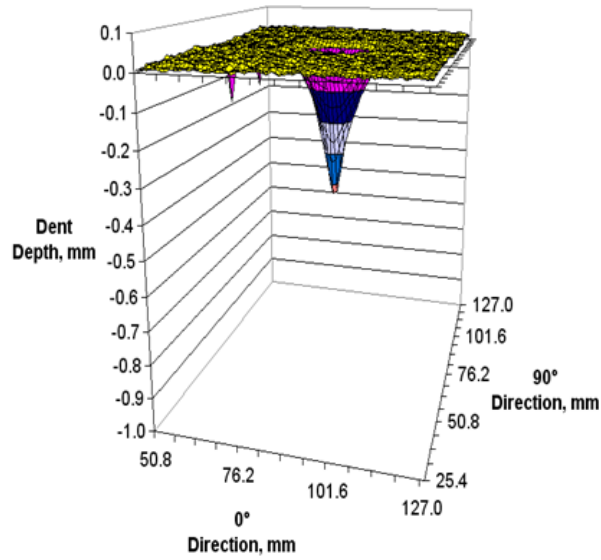
Figure 3.4. Ultrasonic dent measurement validation for an 8 ply small QSI specimen using the dial gauge indicator.

3.6.3 Application of Method to Full-Sized Specimens

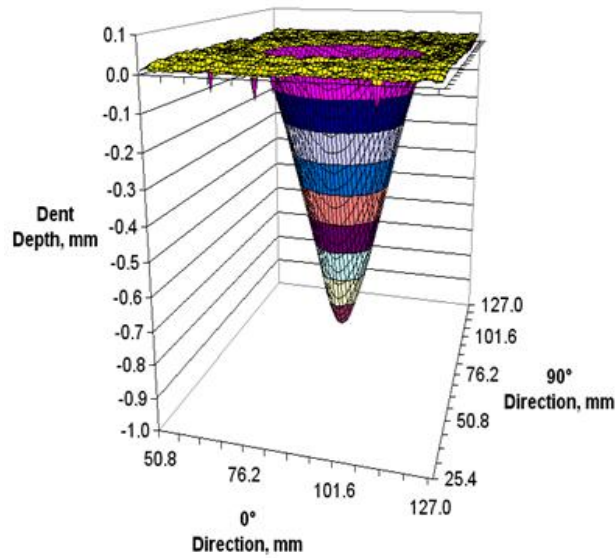
Following the initial verification of the method, the ultrasonic approach, together with the corrective rotation described in the previous paragraph for the small QSI specimens, was utilized exactly the same way for all full sized specimens. Typical indentation profiles that resulted from the above process for both the 8 and 16 ply cases are shown in Figures 3.5 and 3.6. Note that the planar scales of these plots are contracted in comparison to their depth, and the physical dents do not appear nearly as steep as they do in the figures. The figures present results for the Q2-C1 specimen configuration for the 8 ply case and Q1-C2 specimen configuration for the 16 ply case at their BVID load levels. Also, for each of the face sheet thicknesses, indentation profiles for specimens tested with both the indenter sizes are presented in each of the figures.

In addition to dent depth, the data also allowed ready determination of dent diameters and areas. To this end, the general procedure was to first plot the x-z and y-z surface profiles for the x- and y-direction lines that went through the center of the dent. A representative x-z and y-z

surface profile is presented in Figure 3.7 which is taken from a 16 ply specimen indented with 25.4 mm diameter indenter. The dent widths, represented by the distance between the locations marked X and Y in the figure, was determined in both the x-z and y-z directions. If there was a difference in the dent widths, which was mostly the case, an average of dent widths was taken from the x-z and y-z profiles. There was a certain amount of subjectivity in the definition of diameters, i.e., in defining the exact point where the dent ended and the flat region outside of the dent began. Thus, to make the diameter assessments, all x-z and y-z surface profiles from all specimens were plotted using identical expanded scales, and the determination of dent diameters for all specimens was made at the same time. In this manner, it was possible to ensure that a consistent definition was used for all specimens.

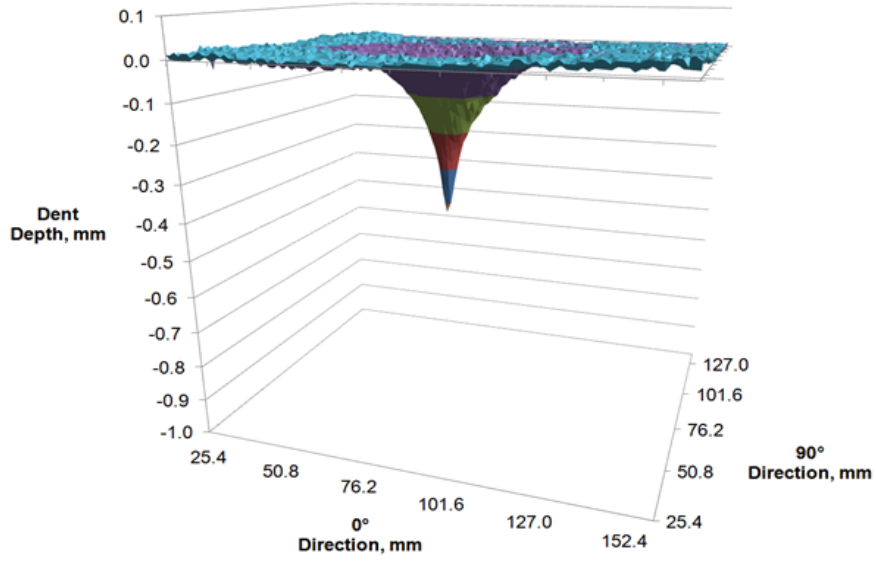


(a)

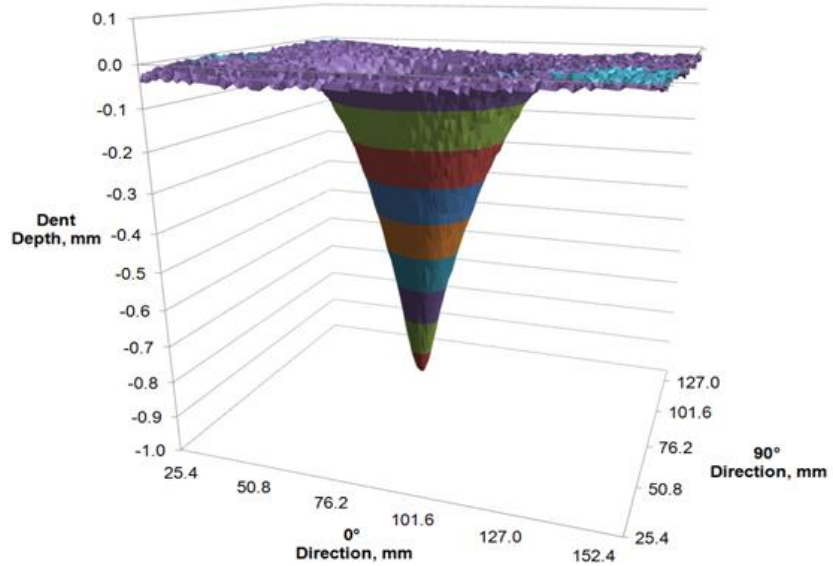


(b)

Figure 3.5. Typical dent profiles for the eight ply case using 25.4 mm (a) and 76.2 mm (b) diameter indentors.



(a)



(b)

Figure 3.6. Typical dent profiles for the 16 ply case using 25.4 mm (a) and 76.2 mm (b) diameter indentors.

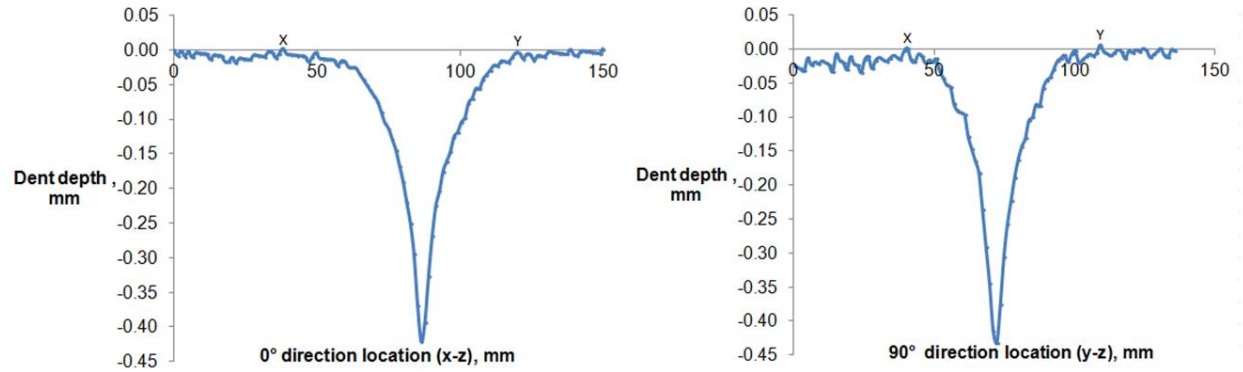


Figure 3.7. Representative x-z and y-z surface profile for a 16 ply specimen indented with the 25.4 mm diameter indenter.

3.7 Delamination Measurements

Delaminations were primarily assessed non-destructively using the c-scan, with a few destructive evaluations performed by sectioning the specimen in all the four ply directions and using an optical microscope to observe the sections. Destructive evaluations were performed in order to validate the non-destructive evaluation technique as well as to reveal more information on the delaminations in the regions that remained shielded in the non-destructive evaluations. Complete step by step details about the non-destructive and destructive evaluation techniques is presented in Chapter 5.

Chapter 4

LOAD-DISPLACEMENT RESULTS

Introduction

As discussed in Chapter 2, damage onset and progression in a sandwich structure is more readily observable in a quasi-static indentation (QSI) test as compared to a low velocity impact (LVI) test. This is done using the load and displacement data which are obtained through the data acquisition system during QSI testing. This chapter presents the experimental load versus displacement (P-d) results for all the sandwich configurations that were damaged quasi-statically in this research.

Generally, all the load versus displacement plots presented in this chapter can be divided into four regions which together describe the overall response of a sandwich panel to indentation loading. Figure 4.1 shows schematically a general P-d plot for all specimens and is used to describe the four regions. These four regions are:

- i. Initial elastic region – this is the initial low load region where linear elastic behavior of the sandwich is observed.
- ii. Transition region – this is the region that shows up as a “knee” or bend in the curve. This region is indicative of the first occurrence of inelastic processes in the sandwich specimens. As described subsequently, these inelastic processes are believed to be primarily core crushing with some matrix cracking and delaminations onset.
- iii. Inelastic region – this is the region beyond the transition region up to the peak load. Although referred to as “inelastic”, this region shows the combined effects of both elastic and inelastic deformation; however, the inelastic response predominates. This

- is due to an increasing amount of core crushing along with delamination advance and additional matrix cracking, and is characterized by a visually observable increase in dent size and depth.
- iv. Unloading region – this is the region of gradual unloading from the peak load to zero load. As indicated in Figure 4.1, the sandwich behavior during unloading is nonlinear and evidences a permanent deformation.

Using the P-d plots that are presented, the chapter discusses the influence of face sheet layup, face sheet thickness, core density and core thickness on the sandwich response to indentation. Different P-d plot combinations based on the parameter(s) of interest are presented, which enable drawing relevant conclusions on the effects of these parameters. The majority of the comparisons are based on tangent stiffnesses, i.e., the relative values of the slope of the P-d curves. The key learning outcomes are summarized at the end of the chapter.

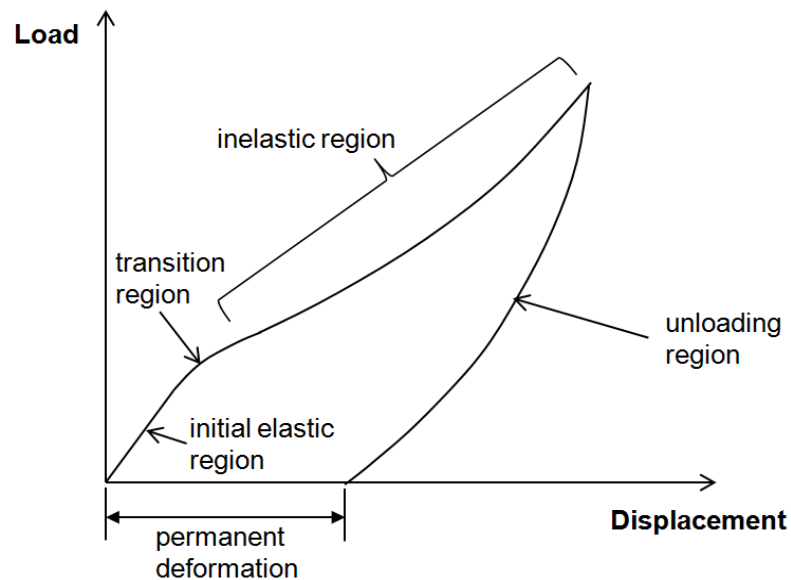


Figure 4.1. Schematic representing the general P-d plot for all specimens.

4.1 8 Ply Results

4.1.1 QSI Tests with 25.4 mm Diameter Indentor

Figure 4.2 presents representative load versus displacement plots for the various sandwich configurations with 8 ply face sheet indented with the 25.4 mm diameter indentor. These representative plots were chosen from specimens that were tested to the same maximum load, which is the threshold load for barely visible damage for 8 ply specimens indented with the 25.4 mm diameter indentor. A single representative plot is shown for each sandwich configuration in Figure 4.2 as not much specimen to specimen variation was noticed in the P-d data for the different specimens within each sandwich configuration.

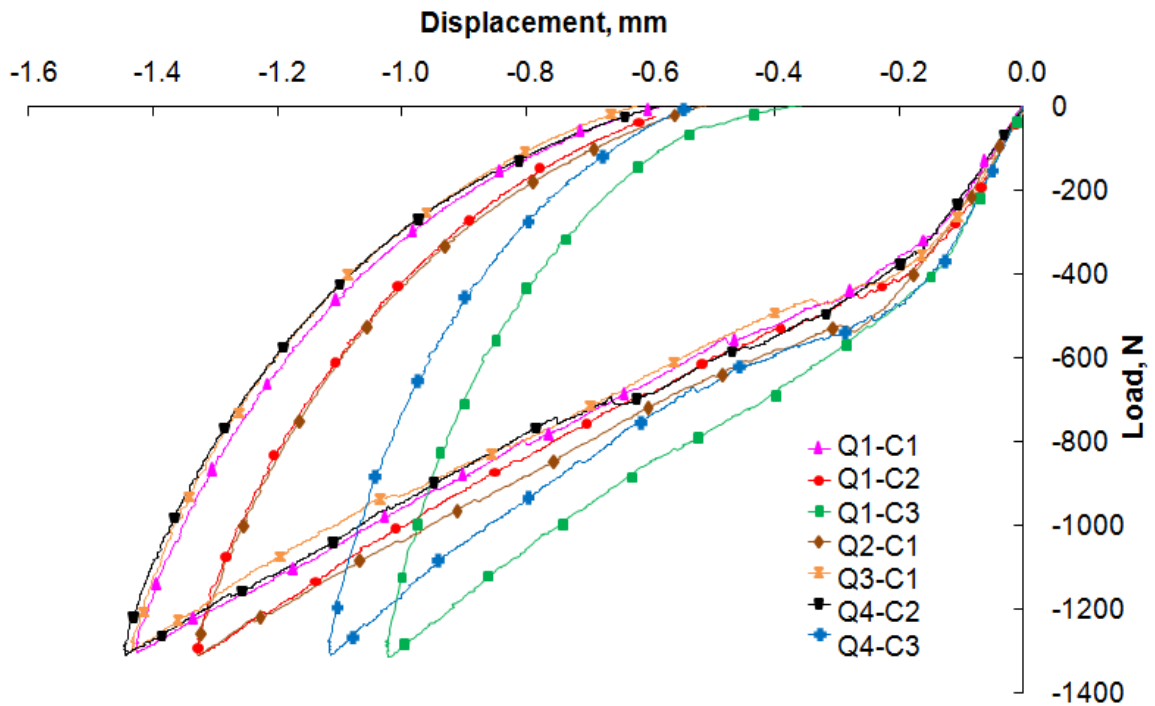


Figure 4.2. Representative P-d plots for the 8 ply specimens indented with the 25.4 mm diameter indentor.

In the initial region of elastic deformation, specimens with the high density C3 core show a stiffer response than those with the low density C1 and C2 cores. The response of the initial region of elastic deformation for the specimens with the C3 core being stiffer than the specimens with the C1 and C2 cores shows that the high core density results in a stiffer sandwich response in the initial loading phase. There are no readily distinguishable differences in the stiffness of the specimens with the C1 and C2 cores for the initial elastic region. The similar slope between the C1 and C2 cores is more clearly shown in Figure 4.3 which presents data from all the eight ply specimens for the sandwich geometries Q1-C1 and Q1-C2 indented with the 25.4 mm diameter indenter. In the initial elastic region, both the Q1-C1 and Q1-C2 sandwich geometries show similar stiffness.

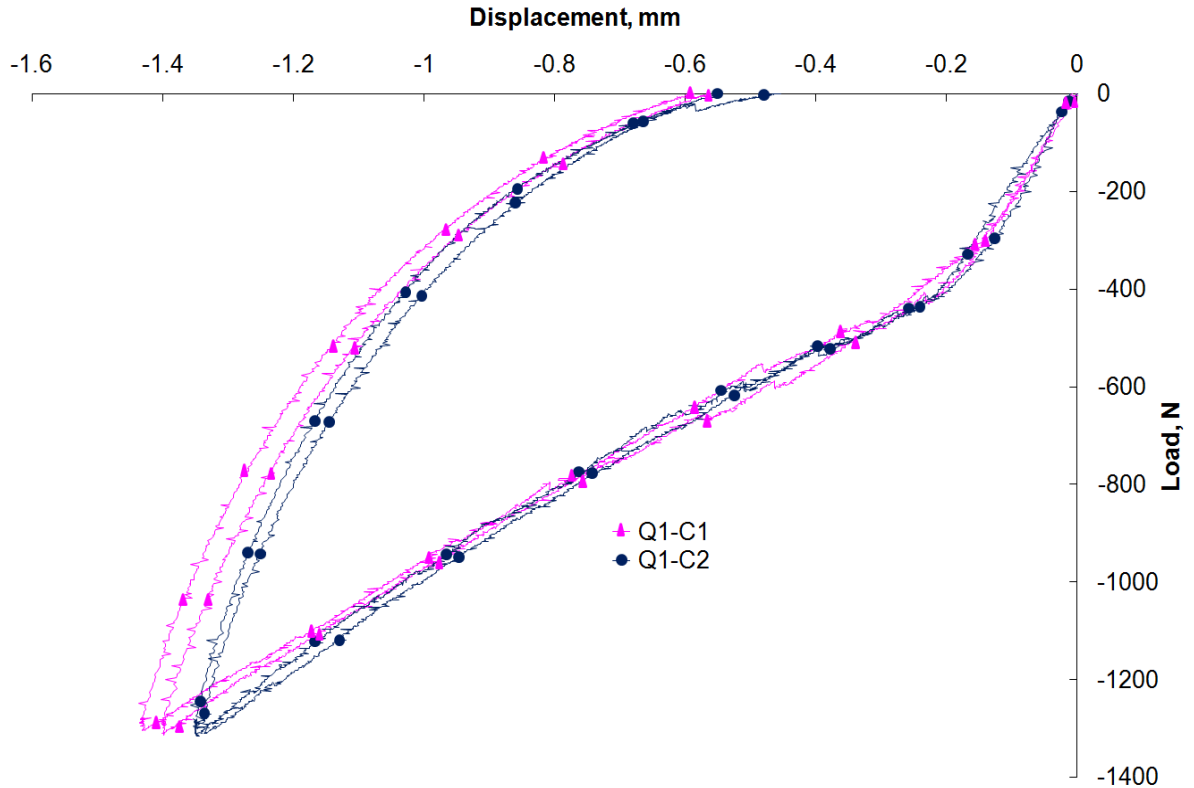


Figure 4.3. Representative P-d plots for Q1-C1 and Q1-C2 8 ply specimens indented with the 25.4 mm diameter indenter.

The slopes in the inelastic region (i.e., in-between the knee and the maximum load as defined in the schematic in Figure 4.1) are also primarily controlled by the core, with a secondary effect of face sheet layup. Figure 4.2 clearly shows us that specimens with the high density C3 core have significantly stiffer response in the inelastic region than the specimens with the C1 and C2 cores. Comparing the stiffness in the inelastic region between the C1 and C2 cores, which have the same core density, Figure 4.3 shows that for the same face sheet layup, specimens with the thinner C2 core behave slightly more stiffly than the specimens with the thicker C1 core. Although these two core types have the same density, the smaller thickness of C2 core gives it less ability to redistribute the load during and after core crushing. It therefore

provides an effectively stiffer structural response than the C1 core once core crushing has initiated. As can be seen from both Figures 4.2 and 4.3, a stiffer response means less deformation at the peak load, which also generally corresponds to a smaller permanent dent depth.

Figures 4.2 also indicates that the face sheet layup has a secondary influence on the specimen's behavior in the "transition region," i.e., around the knee in the curve where core crushing initiates, and in the subsequent load versus deformation response. This is more clearly illustrated by Figures 4.4 - 4.6. Figure 4.4 presents the P-d plots for all the specimens from the Q1-C1 and Q2-C1 sandwich configurations indented with the 25.4 mm diameter indenter. In the initial elastic region, i.e. in the region prior to core crushing, the Q2-C1 sandwich configuration shows slightly stiffer response than the Q1-C1 sandwich configuration. The bend in the curve during the transition region happens over a smaller range of load in the Q1-C1 sandwich configuration as compared to the Q2-C1 sandwich configuration. This may relate to the greater amount of delamination that occurs in the Q2 layup (discussed in chapter 5 on "Delamination Assessments"). That is, it may be that delamination initiation is also occurring around the knee in the curve and that this affects the length and details of the transition region; this sequence of events is supported by the results in References [12] and [27]. In the inelastic region, the Q2-C1 sandwich configuration show slightly stiffer response than the Q1-C1 sandwich configuration.

Figures 4.5 and 4.6 compare the Q1 and Q4 face sheet layups combined with the C2 and C3 cores. Figure 4.5 compares the Q1-C2 and Q4-C2 sandwich configurations while Figure 4.6 compares the Q1-C3 and Q4-C3 sandwich configurations. Considering the slopes of all the specimens qualitatively on an average basis, the slopes of the Q1 and Q4 layups appear to be the same for the C2 core as seen in Figure 4.5. However for the C3 core, as presented in Figure 4.6, the Q1 face sheet layup shows a slightly stiffer response in the transition region when compared

to the Q4 face sheet layup. Also, for the C3 core, the Q1 face sheet layup has a longer transition region as compared to the Q4 face sheet layup.

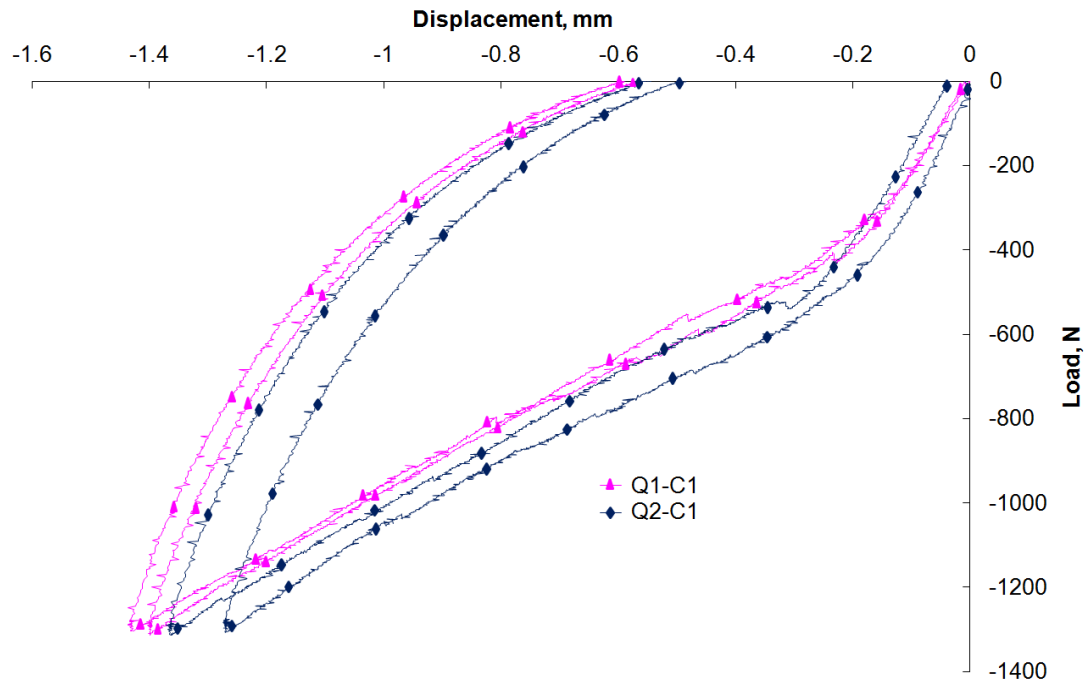


Figure 4.4. Representative P-d plots for Q1-C1 and Q2-C1 8 ply specimens indented with the 25.4 mm diameter indenter.

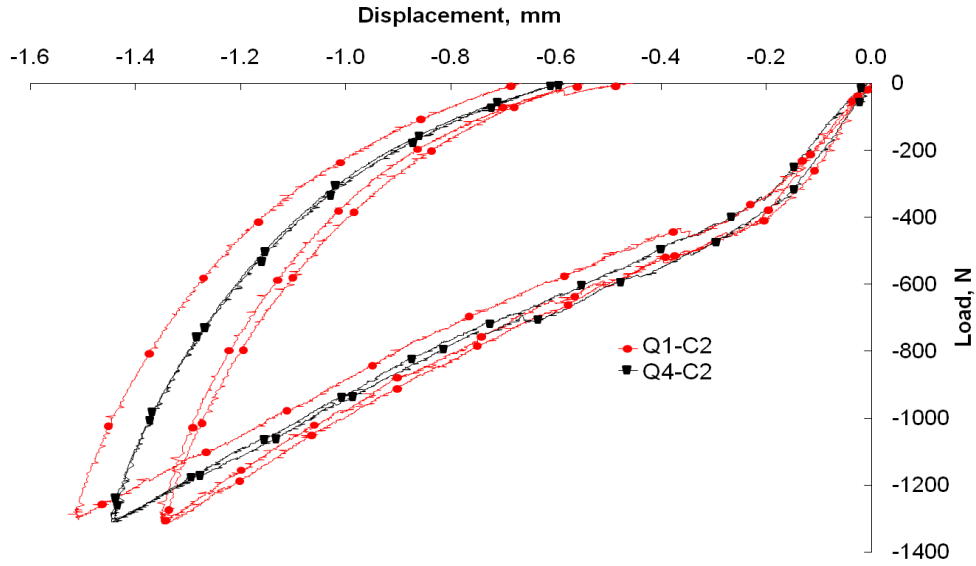


Figure 4.5. Representative P-d plots for Q1-C2 and Q4-C2 8 ply specimens indented with the 25.4 mm diameter indenter.

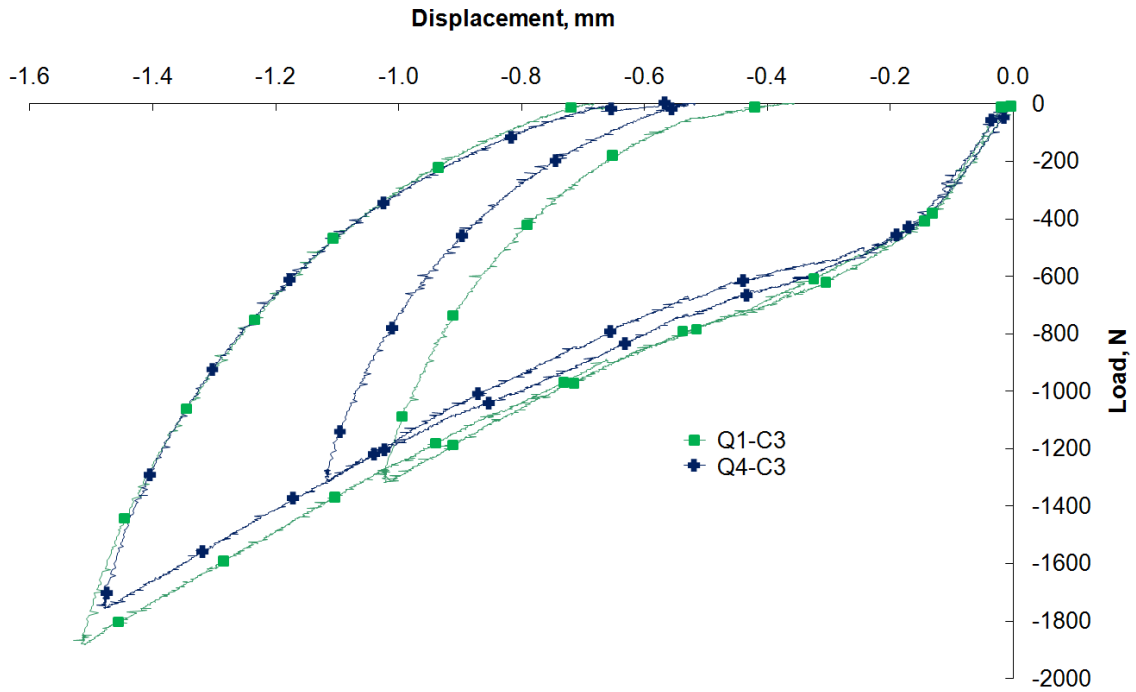


Figure 4.6. Representative P-d plots for Q1-C3 and Q4-C3 8 ply specimens indented with the 25.4 mm diameter indenter.

4.1.2 QSI Tests with 76.2 mm Diameter Indentor

The trends observed in the 8 ply specimens indented with the 76.2 mm diameter indentor were mostly similar to what was seen with the 25.4 mm diameter indentor. In order to meet the BVID criterion, specimens loaded with the 76.2 mm diameter indentor were loaded to a higher force in comparison to the specimens indented with the 25.4 mm diameter indentor. This resulted in the residual dent for the specimens tested with the 76.2 mm diameter indentor being larger than those indented with the 25.4 mm diameter indentor. Figure 4.7 presents the representative load versus displacement plots for the different sandwich geometries indented with the 76.2 mm diameter indentor. Just as in the 25.4 mm diameter indentor case, a single representative plot is presented for each sandwich configuration since not much specimen to specimen variation was noticed in the P-d data for the different specimens within each sandwich configuration.

Like in the 25.4 diameter indentor case, the initial region of elastic deformation show that specimens with the high density C3 core has a stiffer response than those with lower density C1 or C2 cores. The similar slope in the initial region of elastic deformation between the C1 and C2 cores is more clearly shown in Figure 4.8, which presents data from all the 8 ply specimens in the Q1-C1 and Q1-C2 sandwich geometries indented with the 76.2 mm diameter indentor. Here, we see that in the initial elastic region, both the Q1-C1 and Q1-C2 sandwich configurations show similar stiffness.

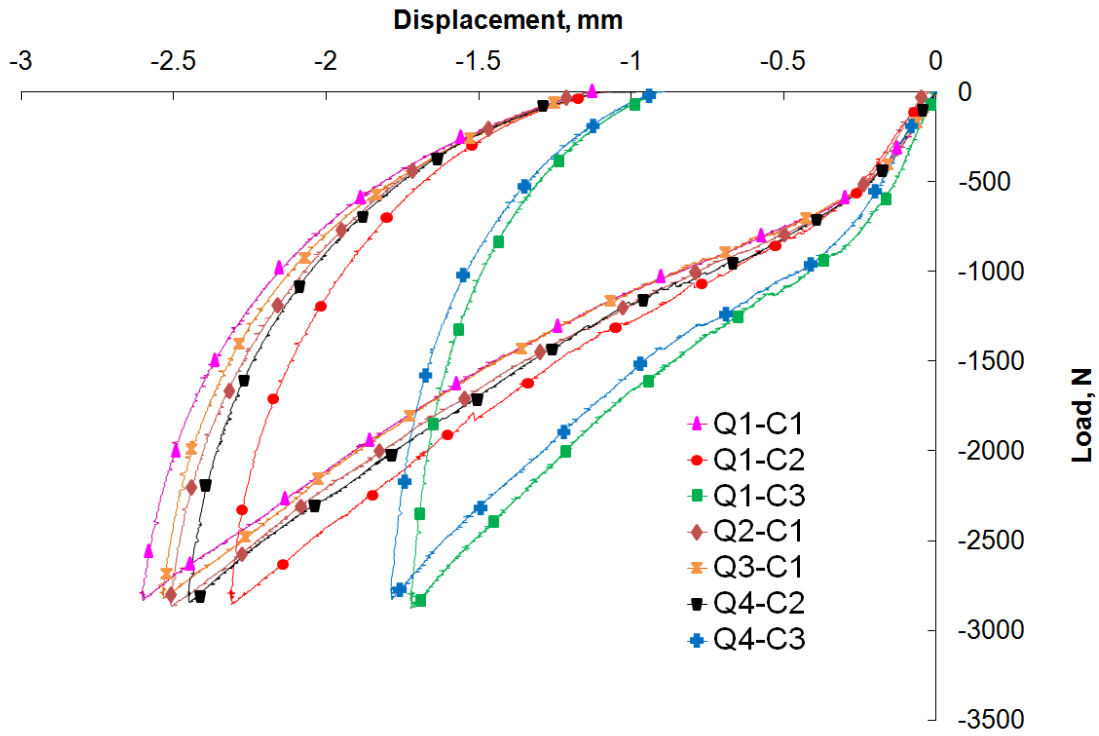


Figure 4.7. Representative P-d plots for the 8 ply specimens indented with 76.2 mm diameter indenter.

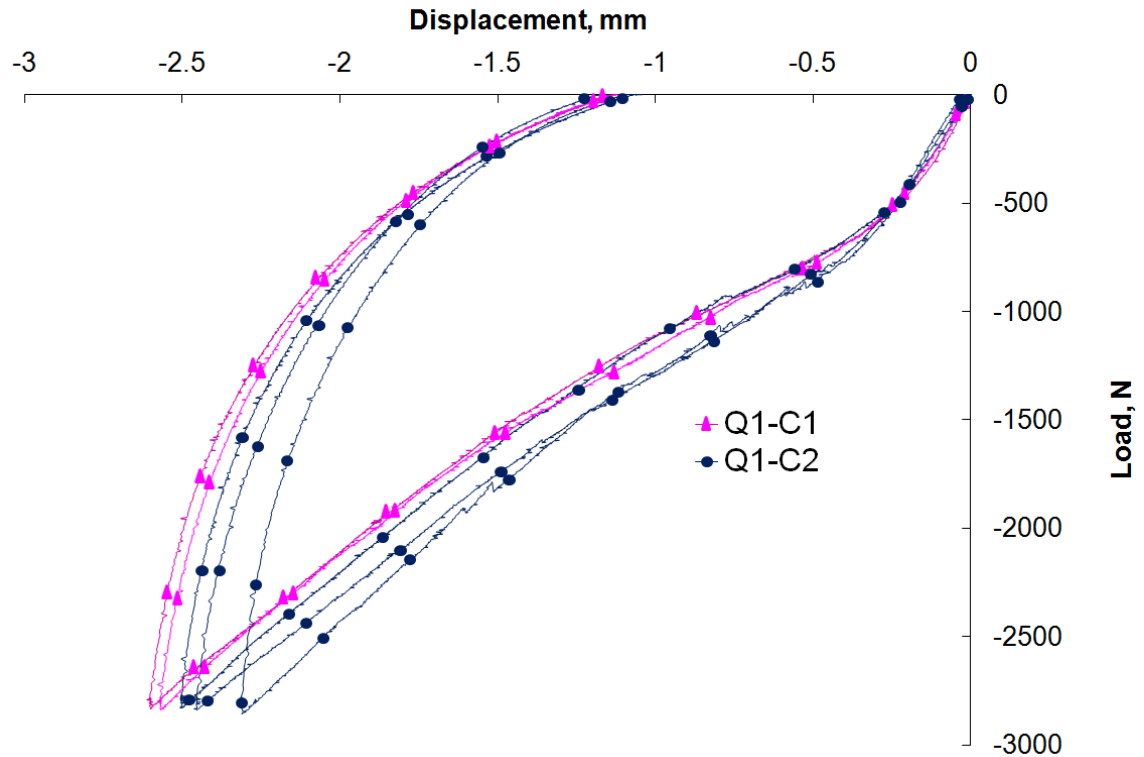


Figure 4.8. Representative P-d plots for Q1-C1 and Q1-C2 8 ply specimens indented with 76.2 mm diameter indenter.

The slope of the initial region of elastic deformation for the specimens with the C3 core behaving more stiffly than the specimens with the C1 and C2 cores show that the higher core density results in a stiffer sandwich response in the initial loading phase. Figure 4.7 clearly shows us that specimens with the high density C3 core have significantly stiffer response in the inelastic region than the specimens with the C1 and C2 cores. The slopes in the secondary region between the knee and the maximum load (i.e. the “inelastic region” as defined by the schematic in Figure 4.1) are also primarily controlled by the core, with a secondary effect of face sheet. As can be seen in Figure 4.7, specimens with the high density C3 core again show the stiffest response. Comparing the sandwich response in the inelastic region for specimens with the C1 and C2 cores which have the same core density, Figure 4.8 shows that for the same face sheet

layup, specimens with the thinner C2 core behave slightly more stiffly than the specimens with the thicker C1 core. A similar difference in behavior between the C1 and C2 cores was also observed for the specimens indented with the 25.4 mm diameter indenter case. This is again due to the smaller thickness of the C2 core giving it less ability to redistribute the load during and after core crushing. It therefore provides an effectively stiffer structural response than the C1 core once core crushing has initiated. As can be seen from both Figures 4.7 and 4.8, a stiffer response means less deformation at the peak load, which also generally corresponds to a smaller permanent dent depth.

Just like in the 25.4 mm diameter indenter case, face sheet layup also has a secondary influence on the indentation response for the specimens indented with the 76.2 mm diameter indenter. This is more clearly illustrated by Figures 4.9 - 4.11. Figure 4.9 presents the P-d plots for all the specimens from the Q1-C1 and Q2-C1 sandwich geometries indented with the 76.2 mm diameter indenter. The Q1-C1 and Q2-C1 sandwich configurations show essentially the same stiffness both prior and subsequent to the onset of core crushing, but the bend in the curve during the transition region happens over a smaller range of load for Q1 than for Q2. A similar observation was noted for the specimens indented with the 25.4 mm diameter indenter. There is no quantitative delamination area data available for the specimens indented with the 76.2 mm diameter indenter in order to be able to say that the larger bend in the Q2 layup could be related to more delamination in the Q2 layup as compared to the Q1 layup.

Figures 4.10 and 4.11 compare the Q1 and Q4 face sheet layups for the C2 and C3 cores. Figure 4.10 compares the Q1-C2 and Q4-C2 sandwich configurations while Figure 4.11 compares the Q1-C3 and Q4-C3 sandwich configurations. Except for one isolated specimen in the Q1-C2 sandwich configuration, both the Q1 and Q4 layups show similar stiffness in the

inelastic region for both the core types. This was mostly true for the specimens of these sandwich configurations indented with the 25.4 mm diameter. The only difference was that in the 25.4 mm indenter diameter tests, the Q1-C3 sandwich configuration showed a slightly steeper and longer transition region than the Q4-C3 sandwich configuration.

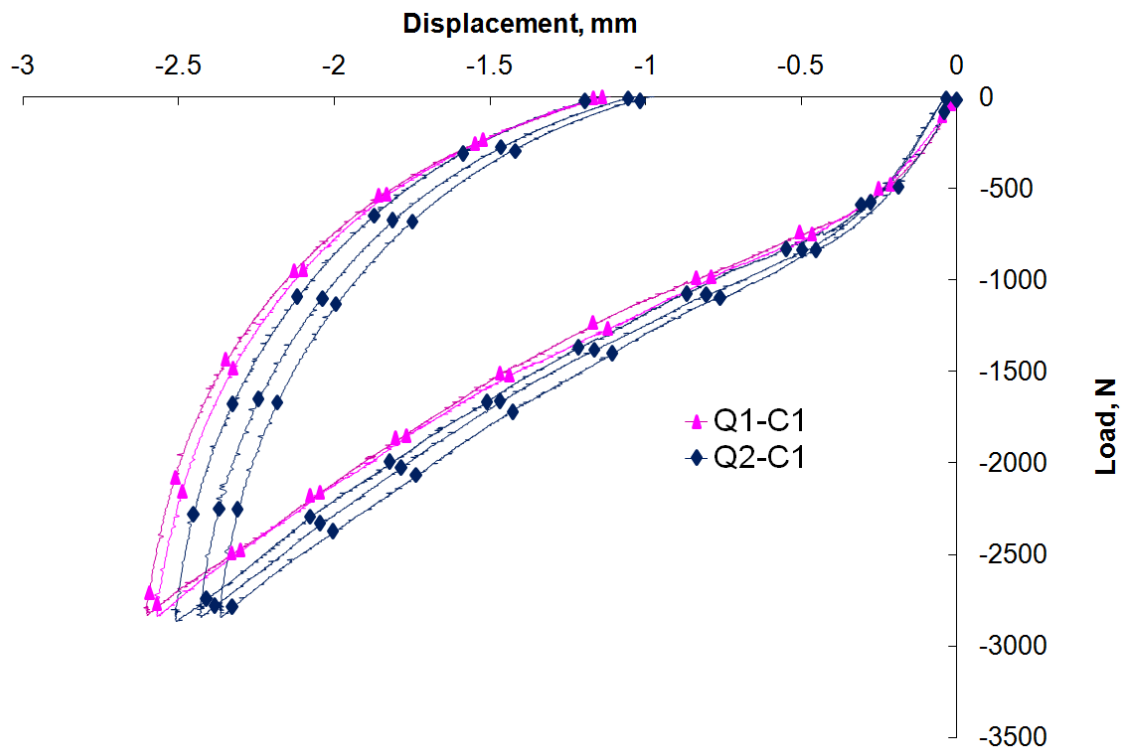


Figure 4.9. Representative P-d plots for Q1-C1 and Q2-C1 8 ply specimens indented with 76.2 mm diameter indenter.

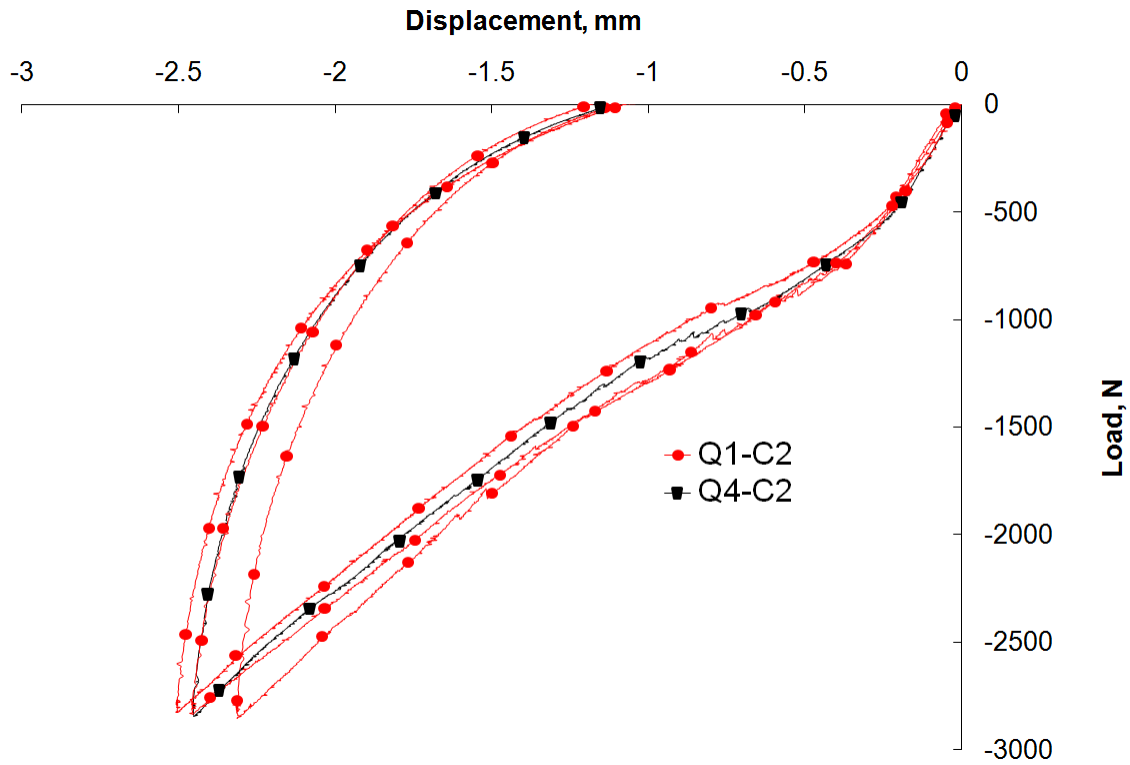


Figure 4.10. Representative P-d plots for Q1-C2 and Q4-C2 8 ply specimens indented with 76.2 mm diameter indenter.

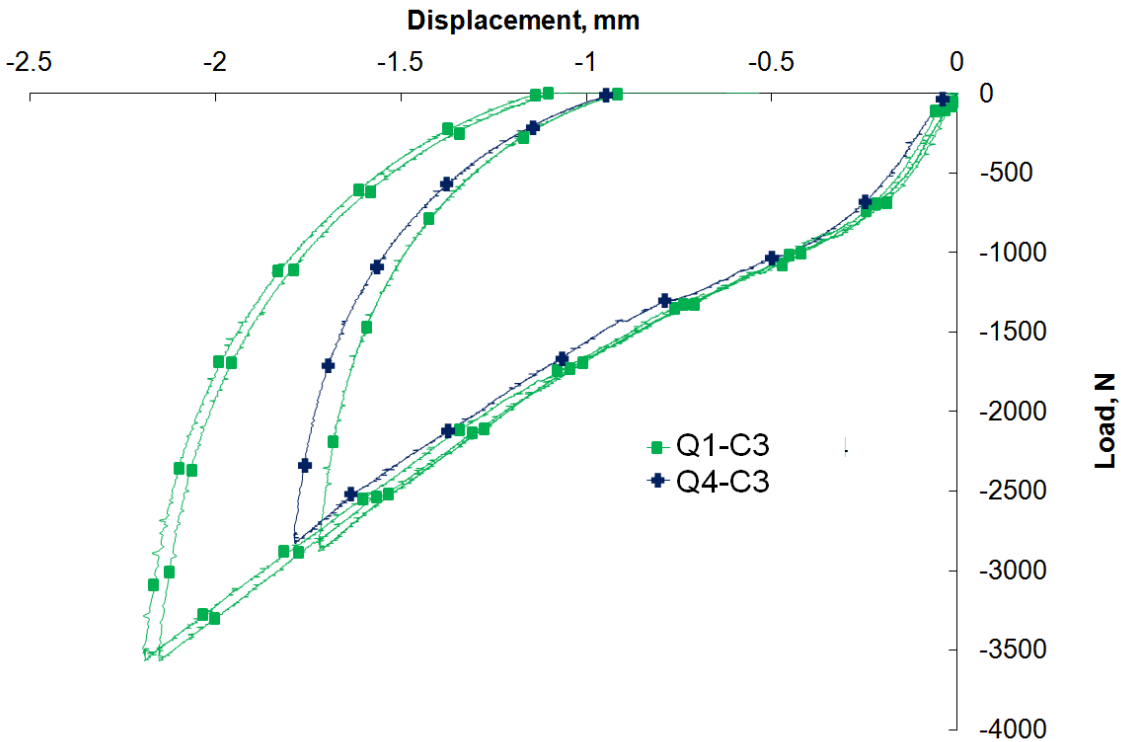


Figure 4.11. Representative P-d plots for Q1-C3 and Q4-C3 8 ply specimens indented with 76.2 mm diameter indenter.

4.2 16 Ply Results

4.2.1 QSI Tests with 25.4 mm Diameter Indentor

Figure 4.12 presents representative load versus displacement plots for the specimens from the various sandwich configuration with 16 ply face sheet indented with the 25.4 mm diameter indenter. Again, because of very little specimen to specimen variation within a particular sandwich configuration, only a representative plot for each sandwich configuration is shown in this figure.

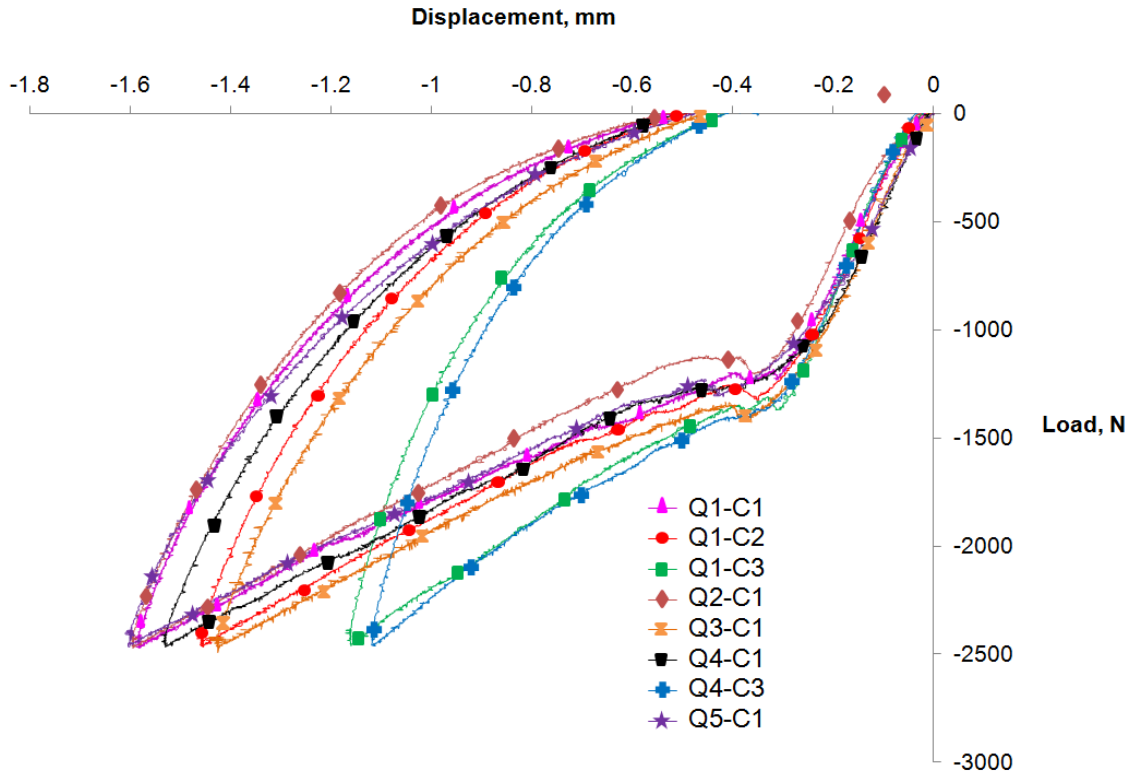


Figure 4.12. Representative P-d plots for the 16 ply specimens indented with the 25.4 mm diameter indenter.

It is clearly evident that in the initial loading phase, the slope of the curves for the Q1-C1 and Q1-C2 sandwich configurations is very similar. The Q1-C3 sandwich configuration shows slightly stiffer response in the initial elastic region, but the difference is very small. This is more clearly seen in Figure 4.13 which compares the Q1-C1, Q1-C2 and Q1-C3 sandwich configurations. Because presenting all the specimen data would have made comparisons difficult due to overcrowding of the plot, only one specimen from each panel that was manufactured for a particular sandwich configuration is presented in this figure. As can be seen clearly in Figure 4.13, only a small effect of core density is seen in the initial elastic region with the specimens with the C3 core behaving only slightly stiffer than the specimens with C1 and C2 cores. No significant difference can be seen in the behavior of the specimens with the C1 and C2 cores in

the initial loading phase. Even though the specimens with the C3 core behave slightly more stiffly than the specimens with the C1 and C2 cores, the difference is relatively less as compared to the 8 ply case. This suggests that increasing the face sheet thickness minimizes the effect of core on the sandwich response in the initial elastic region. It is also evident from Figure 4.13 that specimens with the C3 core have onset of core crushing at a slightly higher load as compared to the C1 and C2 cores. Also, as can be seen from Figure 4.12, for the 16 ply specimens the threshold load at which the core crushes for all layups is typically higher than the 8 ply case. This indicates that, as would be expected, a higher force is needed to initially crush the core in the 16 ply specimens as compared to the 8 ply specimens.

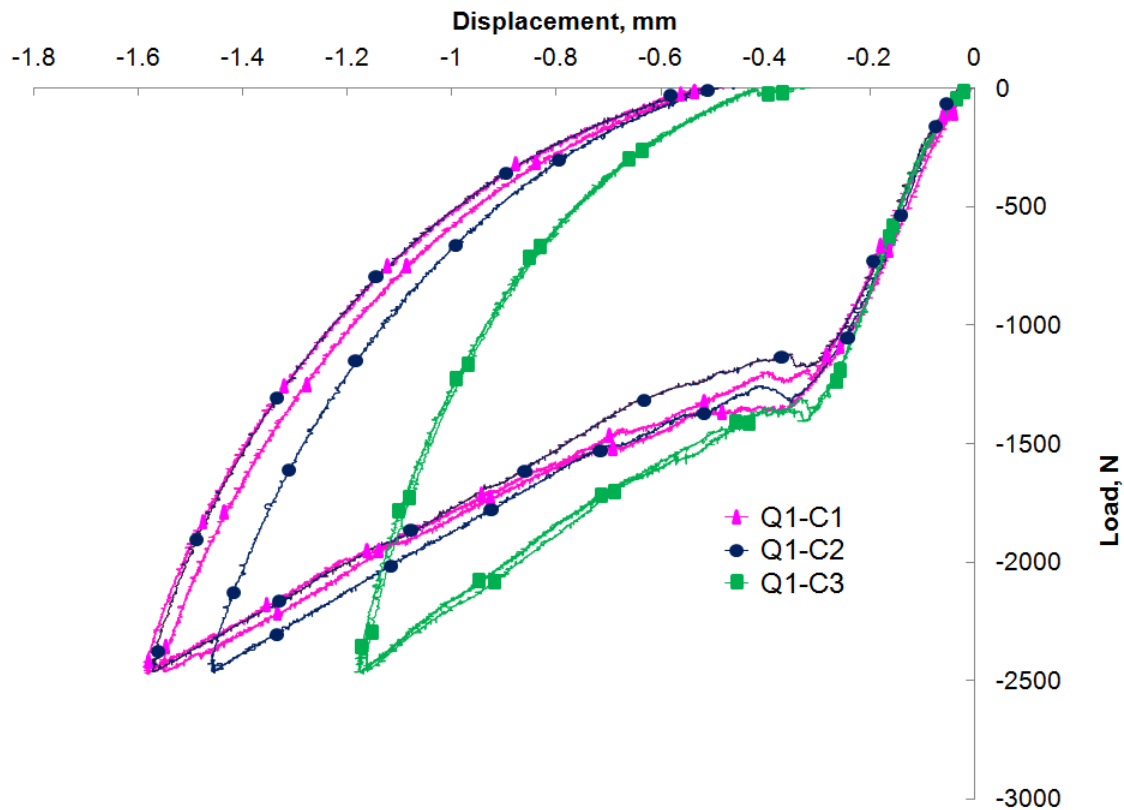


Figure 4.13. P-d plots for Q1-C1, Q1-C2 and Q1-C3 16 ply specimens indented with the 25.4 mm diameter indenter.

Figure 4.13 also shows that post core crushing, i.e., in the inelastic region, C3 core shows the stiffest response while C2 and C1 cores show similar stiffness in response. Core density has a significant influence on the sandwich response post initial core crushing as the higher density, C3, core provides a stiffer structural response as compared to both the lower density C1 and C2 cores. The effect of core thickness however seems more and more diminished for the thicker face sheet as compared to the thinner face sheet.

Figure 4.14 compares data from all the sandwich geometries with a constant C1 core. For sandwich configurations with more than two specimens tested, only a single specimen from each panel manufactured is presented in the plot. This is again to avoid overcrowding of data which makes comparisons difficult. No significant difference in the stiffness of the response in the inelastic region is seen between the different face sheet layups. A further comparison of the Q1 and Q4 face sheet layups for a constant C3 core is presented in Figure 4.15. This again shows no significant difference in stiffness in the inelastic region. It can therefore be concluded that for the 16 ply case, face sheet layup does not influence indentation resistance in the inelastic region. This also explains the similar dent depths discussed in Chapter 6 for the different face sheet layups with the same core.

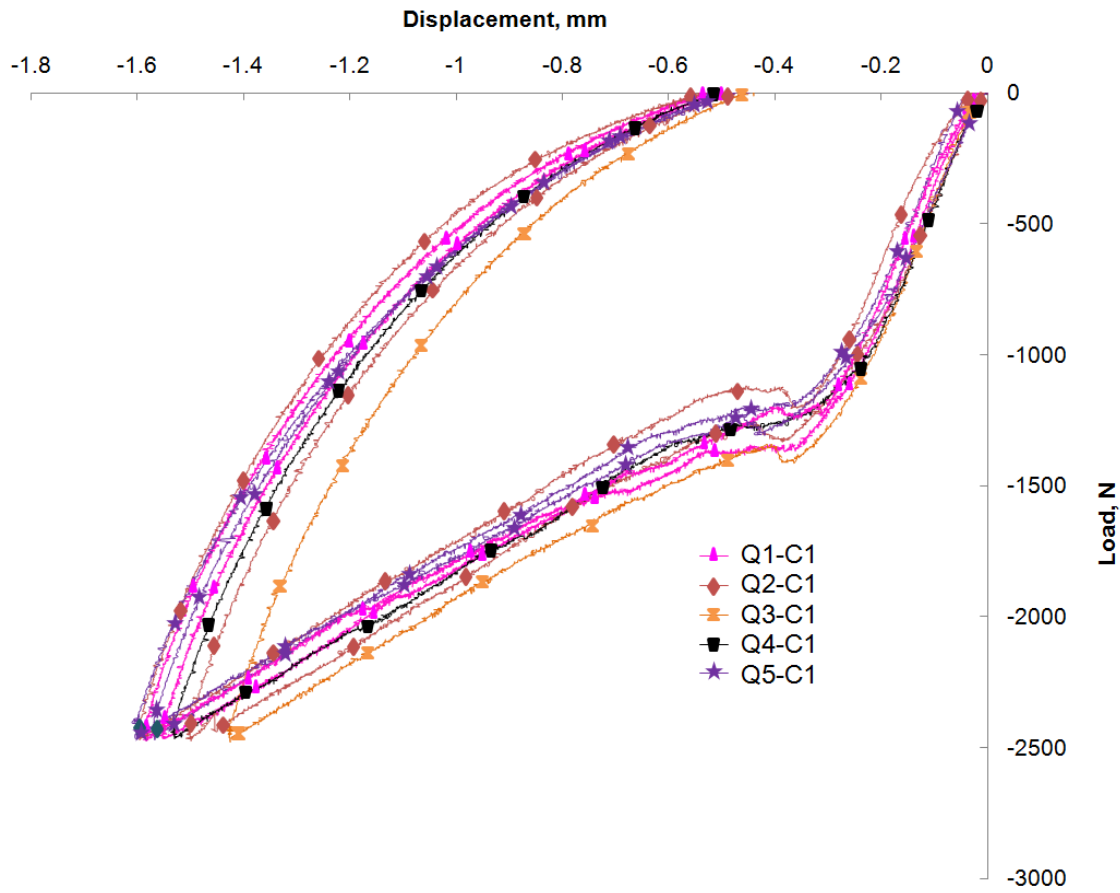


Figure 4.14. P-d plots for different face sheet layups with C1 core for the 16 ply specimens indented with the 25.4 mm diameter indenter.

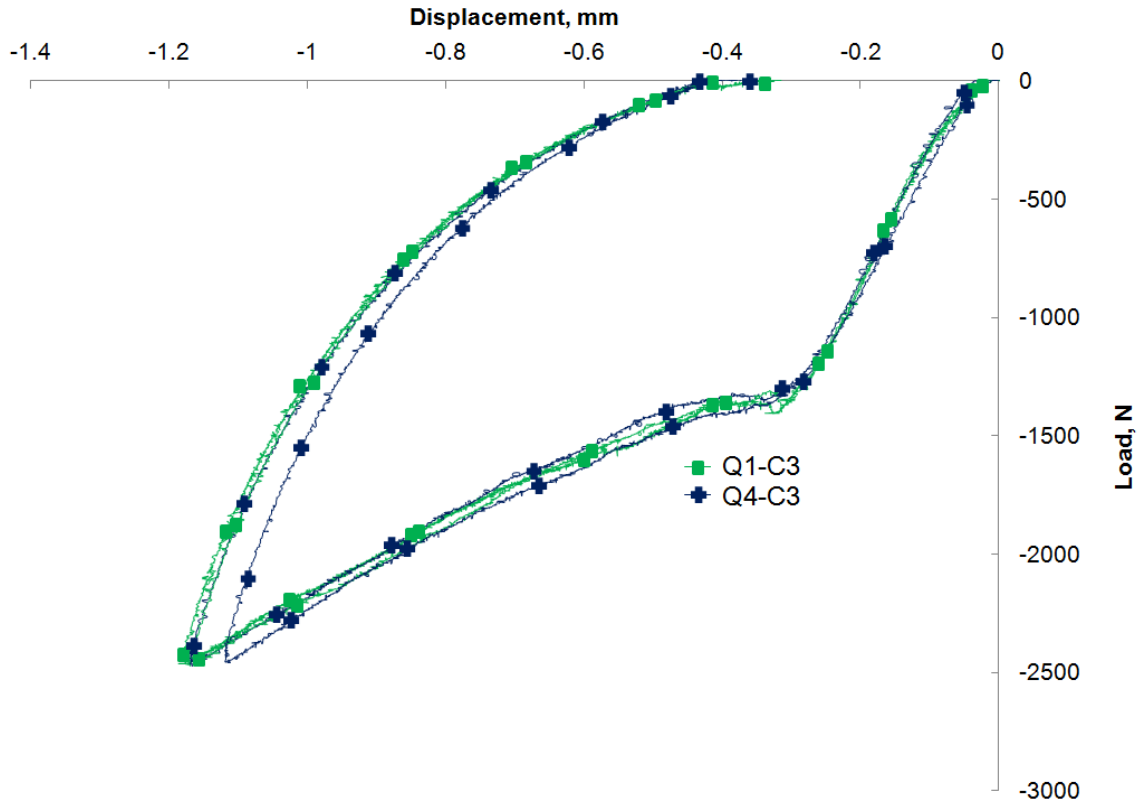


Figure 4.15. P-d plots for Q1-C3 and Q4-C3 sandwich geometries for the 16 ply specimens indented with the 25.4 mm diameter indenter.

4.2.2 QSI Tests with 76.2 mm Diameter Indentor

Figure 4.16 presents representative load versus displacement plots for the various sandwich configurations with 16 ply face sheet indented with the 76.2 mm diameter indenter. Again, because of very little specimen to specimen variation, only a single representative plot for a particular sandwich configuration is shown in this figure. Prior to core crushing, the C3 core appears to have slightly stiffer response when compared to the C1 and C2 cores. This is more clearly illustrated by Figure 4.17 which compares the C1, C2 and C3 cores for the Q1 face sheet layup. Because presenting all specimens would have made comparing data difficult for these sandwich configurations, only one specimen from each panel that was manufactured for a

particular sandwich configuration is presented in this figure. The higher density core, C3, begins to show a stiffer structural response earlier on in the initial loading phase when compared to other two lower density cores. The effect of core density in the initial loading phase is more pronounced in the 76.2 mm diameter indenter case as compared to the 25.4 mm diameter indenter case. Core thickness seems to have no effect on sandwich response prior to core crushing as can be seen by no difference in stiffness between the Q1-C1 with Q1-C2 sandwich geometries.

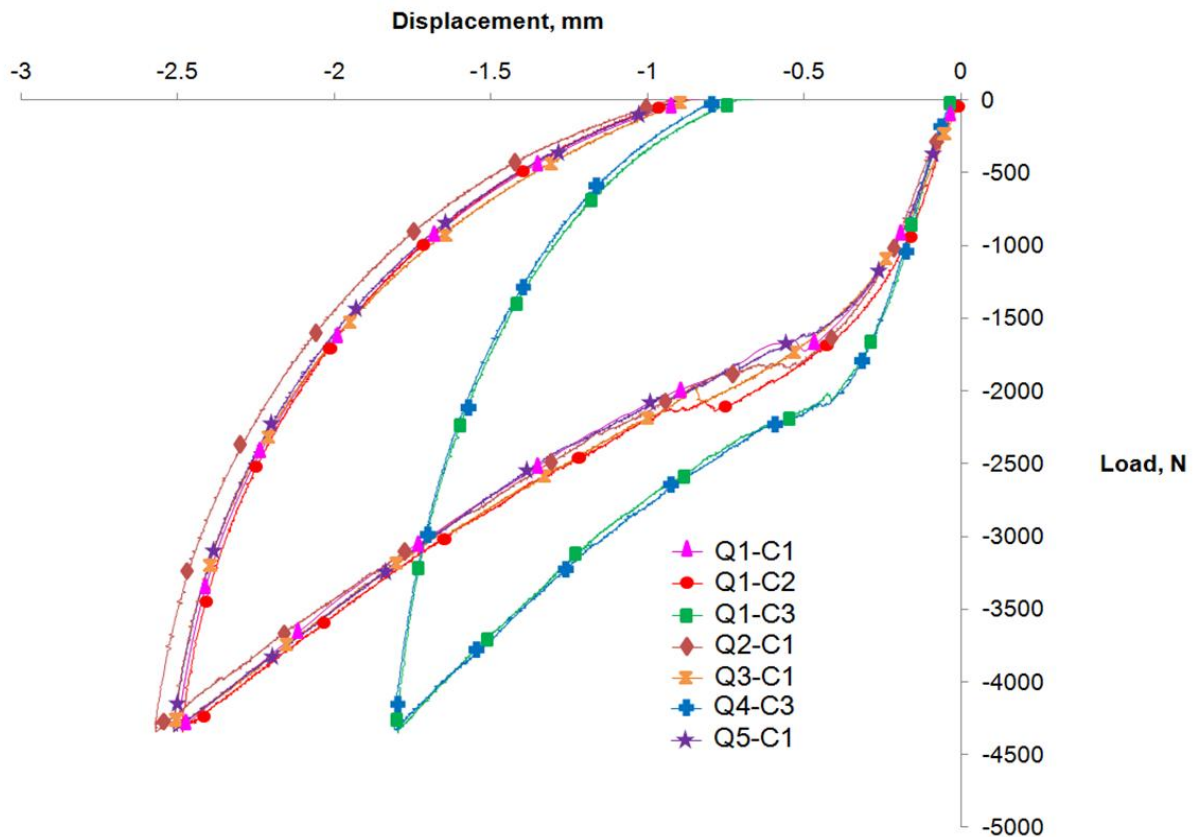


Figure 4.16. Representative P-d plots for 16 ply specimens indented with the 76.2 mm diameter indenter.

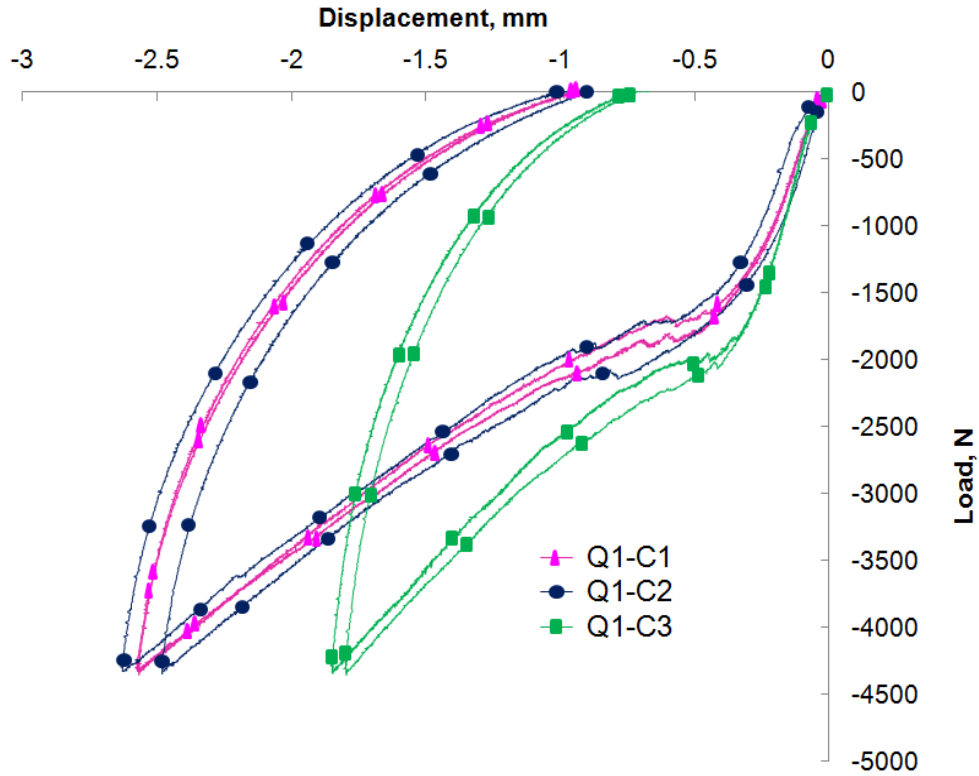


Figure 4.17. P-d plots for Q1-C1, Q1-C2 and Q1-C3 16 ply specimens indented with the 76.2 mm diameter indenter.

In the inelastic region, it is clear that C3 shows a much stiffer response than the C1 and C2 cores – a behavior that is also observed in the specimens indented with the 25.4 mm diameter indenter. The higher density core (C3) contributes to a stiffer structural response as compared to the lower density cores (C1 and C2), thus clearly indicating that core density greatly influences sandwich response post core crushing. Also C3 core has a higher non-linear point as compared to the C1 and C2 cores, indicating that the onset of core crushing is at a higher load. The same was observed and reported earlier for the specimens indented with the 25.4 mm diameter indenter. As was also reported for the specimens indented with the 25.4 mm diameter indenter, the effect of

core thickness however seems more and more diminished for the thicker face sheet in the inelastic region.

Figure 4.18 compares all the sandwich configurations with a constant C1 core. There is no specimen from the Q4-C1 sandwich geometry that was tested with the 76.2 mm diameter indenter and thus is not presented in the figure. For sandwich configurations with more than two specimens tested, only a single specimen from each panel manufactured is presented in the plot. This is again to avoid overcrowding of data which makes comparisons difficult. No significant stiffness difference in the sandwich response is seen between the different face sheet layups in the inelastic region. A further comparison of the Q1 and Q4 face sheet layups for a constant C3 core is presented in Figure 4.19. This again shows no significant difference in response stiffness in the inelastic region. As was in the case of the specimens indented with the 25.4 mm diameter indenter, it can be said that the face sheet layup does not influence indentation resistance in the inelastic region.

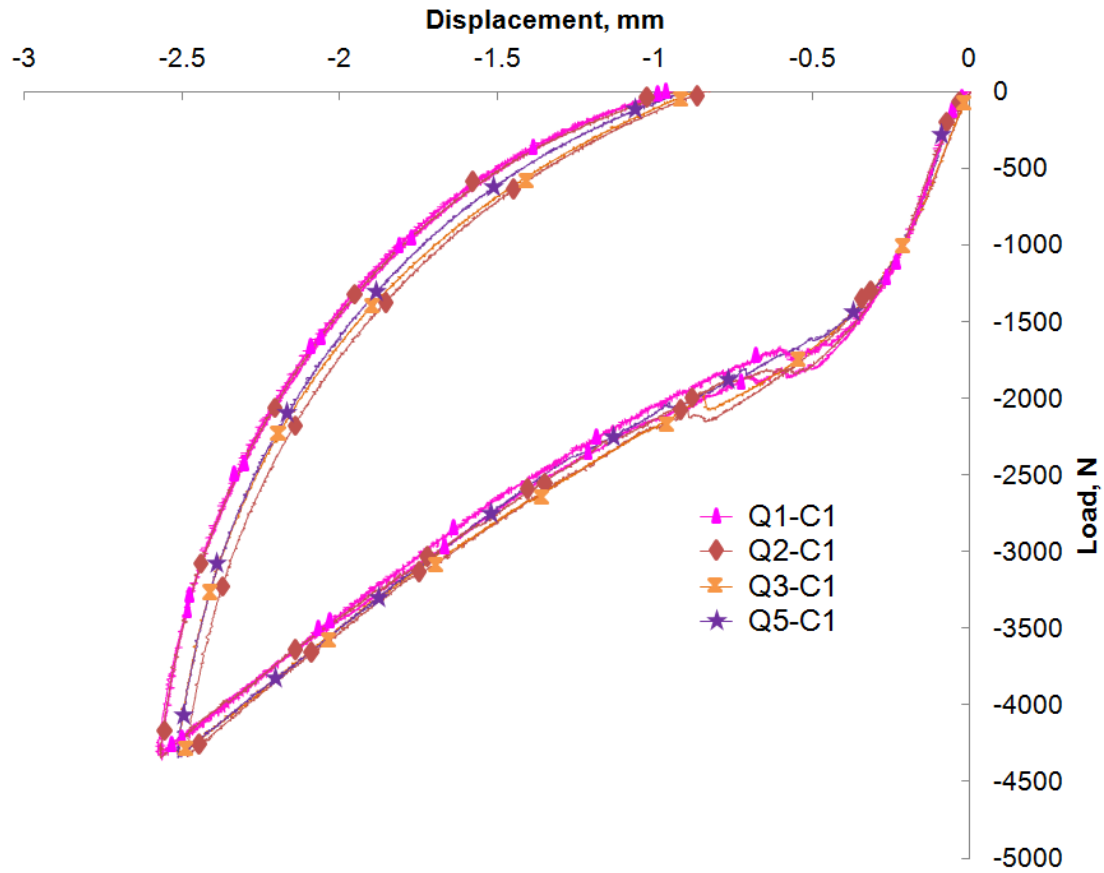


Figure 4.18. P-d plots for different face sheet layups with C1 core for the 16 ply specimens indented with the 76.2 mm diameter indenter.

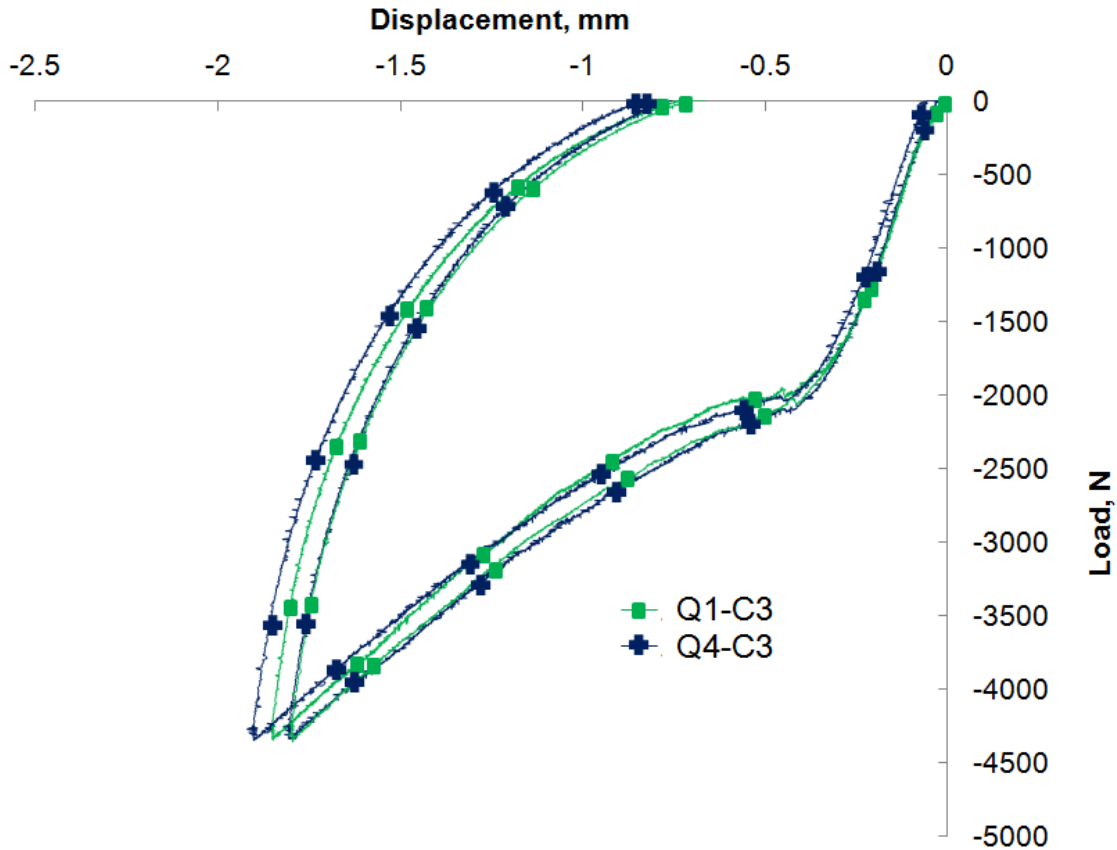


Figure 4.19. P-d plots for Q1-C3 and Q4-C3 sandwich geometries for the 16 ply specimens indented with the 76.2 mm diameter indenter.

4.3 Summary

Similar trends are observed for specimens tested with the 25.4 mm and 76.2 mm diameter indentors for the 8 ply case. For the 8 ply case, the sandwich configurations with the C3 core show the stiffest response both in the initial elastic and inelastic regions. While the difference in response between the C1 and C2 cores is not so pronounced in the initial elastic region, the C2 core clearly shows stiffer response than the C1 core in the inelastic region in the 8 ply case. The effect of face sheet layup on sandwich response is only slight in the 8 ply case and observed only

in the 25.4 mm indenter diameter tests. For the 25.4 mm indenter diameter tests in the 8 ply case, the Q2 face sheet layup shows a slightly stiffer response than the Q1 face sheet layup and the Q4 face sheet layup shows a slightly steeper and longer transition period than the Q1 face sheet layup. The Q4 and Q1 face sheet layup show similar stiffnesses in the inelastic region.

The core crushing threshold load is larger for the 16 ply case as compared to the 8 ply case. Just as it was in the 8 ply case, the C3 core clearly shows a significantly stiffer response than the C2 and C1 cores in the inelastic region for the 16 ply case. The effect of core density in the initial elastic region is less pronounced in the 16 ply case as compared to the 8 ply case. Specimens with the C2 and C1 cores in the 16 ply case show very similar stiffnesses in response in the inelastic region. This is different from what was seen for the 8 ply case, where the C2 core showed slightly stiffer response than the C1 core in the inelastic region. No effect of face sheet layup on sandwich response is seen in the 16 ply case.

In view of the above discussion, the key observations from the load versus displacement data can be summarized as follows:

- i. the 16 ply specimens show the core crushing threshold load at a higher load level as compared to the 8 ply specimens.
- ii. in the initial elastic region, the C3 core shows the stiffest response. This is more significant in the 8 ply case than in the 16 ply case.
- iii. core density continues to influence the sandwich response in the inelastic region. The higher density core, C3, shows the stiffest response in the inelastic region for both the 8 and the 16 ply cases.

- iv. the effect of core thickness on the sandwich response is seen only in the 8 ply case where the thinner, C2, core shows a stiffer response than the thicker, C1 core.
- v. the effect of face sheet layup is only seen in the transition and inelastic regions of the 8 ply specimens indented with the 25.4 mm diameter indenter. No influence of face sheet layup is seen for the 8 ply specimens indented with the 76.2 mm diameter indenter or for any of the 16 ply specimens.

The change in face sheet compliance, as seen in the P-d plots at the transition region and in the inelastic region occur as a result of damage that is taking place in the sandwich structure. While core crushing is believed to be one of the first damage modes that occur, delamination onset and growth may also influence the structural response. As described in chapters 2 and 3, these also have a significant effect on the post-impact strength of the structure. Evaluation of delamination damage in the indented structure is discussed in detail in the next chapter. Assessment of the effects of the combined damage types are presented in the subsequent chapter.

Chapter 5

DELAMINATION ASSESSMENTS

Introduction

Delaminations are a major damage mode in sandwich structures undergoing impact or indentation loading. As discussed in chapters 2 and 3, the characterization of delaminations is essential as a measure for damage in sandwich structures and more importantly, to understand the influence of delaminations on the post-impact residual compressive strengths and failure modes of sandwich structures.

This chapter presents the delamination assessment results where the nature of the delaminations for the indented sandwich structures is discussed in detail. Non-destructive evaluation (NDE), via ultrasonic c-scan, was primarily the means for the characterization of delaminations. This NDE technique is discussed in detail, with additional information provided in the appendix. C-scan images that reveal the delaminations are presented and discussed in this chapter. All the comparisons made between the c-scan images in this chapter are qualitative in nature. Quantitative assessments are presented in this chapter, and quantitative assessments are presented and discussed separately in the next chapter. Selected destructive evaluation (DE) results for both the 8 and 16 ply cases are also presented. These DEs were performed primarily to validate the accuracy of the NDE technique as well as to shed more light on the shielded (hidden) delaminations, i.e., the delaminations at the deeper interfaces that lie right beneath the delaminations at the shallower interfaces.

5.1 Delamination Measurements

Delaminations were primarily assessed non-destructively using a c-scan. The working of c-scan is based on ultrasonic sound waves that are passed through a sandwich structure. Two of the commonly used c-scan methods are the “pulse echo” and the “through transmission” methods. In the pulse echo method, the principle of reflection of ultrasonic waves is used. The ultrasonic waves reflect from pre-existing defects and the reflected waves are received again by the transducer which also acts as a receiver. The velocity of sound in distilled water, which is the common medium of wave travel in the c-scan, as well the total travel time of the wave can be used to find the depth of the defect using the pulse-echo method. The through-transmission method involves two ultrasonic transducers where one acts as the transmitter and the other as the receiver. The transducers face directly opposite each other and are separated by the specimen. Defects in the structure will either block or attenuate the transmitted ultrasonic signal, causing a reduction in the signal amplitude or a total loss of signal. In both the pulse-echo and the through-transmission methods, the existing defect is identified through the time of flight or amplitude display of the received signals in the form of a 2D image that shows a variation of these parameters as a function of the locations where the scan is run.

Both pulse-echo and through-transmission c-scan methods were initially explored for internal delamination assessments. Perhaps due to the large overall sandwich panel thickness, the through-transmission approach produced relatively poor results. As such, internal delamination assessments for both the 8 and 16 ply specimens were performed using the SU-CML c-scan unit with the same 50 MHz pulse-echo transducer that was used for the surface indentation profile evaluations described in Chapter 3. The small wavelength of this transducer allowed resolution of relatively near-surface delaminations and, due to the small thickness of the face sheets in the 8

ply case, did not appreciably affect the ability to resolve delaminations that were close to the core to face sheet bond.^{19-20, 84} That is, a reflected ultrasonic signal from the back surface of the top face sheet was obtained for the 8 ply specimens, thus indicating the ability of the transducer to resolve delaminations up to the last interface for the 8 ply specimens. However, this was not the case with the 16 ply specimens. No back surface reflection was obtained for the 16 ply specimens and only delaminations up to interface 11 were clearly resolvable by the 50 MHz transducer for the 16 ply case. Other lower frequency transducers of 25, 10 and 5 MHz were also tried for the 16 ply case in case they gave delamination information beyond interface 11. No delaminations were seen beyond interface 11 even with these transducers and the overall scan quality became poorer with smaller frequency transducer. From the viewpoint of both the scan quality and the resolution, the 50 MHz transducer gave far superior results than all the other low frequency transducers. Thus, it was deemed the best choice for the 16 ply delamination assessments.

For the undamaged regions of the face sheet, the time of flight between the front and back surface reflection was found to be approximately 0.6 μs for the 8 ply case. Thus, a reflection received 0.075 μs after the front surface reflection corresponded to the delaminations in the first interface, a reflection after 0.15 μs corresponded to the second interface, and so on. These times were not always exact and fluctuated slightly around these values. Similar time increment from interface to interface was assumed for the 16 ply specimens since the ply thickness remained the same as the 8 ply specimens. The front surface reflection was generally so long for both the 8 and 16 ply specimens that it merged with the reflection from the first interface, making resolution of any delaminations at this interface nearly impossible. However,

reflections from the remaining interfaces could be resolved for the 8 ply case and at least up to interface 11 for the 16 ply case.

The planar area of delamination, which is the overall projected delamination area, was determined for all the 8 and 16 ply specimens except for the specimens in the 8 ply tests that were indented with the 76.2 mm diameter indenter. The data on the planar area of delamination for all the sandwich specimens is presented in chapter 6. In the case of the 8 ply specimens indented with the 76.2 mm diameter indenter, the slope of the specimen's external surface was such that the reflected signal could not adequately be captured at distances away from the dent center closer to the dent periphery. This resulted in the c-scan images becoming increasingly blurred away from the dent center with no clear information on the delaminations. Also, planar delamination boundaries could not be clearly identified for this case. This was not so with the 16 ply specimens indented with 76.2 mm diameter indenter since all delaminations were apparently contained in a smaller region in comparison to the overall dent periphery and the full extent of planar delamination could be fully captured by the c-scan. For all the cases where the planar delamination boundaries were clearly defined in the c-scan images, the planar area of delamination was quantitatively determined. This was done using the c-scan data evaluation software which allowed the user to create a boundary around the delaminated region and the software automatically calculated the value of the area enclosed within the boundary.

One major drawback of the ultrasonic delamination assessment technique was that it could not capture shielded delaminations, i.e. deep interface delaminations that were right underneath the shallow interface delaminations and thus, remained undetected by the ultrasonic signals. In order to determine the amount of shielded delaminations as well as to validate the NDE results, select small QSI specimens were destructively evaluated for both 8 and 16 ply

cases. The NDE results were obtained before assessing the specimens destructively and the DE results were then compared to the NDE results. In the destructive evaluations, the small QSI specimens were cut in the four ply angle directions of 0° , 90° , 45° and -45° . The cuts were made through the dent center using a thin diamond blade. Due to the large number of cuts that were made, specimens were not polished, but rather viewed with an optical microscope “as is.” This likely somewhat affected the ability to resolve all delaminations but, as will be shown, is not believed to affect the overall interpretations. Thus, after cutting, sections were imaged using a “scanning optical microscope”; that is, an optical microscope that takes several auto-focused images across a large planar area and then appropriately reconstructs these into a single image. These images were then inspected for delaminations and matrix cracks, and corresponding “2D damage maps” were constructed. The 2D damage maps are drawings of the microscope images and were made for ease-of-use, i.e., so that the actual micrographs would not need to continually be referred to. They were intended to show all salient details. The overall process is illustrated in Figure 5.1, which presents the NDE image of an 8 ply Q1-C1 small QSI specimen, the corresponding DE image from a 0° direction cut, and the 2D damage map. This specimen was QSI tested using a 25.4 mm diameter indenter to 1300 N and had a dent depth of 0.53 mm. Delaminations that appear in the photomicrograph from the DE have been enhanced with white lines to aid in viewing at the scale of the image. Also included in the figure is a c-scan scale bar showing the time of flight and corresponding color scales. As can be seen in Figure 5.1, along the cut line the NDE and DE images show good correlation for the center delamination at interface 3 (blue) and for the delaminations extending to the left and right of it at the 5th (green) and 6th (yellow) interfaces.

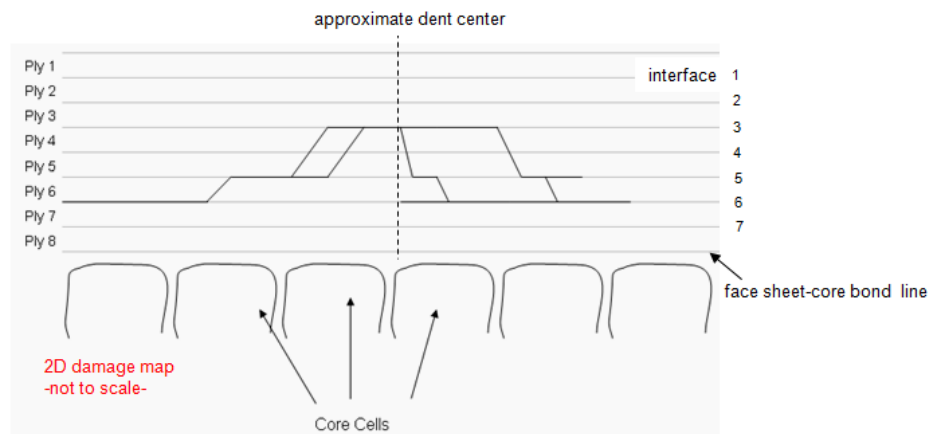
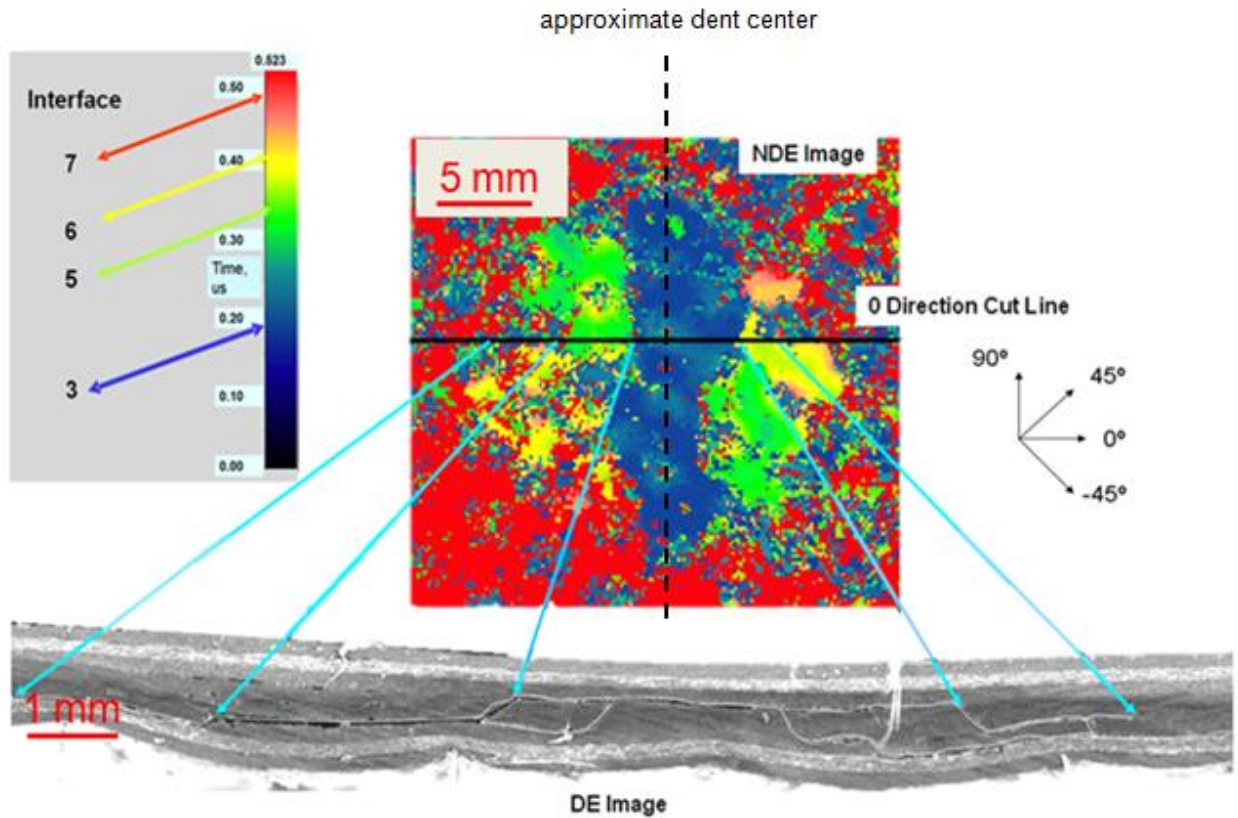


Figure 5.1. C-Scan image, destructively obtained cross-sectional view, and corresponding 2D damage map in the 0° cut direction for an 8 ply Q1-C1 sandwich specimen indented with the 25.4 mm diameter indenter.

In order to better understand the nature of the delaminations at shielded interfaces, information from the 2D damage maps for each of the four ply direction were assembled into

“3D damage maps.” To this end, the distances to each delamination’s starting and ending points were measured from a common datum and then assembled together for each interface. The information from the c-scan images was also overlaid on these individual interface drawings in order to give a more complete picture of the extent of delaminations at each interface, i.e., by combining the information retrieved from both the non-destructive and destructive evaluations. A typical result is presented in Figure 5.2, which presents the 3D damage map for the Q1-C1 specimen shown in Figure 5.1. The dotted lines in Figure 5.2 utilize the combination of the NDE and DE results to make a conservative estimation of the delaminated area at each interface. This was done primarily to better understand the nature of the shielded damage. This approach provided a simple and quantitative comparison of the NDE and DE data and, for all specimens evaluated, provided strong validation of the accuracy of the NDE results. It is pointed out that the 3D damage maps can also be displayed three dimensionally, i.e., by representing each of the interfaces as projection drawings and then by stacking the various planes appropriately in a 3D projection view. However, it was found that the information is more readily conveyed and understood in the format used in Figure 5.2.

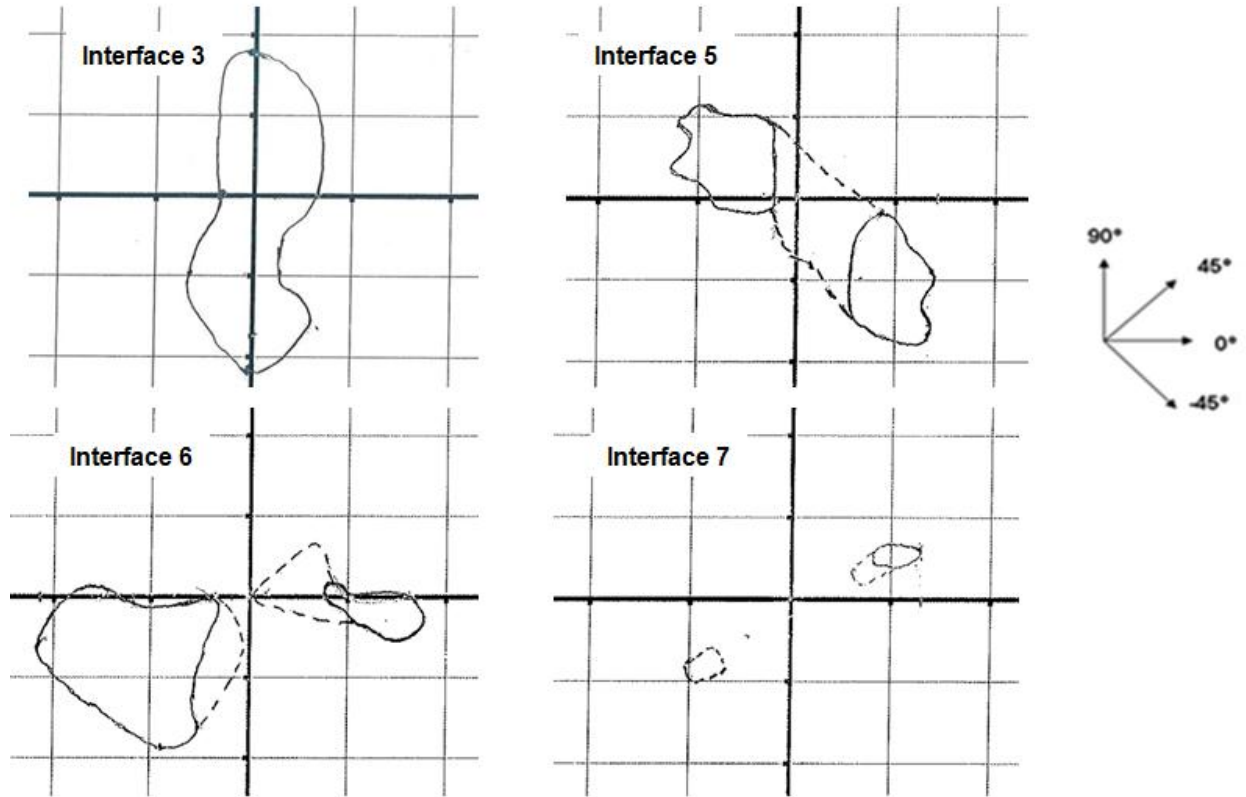


Figure 5.2. 3D damage map for the Q1-C1 specimen of Figure 5.1. Squares in the grids measure 5.00 mm x 5.00 mm.

Figures 5.3 and 5.4 present analogous NDE vs. DE comparisons for the 16 ply case. Herein, a Q4-C1 specimen indented with the 25.4 mm diameter indenter to a load level of 2200 N was destructively evaluated using the same procedure as described for the 8 ply case. Figure 5.3 presents the NDE image as well as the micrograph and the 2D damage map for the 0° direction cut. Figure 5.4 presents the corresponding 3D damage map which combines the NDE information with all the DE results for sections made in the four ply directions. Note from Figure 5.3 that there are non-shielded delaminations at interfaces 11 and 12 shown in the DE image which are not captured in the NDE image. For interface 11 delaminations, this appears to be an isolated case: in most other cases, as proven by the NDE images of the full-sized specimens

presented in section 5.6, the delaminations up to interface 11 were clearly captured in the NDE. However, just as it is in the case of Figure 5.3, any interface 12 delaminations which possibly existed were not captured by the NDE since none of the images presented in section 5.6 show interface 12 delaminations. This is likely due to the inability of the transducer to capture delaminations beyond interface 11. Correctly capturing the deep interface delaminations was a major consideration in the choice of the transducer, especially for the 16 ply case. However, as discussed in section 5.1, lower frequency transducers surprisingly did not make a difference in the depth to which the delaminating interfaces could be resolved. Figure 5.3 also shows that except a portion of interface 11 and 12 delaminations, most of the deep interface delaminations remain shielded. This is consistent with the literature¹² which shows that the size of the delaminations for sandwich structures continue to increase up to a certain interface with increasing depth from the impacted end, and then starts to decrease as the core is approached. This type of result is supported by the 3D damage map in Figure 5.4 where relatively small delaminations (compared to the delaminations at the other interfaces) are seen at interface 14. It is therefore suspected that the delaminations at the interfaces closest to the core mostly remained shielded. This however cannot be ascertained because of the limited destructive evaluations performed. Most of the full sized specimens depended on the NDE results for delamination information as DE was not possible due to the specimens being used for the CAI tests. In this regard, the importance of any missed delamination information cannot be underestimated since delaminations are one of the major damage modes that drive failure in the post-impact study.

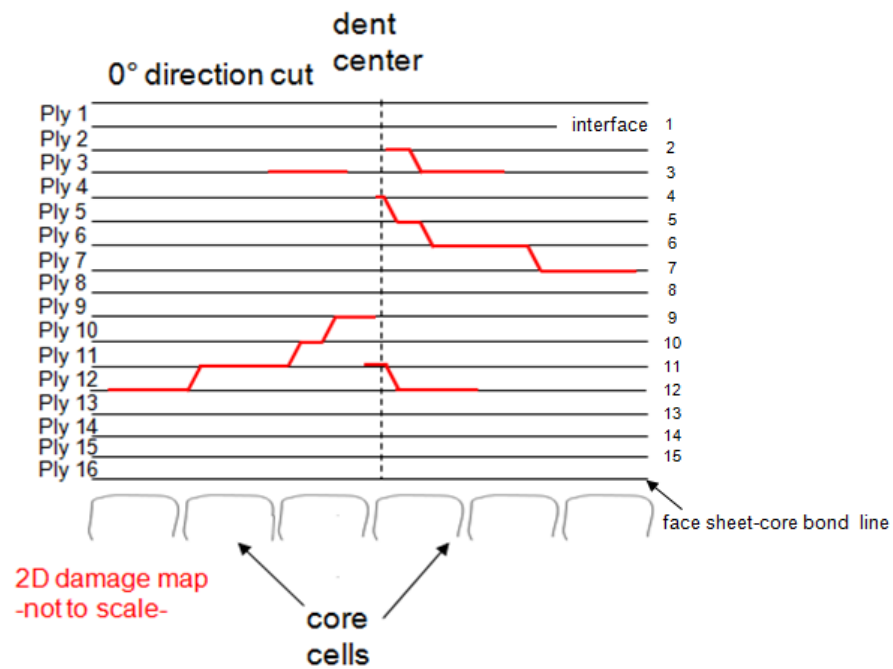
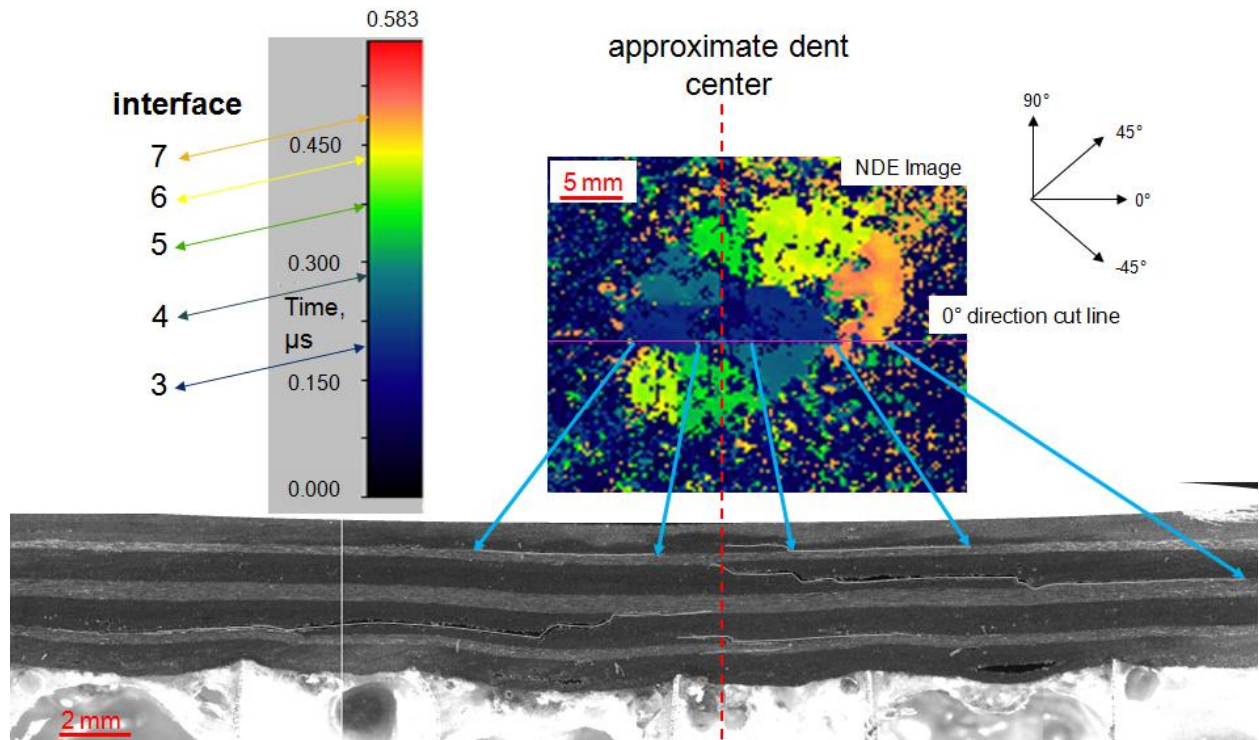


Figure 5.3. C-Scan image, destructively obtained cross-sectional view, and corresponding 2D damage map in the 0° cut direction for a 16 ply Q4-C1 sandwich specimen indented with the 25.4 mm diameter indenter.

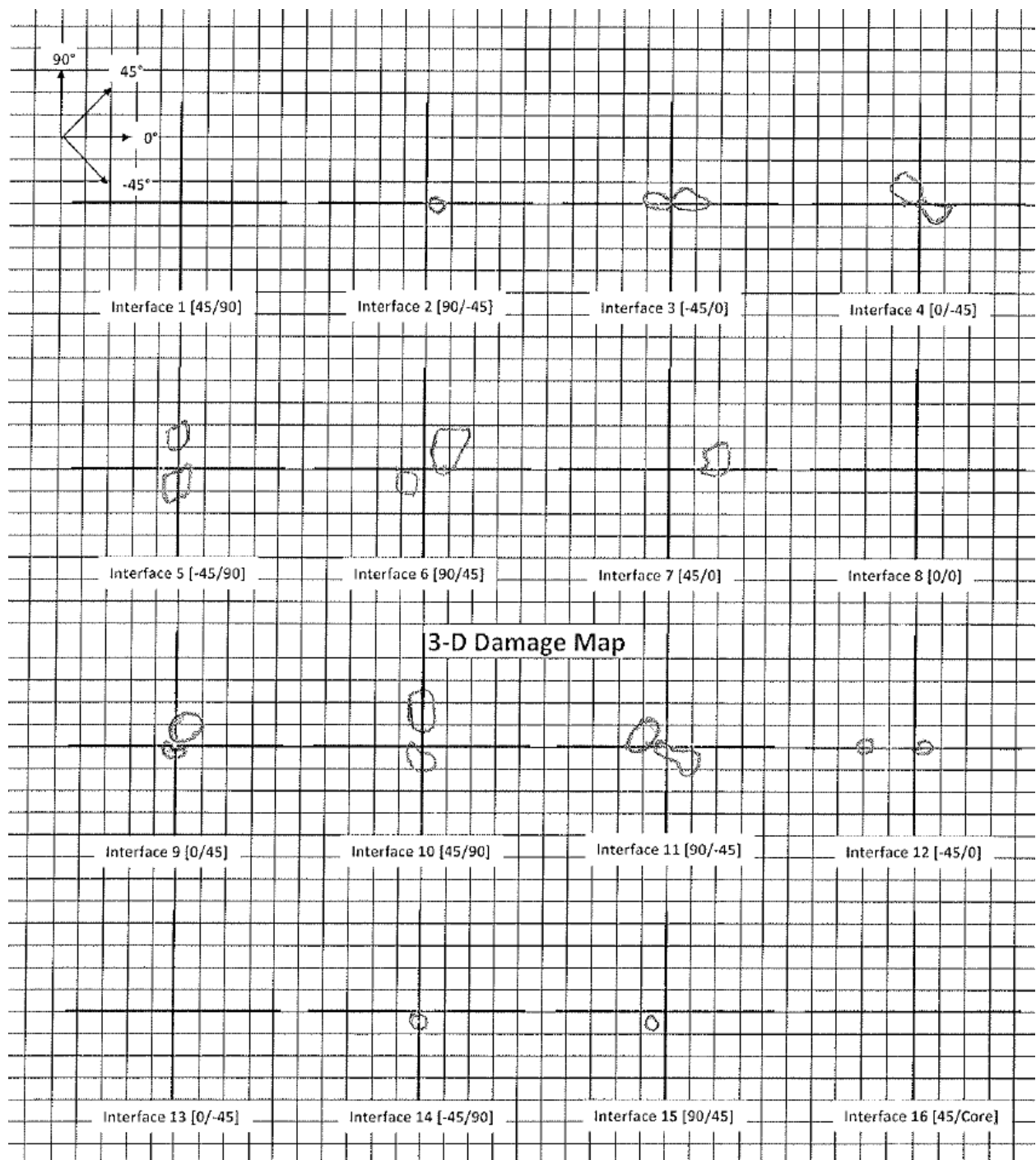


Figure 5.4. 3D damage map for the Q4-C1 specimen of Figure 5.3. Squares in the grids measure 6.35 mm x 6.35 mm.

The different destructive evaluations showed traits of delaminations in all interfaces except in interface 1 and the midplane. The DE image of Figure 5.3 and the 3D damage map in Figure 5.4 also show a small portion of delamination at interface 2 that was not captured non-destructively. As will be discussed in section 5.3, NDE images of the face sheet layups Q2 and Q3 captured distinct delaminations at interface 2 for the 16 ply specimens indented with 25.4 mm diameter indenter. However, no interface 2 delaminations were observed non-destructively for face sheet layups Q1, Q4 and Q5. No DE results are available for Q1 and Q5 layups and therefore it cannot be ascertained whether interface 2 delaminations existed in these as well. However, we do observe interface 2 delaminations in the DE image of the Q4 layup as presented in Figure 5.3 but this information was not captured non-destructively

5.2 8 Ply QSI Delamination Assessments

Quantitative planar areas of delaminations and other associated quantitative results are presented and discussed in Chapter 6 and only a qualitative evaluation is presented in this section. Figure 5.5 presents typical c-scans of the four different face sheet layups for the 8 ply specimens that were indented using the 25.4 mm diameter indenter at BVID load. The images presented are independent of core type, i.e., the sandwich configurations from which they were taken did not necessarily have the same core type but there is not any effect of core in the qualitative discussion that follows; this is addressed later in this section. A separate discussion on the effects of the core on the face sheet delamination together with the associated c-scan images is presented later in this section. The color scale in Figure 5.5 is in μs and represents the time of flight to each of the delaminating interfaces for the images labeled as “full image” in the figure, while the angle convention presented shows the ply angle directions. For each of the face sheet layups presented in Figure 5.5, interface by interface delamination details are also shown. This is

obtained by optimizing the image palette through changing the time of flight scales. As a result of this exercise, delaminations at different interfaces can be observed more clearly.

As discussed earlier in section 5.1, 8 ply specimens indented with 76.2 mm diameter indentors showed poor quality c-scan images with delamination boundaries not clearly defined. Therefore, these results are not presented here. Destructive evaluations of a few specimens indented with the 76.2 mm diameter indenter indicated that the delaminations always extended beyond the point where information was lost by the c-scan near the dent perimeter, i.e., the delaminations were always larger than that captured by the NDE. The limited information that was retrieved from the interior portions of the dent in the NDE images of these specimens indicated that the delaminations in these specimens were larger than those in the specimens indented with the 25.4 mm diameter indenter, and that the “delamination pattern,” i.e., the interfaces at which they occurred and their shapes and orientations, were essentially the same for both indenter sizes. Thus, in what follows in this chapter and the next, assessments on the effect of the delaminations for the 8 ply specimens will be restricted to those specimens indented with the 25.4 mm diameter indenter.

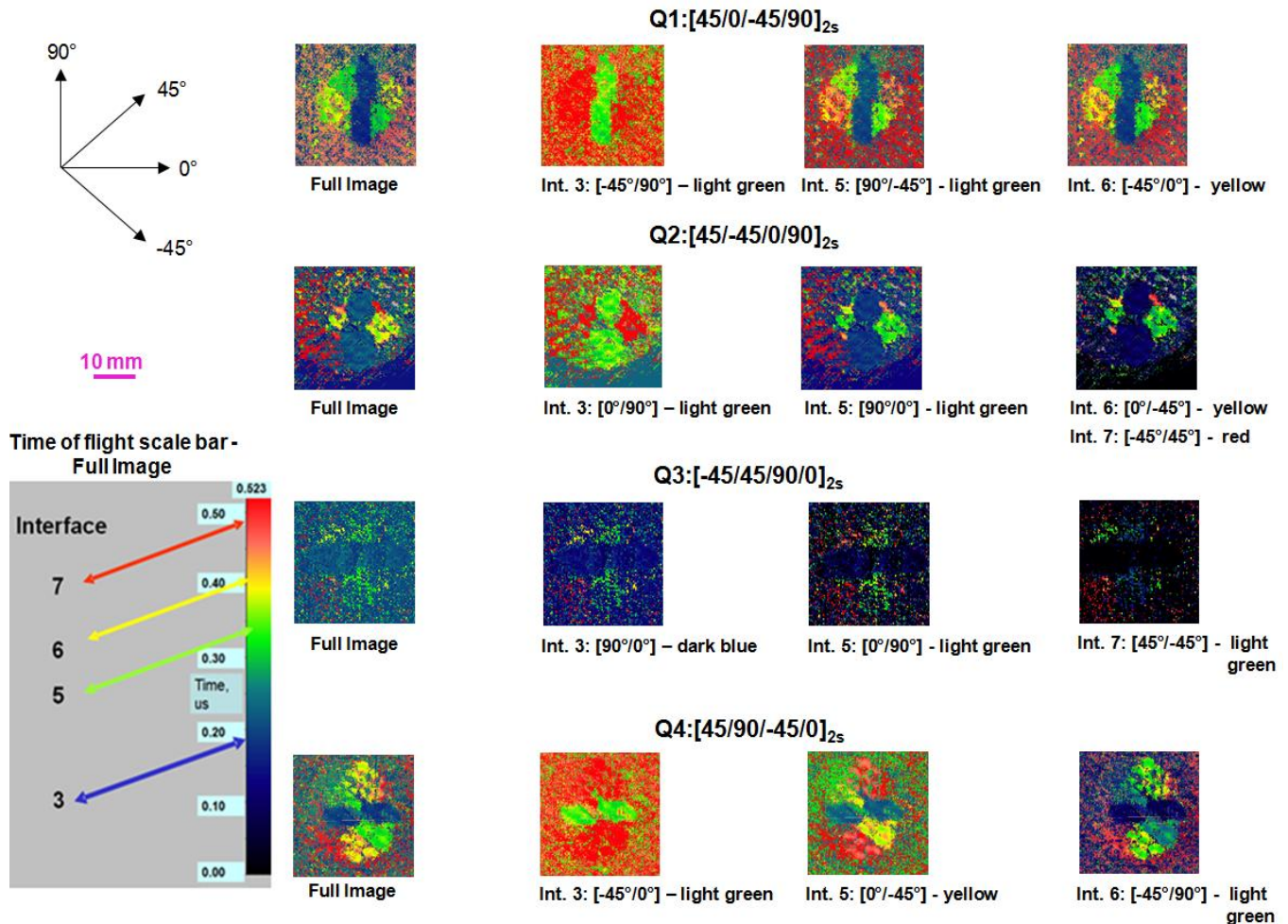


Figure 5.5. Representative c-scan images and the interface by interface details for the four different 8 ply face sheet layups indented with the 25.4 mm diameter indenter.

Delaminations were observed only at interfaces 3, 5, 6 and 7 for the 8 ply specimens. Delaminations at interface 7 were often difficult to distinguish from the back surface reflections that were obtained in the regions where no delaminations existed. Note that for the Q1 and Q4 layups, most of the delamination information that was obtained was for interfaces 3, 5 and 6, with limited and in some cases no information at interface 7 due to shielding effect. For the Q2 and Q3 layups, most of the delamination information that was obtained was for interfaces 3 and 5 with very limited information for interfaces 6 and 7. This was because in the Q2 layup, large

interface 5 delaminations in the 0° direction shielded the interface 6 and interface 7 delaminations. Likewise, in the Q3 layup, large interface 5 delaminations in the 90° direction shielded the interface 6 and 7 delaminations.

By combining results such as those shown in Figure 5.5 with the DE results, it was possible to make a variety of observations across and between face sheet layups and core types. For all panel geometries, if it is assumed that all delaminations are continuous through the shielded region, then all delaminations are either lemniscates or oblong, with the direction of the major axis of each delamination primarily controlled by the direction of its back surface ply. This is independent of core type and agrees with previous results studying low velocity impact damage in sandwich structures.^{12,21} The delaminations at interface 3 were always lemniscates. For the Q2 and Q3 layups, the major axis of interface 3 delaminations is aligned with their back surface ply angle, whereas for the Q1 and Q4 layups, the two portions of the lemniscates are slightly offset, giving the major axis a very slight tilt towards the positive 45° direction. Each layup has one other delamination at 0° or 90° , which occurs at either interface 5 or 6, depending on the layup. These delaminations are generally continuous through the shielded region and are either elliptical or lemniscates in shape. As in the case of interface 3, the interface 5 and 6 delaminations are aligned with the back surface ply angle for the Q2 and Q3 layups, but have a slight tilt towards the positive 45° direction for the Q1 and Q4 layups.

One major layup difference between the Q1 and Q2 layups was that in the Q1 layup, the face sheet ply angle change at the different interfaces was mostly 45° while for the Q2 layup, it was mostly 90° . It was observed that for the same load level, the overall size of the planar delamination was larger for the Q2 face sheet layup as compared to the Q1 face sheet layup.

Figure 5.6 presents the c-scan images of Q1-C1 and Q2-C1 sandwich configurations indented

with the 25.4 mm diameter indenter at the BVID load. These images presented are to the same scale in order to make the qualitative comparisons easier. Exact planar area of delamination for these sandwich configurations is tabulated in chapter 6. This Q1 face sheet layups having smaller planar area of delamination as compared to the Q2 face sheet layup is consistent with literature where it is shown that large ply angle changes result in larger planar area of delamination due to greater bending stiffness mismatch between the plies at an interface.¹²

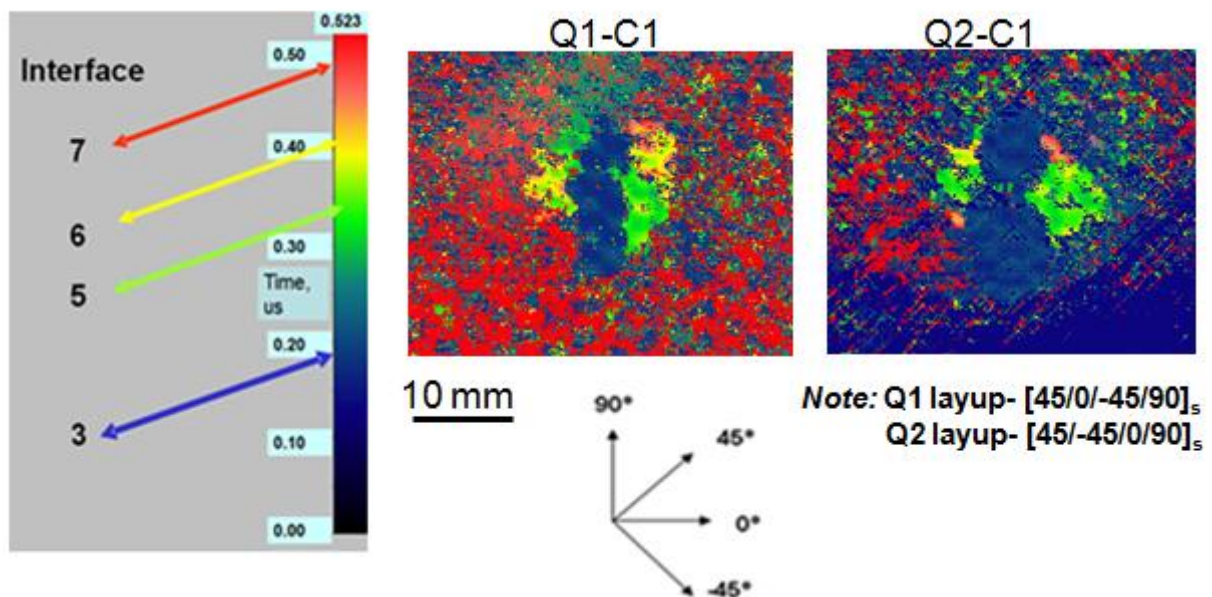


Figure 5.6. Representative c-scan images of the Q1-C1 and Q2-C1 sandwich configurations for the 8 ply specimens indented with the 25.4mm diameter indenter at BVID load.

The core density and thickness clearly had an influence on the overall delamination size. Figure 5.7 presents the c-scan images from the Q1-C1, Q1-C2 and Q1-C3 sandwich configurations indented with the 25.4 mm diameter indenter at the BVID load. These images are presented to the same scale in order to be able to make qualitative comparisons easier. As clearly obvious from the figure, the overall planar delamination size was larger in panels with the C2

and C3 cores than in those with the C1 core. Exact planar area of delamination data is presented in chapter 6. The C3 core having a larger planar area of delamination than the C1 core is due to the larger density of the C3 core which causes it to behave more stiffly, resulting in more energy being absorbed through the inelastic processes in the face sheet. Likewise, because of its smaller thickness, the C2 core has larger “effective stiffness” compared to the C1 core which again results in more face sheet delaminations in the Q1-C2 sandwich configuration. Therefore it can be concluded that as the effective core stiffness increases, more energy goes into delamination growth as compared to being absorbed via core crushing, resulting in larger planar areas of delamination in the face sheet. Another remarkable observation in Figure 5.7 is that the Q1-C2 sandwich configuration has a relatively large 0° delamination at interface 6 when compared to Q1-C1 or Q1-C3 sandwich configurations. This shows that the thinner core has a greater propensity for near core 0° delaminations as compared to the thicker core.

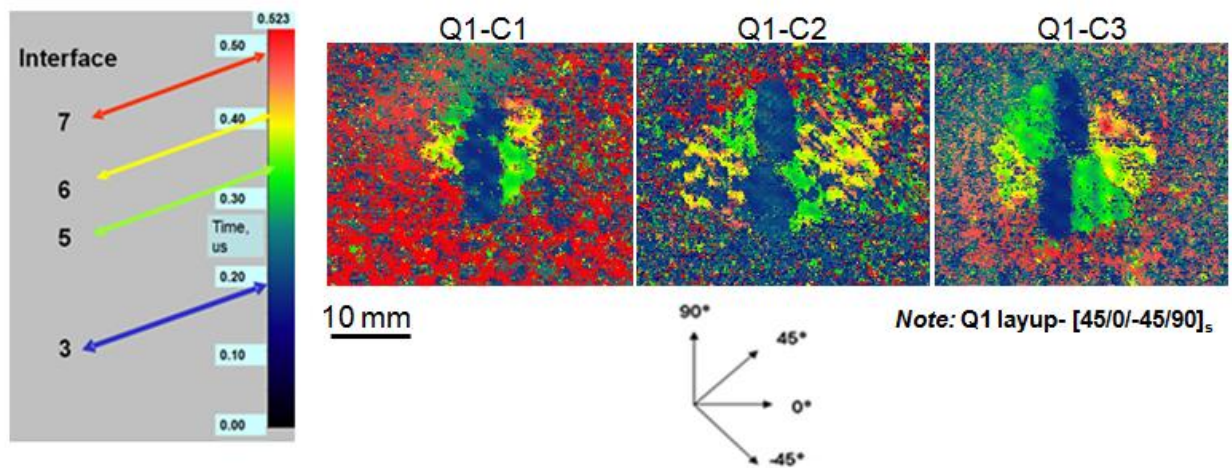


Figure 5.7. Representative c-scan images of the Q1-C1, Q1-C2 and Q1-C3 sandwich configurations for the 8 ply specimens indented with the 25.4mm diameter indenter at BVID load.

The Q1 and Q4 layups are essentially identical if core orthotropy is ignored, i.e., one layup is essentially obtained from the other by a 90° rotation, with a swap of the $\pm 45^\circ$ plies. Figure 5.8 presents the c-scan images of Q1-C2 and Q4-C2 sandwich configurations indented with the 25.4 mm diameter indenter at BVID load. The images are presented to the same scale in order to make qualitative comparisons easier. The boundary conditions were also the same in the 0° and 90° directions, and preliminary experiments indicated that the specimens were sufficiently large that the specimen dimensions did not affect the damage. Since the core is orthotropic, any differences in the delamination patterns between the Q1 and Q4 layups may be attributable to the core orthotropy. Examining this issue, it was found that the Q1 and Q4 layups have very similar delamination patterns. That is, both the layups have tilted, lemniscate shaped delaminations at interface 3 and a somewhat longer and wider trapezoidal shaped delaminations at interface 5. The Q1 layup however has a relatively larger 0° delamination at interface 6 compared to the 90° delamination at interface 6 for the Q4 layup. This shows that for the near core interfaces, the face sheet layup along the core ribbon direction has a greater propensity for delamination. The same cannot be said for the near surface interfaces since the 0° delamination in interface 3 for the Q4 layup, as according to Figure 5.8, appears slightly smaller in size to the 90° delamination at interface 3 of the Q1 layup.

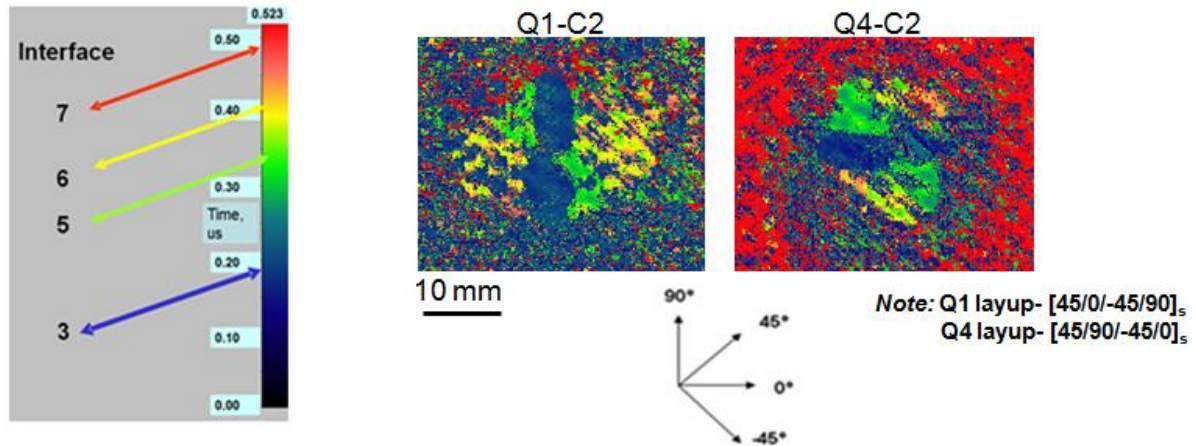


Figure 5.8. Representative c-scan images of the Q1-C1 and Q1-C2 sandwich configurations for the 8 ply specimens indented with the 25.4mm diameter indenter at BVID load.

A similar evaluation to that described for Q1 and Q4 layups was also conducted for the Q2 and Q3 layups, as one layup is obtained by a 90° rotation of the other. Here, there was less information available for comparison since only one specimen from the Q3-C1 sandwich configuration was available with an NDE image of relatively poor quality. Figure 5.9 presents the c-scan images of the Q2-C1 and Q3-C1 face sheet layups. These images are also presented to the same scale in order to make qualitative comparisons easier. Specifically, the Q3 layup had the longest and widest delamination at interface 3 out of all layups considered. This is clearly obvious in Figure 5.5, where all the specimens presented are tested at BVID load and the images are presented at the same scale. In the Q3 layup, there are two consecutive 0° plies at the delamination's back surface which coincide with the ribbon direction of the core. The poor scan quality of the Q3-C1 specimen presents a low resolution interface 5 delamination, as seen by the light green in the Q3-C1 image presented in Figure 5.9. However, it appears that the interface 5 delamination in the Q3 layup is overall smaller in size than the interface 3 delaminations. The Q2 layup showed relatively smaller delamination at interface 3 than the Q3 layup. The interface 5

delamination in the Q2 layup was significantly large, and again coincided with a 0° ply at the delamination's back surface that coincided with the ribbon direction of the core. In general, then, core orthotropy may affect the pattern of delamination growth, but there is an interplay between core orthotropy and face sheet layup. Specifically, it appears that grouping the $\pm 45^\circ$ plies together at the outside surface of the face sheet causes core orthotropy to play a role, whereas separating these plies mitigates its effect. For the Q2 and Q3 layups, the effect of core type on the above conclusions cannot be determined since Q2 and Q3 were only bonded to C1 core.

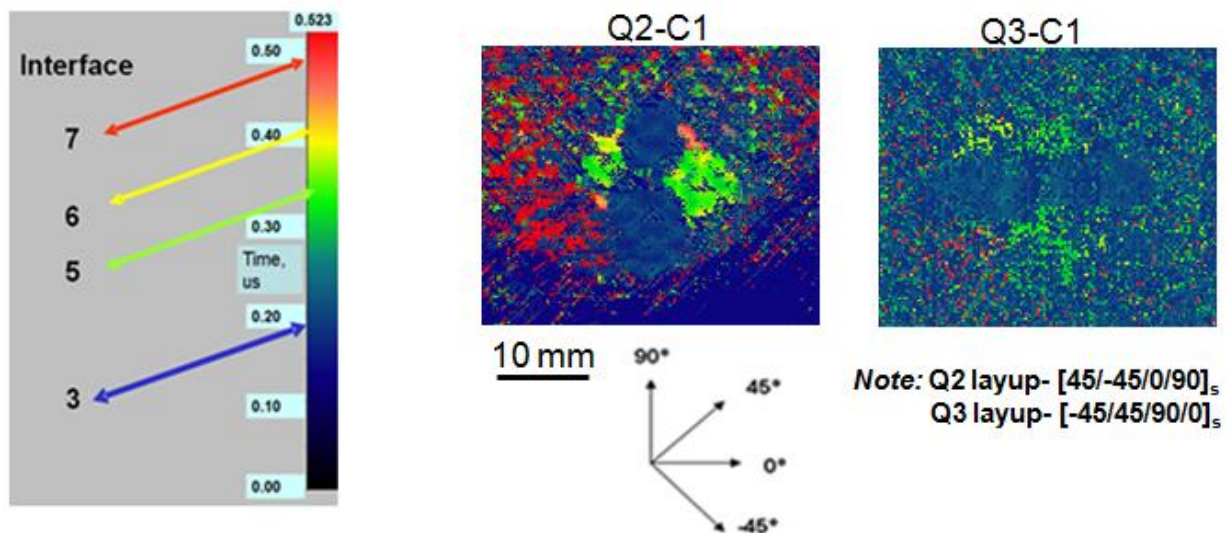


Figure 5.9. Representative c-scan images of the Q2-C1 and Q3-C1 sandwich configurations for the 8 ply specimens indented with the 25.4mm diameter indenter at BVID load.

5.3 16 Ply QSI Delamination Assessments

Delamination boundaries were very clearly defined in the NDE results for both the 25.4 mm and 76.2 mm QSI tests for specimens with 16 ply face sheet. This enabled quantitative planar areas of delamination data to be determined for specimens tested with both the indenter sizes. Quantitative planar areas of delaminations are presented and discussed in Chapter 6 and

only a qualitative evaluation is presented in this section. Delaminations up to interface 11 were generally present in the results captured by the c-scan. As described previously, destructive evaluations of select specimens revealed that unshielded delaminations may have existed at interface 12 that were not captured by the NDE technique. Destructive evaluations also reveal delaminations beyond interface 12 and in some cases all the way up to interface 15. The full-sized specimens depended only on the NDE results for delamination information because of the need to use these specimens for the CAI tests. In this regard, the importance of any delamination information that was missed in the NDE cannot be undermined as delaminations are one of the major damage modes that drive failure in the post-impact study.

In all the sandwich configurations for both indenter sizes and just as it was with the 8 ply specimens, delaminations at any interface had their major axis aligned with the direction of the back ply angle, i.e, with the deeper ply at that interface when looking from the specimen's surface. As in the case of 8 ply specimens, delamination shapes were mostly lemniscates with the overall delamination sizes clearly influenced by face sheet layup, core type as well as indenter size. Figure 5.10 shows representative c-scan images of planar delaminations for the different face sheet layups indented with the 25.4 mm diameter indenter at BVID load. The time of flight scale bar as well as the ply angle orientation convention is also shown in the Figure. The images presented are independent of core type i.e. the sandwich configurations from which they were taken did not necessarily have the same core type. A separate discussion on the effects of the core on the face sheet delamination as well as the associated c-scan images is presented later in this section. The color scale in the c-scan images of the different specimens was varied in order to see individual interface delaminations more clearly. These interface by interface delamination details for each of the face sheet layups are presented in Figure 5.11. Because of the varying

degree to which the color scale had to be manipulated in order to get information on each of the delaminating interfaces, the time of flight scale bar is not shown in Figure 5.11.

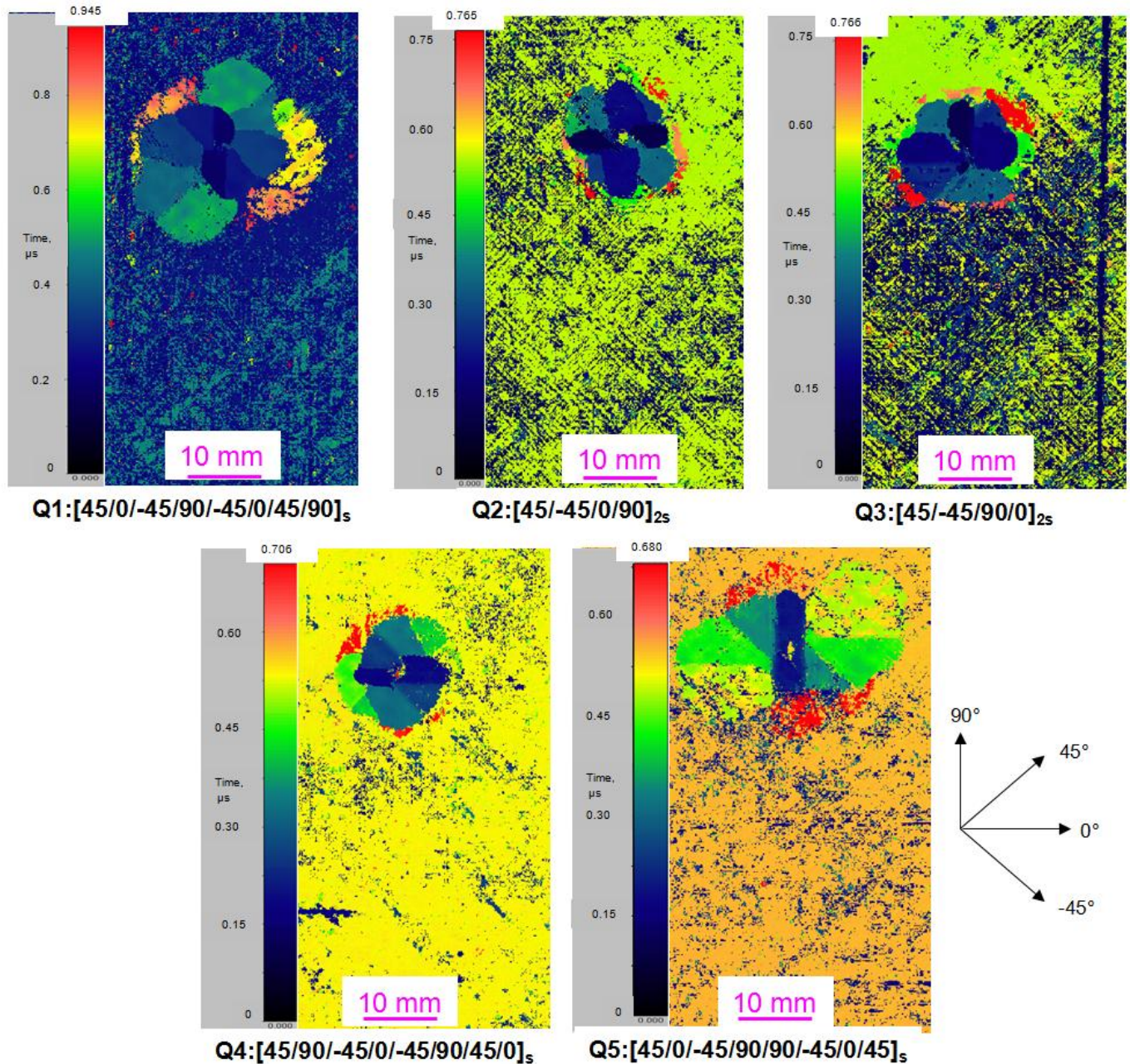


Figure 5.10. Representative c-scan images for the five different 16 ply face sheet layups indented with the 25.4 mm diameter indenter.

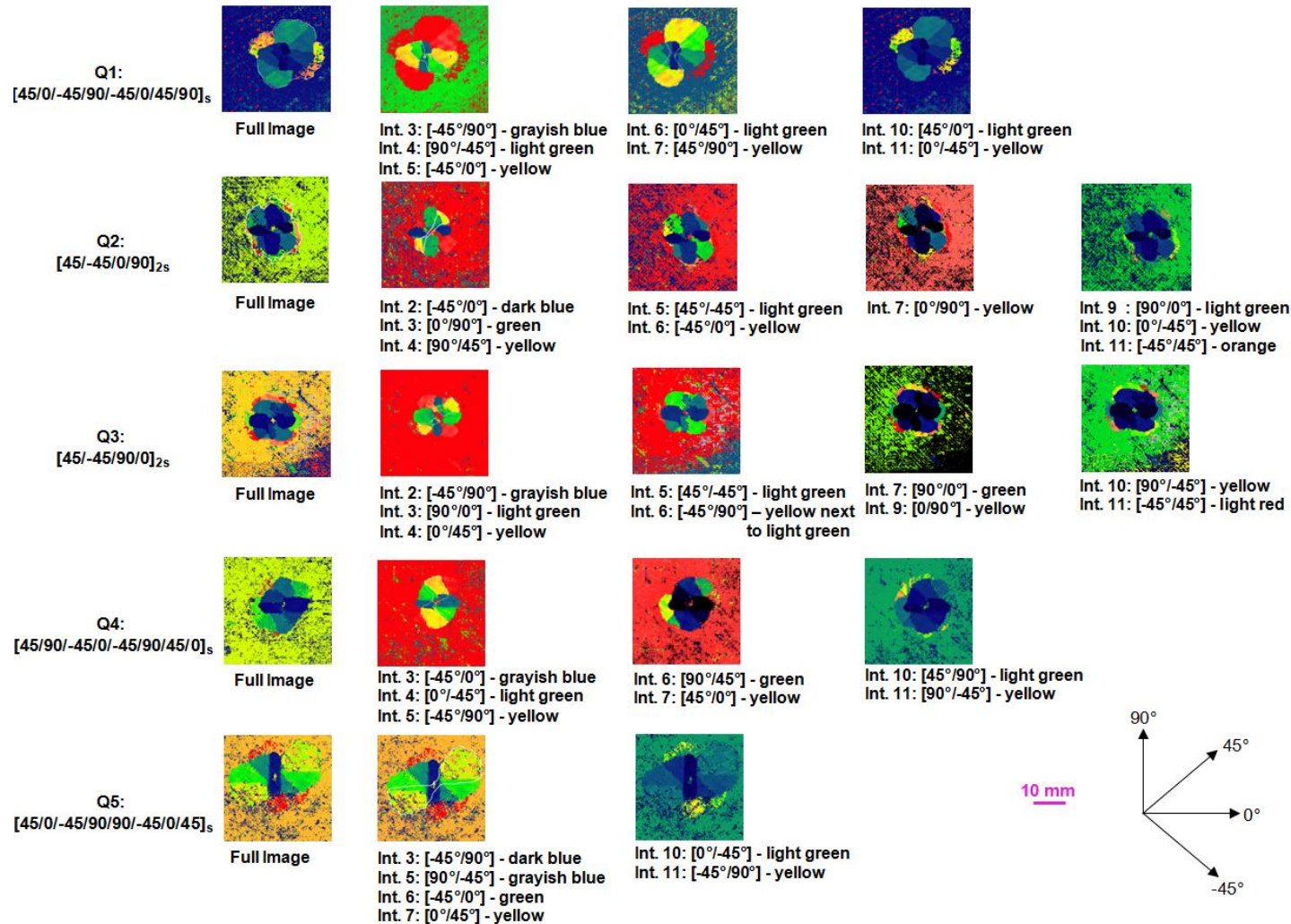


Figure 5.11. Interface by interface layups for the representative c-scan images for the 16 ply face sheet layups presented in Figure 5.10.

The first delaminations captured in the Q1 layup for the specimens indented with the 25.4 mm diameter indenter are delaminations oriented at 90°, referred to subsequently as “90° delaminations at interface 3”. A similar referencing convention is used to refer to other delaminations oriented at different angles for the different delaminating interfaces. For the Q1 layup delaminations were seen at every other interface from interfaces 3-11 apart from the

midplane, interface 8. As clearly obvious from Figure 5.11, the delaminations for the Q1 layup increase in overall size from interface 3 to interface 7 with the largest delaminations being the 90° delamination at interface 7. No delaminations are seen at interface 9 in the Q1 layup. It is possible that the interface 9 delaminations for the Q1 layup remain hidden due to shielding, especially by the 45° delaminations at interface 6. Interface 10 and 11 delaminations appear slightly smaller both lengthwise and widthwise than interface 7 delaminations for the Q1 layup. Delaminations are only captured up to interface 11 and nothing is seen beyond that in the c-scan images.

For the Q2 layup, the first delaminations are seen at interface 2 in the 0° direction. These were mostly noticed as two separate lobes with a small discontinuity between them. Delaminations were observed at every interface from interfaces 2-11 in the Q2 layup except at the midplane which is interface 8. Even though most of it remains shielded, the longest delamination in the Q2 layup seems to be in the 90° direction at interface 7. This is similar to what was seen in the Q1 layup where the largest delamination was seen at interface 7. One remarkable comparison between the Q1 and Q2 face sheet layups is that of planar area of delamination. For the same core types and indented at the same load level, the Q2 face sheet apparently has smaller planar area of delamination than the Q1 layup. A comparison of Q1-C1 and Q2-C1 sandwich configuration c-scan images for specimens indented with the 25.4 mm diameter indenter at BVID load is shown in Figure 5.12. These images are presented to the same scale so that qualitative comparisons between the images can be made. Exact planar area of delamination data for these sandwich configurations are presented in Chapter 6. The Q2 face sheet layup has larger ply angle difference at most of the interfaces as compared to the Q1 face sheet layup. This difference in layup is similar to what was in the 8 ply case. However, contrary

to the 8 ply case, in the 16 ply case the Q1 layup has larger planar area of delamination than the Q2 layup. It must however be noted from Figure 5.11 that the Q2 layup in the 16 ply case has more interfaces that delaminate as compared to the Q1 layup. So possibly, though difficult to exactly quantify, the “total” area of delamination which takes into consideration the delamination areas for the individual interfaces is still larger in the Q2 layup as compared to the Q1 layup because of more interfaces that delaminate.

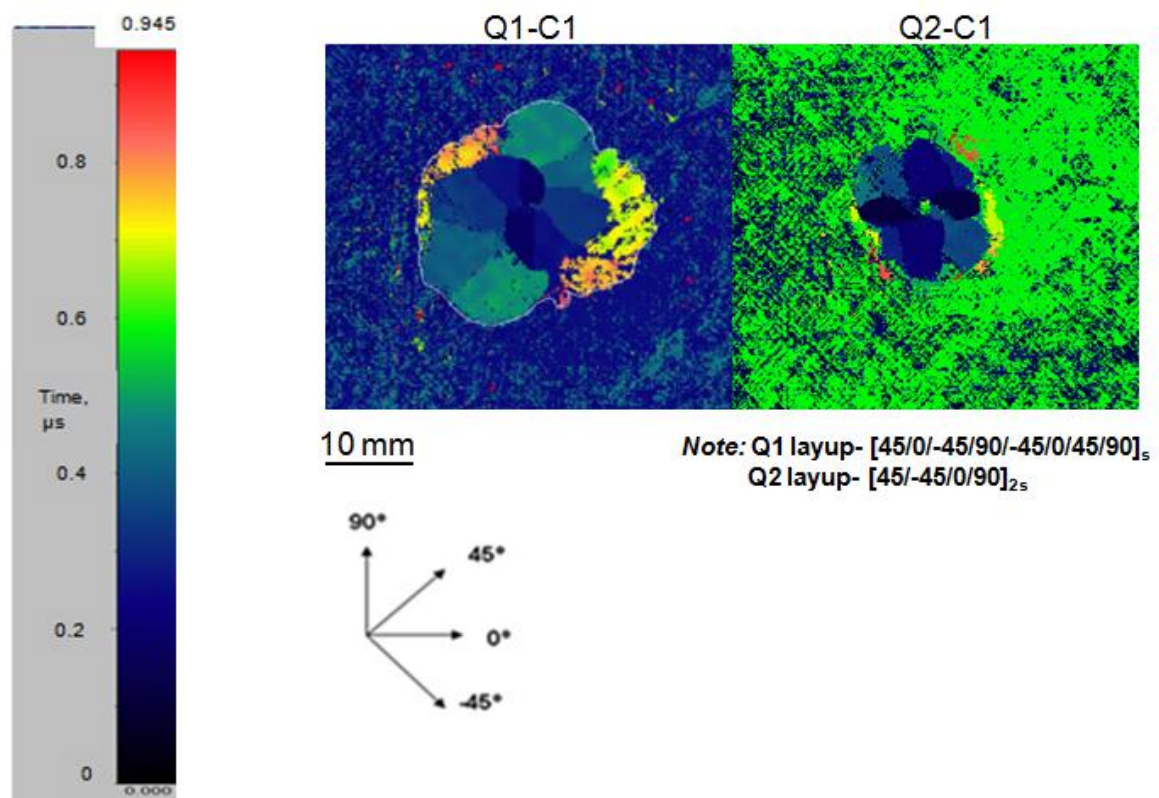


Figure 5.12. Representative c-scan images of the Q1-C1 and Q2-C1 sandwich configurations for the 16 ply specimens indented with the 25.4mm diameter indenter at BVID load.

Just like in the Q2 layup, the Q3 layup also shows first delaminations at interface 2 but in the 90° direction. For the Q3 layup, delaminations are captured non-destructively at every

interface between interfaces 2-11 apart from the midplane interface 8. More delaminating interfaces in the Q3 layup as compared to the Q1 layup again probably hints at larger “total” area of delamination than the Q1 layup and is consistent with smaller ply angle changes in the Q3 layup as compared to the Q1 layup. Even though most of it remains shielded, the portion of interface 7 0° delamination captured by the c-scan appears to indicate the presence of a large interface 7 delamination. Because of heavy shielding in the Q3 layup, it is difficult to tell exactly which interface appears to have the largest delamination area. In every likelihood, according to Figure 5.10, it appears to be either the 0° delamination at interface 7 or the 90° delamination at interface 9.

In the Q4 layup, no delaminations are seen at interface 2 just as was also the case in the Q1 layup. The first delaminations in the Q4 layup are seen at interface 3 in the 0° direction. Except for the midplane interface 8, delaminations are observed at every interface in the Q4 layup from interfaces 3 to 11. Large 90° delaminations at interface 5 and 45° delaminations at interface 6 are also seen in the Q4 layup. Portions of mostly shielded 90° delaminations at interface 10 and -45° delaminations at interface 11 are also seen. Even though most of it remains shielded, these interface 10 and 11 delaminations appear to be the largest delaminations in the Q4 layup. The Q5 layup also shows the first delaminations at interface 3 just like the Q1 and Q4 layups. These delaminations are seen in the 90° direction. For the Q5 layup, delaminations are also captured by the c-scan at every interface from interfaces 3 to 11 except the midplane interface 8. Large 45° delaminations are seen at interface 7, -45° delaminations at interface 10 and 90° delaminations at interface 11. Out of these, the interface 7 delamination appears to be the largest.

Comparing delaminations for the Q1 layup based on the different core types, it is observed that the planar area of delamination is generally largest for Q1-C1, followed by Q1-C2 and then Q1-C3. Figure 5.13 shows the c-scan images from these sandwich configurations indented with the 25.4 mm diameter indenter at BVID load. The images presented are to the same scale. Quantitative planar area of delamination results are presented in chapter 6. Unlike the 8 ply case, planar size of delamination for the 16 ply case does not seem to be influenced by increasing core stiffness either by the way of higher core density or smaller core thickness. On the contrary, planar size of delamination appears to be larger for a softer core.

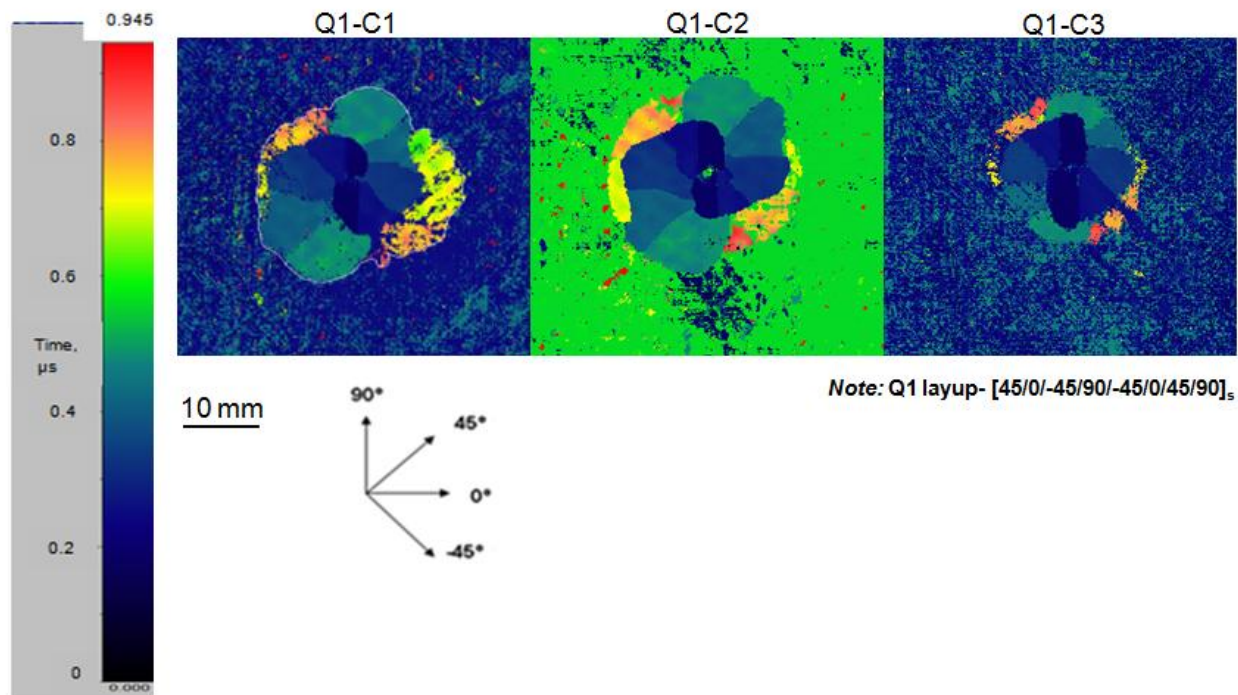


Figure 5.13. Representative c-scan images of the Q1-C1, Q1-C2 and Q1-C3 sandwich configurations for the 16 ply specimens indented with the 25.4mm diameter indenter at BVID load.

Figure 5.14 presents representative c-scan images of planar delamination for all the 16 ply face sheet layups indented with the 76.2 mm diameter indenter at the BVID load. The images are presented for two different c-scan gate settings. A “gate” is a provision in the c-scan software that allows data within a certain time of flight range to be captured. A standard gate setting from the c-scan scope is presented in Figure 5.15 for the 16 ply delamination assessments. In this figure, the gates are the regions in between two of the solid black circles. The waveform seen in this figure is for a damaged region of the specimen. As can be seen, gate 1 covers transducer signals from approximately 0.05 μ s to 0.13 μ s, attempting to capture delaminations at the first interface. Gate 2 extends from 0.13 μ s to 0.6 μ s attempting to capture delaminations from interfaces 2 to 8. Gate 3 extends from 0.6 μ s to 1.2 μ s attempting to capture delaminations from interfaces 9 to 15. Gate 4 extends from 1.2 μ s to 1.6 μ s and is an additional gate set in case there is a variation in average time of flight between interfaces and the signals shift slightly to the right. Gates 2 and 3 combined images therefore are expected to ideally present delaminations from interfaces 2 to the last interface. The gates 2 and 3 combined images however sometimes did not show very clear delamination boundaries especially for delaminations in interfaces 10 and 11 and thus, Gate 3 only images were used to obtain further details on the full extent of these delaminations. In Figure 5.14, time of flight scales for combined gates 2 and 3 as well as gate 3 only are presented together with the ply angle convention. The image palettes are optimized to show distinguish delaminations at the different interfaces and the time of flight scales correspond to these optimized palettes. Just as for the 16 ply specimens indented with the 25.4 mm diameter indenter, representative interface by interface delamination details for each of the 16 ply face sheet layups indented with the 76.2 mm diameter indenter at BVID load is shown in Figure 5.16. The images presented are independent of core type i.e. the sandwich configurations from which

they were taken did not necessarily have the same core type. A separate discussion on the effects of the core on the face sheet delamination as well as the associated c-scan images is presented later in this section. Because of the varying degrees to which the color scale has to be manipulated in order to get information on each of these delaminating interfaces, time of flight scale bars are not shown in Figure 5.16.

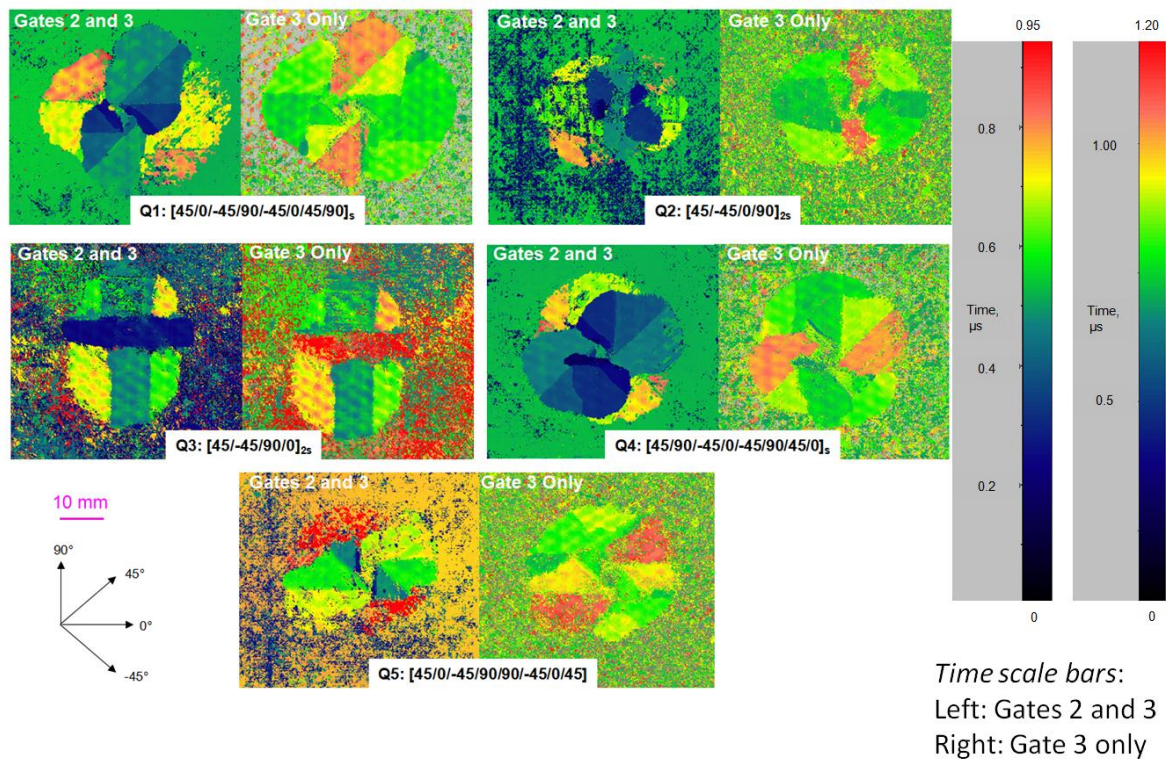


Figure 5.14. Representative c-scan images for the five different 16 ply face sheet layups indented with the 76.2 mm diameter indenter.

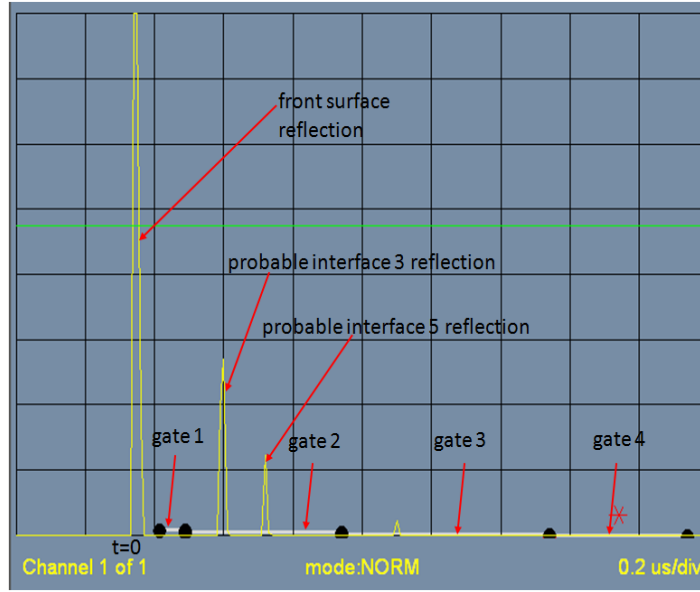
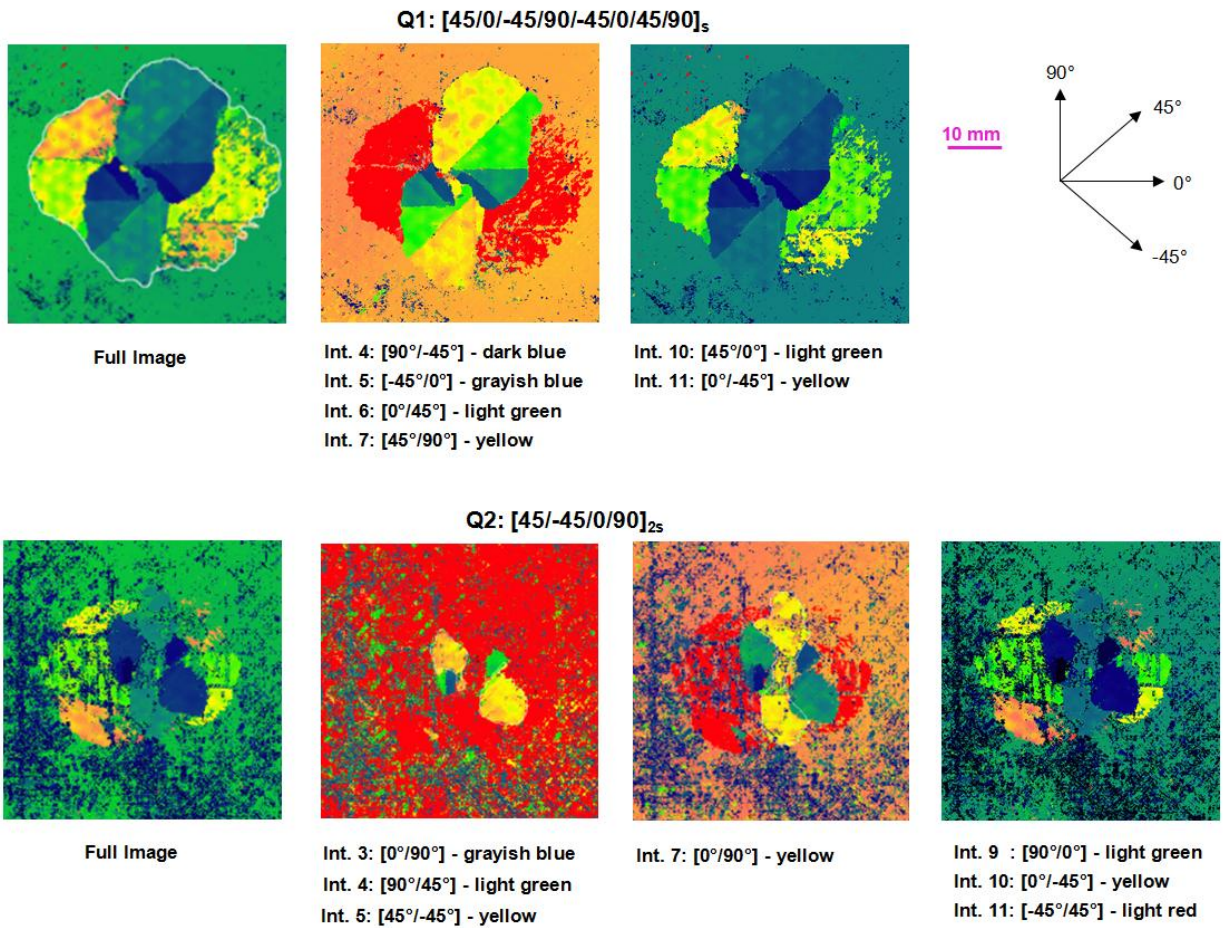


Figure 5.15. Representative c-scan gate settings for the 16 ply delamination assessments.



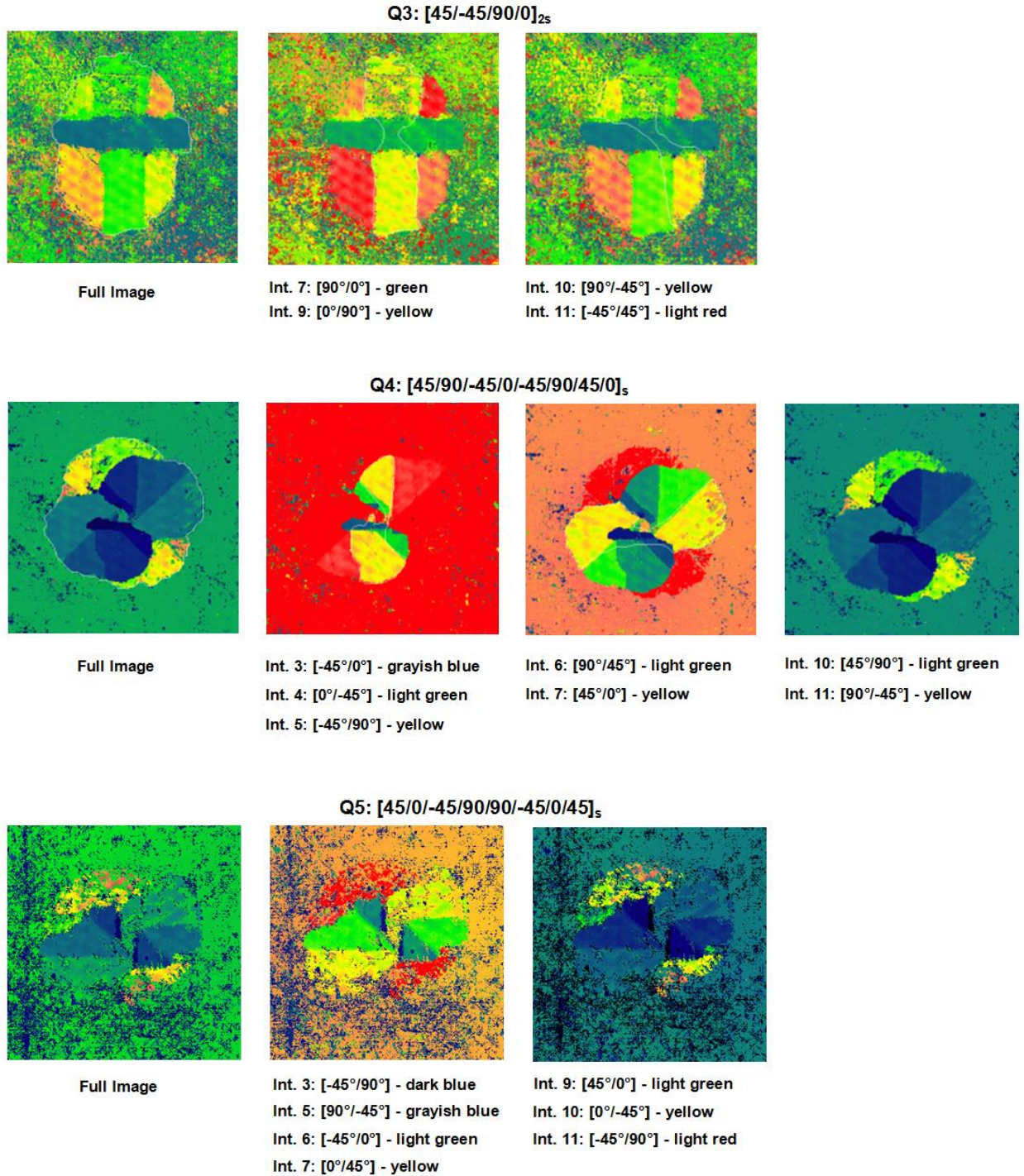


Figure 5.16. Interface by interface layups for the representative c-scan images for the 16 ply face sheet layups presented in Figure 5.14.

For the Q1 layup, the first delaminations seen are the relatively small -45° delaminations at interface 4. Compared to the 16 ply Q1 results for the 25.4 mm diameter indenter, these interface 4 delaminations are much smaller. Delaminations are observed at every interface from interfaces 4-11 apart from the mid-plane interface 8. Large delaminations for the Q1 layup only begin to be seen from interface 5 onwards, where interface 5 has delaminations in the 0° direction. The delaminations continue to increase in size up to interface 11. Huge 90° delaminations at interface 7 and large 0° delaminations at interface 10 are also observed for the Q1 layup, similar to what was seen in the 25.4 mm diameter results. By visual comparison of the interface by interface delamination details presented in Figure 5.16, the interface 10 delaminations in the 0° direction appear to be the largest for the Q1 layup.

The Q2 layup for the specimens indented with the 76.2 mm diameter indenter shows delaminations at every interface from interfaces 3-11 except at the midplane interface 8. In the Q2 layup, relatively smaller delaminations are seen at interface 3 compared to what was observed for the Q2 layup indented with the 25.4 mm diameter indenter. Just like in the Q1 layup, large delaminations only begin to be seen from interface 5 onwards in the Q2 layup. The largest delamination is difficult to identify in the Q2 layup and by visual comparison of the interface by interface details presented in Figure 5.16, it could be the delamination at any of the interfaces 9-11. The Q3 layup shows no delamination at interfaces 1-6 and the first delamination is seen at interface 7 which is a huge oblongish delamination that is unique to this layup. Large delaminations are also observed at interfaces 9, 10 and 11 in the Q3 layup. By visual comparison of the interface by interface details presented for the Q3 layup in Figure 5.16, the largest delamination could either be the delamination at interface 10 or at interface 11. It is difficult to say for certain as to which one since most of these remain shielded.

Apart from the midplane interface 8 and interface 9, delaminations in the Q4 layup are seen at all other interfaces from 3-11. There possibly could be some 0° delaminations at interface 9 which remain fully shielded. Either of the interface 7, 10 and 11 delaminations could be the largest in the Q4 layup. In the Q5 layup, delaminations are noticed at all interfaces from 3-11 except at the midplane interface 8. In the Q5 layup, the largest delamination by visual comparison of the interface by interface delamination details presented in Figure 5.16 appears to be the 45° delamination at interface 7.

Comparing planar delamination sizes for the Q1 layup based on the different core types for the 76.2 mm diameter indenter tests, it is observed that the planar delamination size is the largest for Q1-C1, followed by Q1-C2 and then Q1-C3. Figure 5.17 shows the c-scan images from these sandwich configurations presented to the same scale. Quantitative planar area of delamination results are presented in chapter 6. Unlike the 8 ply case, planar area of delamination for the 16 ply case does not seem to be influenced by increasing core stiffness either by the way of higher core density or smaller core thickness. The same conclusion was made for the specimens indented with the 25.4 mm diameter indenter. Also, just as it was for the 16 ply specimens indented with the 25.4 mm diameter indenter, the planar area of delamination appears to be the largest for a softer core. One other interesting observation for the 16 ply specimens indented with 76.2 mm diameter indenter is that in the Q1-C3 sandwich configuration, the planar delamination boundary is somewhat circular whereas in Q1-C1 and Q1-C2 sandwich configuration, the planar delamination boundary is elliptical with the major axis in the 0° direction.

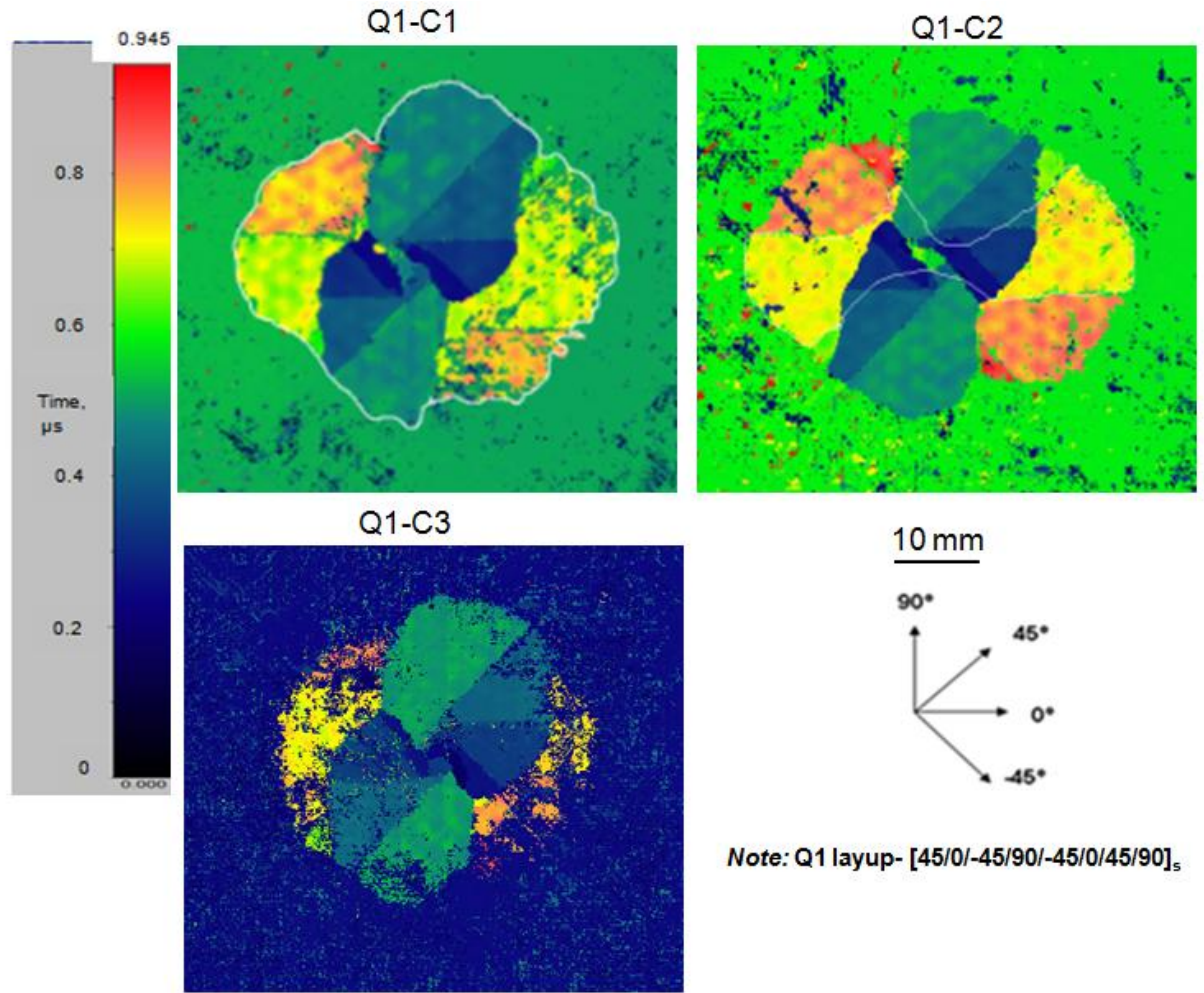


Figure 5.17. Representative c-scan images of the Q1-C1, Q1-C2 and Q1-C3 sandwich configurations for the 8 ply specimens indented with the 76.2 mm diameter indenter at BVID load.

As was also the case with the 16 ply specimens indented with the 25.4 mm diameter indenter, for specimens indented with the 76.2 mm diameter indenter at BVID load, the Q1-C1 sandwich configuration had apparently larger planar delamination size than the Q1-C2 sandwich configuration. A comparison of Q1-C1 and Q2-C1 sandwich configurations for the 76.2 mm diameter indenter case is shown in Figure 5.18. These images are presented to the same scale so that qualitative comparisons between the images could be made. Exact planar area of

delamination data is presented in chapter 6. The Q2 face sheet layup has larger ply angle change at most of the interfaces as compared to the Q1 face sheet layup. This difference between the Q1 and Q2 layups is similar to what was in the 8 ply case. However, contrary to the 8 ply case, the Q1 layup in the 16 ply case has larger planar delamination size than the Q2 layup. However, the Q2 layup in the 16 ply case has more interfaces that delaminate as compared to the Q1 layup. This is obvious from the interface by interface delamination details presented in Figure 5.16. So probably, though difficult to quantify exactly, the “total” area of delamination is still larger in the Q2 layup as compared to the Q1 layup. A similar conclusion was made for the 16 ply specimens indented with the 25.4 mm diameter indenter.

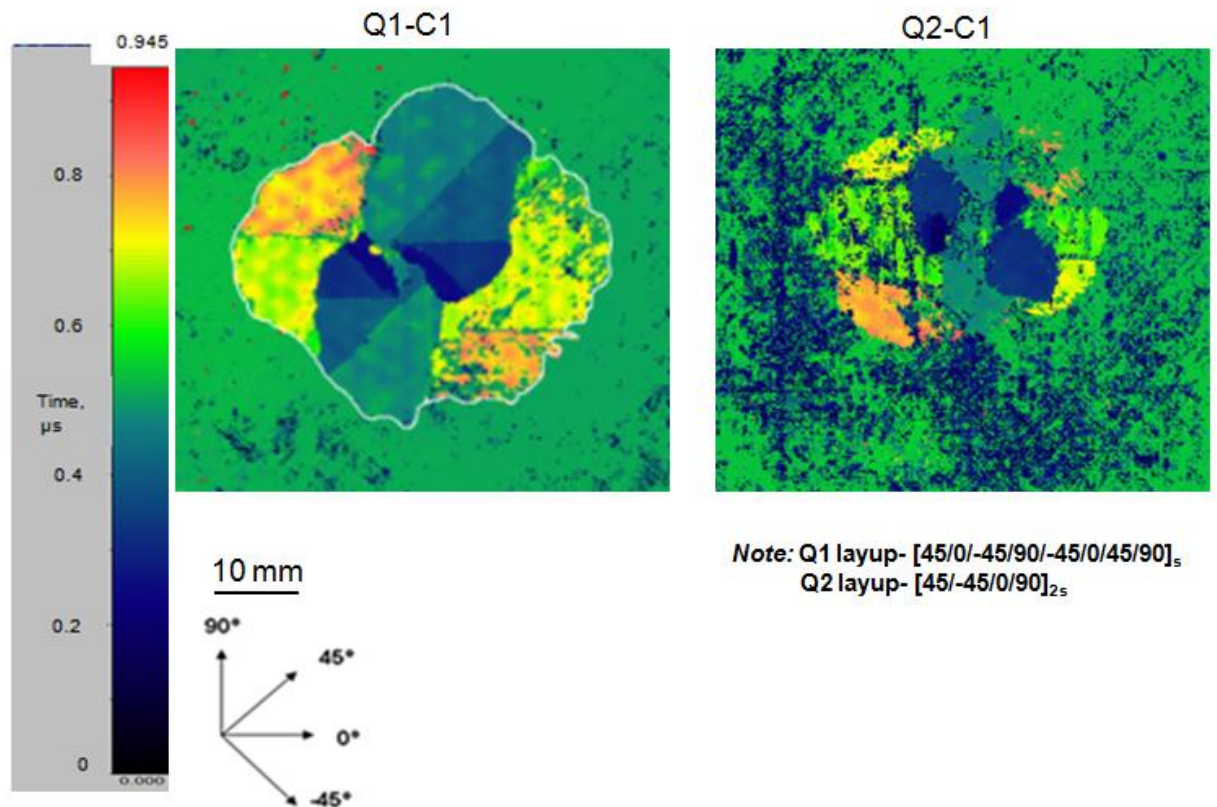


Figure 5.18. Representative c-scan images of the Q1-C1 and Q2-C1 sandwich configurations for the 16 ply specimens indented with the 76.2 mm diameter indenter at BVID load.

5.4 Summary

Delaminations were primarily assessed non-destructively using the ultrasonic c-scan with a few destructive evaluations performed both to validate the NDE technique as well as to reveal further information about the deep interface delaminations that possibly remained shielded in the c-scan images. For the 8 ply case, full planar extent of delamination could only be obtained for specimens indented with the 25.4 mm diameter indenter as these showed clearly defined delamination boundaries. For the 8 ply specimens indented with the 76.2 mm diameter indenter, the dent slope was such that delamination information further away from the dent center was lost. However, for the 16 ply specimens, full planar extent of delamination could be obtained for specimens indented with both the 25.4 mm and 76.2 mm diameter indentors.

Delaminations were mostly lemniscates or oblongish for both the 8 and 16 ply cases and the major axis of the delaminations was always oriented towards the bottom ply orientation for a delaminating interface. Delaminations for the 8 ply case were mostly seen in interfaces 3, 5, 6 and 7 in both the DE and NDE images. For the 16 ply case, the NDE images overall captured delaminations from interfaces 2-11 (except at the midplane interface 8) with variations in the delamination distribution depending upon the face sheet layup and indenter size. No midplane delaminations were ever observed, either destructively or non-destructively, for any of the evaluated 8 and 16 ply specimens. The delaminations at individual interfaces for both the face sheet thicknesses appeared to increase in size as we moved down through the interfaces from the indenter end and again start decreasing in size again as we approach the core. For the 8 ply case, mostly smaller ply angle changes in a face sheet layup showed smaller overall planar delamination size while larger ply angle changes showed larger planar delamination size. This was not so in the 16 ply case but rather it was the opposite i.e the face sheet layup with smaller

ply angle changes showed larger overall planar delamination size. However, it was noted in the 16 ply case that the face sheet layup with mostly smaller ply angle changes had more delaminating interfaces than the face sheet layup with larger ply angle changes. Though difficult to exactly quantify, it is possible that the “total” delamination area incorporating delamination areas of the individual interfaces is still larger in the face sheet layup with smaller ply angle changes.

The effect of core stiffness on the delamination sizes was clearly obvious in the 8 ply case where it was observed that larger effective core stiffness, either by way of higher core density or smaller core thickness, resulted in larger overall planar delamination size. This was not so in the 16 ply case but rather it was the opposite i.e. a softer core resulted in a larger overall planar delamination size for the 16 ply case. Exact quantitative delamination areas in this regard are presented and discussed in chapter 6. Grouping of the $\pm 45^\circ$ plies together at the outside surface of a face sheet apparently caused core orthotropy to play a role in delamination pattern whereas separating these plies seemed to mitigate its effect.

The findings on the distribution of delamination in both the 8 and 16 ply cases influence the choices made on the interfaces assumed to be delaminating when implemented in the analytical QSI model. The relative sizes, nature and distribution of delaminations in the different sandwich configurations would also be vital in understanding the correlation of the nature and extent of face sheet delamination with the post impact compressive failure modes.

Chapter 6

DAMAGE RESISTANCE EVALUATIONS

Introduction

As defined in Chapter 1, the damage resistance of a composite structure is used to denote the ability of the structure to resist damage by an external object. In this section, the preceding methods are applied to evaluate the damage resistance of the various sandwich geometries. The damage event may be thought of as a particular quasi-static indentation (QSI) force and indenter, in which case the damage metrics of dent depth, dent diameter and planar area of delamination are considered. Alternatively, imparting a dent of a given depth could be taken as the damage event, in which case the latter two metrics would be of interest. To this end, this chapter presents dent depth, dent diameter and planar area of delamination data for the different 8 ply and 16 ply specimens. The results are based on the ultrasonic determination of dent depths and dent diameters discussed in Chapter 3 and the determination of planar area of delamination discussed in Chapter 5. In the tables where these data are presented, specimens follow the nomenclature AWWX-QY-CZ-N, where

- “A” refers to autoclave curing for the manufacture;
- “WW” refers to the number of plies on each face sheet of the sandwich structure;
- “X” refers to the order in which the panels are manufactured. For instance, A refers to the first panel manufactured in a particular sandwich geometry, B to the second panel manufactured, and so on;
- QY refers to the face sheet layups (Q1, Q2 etc.) as defined for both the 8 and 16 ply cases in Chapter 3;

- CZ refers to the core types C1, C2 or C3 as defined in Chapter 3; and
- N refers to the specimen number as retrieved from a particular panel.

For all the evaluations that are presented in this chapter, no differences were observed in the mean results or in the amount of scatter between specimens cut from the same panel versus those cut from different panels. Therefore, except in the tabulated data, panel number is not identified in any other evaluation.

6.1 8 Ply Damage Resistance Evaluations

Tables 6.1.a and 6.1b present all the dent diameter, dent depth and planar area of delamination data for the 8 ply specimens indented with the 25.4 mm and 76.2 mm diameter indenter respectively. All the data presented in these tables were retrieved non-destructively. As discussed in Chapter 5, poorly defined planar delamination boundaries for the 8 ply specimens indented with the 76.2 mm diameter indenter prevented accurate determination of planar area of delamination for these specimens. Therefore no planar area of delamination data for these specimens is presented in Table 4.1.b and they are stated as “not available” (NA).

Table 6.1.a Dent depth, dent diameter and planar area of delamination data for the 8 ply specimens indented with the 25.4 mm diameter indenter.

Specimen	QSI load, N	Dent depth, mm	Dent diameter, mm	Planar area of delamination, mm ²
A08B-Q1-C1-2	1302	0.51	38	206
A08B-Q1-C1-3	1311	0.49	38	187
A08B-Q1-C1-4	1882	0.73	46	252
A08A-Q1-C2-2	1300	0.55	36	400
A08B-Q1-C2-3	1313	0.48	34	400
A08B-Q1-C2-4	1308	0.38	34	400
A08C-Q1-C3-2	1879	0.53	32	355
A08C-Q1-C3-3	1315	0.29	24	271
A08B-Q1-C3-2	1767	0.43	28	361
A08B-Q2-C1-2	1312	0.46	34	303
A08B-Q2-C1-3	1311	0.46	37	335
A08C-Q2-C1-2	1306	0.46	35	271
A08C-Q2-C1-3	1423	0.53	39	258
A08C-Q2-C1-4	1881	0.75	48	342
A08A-Q3-C1-2	1301	0.47	39	400
A08A-Q4-C2-1	1308	0.53	38	226
A08A-Q4-C2-3	1306	0.52	36	232
A08A-Q4-C3-2	1309	0.30	28	284
A08A-Q4-C3-4	1756	0.46	31	394

Table 6.1.b. Dent depth, dent diameter and planar area of delamination data for the 8 ply specimens indented with the 76.2 mm diameter indenter.

Specimen	QSI load, N	Dent depth, mm	Dent diameter, mm	Planar area of delamination, mm ²
A08A-Q2-C1-1	4449	1.69	71	NA
A08A-Q2-C1-4	4444	1.68	72	NA
A08A-Q3-C1-4	4400	1.49	72	NA
A08A-Q1-C1-2	2807	1.07	59	NA
A08B-Q1-C1-1	2811	1.01	57	NA
A08A-Q1-C2-1	2802	0.97	56	NA
A08B-Q1-C2-1	2829	0.96	54	NA
A08B-Q1-C2-2	2810	1.03	55	NA
A08B-Q1-C3-1	3531	1.01	47	NA
A08C-Q1-C3-1	3531	1.06	47	NA
A08C-Q1-C3-4	2849	0.91	39	NA
A08A-Q2-C1-2	2836	1.04	57	NA
A08B-Q2-C1-1	2817	0.93	57	NA
A08B-Q2-C1-4	2953	1.05	57	NA
A08C-Q2-C1-1	2819	0.91	57	NA
A08A-Q3-C1-1	2798	1.10	55	NA
A08A-Q4-C2-2	2819	1.02	57	NA
A08A-Q4-C3-1	2801	0.91	42	NA

6.1.1 Parametric Effects

Figure 6.1 presents the average QSI force versus the average dent depth for all the panels tested. As indicated in the legend, different symbols are used to represent the different face sheet and core combinations as well as the barely visible impact damage (BVID) and “above BVID” load levels. A discussion on the load levels is presented in Section 3.2 of Chapter 3. Even though impact was not the damage event, the acronym BVID is still used in these plots because of it being a common engineering reference to indicate damage that is barely visible. That is, rather than using the less conventional notation “BVD” for barely visible damage, we have used the more widely accepted conventional notation “BVID”. As also discussed in Chapter 3, the “above

BVID” load levels were used in a few specimens to match dent depths of the different panels or to elucidate trends. Differently colored symbols are used for each of the different core types. The same symbol and color conventions are used in all the other plots in this chapter except in those where certain ratios are plotted and which have their own unique symbols as described in the plots. To obtain the average values in the figure, specimens of the same type were first grouped. These were then further divided into groups that experienced very similar load. The average force and dent depth were then determined for each group. These average results are presented in order to illustrate general trends. Analogous results for average QSI force versus average dent diameter are presented in Figure 6.2.

The effect of core on the damage metrics of dent depth and dent diameter was clearly visible from the results. Considering the specimens with the Q1 layup, Figures 6.1 and 6.2 show that for a given QSI load and indenter, the largest average dent depths and dent areas are observed in those specimens that have the C1 and C2 cores while the smallest dent depths and dent areas are in the specimens with the C3 core. This corresponds well to the load vs. displacement results presented in section 4.1 of Chapter 4. Core crushing was seen directly underneath the dented region upon destructive evaluation. The DE images showed that the region of core crushing, as indicated by permanent buckling type deformation of the cell walls, closely corresponded to the dented region. Thus, the dented areas that are reported may also be interpreted as the area of the permanent crushing of the core.

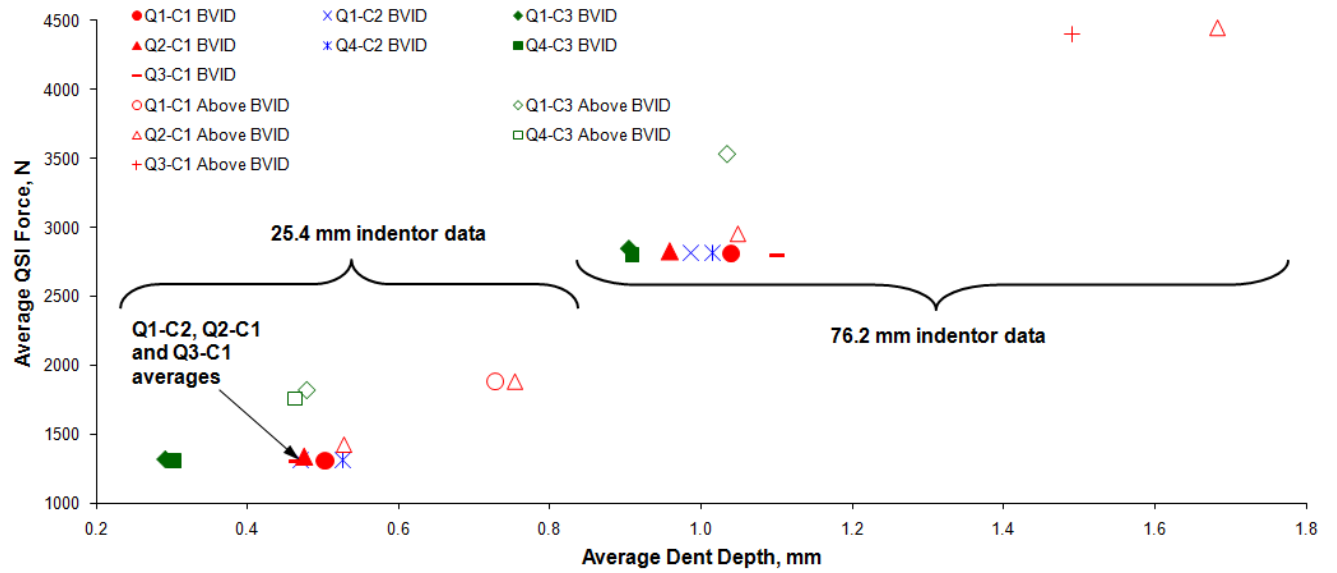


Figure 6.1. Results for average QSI force versus average dent depth for the 8 ply specimens.

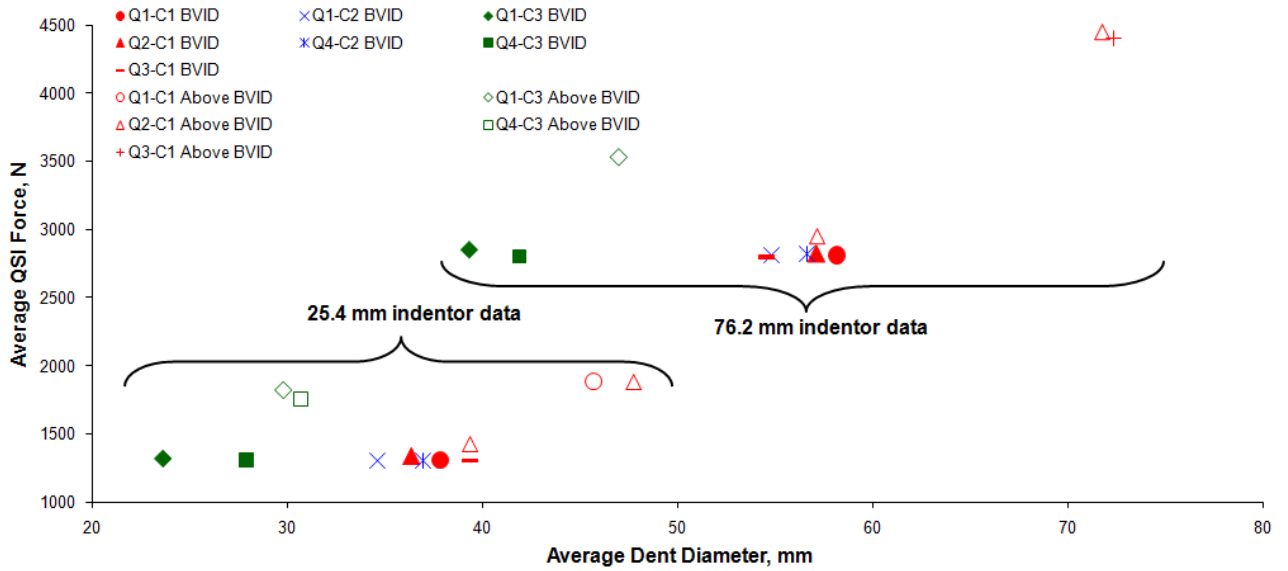


Figure 6.2. Results for average QSI force versus average dent diameter for the 8 ply specimens.

Figure 6.3 presents results that are similar to those in Figures 6.1 and 6.2, but here all specimens tested are presented. This allows the scatter in results to be observed, and allows for a determination of the strength of any conclusions drawn from Figures 6.1 and 6.2. For example, considering specimens with the C1 core at the BVID load level, Figures 6.1 and 6.2 indicate that specimens with the Q1 layup show somewhat larger average dent depths and diameters than those with the Q2 layup. Figure 6.3 indicates that this is true for all specimens for the 25.4 mm diameter indenter, but only true in an average sense for the 76.2 mm diameter indenter. Also note that the trend is reversed for the higher load level specimens indented with the 25.4 mm diameter indenter. Figures 6.2 and 6.3 indicate that specimens with the Q4 layup and either the C2 or C3 cores show somewhat larger average dent depths and diameters than the same core type with the Q1 layup. Figure 6.3 shows that this result is true only on average, and that there is considerable scatter in these results for any specimen type. Thus, if dent depth or dent diameter were the damage metric, both the average and individual results presented in Figures 6.1-6.3 show that that the C3 core provides the most damage resistant panels and the C1 core the least. This is clearly due to the difference in density between the C3 and C1 cores where the denser C3 core provides a greater indentation resistance than the C1 core resulting in smaller dent diameters and dent depths.

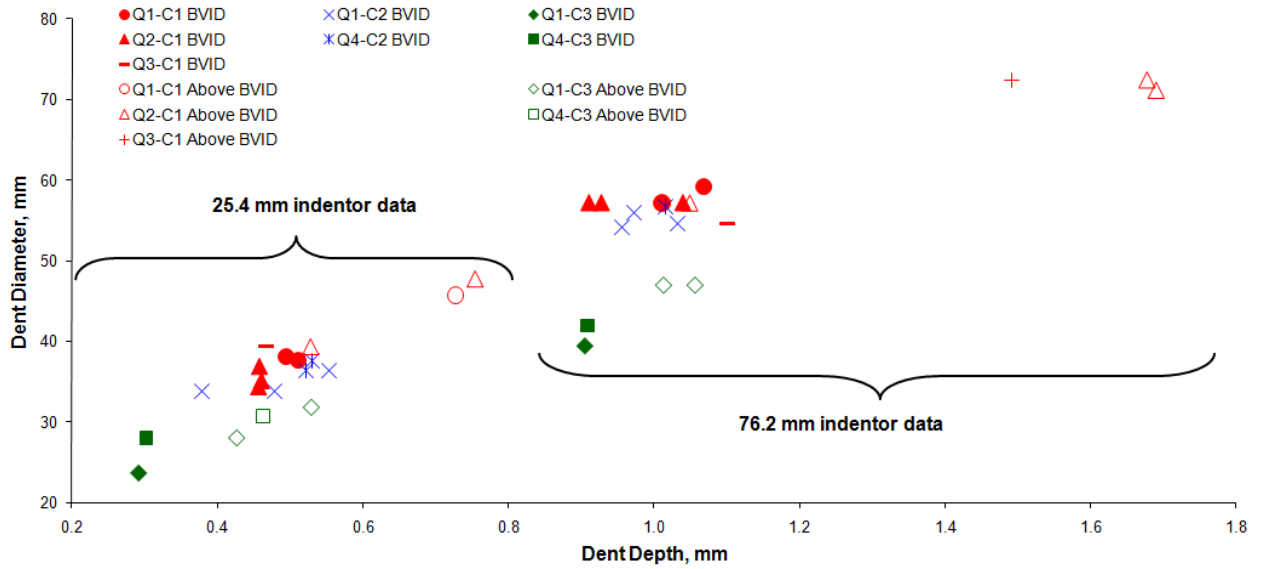


Figure 6.3. Dent diameter versus dent depth for all the 8 ply specimen types.

Figure 6.3 shows that when the force levels are increased so that the dent depth in the C3 core specimens agrees with those in the other specimen types, the dent diameter for the C3 core remains smaller. This is further illustrated in Figure 6.4, which shows the ratio of dent diameter to dent depth for the various panel types. The ratio of dent diameter to dent depth is essentially independent of the load level. Also, from the results presented, no trend on the effect of indenter diameter on the dent diameter to dent depth ratios can be established. Specimens with the C3 core clearly show a lower diameter for a given depth. This is in agreement with previous studies that found that the resistance to external denting increases with the increasing core density.^{7,27,37} A comparison of the C1 versus C2 results shows that the ratio of dent diameter to dent depth is essentially the same for these cores.

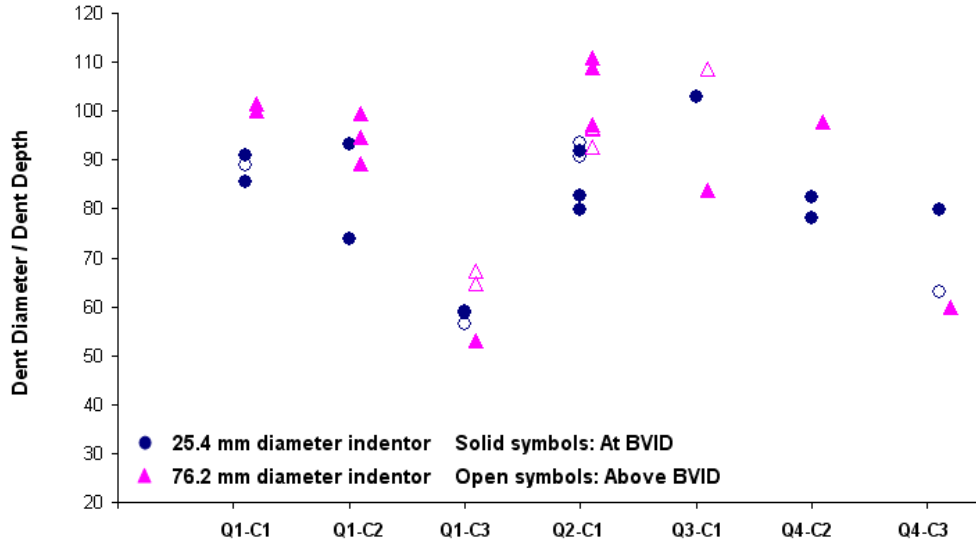


Figure 6.4. Ratio of dent diameter to dent depth by specimen type for the 8 ply specimens.

Figure 6.5 presents the ratio of the dent diameter to the local chord length of the indenter for all specimen types. The local chord length, c , is as defined in Figure 6.6. It was computed for each specimen based on the indenter radius, r , that was used and the permanent dent depth, d , that was measured, and was obtained using the relation

$$c = 2\sqrt{d(2r - d)} \quad (6.1)$$

As indicated in Figure 6.6, the chord length represents the “planar length” of the indenter at the measured indentation depth. That is, the dent diameter would equal the chord length if the specimen fully conformed to the shape of the indenter. From Figure 6.5, it is observed that, regardless of the indenter diameter and specimen type, the dent diameter was always significantly larger than the chord length. As indicated in Figure 6.6, the chord length is larger than the region of the indenter that was contacting the specimen. However, it would be quite difficult to quantify contact length, so chord length is chosen in this instance. Figure 6.5 clearly shows that bending of the face sheet outside of the contact region contributes to core crushing. It

may be observed that the difference between the dent diameter and the chord length increases with increasing QSI load and displacement, i.e., as the face sheet undergoes more bending. As would be expected, the ratios presented in Figure 6.5 are always greater for the smaller diameter indenter. As a result of the larger density and associated smaller dent diameter, the ratio for specimens with the C3 core is the smallest. Given its effective stiffness, it is consistent that the ratio for the C2 core is slightly smaller than that for C1.

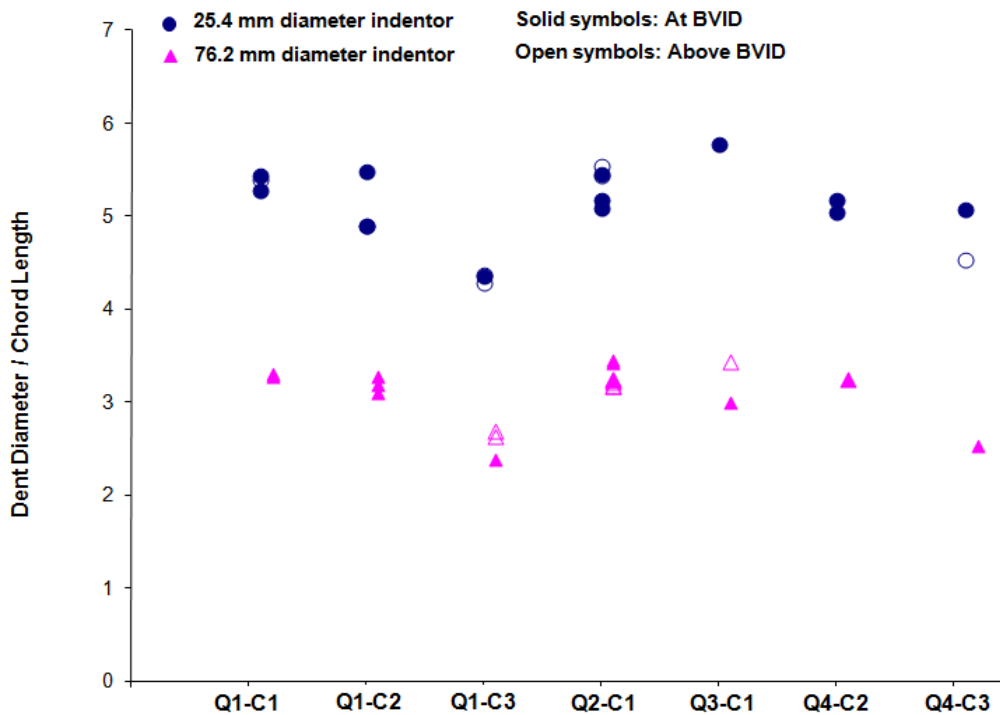


Figure 6.5. Ratio of dent diameter to local chord length of the indenter for the 8 ply specimens.

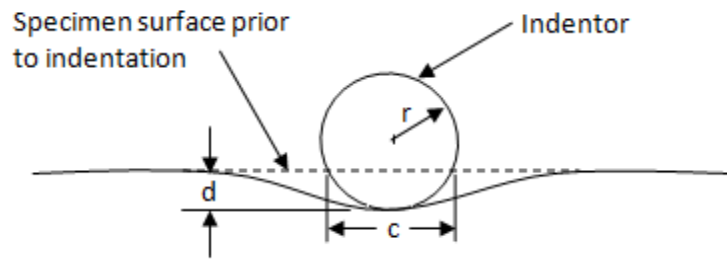


Figure 6.6. Sketch illustrating local chord length definition.

6.1.2 Damage Resistance Metrics

Figure 6.7 considers the case where the planar area of delamination is chosen as the damage metric. As previously described, quantitative planar area of delamination could only be determined for specimens indented with the 25.4 mm diameter indenter in the 8 ply case. Thus, Figure 6.7 presents QSI force versus the planar area of delamination for only these specimens. Considering specimens with the C1 core, if damage resistance is based on QSI force versus the planar area of delamination, then specimens with the Q1 layup are more resistant than those with the Q2 layup which in turn are more resistant than the Q3 layup. The C2 core results indicate that the Q4 layup is more resistant than the Q1 layup, but the C3 core results indicate similar resistance between the Q4 and Q1 layups. Thus, by comparing results for each core type individually, it may be deduced that less delamination occurs in the Q1 and Q4 layups than in the Q2 and Q3 layups. This likely relates to the fact that the Q1 and Q4 layups only have 45° angle changes between adjacent plies. This results in a lower thermal and mechanical mismatch, and therefore lower interlaminar shear stresses during QSI than what occurs in the Q2 and Q3 layups, which have 90° angle changes between adjacent plies. This result agrees with what has been reported in the literature for monolithic^{12,18} and sandwich composites.¹²

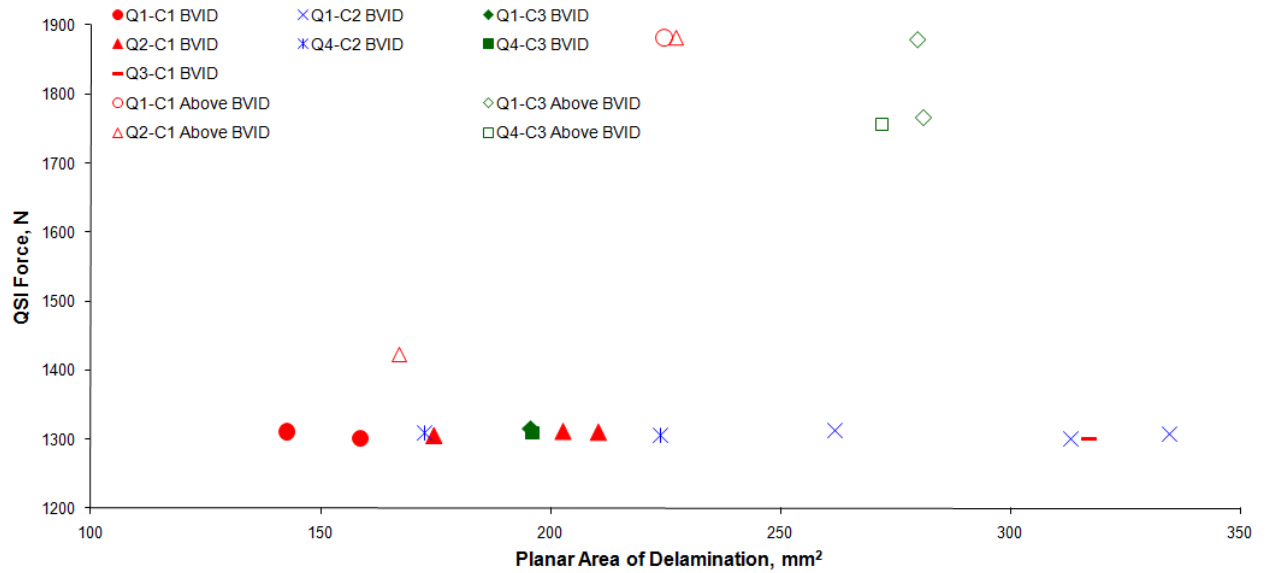


Figure 6.7. QSI force vs. planar area of delamination for the 8 ply specimens indented with the 25.4 mm diameter indenter.

The effect of the core on the planar area of delamination may be observed by comparing specimens with the same face sheet. Specimens with the C1 core show a smaller planar area of delamination than those with the C2 or C3 cores. As described previously, for the boundary conditions chosen, the C2 core is stiffer than the C1 core due to the effect of thickness. Thus, since the C2 and C3 cores are stiffer than the C1 core, less energy is dissipated through core crushing, and more energy goes into delamination in the former cases than the latter. More delamination in specimens with higher density cores has been reported for low velocity impact tests on sandwich panels with similar boundary conditions to those used herein³⁷, but different results were observed for the effect of core thickness on low velocity impact of sandwich plates with simply supported boundaries;⁴⁰ here, thicker cores produced more planar area of delamination. Note, however, that in the simply supported case, a thicker core increases the plate's rigidity and therefore causes more energy to be absorbed locally through delamination growth, similar to the effect of decreasing the core thickness in the current study where a rigid

back surface was utilized. That is, the energy absorption argument leads to the different effects observed experimentally. No clear trend was observed in the current study between the C2 and C3 cores: with the Q1 layup, specimens with the C2 core show a greater planar area of delamination, but the reverse is true with the Q4 layup.

Figure 6.8 illustrates the situation where the damage event is considered to be indentation to a certain depth, and the damage metric is again the planar area of delamination. This figure illustrates the same behaviors as those described above with respect to the effect of QSI load. As would be expected, Figures 6.7 and 6.8 show that for any given panel type, the delaminated area increases with increasing QSI force and with increasing dent depth. This is most obvious by considering the four panel types that were tested both at and above BVID. Overall, if the planar area of delamination is the damage metric, then the Q1 or Q4 layups will provide the most damage resistant result. That is, although Q4-C1 data is not presented, this conclusion is based on the previously established similarity between the Q1 and Q4 layup behaviors.

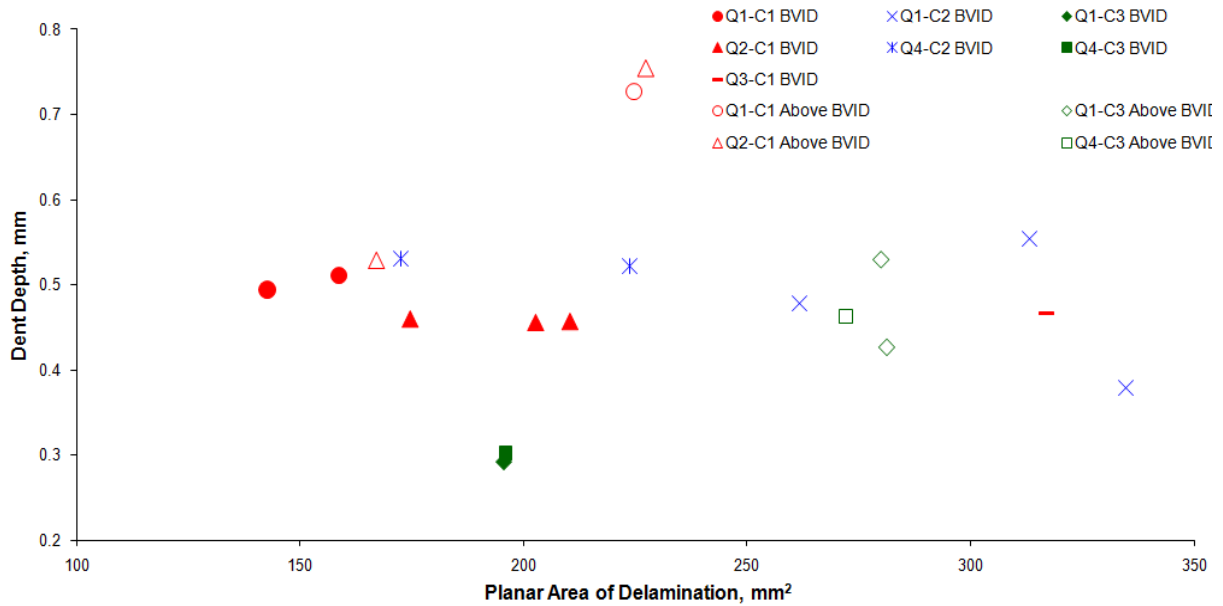


Figure 6.8. Dent depth versus planar area of delamination for the 8 ply specimens indented with the 25.4 mm diameter indenter.

Figure 6.9 presents the ratio of the planar area of delamination to the dent area as a function of panel type. All the ratios of planar area of delamination to dent area are less than one, and there was never an instance where either the destructive or nondestructive evaluations showed the delamination to extend outside of the dented region. Figure 6.9 may be used to draw conclusions when dent area is the damage event and planar area of delamination is the damage metric. Considering the effect of core, a comparison of Q1-C1, Q2-C1 and Q3-C1 sandwich geometries indicates that for a given dent area, specimens with the C1 core show the smallest planar area of delamination; this is consistent with the conclusions for delamination at a given dent depth or for a given QSI force. Note that this comparison, as well as that of the Q4-C2 sandwich geometry to the Q4-C3 sandwich geometry, shows that specimens with the C3 core will contain the largest planar area of delamination, and that the planar area of delamination that occurs in specimens with the C2 core will be intermediate to that which occurs in specimens with

the C1 and C3 cores. This is different from what could be deduced for the cases of fixed QSI force (Figure 6.7) or fixed dent depth (Figure 6.8), and is due to the fact that specimens with the C3 core show a smaller dent diameter at a given dent depth than those with the C2 core (Figure 6.3).

When considering the effects of layup, a comparison of Q1-C2 sandwich geometry to Q4-C2 and of Q1-C3 sandwich geometry to Q4-C3 at the BVID load level shows that for a given core type and dent area, the Q4 layup will show less delaminated area than the Q1 layup. Comparing the Q1-C1, Q2-C1 and Q3-C1 sandwich geometries, the Q2 and Q3 layups are observed to show more delamination than the Q1 layup. Combining this with the conclusions on the effect of core, we would therefore hypothesize that the Q4-C1 sandwich geometry would be the best choice and Q2-C3 or Q3-C3 sandwich geometries would be the worst for the metric of Figure 6.9.

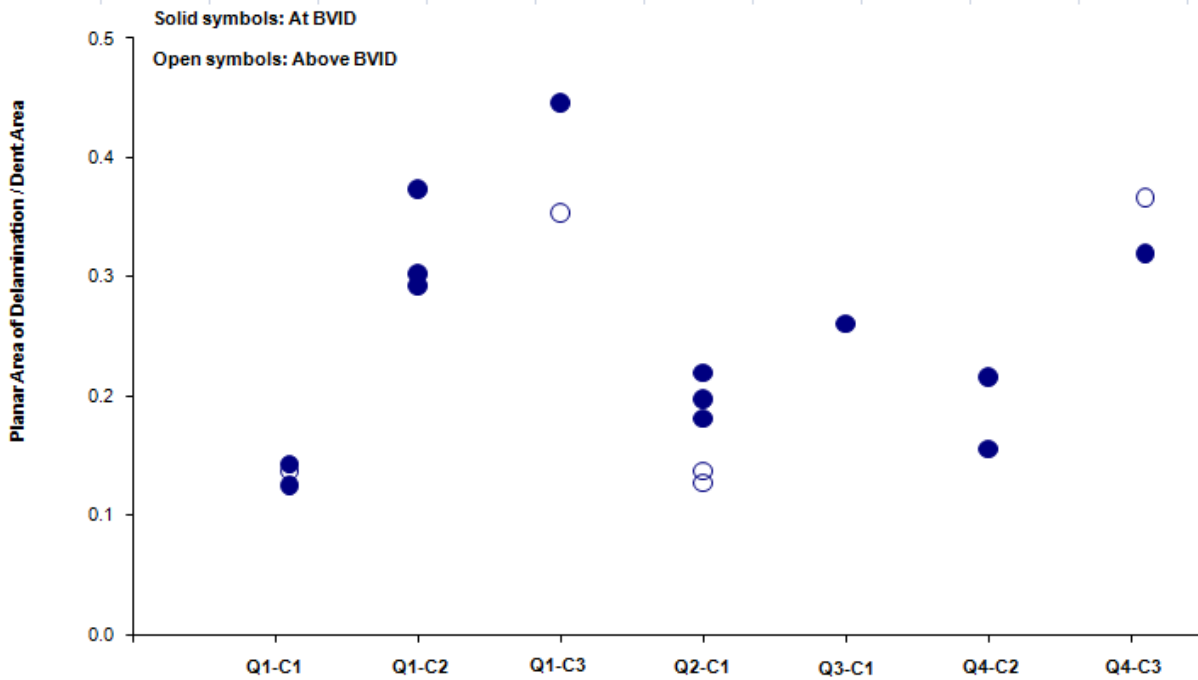


Figure 6.9. Ratio of planar area of delamination to dent area for the 8 ply specimens indented with the 25.4 mm diameter indenter.

6.2 16 Ply Damage Resistance Evaluations

The damage resistance evaluations were done analogous to what was done for the 8 ply case. Tables 6.2.a and b presents all the dent diameter, dent depth and planar area of delamination data for the 8 ply specimens. All data was retrieved non-destructively. Unlike the 8 ply case, planar area of delamination data is presented for the 16 ply specimens indented with the 76.2 mm diameter indenter.

Table 6.2.a. Dent depth, dent diameter and planar area of delamination data for 16 ply specimens indented with 25.4 mm diameter indenter.

Specimen	QSI Load, N	Dent depth, mm	Dent diameter, mm	Planar area of delamination, mm ²
A16A-Q1-C1-1	2447	0.42	64	439
A16A-Q1-C1-4	2459	0.44	74	516
A16B-Q1-C1-1	2457	0.42	70	639
A16B-Q1-C1-4	2463	0.42	69	658
A16A-Q1-C2-1	2457	0.40	57	418
A16A-Q1-C2-4	2444	0.41	64	477
A16B-Q1-C2-1	2458	0.43	70	588
A16B-Q1-C2-4	2456	0.44	66	643
A16A-Q1-C3-1	2463	0.26	54	368
A16A-Q1-C3-4	2465	0.35	51	310
A16B-Q1-C3-1	2448	0.31	52	344
A16B-Q1-C3-4	2463	0.29	47	314
A16A-Q2-C1-1	2468	0.41	67	297
A16A-Q2-C1-4	2440	0.36	69	238
A16B-Q2-C1-1	2455	0.41	65	332
A16B-Q2-C1-4	2463	0.38	61	375
A16A-Q3-C1-1	2012	0.29	64	222
A16A-Q3-C1-3	2472	0.40	67	272
A16A-Q4-C1-1	2010	0.32	65	209
A16A-Q4-C1-2	2453	0.45	63	288
A16A-Q4-C3-1	2456	0.33	36	332
A16A-Q4-C3-4	2442	0.23	44	284
A16A-Q5-C1-2	2465	0.41	68	444
A16A-Q5-C1-4	2463	0.42	69	540

Table 6.2.b. Dent depth, dent diameter and planar area of delamination data for 16 ply specimens indented with 76.2 mm diameter indenter.

Specimen	QSI Load, N	Dent depth, mm	Dent diameter, mm	Planar area of delamination, mm ²
A16A-Q1-C1-2	4294	0.83	81	1329
A16A-Q1-C1-3	4310	0.76	84	1394
A16B-Q1-C1-2	4329	0.85	83	1787
A16B-Q1-C1-3	4303	0.75	79	1645
A16A-Q1-C2-2	4325	0.82	79	1186
A16A-Q1-C2-3	4302	0.82	75	1146
A16B-Q1-C2-2	4302	0.85	80	1442
A16B-Q1-C2-3	4316	0.78	82	1676
A16A-Q1-C3-2	4322	0.68	65	1097
A16A-Q1-C3-3	4322	0.64	54	1000
A16B-Q1-C3-2	4336	0.63	66	1019
A16B-Q1-C3-3	4315	0.62	64	907
A16A-Q2-C1-2	4307	0.73	85	920
A16A-Q2-C1-3	4302	0.71	84	813
A16B-Q2-C1-2	4310	0.79	86	1132
A16B-Q2-C1-3	4307	0.74	80	1251
A16A-Q3-C1-2	4299	0.77	91	903
A16A-Q4-C3-2	4309	0.72	57	1130
A16A-Q4-C3-3	4301	0.69	55	908
A16A-Q5-C1-1	4325	0.80	88	923
A16A-Q5-C1-3	4326	0.85	85	891

6.2.1 Parametric Effects

Figures 6.10 and 6.11 show the average dent depth and dent diameter as a function of average QSI force respectively. Figure 6.12 shows the scatter in these average results by presenting dent depth as a function of dent diameter for every specimen tested at both indenter sizes.

By considering only the Q1 layup, the effect of core type on dent depth can be examined.

It can be said from Figure 6.10 that the Q1-C1 and Q1-C2 sandwich geometries show similar

dent depths. The Q1-C3 sandwich geometry on the other hand shows smaller dent depth than both the Q1-C1 and Q1-C2 sandwich geometries, implying that higher core density results in smaller dent depth. However, the difference in dent depth between the C3 core and the C1 and C2 cores is not as much as what was seen in the 8 ply case. It therefore suggests that for the thicker face sheet, core density has lesser effect on dent depth as compared to the thinner face sheet.

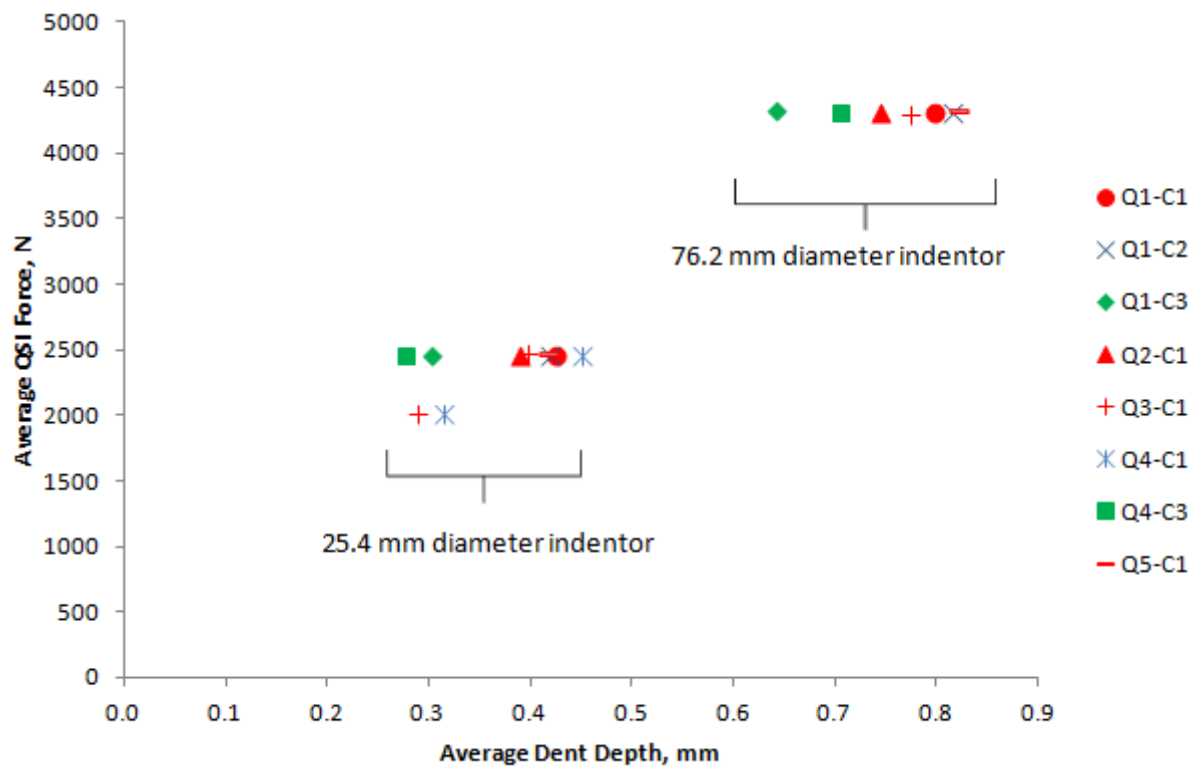


Figure 6.10. Results for average QSI force versus average dent depth for the 16 ply specimens.

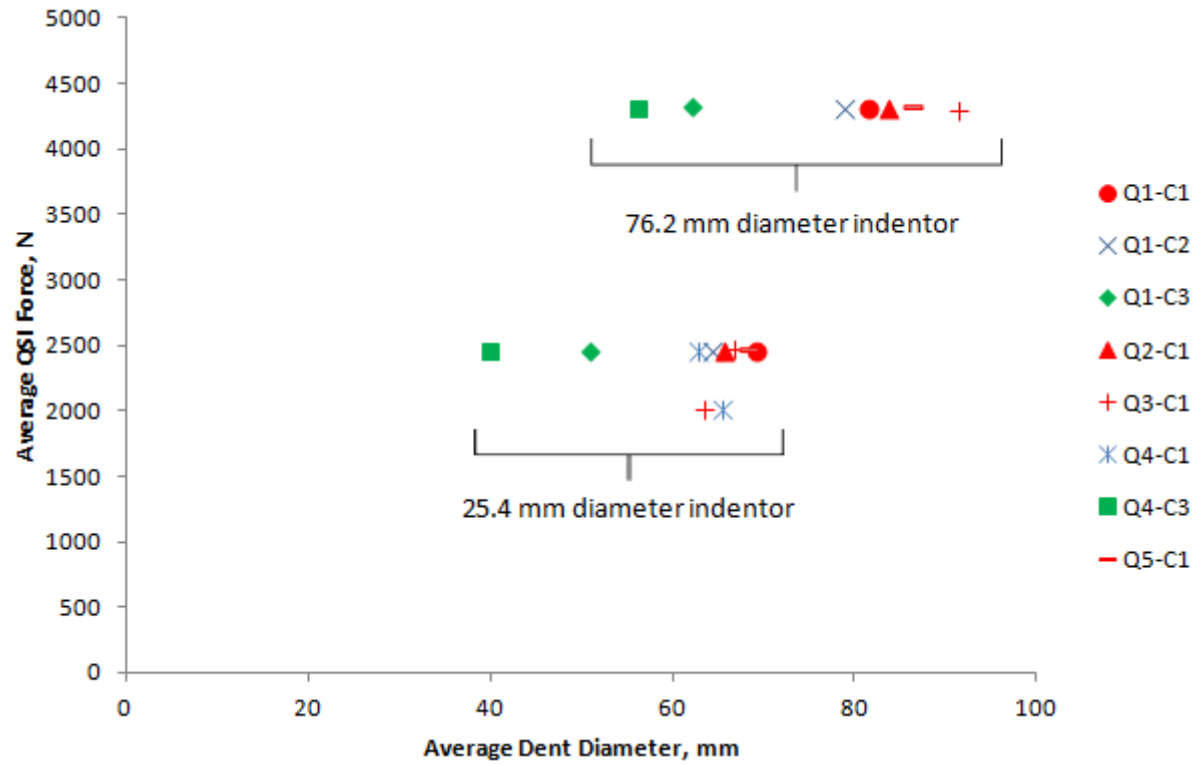


Figure 6.11. Results for average QSI force versus average dent diameter for the 16 ply specimens.

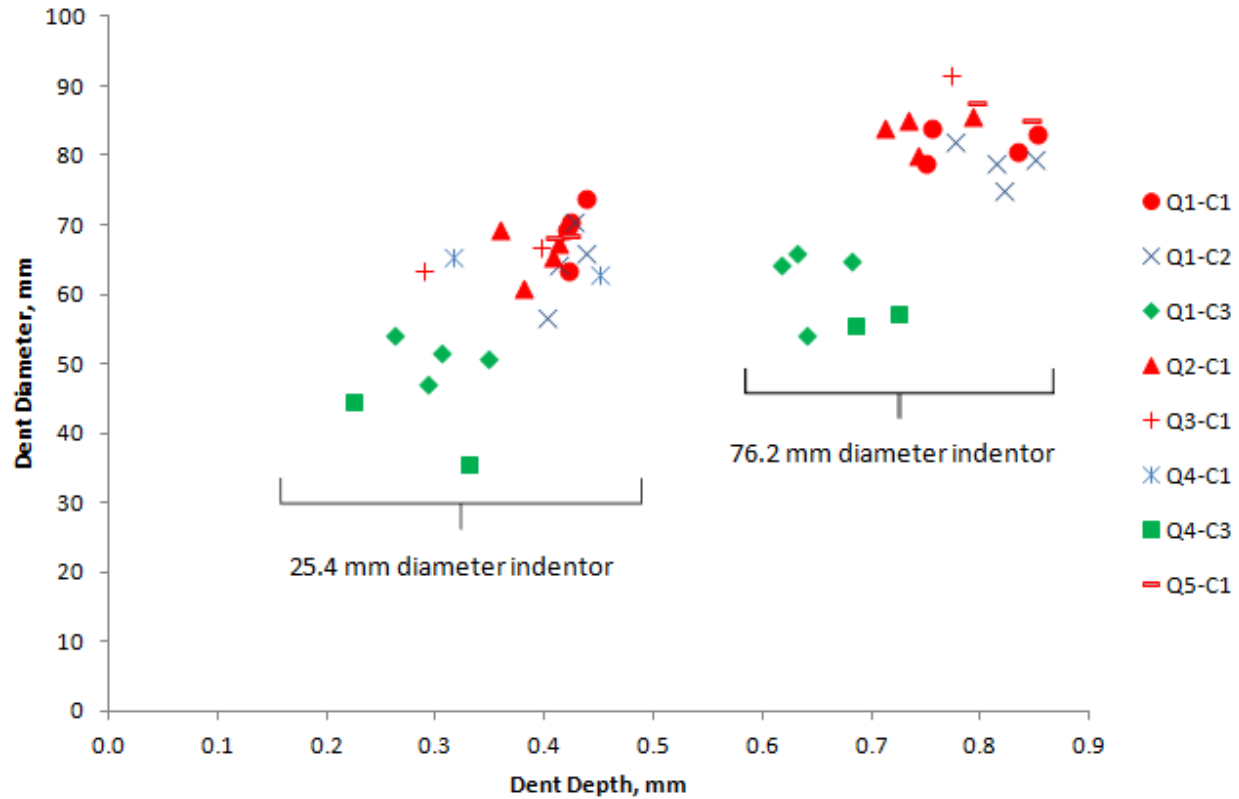


Figure 6.12. Dent diameter versus dent depth for all the 16 ply specimen types.

By considering only the C1 core, the effect of face sheet layup on dent depth can be studied. The face sheet layups Q1, Q4 and Q5 show slightly larger dent depths than the Q2 and Q3 layups. The Q1, Q4 and Q5 layups have mostly 45° ply angle changes while the Q2 and Q3 layups have 90° ply angle changes. It was observed in the 8 ply case that the Q2 layup, which had large ply angle changes, produced smaller dent depths than the specimens with the Q1 layup. A similar result is seen in the 16 ply case where the Q2 and Q3 layups, which have large (90°) ply angle changes, show smaller dent depths than the Q1, Q4 and Q5 layups which have small (45°) ply angle changes. When comparing the Q4-C3 sandwich geometry with the Q1-C3 sandwich geometry, it can be noticed that both the sandwich geometries have similar average dent depths when indented with the 25.4 mm diameter indenter. However, for the specimens

indented with the 76.2 mm diameter indenter, the Q4 layup shows slightly larger dent depth than the Q1 layup.

In almost all cases, it was observed the dent diameter in the 0° direction was larger than the dent diameter in 90° direction resulting in dent shape which was elliptical in nature. This was contrary to the 8 ply case where the dent shape was somewhat circular in nature. Considering just the Q1 layup from the results presented in Figure 6.11, the C1 and C2 cores show essentially the same dent diameters while the C3 core shows the smallest dent diameter out of all the three cores. If dent diameter is considered as the damage metric, it can be said that the C3 core is the most damage resistant.

The effects of face sheet layup on dent diameter can be studied by considering only the C1 core. In Figure 6.11, the Q2 and Q3 layups show lower average dent diameters than the Q1 layup for the specimens indented with the 25.4 mm diameter indenter and higher average dent diameter than the Q1 layup for the specimens indented with the 76.2 mm diameter indenter. The Q5 layup shows higher average dent diameter than the Q2 and Q3 layups for the specimens indented with the 25.4 mm diameter indenter. However, for the specimens indented with the 76.2 mm diameter indenter, the Q5 layup shows an average dent diameter value in-between the Q2 and Q3 layups. The Q4 layup at the barely visible damage load shows the lowest dent diameter out of all the other layups when indented with the 25.4 mm diameter indenter. No Q4-C1 sandwich geometry results are available for specimens indented with the 76.2 mm diameter indenter. At load levels lower than the BVID load level, the Q4 layup shows a slightly higher dent diameter than the Q3 layup. Comparing the Q1, Q2 and Q3 layups, it appears that the Q2 and Q3 layups, which have large ply angle changes, show smaller dent diameter than the Q1 layup when indented with the 25.4 mm diameter indenter and larger dent diameter when

indented with the 76.2 mm diameter indenter. The Q5 layup shows lesser dent diameter than the Q1 layup when indented with the 76.2 mm diameter indenter, but larger dent diameter than the Q1 layup when indented with the 25.4 mm diameter indenter. A better comparison of the Q4 layup to the Q1 layup is presented by the C3 core results where the Q4 layup shows lesser dent diameter than the Q1 layup for both the 25.4 mm and 76.2 mm diameter indenter tests.

Figure 6.13 shows the dent diameter to dent depth ratios for each of the sandwich geometries tested with both the indenter sizes. Unlike what was reported for the 8 ply case in Figure 6.4, the dent diameter to dent depth ratio has a significant dependence on the indenter size in the 16 ply case at the BVID load level. For all the sandwich geometries considered, dent diameter/dent depth ratio is higher for the specimens indented with the 25.4 mm diameter indenter as compared to the ones indented with the 76.2 mm diameter indenter, the former having lower barely visible damage load threshold and of course smaller indenter size. The Q2-C1 and Q3-C1 sandwich geometries have the highest dent diameter/dent depth ratio out of all geometries for both the indenter sizes. The Q2 and Q3 layups are the only layups with mostly 45° angle changes and end up showing a larger dent diameter for a given dent depth. When considering only the Q1 layup, both the Q1-C1 and Q1-C2 sandwich geometries have similar dent diameter/dent depth ratio at both the indenter sizes. The Q1-C3 sandwich geometry has a little lower dent diameter/dent depth ratio than the Q1-C1 and Q1-C2 sandwich geometries for the specimens indented with the 25.4 mm diameter indenter but similar dent diameter/dent depth ratio with the Q1-C1 and Q1-C2 sandwich geometries for the specimens indented with the 76.2 mm diameter indenter. This is quite different from what was seen in the 8 ply case where the C3 core had significantly smaller dent diameter/dent depth ratio than the C1 and C2 cores when considered for the same face sheet layup.

Overall, the dent diameter over dent depth ratio in the 16 ply case is larger than in the 8 ply case for both 25.4 mm and 76.2 mm diameter indentors. For the 16 ply case at BVID, dent depths are smaller than the 8 ply case while dent diameters are larger than the 8 ply case. This results in a larger dent diameter to dent depth ratio for the 16 ply case as compared to the 8 ply case. Therefore, the qualitative definition of BVID for the thicker face sheet differs from the qualitative definition of BVID for the thinner face sheet. For the thicker face sheet, BVID implies a larger dent area and a smaller dent depth than a thinner face sheet. Therefore the crushed core zone is expected to be larger for the thicker face sheet compared to the thinner face sheet at BVID. Also, the results presented in Tables 6.1 and 6.2 show that the planar area of delamination is larger for the thicker face sheet compared to the thinner face sheet at BVID.

The difference in dent diameter/dent depth ratio between the large and the small indenter sizes is significantly more in the 16 ply case as compared to the 8 ply case. This implies that the effect of indenter size on face sheet deformation for a constant dent depth is more in the thicker face sheet as compared to the thinner face sheet.

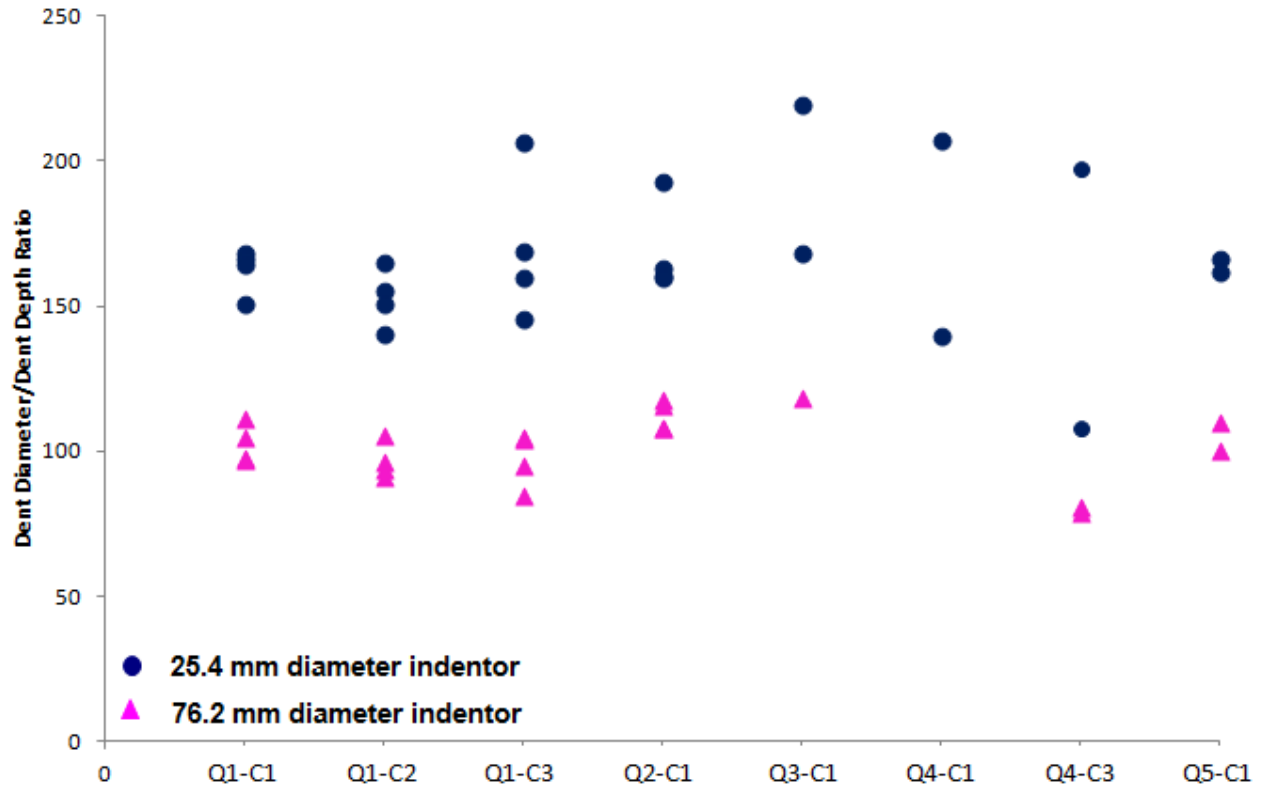


Figure 6.13. Ratio of dent diameter to dent depth by specimen type for the 16 ply specimens.

Figure 6.14 shows the dent diameter/chord length ratio for all the sandwich geometries indented with both the 25.4 mm diameter indenter and the 76.2 mm diameter indenter. Chord length is defined by the schematic in Figure 6.6. In every case, dent diameter was larger than the chord length and the dent diameter/chord length ratio was higher for the specimens indented with the 25.4 mm diameter indenter as compared to the specimens indented with the 76.2 mm diameter indenter. A similar observation was made for the 8 ply case as well. The Q2 and Q3 layups show larger dent diameter/chord length ratio when compared to all other face sheet layups for both the indenter sizes. When considering only the Q1 layup, the lowest dent diameter/chord length ratio is seen for the C3 core and the highest for the C1 core. This was also the case with

the 8 ply specimens. As was in the case for the 8 ply specimens, it is expected that in the 16 ply case as well that bending of face sheet outside the contact region contributes to core crushing.

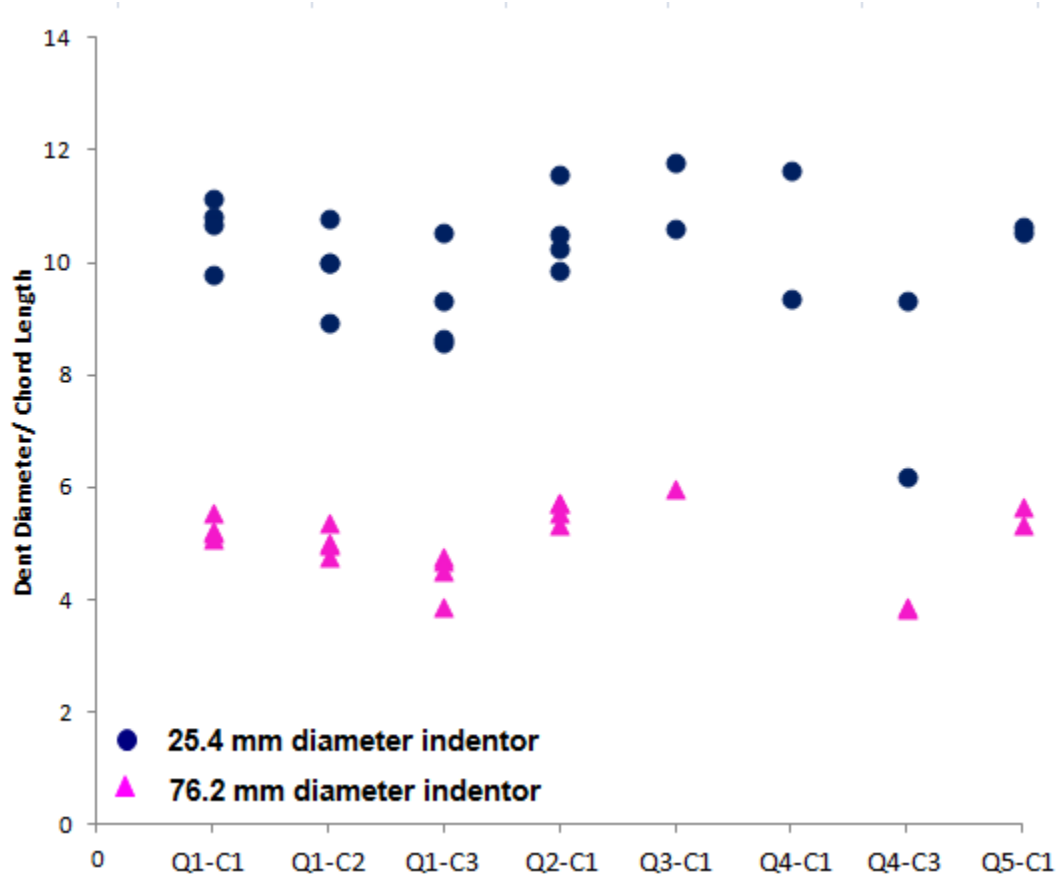


Figure 6.14. Ratio of dent diameter to local chord length of the indenter for the 16 ply specimens.

6.2.2 Damage Resistance Metrics

Figure 6.15 shows the QSI force versus the planar area of delamination results for all the full-sized specimens tested with both the 25.4 mm and the 76.2 mm diameter indentors. If we consider just the Q1 layup, the Q1-C1 and Q1-C2 sandwich geometries show similar planar areas of delamination while the Q1-C3 sandwich geometry shows the least. This is different from what was observed in the 8 ply case where when considered for the same face sheet, the C1 core

showed the lowest delamination area, followed by the C3 core while C2 core showed the highest. The hypothesis put forward for this kind of behavior in the 8 ply case was that for the effectively stiffer core i.e. the C2 and C3 cores, less energy is dissipated through core crushing while more energy is dissipated through face sheet delamination. For the 16 ply case, it appears that the propensity of core crushing does not dictate delamination behavior, but just as in the case of dent diameter and dent depth, the stiffest core (C3) causes the smallest delamination area while the least stiff core causes the largest.

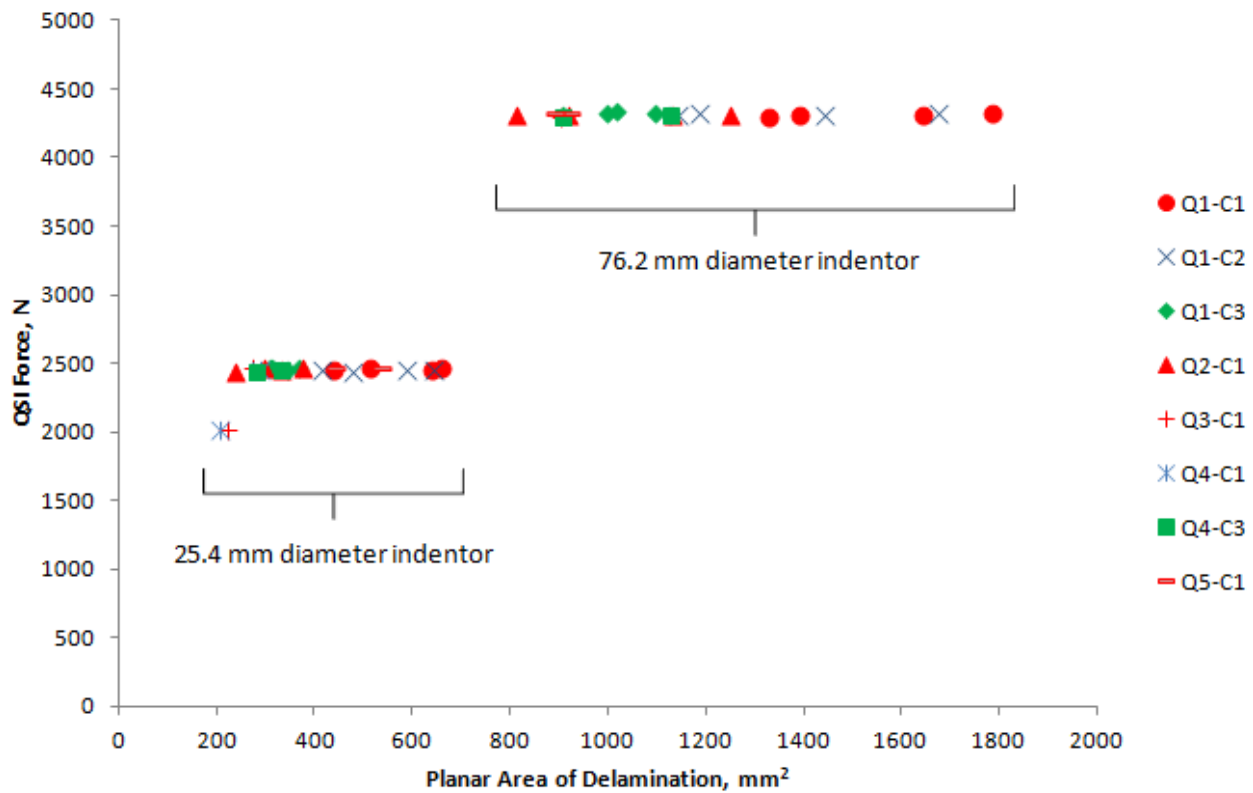


Figure 6.15. QSI force vs. planar area of delamination for the 16 ply specimens.

When considering only the C1 core, the Q1 layup generally shows the highest planar area of delamination, followed by the Q2 and the Q3 layups. Even though the Q1 layup has smaller ply angle changes and thus lower mechanical and thermal stiffness mismatch, it still has higher

planar area of delamination than the Q2 and Q3 layups. This is contrary to what was observed in the 8 ply case where the lower ply angle changes resulted in small planar areas of delamination. The Q5 layup has similar planar area of delamination as the Q1 layup for the specimens indented with the 25.4 mm diameter indenter and small planar area of delamination for the specimens indented with the 76.2 mm diameter indenter. When considering the C3 core, comparison of the Q1 and Q4 layups show that average planar area of delamination is higher for the Q1 layup when compared to the Q4 layup for both indenter sizes.

Figure 6.16 shows planar area of delamination as a function of dent depth for all layups. The damage event in this case is considered as indentation depth and the damage metric is the planar area of delamination. Overall, the Q1 face sheet and the C1 core causes the most delamination for both the indenter sizes of 25.4 mm and 76.2 mm. The results presented in this plot concur with what has been reported in the previous paragraphs on the trends of planar area of delamination when compared for the different sandwich geometries. The Q4-C3 sandwich geometry shows slightly higher dent depth for a given planar area of delamination for the specimens indented with the 76.2 mm diameter indenter while the scatter of results in the specimens indented with the 25.4 mm diameter indenter point more towards both the Q4-C3 and the Q1-C3 sandwich geometries having similar “average” dent depth for a given planar area of delamination.

Figure 6.17 presents the plot of the ratio of planar area of delamination to dent area for the different sandwich geometries for both the 25.4 mm and 76.2 mm diameter indentors. The ratio of planar area of delamination to dent area is always less than 1, implying that the delamination never extended out of the dented area. This was also observed with the 8 ply specimens. The ratios are greater for the specimens indented with the 76.2 mm diameter indenter

as compared to those indented with the 25.4 mm diameter indenter for the 16 ply data. This implies that there is a larger relative spread of delaminations as gauged from the size of external dent for the 76.2 mm tests as compared to the 25.4 mm tests. Smallest planar area of delamination/dent area ratios are seen for the Q2-C1, Q3-C1 and Q4-C1 sandwich geometries. For specimens tested with the 76.2 mm diameter indenter, the Q1-C3 and Q4-C3 sandwich geometries show relatively larger ratios than all the other layups. This implies that higher core density affects the size of delamination area with reference to the dent area for the large indenter. The difference in the ratios between C3 core and the other cores in the 25.4 mm QSI case is not as much as in the 76.2 mm QSI case.

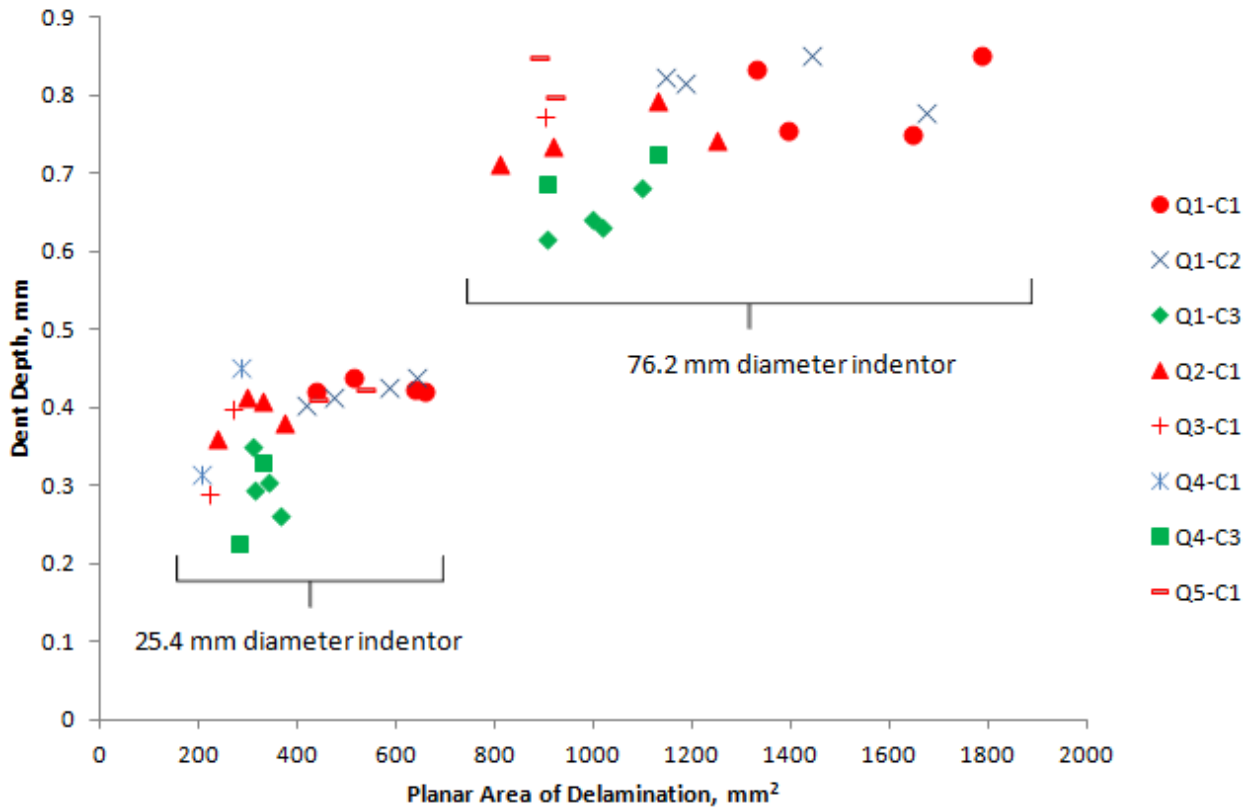


Figure 6.16. Dent depth versus planar area of delamination for the 16 ply specimens.

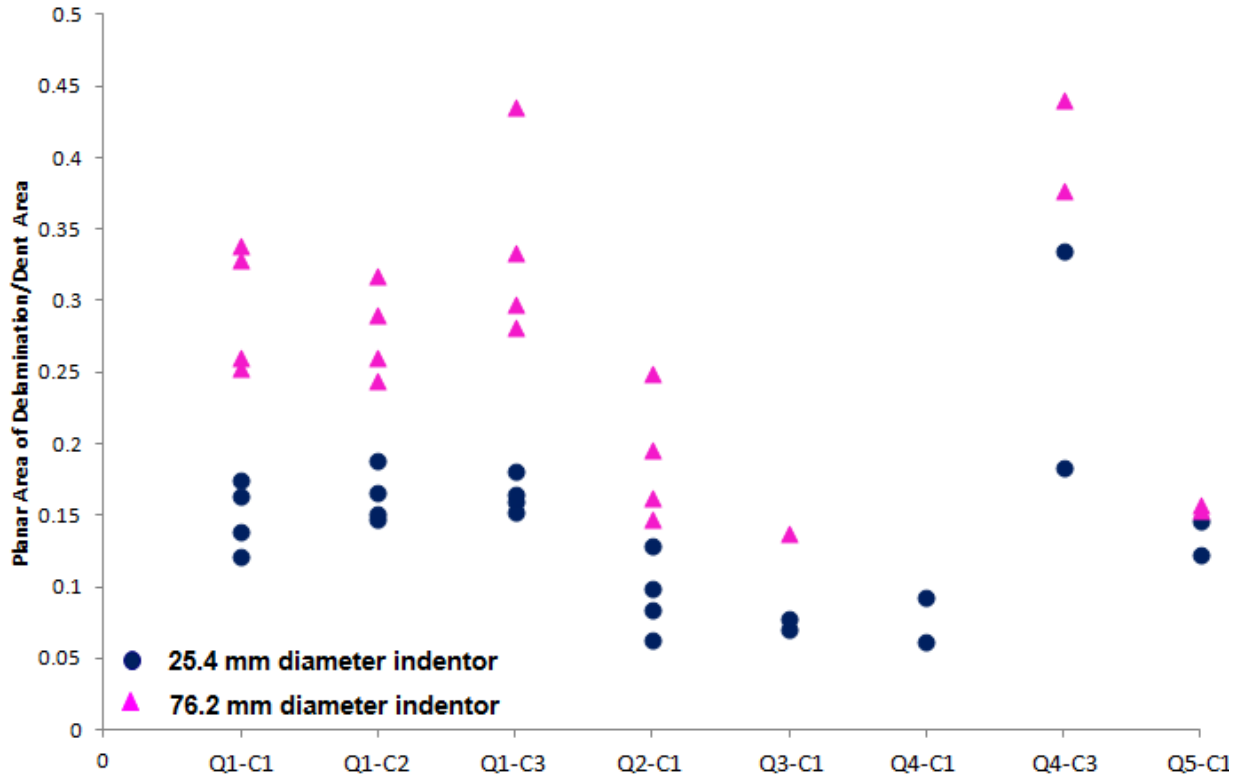


Figure 6.17. Ratio of planar area of delamination to dent area for the 16 ply specimens.

6.3 Comparison of Results – 8 versus 16 Ply

From the damage resistance evaluations that were done on the 8 and 16 ply specimens based on the damage metrics of dent depth, dent diameter and planar area of delamination, the following comparisons can be made between the 8 and the 16 ply results.

- i. The higher density C3 core shows the lowest dent depths and dent diameters for both the 8 and 16 ply cases. The effect of core density however appears to be stronger in the 8 ply case than in the 16 ply case since in the former, the difference in the dent depth and dent diameter results between the C3 core and the other types was slightly more.

- ii. Very minimal effect of face sheet layup on dent depth and dent diameter is seen for both the 8 and 16 ply cases.
- iii. Overall, the dent diameter to dent depth ratio in the 16 ply case is larger than in the 8 ply case for both the 25.4 mm and 76.2 mm diameter indenter. Compared to the 8 ply case, the dent depths for the 16 ply case at BVID are smaller while the dent diameters are larger. This results in a larger dent diameter to dent depth ratio for the 16 ply case as compared to the 8 ply case. Therefore, the qualitative definition of BVID for the thicker face sheet differs from the qualitative definition of BVID for the thinner face sheet. For the thicker face sheet, BVID implies a larger dent area and a smaller dent depth than for a thinner face sheet. Because of a larger dent area, a larger crushed core zone is also expected for the thicker face sheet as compared to the thinner face sheet at BVID. Also, as the results presented in Tables 6.1 and 6.2 show, the planar area of delamination is larger for the thicker face sheet as compared to the thinner face sheet at BVID.
- iv. The dent diameter to dent depth ratio shows a significant dependence on the indenter diameter in the 16 ply case at the BVID load level where the ratios for the 25.4 mm diameter indenter are higher than the 76.2 mm diameter indenter. The effect of indenter diameter on the dent diameter to dent depth ratios could not be clearly established for the 8 ply case.
- v. For the 8 ply case, specimens with the C3 core showed significantly low dent diameter to dent depth ratios compared to the other core types. No such clear difference could be seen in 16 ply case.

- vi. The ratio of planar area of delamination to dent area is always less than 1 for both the 8 and 16 ply cases.
- vii. For the 16 ply case, the ratio of planar area of delamination to dent area is larger for the specimens indented with the 76.2 mm diameter indenter compared to the specimens indented with the 25.4 mm diameter indenter. No such comparison could be made for the 8 ply case because, as discussed in Chapter 5, the planar area of delamination data for the specimens indented with the 76.2 mm diameter indenter was unavailable for the 8 ply case.

6.4 Summary

In order to assess the damage resistance of the different sandwich geometries used in the test matrix, the damage metrics of dent depth, dent area and planar area of delamination were evaluated for both the 8 and 16 ply specimens. All these damage metrics were determined ultrasonically. If dent depth or dent diameter is chosen as the damage metric, then increasing the core density significantly increases the damage resistance in both the 8 and 16 ply cases. The effect of core density on dent depth and dent diameter however is slightly less in the 16 ply case than in the 8 ply case. If planar area of delamination is considered as the damage metric, then different trends are seen for the 8 and 16 ply cases. For the damage metric of planar area of delamination, the lower density core, C1, and face sheet with small ply angle change, Q1, provides the best damage resistance in the 8 ply case, i.e., the least amount of planar area of delamination for a given indentation event. However for the 16 ply case, the low density core, C1, and face sheet with small ply angle change, Q1, provides the worst damage resistance.

Chapter 7

EXPERIMENTAL DETERMINATION OF MODEL PARAMETERS

Introduction

This chapter presents the face sheet and core properties that are used in the analytical model and the methods used for their determination. Composite properties generally vary from batch to batch and with manufacturing methods. Despite many of these properties being available in a published form from the manufacturer, it was imperative that these be determined again since the experimental conditions that were used for the determination of the published properties were different from the local application of the face sheet and the core in this research. Determination of the properties in-house enabled more accurate values of these properties to be used in the model. Unless otherwise stated, all the experimental determination of the face sheet and core properties was done by fellow researchers from Cornell University who collaborated with us in this research.

7.1 Experimental Determination of Face Sheet Properties

The IM7/8552 lamina properties available from the manufacturer⁸⁵ were obtained using monolithic laminates containing lamina fiber that are generally straight. However in the case of the sandwich composites, in particular due to the autoclave technique used in the cure of the sandwich composites, face sheet plies especially near the adhesive bond line show a certain amount of waviness. This is a result of the face sheet being pressed into the core during autoclaving. Figure 5.3 in Chapter 5 presents a photomicrograph of a sectioned 16 ply sandwich specimen that clearly shows the face sheet waviness at the adhesive bond line. The co-cured face sheets with wavy plies are generally less stiff both in compression and bending as compared to

monolithic laminates. Therefore, slight adjustments to the published face sheet properties were needed.

In order to adjust the IM7/8552 published properties, the in-plane compliance, α_{11} , and the flexural compliances, δ_{11} and δ_{12} , for the 8 ply Q1 face sheet layup were first determined experimentally. The experimentally evaluated compliance values were then compared to the compliances predicted by the classical laminate plate theory (CLPT)⁸⁹ using the published lamina properties, and then the lamina properties were adjusted to improve correlation. This is described in what follows.

The CLPT relates the applied loads, N , and the applied moments, M , that act on a laminate to the midplane strains, ε^o , and curvatures, κ , by

$$\begin{bmatrix} N \\ M \end{bmatrix} = \begin{bmatrix} A & B \\ B & D \end{bmatrix} \begin{bmatrix} \varepsilon^o \\ \kappa \end{bmatrix} \quad (7.1)$$

Here, A is the extensional stiffness matrix, B is the coupling stiffness matrix and D is the bending stiffness matrix. Conversely, the laminate midplane strains and curvatures can be determined as a function of applied loads and moments using the compliance matrix, $\begin{bmatrix} \alpha & \beta \\ \beta^T & \delta \end{bmatrix}$ as

$$\begin{bmatrix} \varepsilon^o \\ \kappa \end{bmatrix} = \begin{bmatrix} \alpha & \beta \\ \beta^T & \delta \end{bmatrix} \begin{bmatrix} N \\ M \end{bmatrix} \quad (7.2)$$

Here, α is the in-plane compliance matrix, β is the coupling compliance matrix and δ is the flexural compliance matrix. The stiffness matrix and the compliance matrix can therefore be related as

$$\begin{bmatrix} \alpha & \beta \\ \beta^T & \delta \end{bmatrix} = \begin{bmatrix} A & B \\ B & D \end{bmatrix}^{-1} \quad (7.3)$$

With this background of the CLPT, edgewise compression (EC) tests⁸⁶ were performed on sandwich specimens to determine the in-plane compliance, α_{11} . A figure showing the edgewise compression test set-up is presented in Appendix D. Four alignment gauges were used for strain measurements in the 1 direction, i.e., the direction corresponding to the fiber direction of the 0° ply in the face sheet laminate. The in-plane compliance was then determined based on the inverse slope of the applied edge load per specimen width, N_1 , and the average strain data from the four alignment gauges that were used for the strain measurements.

The flexural compliances, δ_{11} and δ_{12} , were determined using a four point bend test on the 8 ply face sheet laminate. The outer span of the four-point bend fixture was 107 mm and the inner span was 51 mm. The support and the loading roller diameters were 10 mm. A figure showing the four point bend test set-up is presented in Appendix E. The face sheet laminates for the flexural tests were obtained by creating a debond in some of the sandwich panels using a Teflon insert. Before undergoing flexural tests, the face sheets were completely removed from the core and the specimens were trimmed with a water jet cutter to a length of 130 mm and a width of 26 mm and instrumented with a CEA-06-125-UT-350, 350 Ω , Vishay Micromasurement 0°/90° strain gauges at the face sheet midspan. The strain gauges were placed on both the top and the bottom surfaces of the face sheet used in the four point bend test. Because of the relatively small forces needed to apply sufficient bending moments, load was incrementally applied using dead-weights in increments of 3N, 5N, 8N and 13N. The applied load was converted to the edge bending moment per unit width, M_1 . The average magnitude of the 0° strain measurement, ϵ_0 , and the average magnitude of the 90° strain measurement, ϵ_{90} , were obtained as the average of the magnitude of the strain gauge readings from the top and the

bottom face sheet surfaces. The face sheet thickness, h_f , and the average strain measurements were used to determine the middle surface curvatures κ_{11} and κ_{22} as follows:

$$\kappa_{11} = \frac{2\varepsilon_0}{h_f} \quad (7.4)$$

and

$$\kappa_{22} = \frac{2\varepsilon_{90}}{h_f} \quad (7.5)$$

The inverse slopes of M_1 with κ_{11} and M_1 with κ_{22} were then used to determine δ_{11} and δ_{12} respectively.

As stated earlier in this section, the measured compliance values were compared to those determined by CLPT using the published lamina properties. The results of both the experimentally determined and the published compliance values are presented in Table 7.1. The percentages presented with the values represent the percentage difference between the experimentally measured compliance values and those calculated using the published lamina properties. For α_{11} and δ_{11} , a significant difference was seen between the experimentally measured compliance values and the compliance values computed by CLPT using the published values. This implied that the published values would have resulted in higher in-plane and flexural stiffnesses for the face sheet laminate. To correct the difference between the experimental and the published values, the published lamina properties were adjusted such that the compliance values calculated by CLPT using these adjusted properties, in particular for the critical compliances of α_{11} and δ_{11} , were within 6% of the experimentally determined

compliance values. These newly computed compliance values based on the adjusted lamina properties are also presented in Table 7.1. Table 7.2 presents the original published lamina properties as well as the adjusted lamina properties of the in-plane modulus, E , and the Poisson's ratio, ν . The subscript 1 in the presented properties refer to the fiber direction of the lamina, the subscript 2 refers to the direction 90° to the fiber direction of the lamina and the subscript 3 refers to the through-the-thickness direction of the lamina. In the analytical model, the adjusted lamina properties presented in Table 7.2 were used.

Table 7.1. The in-plane and flexural compliance values for the 8 ply Q1 face sheet layup.

Method of Property Determination	α_{11} (m/N)	δ_{11} (1/Nm)	δ_{12} (1/Nm)
experimentally determined	1.719E-8	0.224	-0.112
determined using CLPT/published data	1.566E-8 (-8.9%)	0.183 (-18.3%)	-0.112 (0%)
determined using CLPT/adjusted data	1.780E-8 (3.5%)	0.211 (-5.8%)	-0.133 (18.8%)

Table 7.2 Published and adjusted IM7/8552 lamina properties.

Property	Published Value*	Adjusted Value
ply thickness, t (mm)	0.127	0.127
E_{11} (GPa)	164.0	143.0
E_{22} (GPa)	12.0	12.9 GPa
E_{33} (GPa)	12.0	12.9 GPa
ν_{12}	0.32	0.32

*The published values are as retrieved from the manufacturers manual [85].

O'Brien et al. [87] performed end-notched flexure tests to determine the mode II interlaminar fracture toughness, G_{IIc} , of IM7/8552 carbon/epoxy specimens. The G_{IIc} values for IM7/8552 were needed to analytically predict delamination onset loads for the sandwich specimens. Two different manufacturers supplied five specimens each that were tested to obtain both the “non-precracked” and “precracked” values of G_{IIc} . Here, “non-precracked” refers to the toughness as obtained from a 13 μ m thick preimplanted Teflon insert, and “precracked” refers to the toughness as obtained from a mode II precrack. The mean results from all the specimens were a non-precracked toughness of 1233 J/m² and a precracked toughness of 772 J/m². In cases where matrix cracks within the laminate are sufficient in quantity and size that they can act as delamination onset points, the precracked value is likely more appropriate to be used for delamination onset predictions. For laminates where matrix cracking does not occur prior to delamination onset, the non-precracked value is more appropriate.

7.2 Experimental Determination of Honeycomb Core properties

To support the analytical QSI model, the responses of the different cores were modeled using the honeycomb core foundation model proposed by Minakuchi et al. [65]. The model proposed by Minakuchi et al. [65] is an idealized version of the observed stress versus strain cycle of aluminium honeycomb core. The assumed stress versus strain cycle for the idealized core behaviour is shown schematically in Figure 7.1. Here, the core is first subjected to elastic compression from A to B, which is controlled by the transverse compressive modulus E_{zc} . Point B represents the compressive crush strength, p_{cr} , where the core crushes. Following crushing, the stress drops to the compressive yield strength p_{oc} , which is represented by point C in the schematic. Under further compressive stress, the core undergoes perfectly plastic behaviour as long as the load is continued to be applied. The point where the loading stops is marked by D in

the schematic. Here, the load is removed and tensile stress is placed on the core by the face sheet. The core initially reacts linearly elastically with transverse tensile modulus E_{zt} up to point E which is the core tensile yield strength, p_{ot} . Upon further unloading, plastic stretching occurs. The five parameters (E_{zc} , E_{zt} , p_{cr} , p_{oc} and p_{ot}) that describe this cycle are obtained experimentally for use in the analytical model.

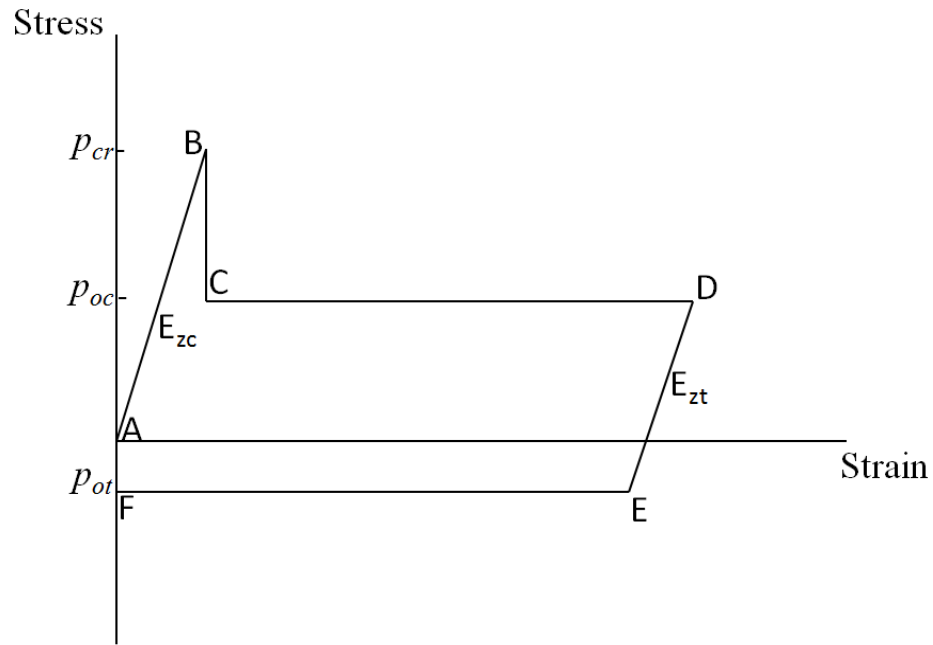


Figure 7.1. Schematic showing honeycomb core stress-strain idealized behavior proposed by Minakuchi et al. [65] for loading-unloading of the core in the transverse direction.

Flat-wise compression experiments similar to those described by Minakuchi et al. [65] were performed to obtain the above mentioned parameters for each of the three core types. Appendix F presents a figure representing the flat-wise compression test set-up. The test specimens consisted of 50.8 mm x 50.8 mm square honeycomb core bonded to aluminum loading blocks using the AF-555 film adhesive. The specimen deformation was measured

between the two loading blocks was performed using the MTS LX-500, non-contact laser extensometer. In order to characterize the core in terms of the parameters defined in the model, the load cycle applied to the core needed to be consistent with the model. Prior to the compression test, the core was loaded in tension to obtain the tensile modulus. The tensile test was performed well within the elastic range. The load was then reversed to compression until a predetermined strain level was reached. For these experiments, 5% and 15% strain levels were used. The latter reflected the approximate maximum strain during the QSI tests, and the former was chosen to evaluate whether the parameters that were extracted from the tests were strain dependent. Once the peak strain was reached, the load was reversed to tension and tensile loading was applied until the core failed. One test to each maximum strain level was performed for the C1 and C2 cores, and two tests to each strain level were performed for the C3 core.

The flat-wise core compression experimental results are presented in Figures 7.2 – 7.4. The figures indicate the values of p_{cr} , p_{oc} and p_{ot} that were extracted. The compressive crush strength, p_{cr} , was computed as the average from all tests of a given core type. The 5% strain level tests did not give sufficient information to extract the compressive and tensile yield strengths p_{oc} and p_{ot} , so these were obtained only from the tests to 15% strain. Figures 7.5-7.7 separately present the elastic compression and tension results for all the three core types for the determination of E_{zc} and E_{zt} . The individual results for all the core samples that were tested in both the compression and tension tests were combined and plotted together as single data sets. Compared to the idealized behavior presented in Figure 7.1, the plots show that the elastic stress-strain behavior for both the compression and the tension tests were not perfectly linear. Therefore, a simple linear best fit was used to approximate the values of E_{zc} and E_{zt} from the stress-strain data. The slope of the line of best fit was rounded off to a single decimal place and

the resulting values were used as the core compressive and tensile modulus in the analytical model. Table 7.3 presents a summary of all the core properties that were obtained experimentally.

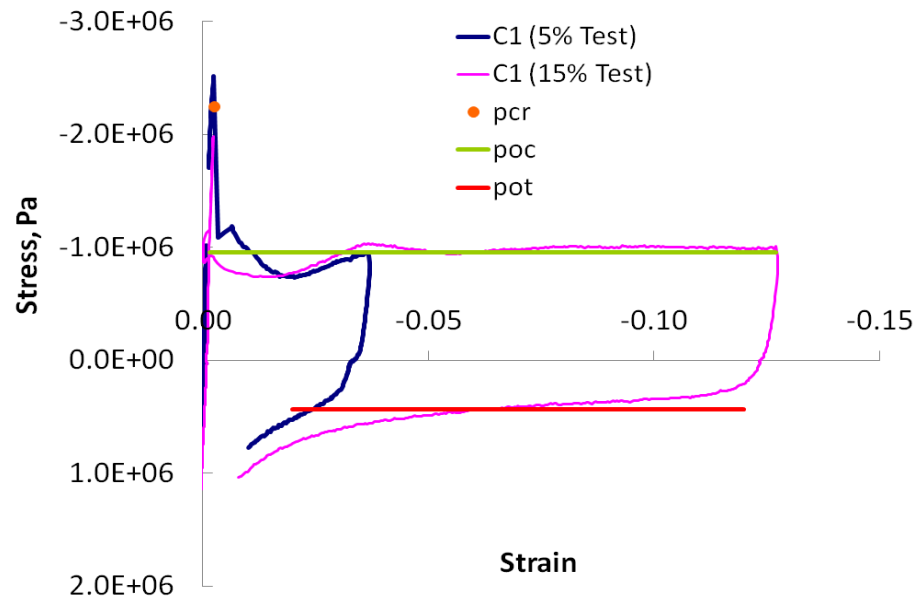


Figure 7.2. Stress-strain behavior of C1 core for transverse compressive-tensile loading.

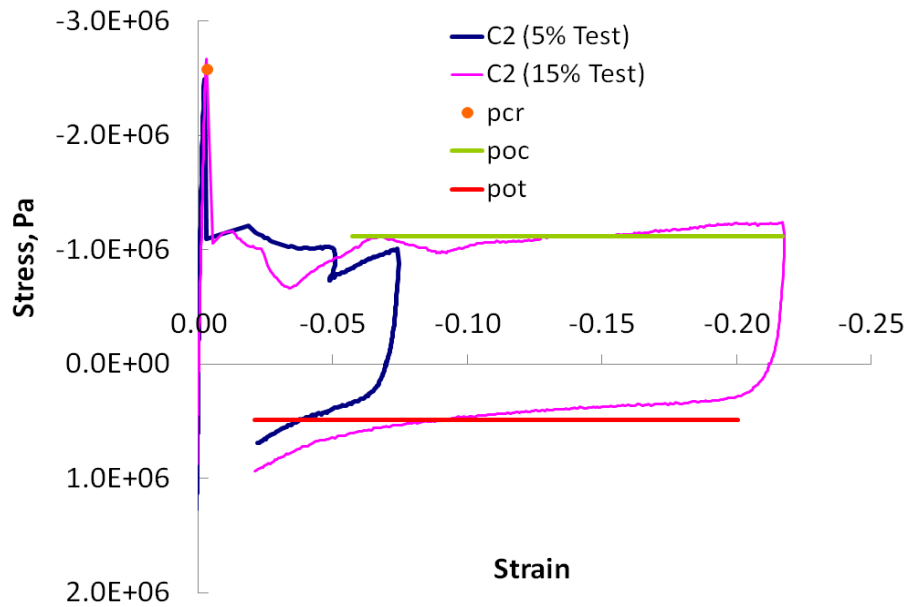


Figure 7.3. Stress-strain behavior of C2 core for transverse compressive-tensile loading.

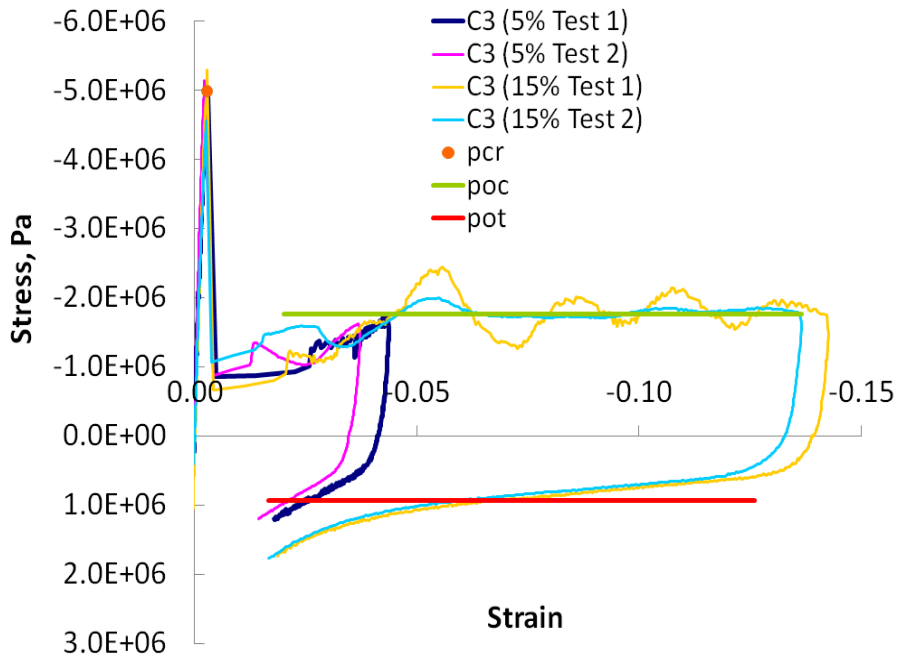


Figure 7.4. Stress-strain behavior of C3 core for transverse compressive-tensile loading.

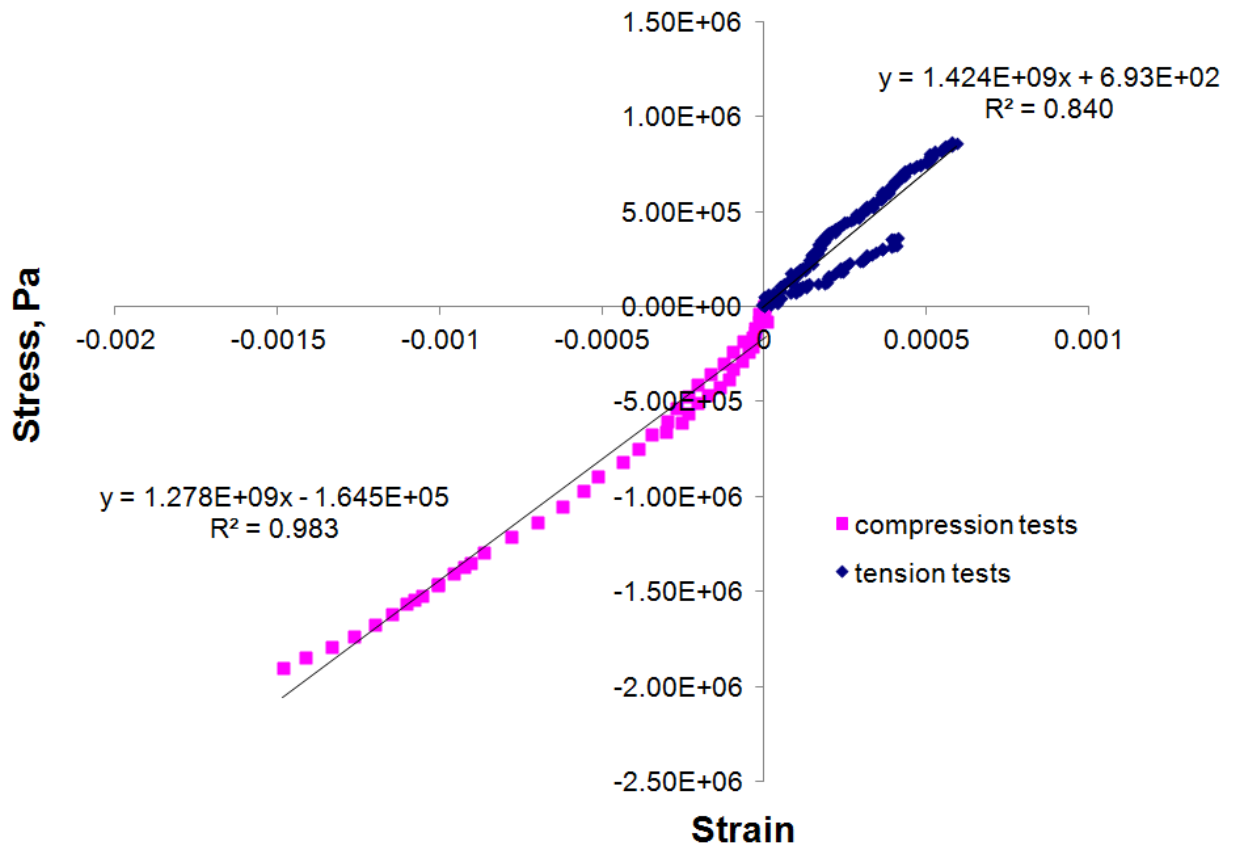


Figure 7.5. C1 core experimental stress vs. strain data for the compression and tensile tests for the determination of E_{zc} and E_{zt} respectively.

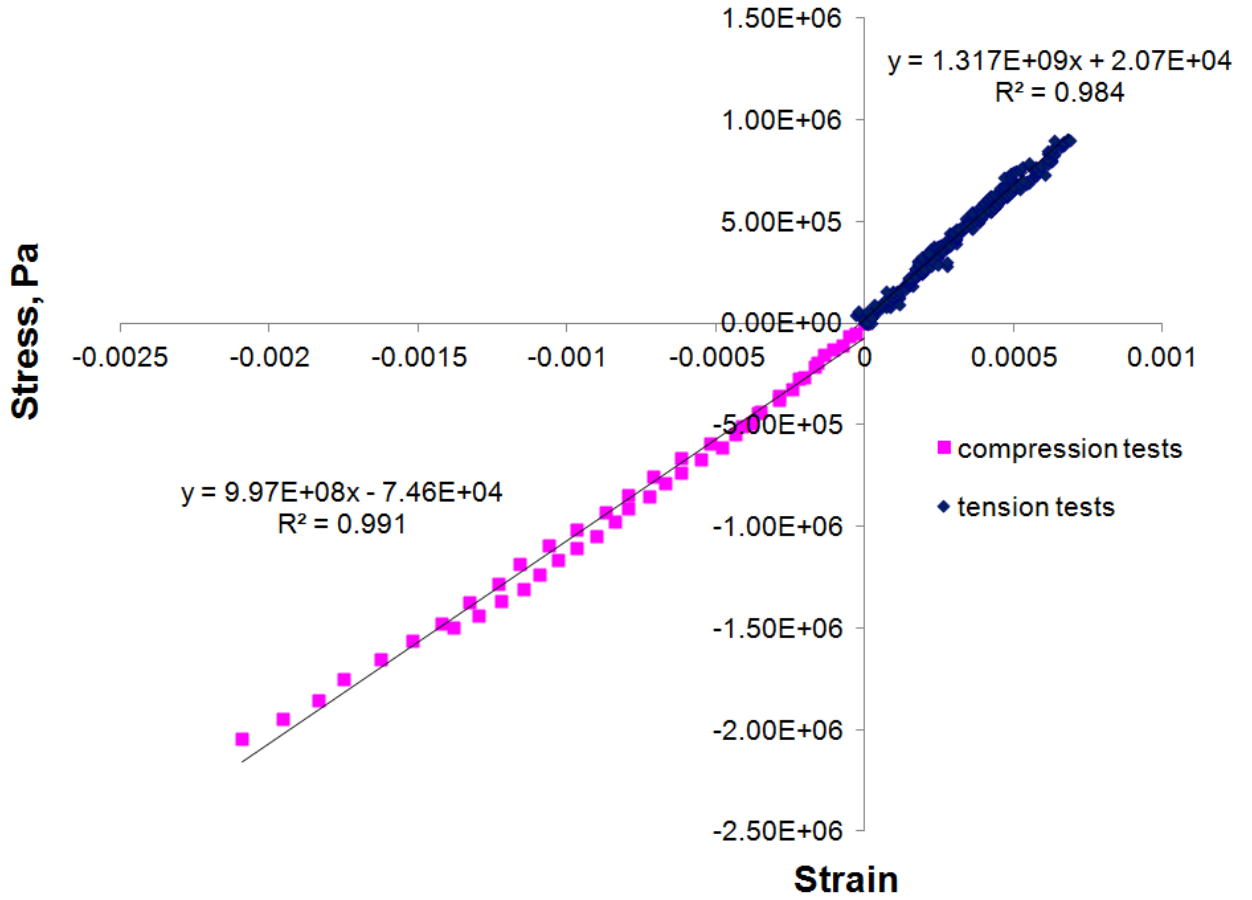


Figure 7.6. C2 core experimental stress vs. strain data for the compression and tensile tests for the determination of E_{zc} and E_{zt} respectively.

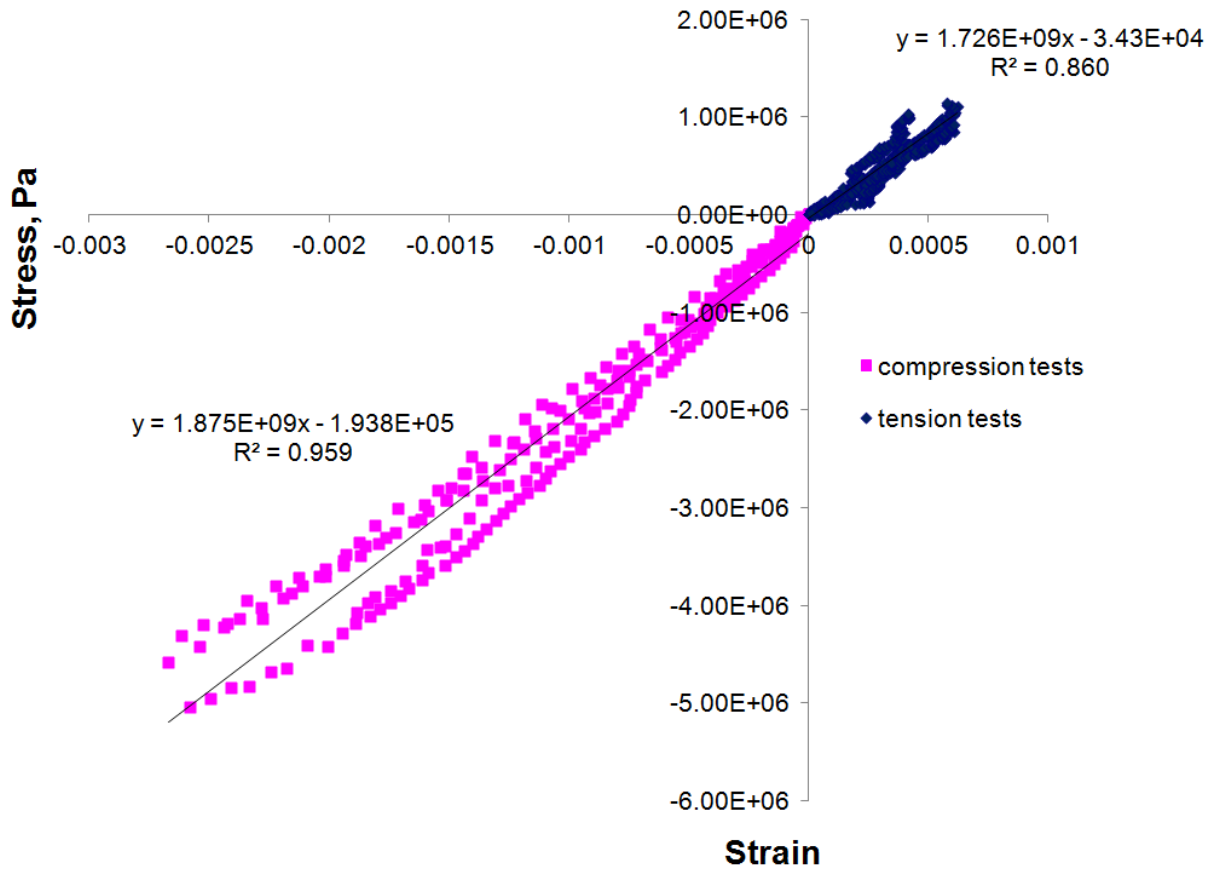


Figure 7.7. C3 core experimental stress vs. strain data for the compression and tensile tests for the determination of E_{zc} and E_{zt} respectively.

Table 7.3. Summary of honeycomb core properties.

Property	C1 Core	C2 Core	C3 Core
Density, kg/m ³	49.7	49.7	72.1
Thickness, mm	25.4	16.5	25.4
E_{zc} , GPa	1.3	1.0	1.9
E_{zt} , GPa	1.4	1.3	1.7
p_{cr} , MPa	2.2	2.6	5.0
p_{oc} , MPa	0.96	1.1	1.8
p_{ot} , MPa	0.44	0.49	0.94

Chapter 8

EXPERIMENTAL MASTER PLOTS

Introduction

The analytical model presented in Chapter 9 primarily compares the load vs. displacement (P-d) experimental data with model predictions for the different sandwich configurations tested under the different load and indenter diameter conditions. However, considering the large number of test replicates, it would be difficult to do this on a specimen-by-specimen basis. In addition to the large number of plots required, it would be difficult to synthesize the results and obtain conclusions that account for specimen-to-specimen variations and potential load level effects for specimens from the same sandwich configuration tested to approximately the same maximum load and with the same indenter diameter. To address this, “master plots” were developed. The master plots are defined as an average plot for a specific sandwich configuration, peak load level and indenter diameter. This allowed for the combination of test data from specimens that were tested to approximately the same maximum load without any essential alterations to the data. For those specimens that could not be combined into a single master plot because of significant peak load differences, the comparisons were made to the model on a specimen-by-specimen basis.

In this chapter, the method of obtaining the experimental master plots is described. Only selected master plots are presented in this chapter to help take the discussion forward. The individual master plots for all the sandwich configurations tested to BVID are presented in Chapter 10 together with the analytical modeling results.

8.1 Experimental Master Plots

The master plots were created using the specimens from a particular sandwich configuration that were tested to the same load level using the same indenter diameter. This was done to help synthesize results better and obtain conclusions that accounted for specimen-to-specimen variation. The following steps were followed in the creation of the master plots:

1. Data sets from the same sandwich configuration indented with the same indenter diameter were identified and grouped together.
2. In each of the groups, specimens with similar peak loads were identified. Peak loads between specimens were considered similar if they were within 15N of each other for the 8 ply case and within 26 N of each other for the 16 ply case. These variations in load levels were inevitable and happened during testing when the test was stopped at the target peak load in order to make the switch from the loading to the unloading mode.
3. Because of a lot of noise in the data, an algorithm was first applied to smooth the individual specimen data.
4. Each of the individual specimen data from a particular group were interpolated with Piecewise Cubic Hermite Interpolating Polynomial through an algorithm that was written for this purpose. Displacement values at “common load levels”, i.e., the same load level for each specimen belonging to a particular group, were obtained.
5. The displacements obtained for the different specimens belonging to a particular group through the interpolation described in step 4 were then averaged. This resulted in a single average displacement for each common load level. These resulting load and displacement values were then used to develop the master plots.

The average displacement values for the specimens belonging to a particular group, obtained as described in step 5, however did not account for the “machine error” in the load train of the test set up. Upon comparing the final displacements obtained from the machine data with the residual dent depths obtained ultrasonically, it was seen that the dent depth given by the load versus displacement machine data was slightly larger than that determined ultrasonically. Figure 8.1 presents the ultrasonic dent depth measurement data versus the MTS machine dent depth data for the various 8 ply specimens. Because no trends in the differences between the MTS machine data and the ultrasonic dent depth data could be found based on all the parametric variations, the results presented are not classified by sandwich geometry or test indenter size. As can be seen in the figure, the MTS data was always a little larger than the values obtained ultrasonically. Therefore, there was a need to correct for this difference in the master plots. Machine error was implemented in the master plot by assuming a linear increase from the zero load to the “maximum machine error” at peak load, where maximum machine error is defined as the difference between the MTS obtained residual dent depth and the ultrasonically determined residual dent depth. For the unloading portion, the maximum machine error value was used as a constant to correct the master plot.

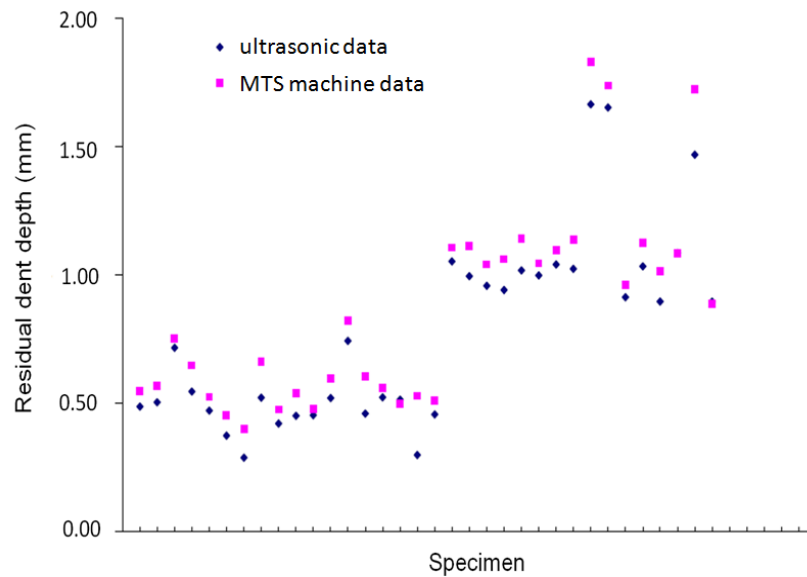


Figure 8.1. Plot of dent depths for the different 8 ply specimens using both the MTS machine data and the ultrasonic measurements.

Figures 8.2-8.5 show the experimental P-d plots as well as the master plots for the 8 and 16 ply Q1-C1 sandwich configuration tested with both the indenter sizes. The master plots with and without machine error correction are presented. Overall, the master plots reflect the experimental data quite accurately and serve the purpose for which they were intended. As expected, accounting for the machine error results in a slightly lower displacement at a particular load. The plots that included the machine error correction were eventually used for comparison with the analytical model.

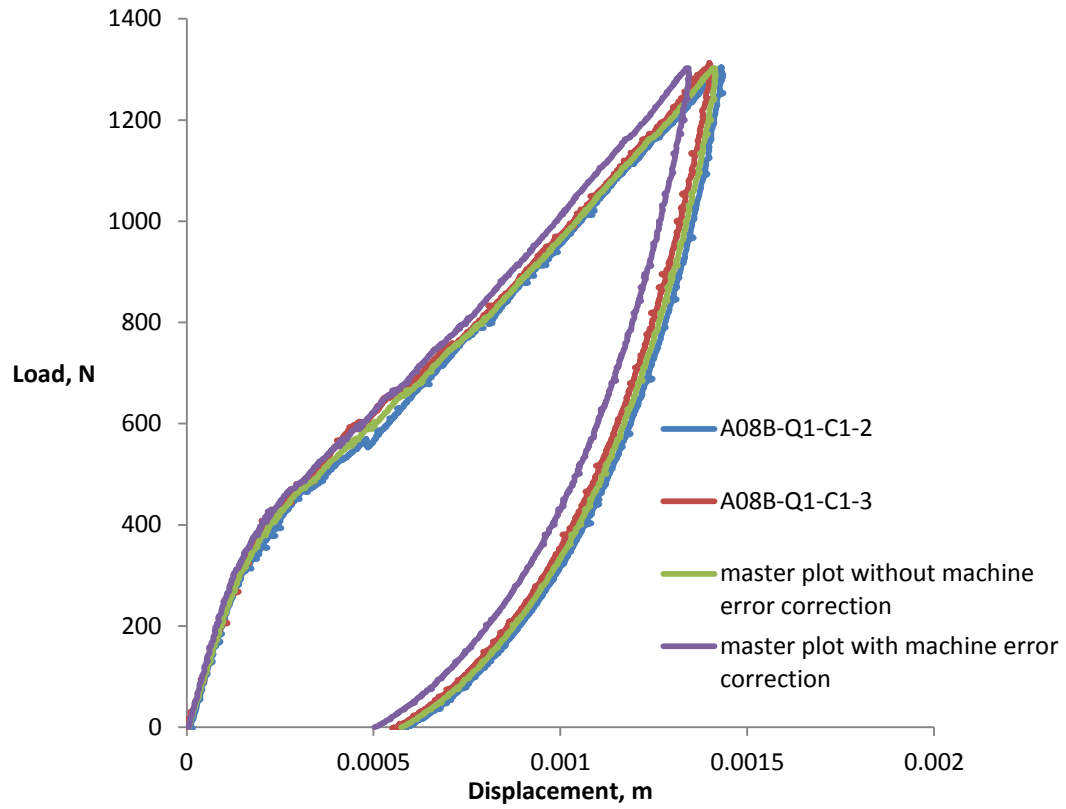


Figure 8.2. Comparison of master plot with individual specimen data for 8 ply Q1-C1 specimens indented with the 25.4 mm diameter indenter.

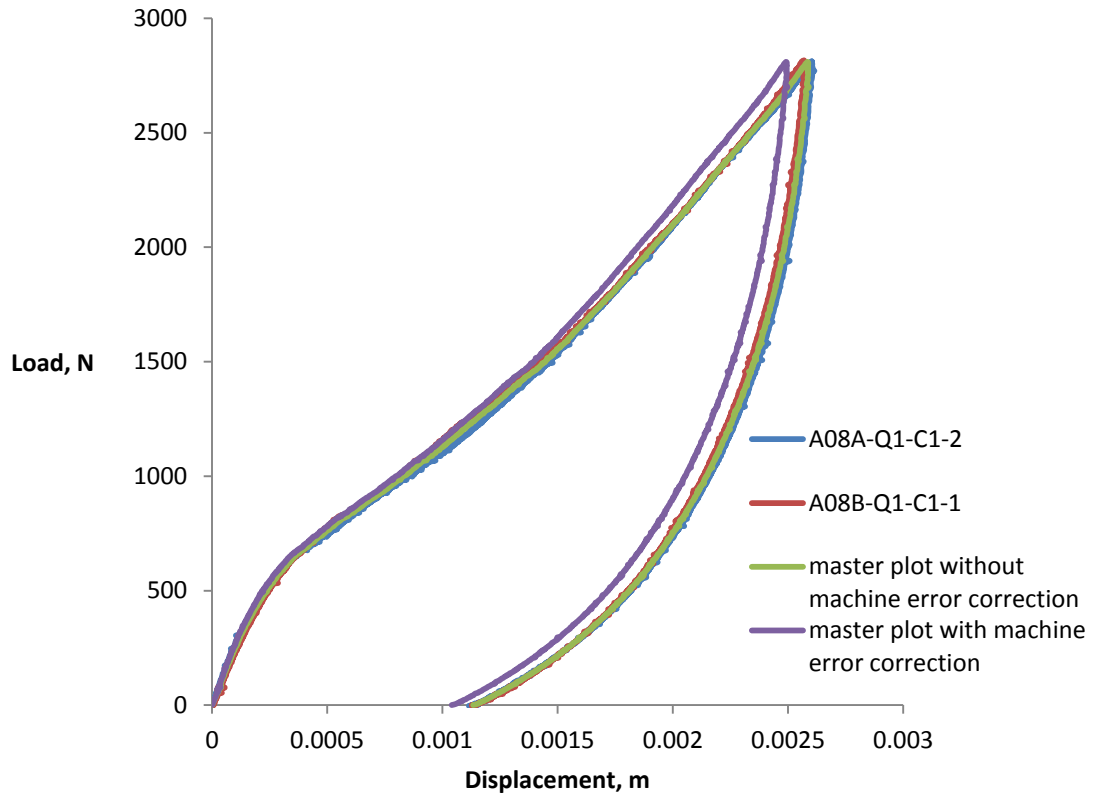


Figure 8.3. Comparison of master plot with individual specimen data for 8 ply Q1-C1 specimens indented with the 76.2 mm diameter indenter.

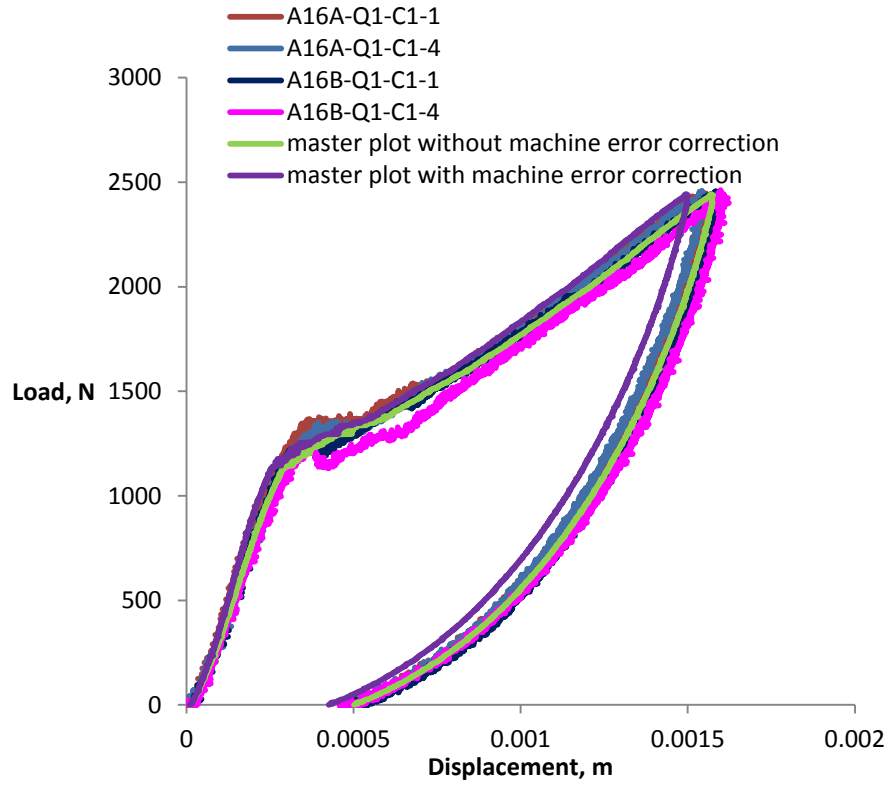


Figure 8.4. Comparison of master plot with individual specimen data for 16 ply Q1-C1 specimens indented with the 25.4 mm diameter indenter.

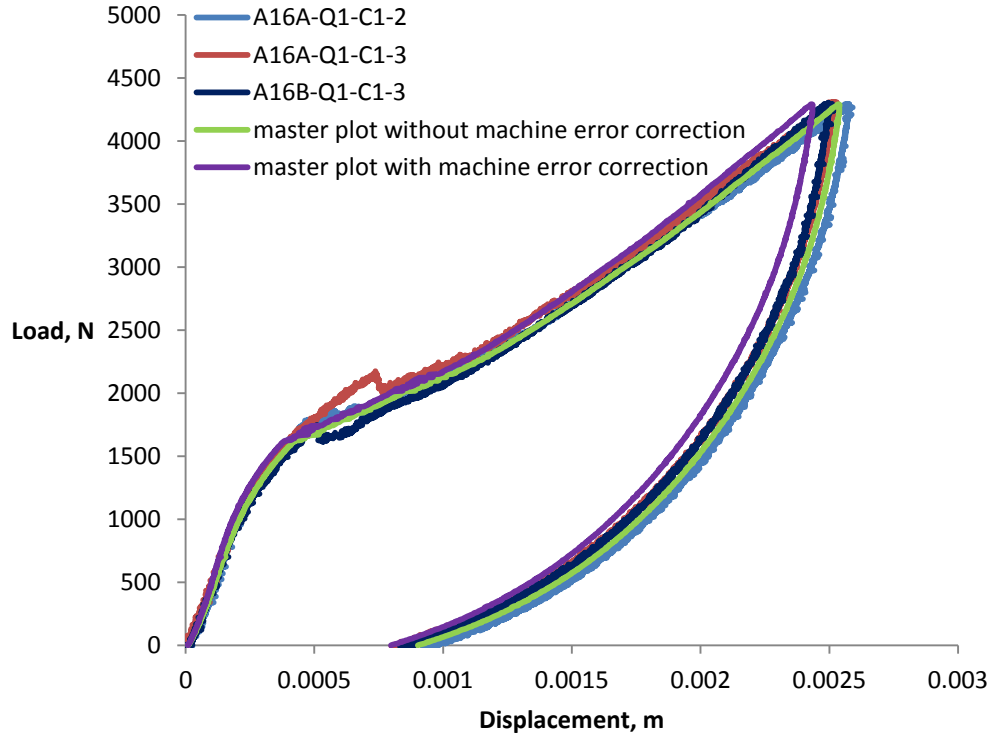


Figure 8.5. Comparison of master plot with individual specimen data for 16 ply Q1-C1 specimens indented with the 76.2 mm diameter indenter.

Tables 8.1-8.4 present a summary of the data available for different test conditions as well as the number of “master plots” that were created. In some sandwich configurations where certain specimens could not be combined into a master plot because of significant load differences, these specimens are listed separately in these tables under the column heading “no. of stand-alone specimens”. For these specimens, the comparison with the model was based on a specimen-by-specimen basis. A summary of the reduced number of P-d plots for model comparisons due to the development of the master plots is presented in Table 8.5. From a total of 82 individual plots, final model comparisons were done using a total of 43 plots.

Table 8.1. Comparison of the number of experimental specimen data available to the number of resulting master plots for the 8 ply specimens indented with the 25.4 mm diameter indenter.

8 Ply 25.4 mm diameter indenter			
sandwich configuration	no. of experimental plots	no. of master plots	no. of stand-alone specimens
Q1-C1	3	1	1
Q1-C2	3	1	-
Q1-C3	3	-	3
Q2-C1	5	1	2
Q3-C1	1	-	1
Q4-C2	2	1	-
Q4-C3	2	-	2
Total	19	4	9

Table 8.2. Comparison of the number of experimental specimen data available to the number of resulting master plots for the 8 ply specimens indented with the 76.2 mm diameter indenter.

8 Ply 76.2 mm diameter indenter			
sandwich configuration	no. of experimental plots	no. of master plots	no. of stand-alone specimens
Q1-C1	2	1	-
Q1-C2	3	1	1
Q1-C3	3	1	1
Q2-C1	6	2*	1
Q3-C1	2	-	2
Q4-C2	1	-	1
Q4-C3	1	-	1
Total	18	5	7

*Two different sets of load levels exist in this sandwich configuration with a number of specimens within each set at similar load. That is why this set has two master plots.

Table 8.3. Comparison of the number of experimental specimen data available to the number of resulting master plots for the 16 ply specimens indented with the 25.4 mm diameter indenter.

16 Ply 25.4 mm diameter indenter			
sandwich configuration	no. of experimental plots	no. of master plots	no. of stand-alone specimens
Q1-C1	4	1	-
Q1-C2	4	1	-
Q1-C3	4	1	-
Q2-C1	4	1	-
Q3-C1	2	-	2
Q4-C1	2	-	2
Q4-C3	2	1	-
Q5-C1	2	1	-
Total	24	6	4

Table 8.4. Comparison of the number of experimental specimen data available to the number of resulting master plots for the 16 ply specimens indented with the 76.2 mm diameter indenter.

16 Ply 76.2 mm diameter indenter			
sandwich configuration	no. of experimental plots	no. of master plots	no. of stand-alone specimens
Q1-C1	4	1	1
Q1-C2	4	1	-
Q1-C3	4	1	-
Q2-C1	4	1	-
Q3-C1	1	-	1
Q4-C1	-	-	-
Q4-C3	2	1	-
Q5-C1	2	1	-
Total	21	6	2

Table 8.5. Summary of the original number of experimental P-d plots versus the reduced number of plots due to the development of the master plots.

test condition	no. of P-d Plots available experimentally	reduced no. of P-d plots for model comparisons
8 Ply 25.4 mm indenter diameter	19	13
8 Ply 76.2 mm indenter diameter	18	12
16 Ply 25.4 mm indenter diameter	24	10
16 Ply 76.2 mm indenter diameter	21	8
Total	82	43

Chapter 9

MODEL FORMULATION

Introduction

As described in Chapter 2, a variety of models have been developed and proposed in the literature for modeling the impact or indentation response of sandwich structures. These models can broadly be classified as finite element models or analytical models. The finite element models typically are capable of higher accuracy and can include more physical details. However, more complexity is involved in their development as compared to analytical models. Some of the popular analytical models include the spring-mass models, the energy based models and the direct plate theory models. Another advantage of analytical models is that it is relatively quicker to study the effects of parametric variations in analytical models as compared to a finite element models.

This chapter presents an analytical model that predicts the quasi-static indentation (QSI) response of graphite/epoxy-aluminum honeycomb core sandwich panels during loading up to BVID, followed by unloading. Two of the key parameters that are predicted by the model are the residual dent depths and the dent diameters. As part of the model's derivation, comparisons of the model predictions with the experimental Q1-C1 results for the 8 and 16 ply cases are presented to help take the discussion forward. Comparisons of predicted and experimental results for all the sandwich configurations for damage up to BVID are presented and further discussed in Chapter 10.

9.1 Existing Models

The popular existing modeling techniques that have been published in the literature can be broadly classified as finite element models or analytical models. A detailed review of the different existing models has been presented in Chapter 2.

Finite element models are generally capable of higher accuracy and a wider applicability. However, their development is more complex as compared to analytical models. Also, it is easier to change different parameters in analytical models in order to study the various parametric effects as compared to finite element models since in the latter, this process is generally more time consuming. Because of these few disadvantages, the finite element modeling technique was not pursued in this dissertation.

The prominent analytical models can be classified into the spring-mass models, the energy balance models or the direct plate theory models. A spring-mass model is more suitable in the case of elastic material behavior. However, highly non-linear behavior like that due to the damaged core and face sheet is difficult to implement correctly in a spring-mass model. The popular direct plate theory model that exists in literature is the one proposed by Olsson [61]. The model is primarily built upon the principles of small and large deflection thin plate theories. This model with the issues associated with it is further discussed in Section 9.2. While certain ideas from Olsson's plate theory model have been retained in the model derived in this dissertation, there are other major issues with the model in the post core crushing regime that disqualified it from being adopted in its original form. In comparison, the energy based models are somewhat simpler to develop, and accounting for the onset and progression of damage can be more readily implemented in an energy based model as compared to other analytical models. As discussed in Chapter 2, none of the existing energy based models could be adopted in their original form due

to them ignoring either aspects of face sheet bending, face sheet stretching, degradation of face sheet properties due to damage onset and progression, or the changing core response in the different regimes of the loading phase. However, the model proposed by Turk and Hoo Fatt [57] looked promising and certain ideas from their model has been adopted in this dissertation. Further details on their model are presented in Section 9.2. Because bending behavior could not be represented in the model proposed by Turk and Hoo Fatt [57] due to their chosen displacement field not suitable for solving bending deflections through potential energy minimization, the model could not be used in its original or any simplified form.

Only a handful of unloading models have been proposed in the literature and there certainly is a great need for more work in this area. This is because the unloading models are useful in predicting the residual dent depths, an important parameter in the post-impact strength studies. The model proposed by Olsson [63] is based on the assumption that the unloading behavior is linear. He neglects the strain energy due to membrane stresses in the unloading behavior. The model proposed by Zenkert et al. [64] hypothetically detaches the face sheet and the core during unloading. They then evaluate the residual dent by approximating the common displacement that is shared by the face sheet and the core during unloading, where the face sheet is allowed to unload elastically and the crushed core region is ‘pulled up’, assuming elastic behavior. Their approach is not very promising as the face sheet and core is not allowed to naturally deflect together in a combined fashion. They also assume elastic behavior in both the face sheet and the core during unloading which is not true in the physical problem.

The finite element method for modeling the sandwich response to indentation loading was ruled out to be pursued further in this dissertation for reasons cited earlier. Out of the analytical models reviewed, the spring-mass model was also ruled out because of its inability to

correctly model damaged face sheet and core behavior. The options that were left were the direct plate theory models or the energy based models. Different models were reviewed from these categories and out of these, the models proposed by Olsson [61] and Turk and Hoo Fatt [57] had certain aspects implemented in them that were seen as very promising. Therefore, these two models were preliminarily assessed in order to see how well they predict the experimental results. A discussion on the preliminary assessments of these models and the decisions that were made based on these assessments is presented in Section 9.2.

9.2 Preliminary Assessments

In order to define the overall approach for the modeling formulation, existing models that showed some promise first had to be assessed. Out of all the models that were reviewed, the details of which are presented in Chapter 2, the direct plate theory model proposed by Olsson [61] and the energy based model proposed by Turk and Hoo Fatt [57] appeared to be the most promising and these models were first assessed.

Olsson's direct plate theory model is primarily built upon the principles of small and large deflection thin plate theories. It considers a circular isotropic plate, and orthotropy is accounted for by using "equivalent face sheet properties". Upon comparison to the experimental load versus deflection results presented herein, Olsson's small deflection plate theory model worked well for very low loads, and the solution in its entirety worked better for the 25.4 mm indenter diameter than for the 76.2 mm indenter diameter. Figures 9.1 and 9.2 present a comparison of Olsson's small deflection plate theory model with the experimental Q1-C1 8 ply results. The comparison is good for the 25.4 mm diameter indenter (Figure 9.1). For the 76.2 mm indenter diameter (Figure 9.2), the predicted model response is too compliant. This is because Olsson assumed a point load form for his solution, and the effects of indenter diameter are only

reflected through a Hertzian contact solution. This brought about the need to implement the effect of indenter size in the model derived in this dissertation. Olsson's large deflection membrane model was not adopted because of certain inconsistent assumptions. Olsson considers the delaminated region as a pure membrane where the total applied load, F , gets divided into contributions due to the membrane forces, F_m , and the critical out-of-plane shear load, F_d . However in his formulation for the membrane deformation, only the membrane forces are included ,i.e., the out-of-plane shear load is ignored. Rather, the shear load is taken to the edges of the delaminated region where it is believed to propagate delaminations. This is incorrect as the entire applied load must be carried by the membrane, i.e., the membrane cannot carry a portion of the applied load, namely F_d , out to its edges. An earlier work by Olsson and McManus [90] that assumed the total applied load being carried by the membrane itself however resulted in deformations that were too large.

Turk and Hoo Fatt [57] proposed an energy based model where they included the membrane energy of the face sheet as well as the total work done by the external load and the core resistive pressure. The effect of indenter size is included in Turk and Hoo Fatt's model by treating the hemispherical indenter as an equivalent flat-nosed indenter with a radius that is 0.4 times the actual hemispherical indenter radius. The flat-nosed indenter assumption that Turk and Hoo Fatt use is a simple way to include the effects of indenter diameter in the model. Their choice of equivalent flat-nosed indenter radius was not based on any analysis but rather on the experimental results of Williamson and Lagace [5] where it was observed that the contact radius did not vary much in the indentation tests. The absence of a mechanistic way within their model to evaluate the equivalent flat-nosed indenter radius was one of the reasons why their model was not pursued. However, the idea of an equivalent flat-nosed indenter radius was retained and as

would be discussed later, it was implemented through the Hertzian indentation contact theory.⁹¹ Figures 9.1 and 9.2 present a comparison of Turk and Hoo Fatt's membrane energy solution with the experimental Q1-C1 8 ply results. Turk and Hoo Fatt's membrane energy solution worked better for the specimens indented with the 76.2 mm diameter indenter as compared to the 25.4 mm diameter indenter. This is likely because of the lesser face sheet damage in the 25.4 mm diameter indenter case which resulted in both the bending and membrane characteristics together influencing face sheet deformation. Another major reason why Turk and Hoo Fatt's model was not pursued was the exclusion of bending energy. Bending energy could not be included in their model since their assumed displacement field did not work for bending energy and resulted in a slope discontinuity at the indenter-face sheet contact periphery. Because their displacement function is inappropriate for bending, it could not be adopted for modeling in this dissertation as it would not work even if a bending energy term was added to the total system potential energy.

A combined approach that incorporated both the face sheet bending and stretching, the latter being incorporated by treating the face sheet as a membrane, was perceived to be the correct approach for modeling the sandwich response to indentation loading and subsequent unloading. This is backed both by the experimentally obtained peak deflection values relative to the face sheet thickness, as well as by the literature review. For relatively thin face sheets, although it is possible that membrane effects dominate, it is also possible that BVID occurs in the regime where the bending rigidity is important. For the thick face sheets, bending deformation likely predominates; however it is not clear that the membrane effects can be completely ignored. Including both bending and membrane effects in the model allows the mechanics of the problem to dictate the controlling parameters, rather than the preconceived assumptions.

Another important issue that needed to be considered in the model was the onset of delaminations. This is because the face sheet properties change with delamination onset, which in turn influences the deflections. Therefore, delamination onset needed to be appropriately implemented in the model. Olsson [61] proposes a delamination onset load prediction criteria based on the linear elastic fracture mechanics (LEFM). The change in deflection upon the onset of delamination is treated as a perturbation that results in a change in strain energy. The energy release rate therefore is compared to the mode II interlaminar fracture toughness, G_{IIc} , in order to predict the delamination onset load. The delamination onset load prediction results based on Olsson's formulation for the Q1-C1 8 ply specimens is also presented in Figures 9.1 and 9.2.

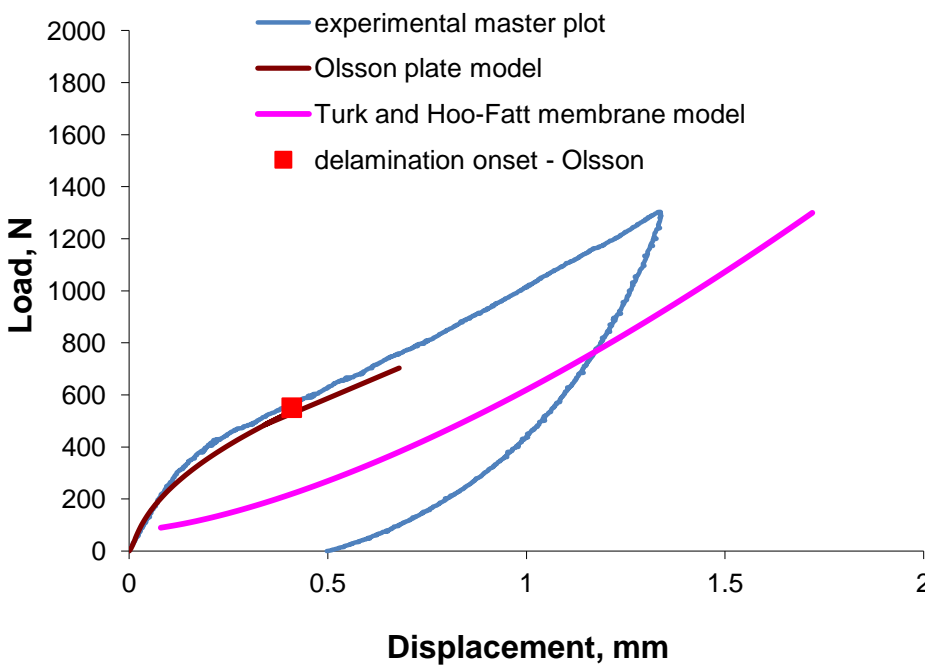


Figure 9.1. Comparison of experimental 8 ply Q1-C1, 25.4 mm indenter diameter test results with Olsson's and Turk and Hoo Fatt's models.

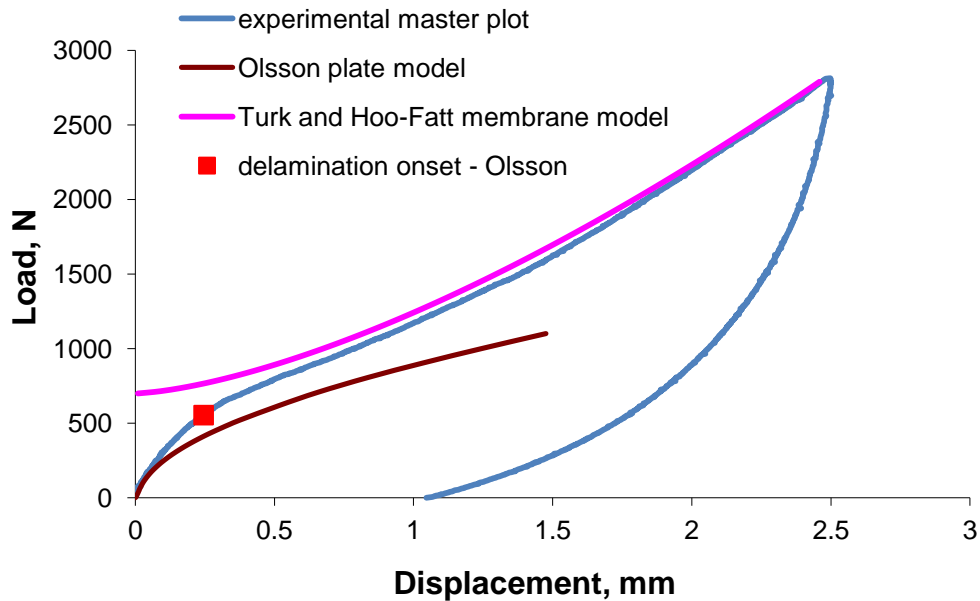


Figure 9.2. Comparison of experimental 8 ply Q1-C1, 76.2 mm indenter diameter test results with Olsson's and Turk and Hoo Fatt's models.

The major decisions that were made on the overall approach for modeling formulation were based on certain ideas adopted from both Olsson [61] and Turk and Hoo Fatt [57]. Olsson's idea of simplifying things to an equivalent circular isotropic plate with homogenized properties, and thereby using the isotropic equations, is a tremendous help in eliminating many of the complexities that would otherwise appear with regards to large deflections of an orthotropic or an anisotropic plate subjected to transverse loading. Turk and Hoo Fatt's energy based model's use of an equivalent flat-nosed indenter is a simple and effective way of including the effects of indenter size in the model provided a mechanics based approach be used for the determination of the equivalent flat-nosed indenter radius. This idea, coupled with a choice of an appropriate displacement field that works for both bending and membrane energy, provides a promising approach for the development of the analytical model for the sandwich response to indentation

loading and subsequent unloading. Based on the assessments presented in this section, major decisions that were made from the aspect of model development were

- i. utilization of an equivalent circular isotropic plate that considered homogenized properties both prior to and post delamination onset;
- ii. utilization of Olsson's method based on the direct plate theory for modeling the initial low load regime up to the onset of core crushing;
- iii. utilization of the thin plate theory that accounted for both face sheet bending and membrane effects;
- iv. utilization of the energy balance approach post the onset of core crushing;
- v. prediction of the onset of delamination in a manner analogous to the method proposed by Olsson.

The energy balance approach that was decided upon to model the post core crushing regime was based on the Rayleigh-Ritz method of energy minimization. This method is highly dependent on the choice of an appropriate displacement function since the strain energy constituents of the total potential energy are a function of the displacement field. Initial exploratory work on choosing an appropriate deflection function considered point loads and ring loads using displacement functions based on variations of the exact solutions presented by Timoshenko and Weinowsky-krieger [88]. These preliminary investigations indicated that point loads produced displacements that were too large in the vicinity of the center load. These results are also obvious from Olsson's plate theory model presented in Figure 9.2 for the large indenter where the load form physically is expected to be more distributed than pointed. However because of the point load form assumption by Olsson, the center deflections predicted by the

model become significantly larger with increasing load as compared to the experimental. This outcome brought about the need to account for the effect of indenter size in the displacement function. To this end, the ring load approach appeared promising. A ring load form has two displacement fields, one inside the ring and the other outside the ring. Connecting the two solutions results in complicated analysis and in this regard, the equivalent flat-nosed indenter approach proposed by Turk and Hoo Fatt [57] was considered analytically simpler for implementing the effects of indenter diameter. Therefore, the flat-nosed indenter assumption was eventually adopted for this dissertation. The equivalent flat-nosed indenter radius that was proposed by Turk and Hoo Fatt did not have a mechanics based approach for its determination. This brought about the need to independently define the flat-nosed indenter radius to be used in the model.

The preliminary assessments helped provide the overall starting guidelines for the modeling formulation. The challenges that continued to remain however were

- i. choice of an appropriate deflection function for use in the energy equations;
- ii. defining the equivalent plate properties in an appropriate manner, both prior and subsequent to delamination onset;
- iii. determining a mechanistic approach for the determination of the equivalent flat-nosed indenter radius post core crushing;
- iv. predicting the onset of delamination and correctly accounting for the change in plate properties once this has occurred;
- v. extending the model to predict the unloading behavior. As described in Chapter 2, this is an important subject that has received very little attention in the literature.

The procedure for the derivation of the analytical model are described from Section 9.3 onwards. The model is divided into four regimes. These regimes are the zero load to the core crush onset load regime, the core crush onset load to the delamination onset load regime, the delamination onset load to peak load regime and finally, the unloading regime.

9.3 Modeling Loading Regime 1: Zero Load to Core Crushing Onset Load

Olsson's direct plate theory model was used to model the initial low load elastic response of the sandwich structure up to the onset of core crushing. The indenter is modeled as a spherical indenter and the externally applied load is treated as a point load. The total maximum displacement of the indenter, w_{el} , is taken to equal the sum of the deformation due to local Hertzian indentation, w_h , and the classical small deflection plate response of the upper face sheet and core, w_o . The total maximum deflection of the indenter therefore is determined as

$$w_{el} = w_h + w_o \quad (9.1)$$

9.3.1 The Local Hertzian Indentation, w_h

The local Hertzian indentation⁹¹ of the indenter into the face sheet was considered in modeling the sandwich response up to the onset of core crushing. One of the difficulties in using the Hertzian contact theory was the identification of the "target body" or the elastic half space. This complication arose because in the sandwich composite, two different materials, which are the core and face sheet, are combined together as a single body. The choices at hand were either to treat the face sheet or the core alone as the target body, or to combine their transverse modulus in some fashion that represented an "equivalent" target body.

The transverse modulus of the face sheet laminate is about 10 times more than that of the core. In the initial loading phase at least up to the core crush onset load, the core is presumed to

compress elastically by the same amount as the bending deflection of the face sheet. The procedure for predicting the core crush onset load is described in Section 9.3.2. It was seen that if the face sheet alone was treated as the target body, the local Hertzian indentation up to the core crush load is always within 3% of the overall face sheet thickness for all the sandwich configurations considered. The bending deflection of the face sheet was also much smaller than the local Hertzian indentation of the face sheet. The significantly smaller Hertzian deformation relative to the face sheet thickness, the relatively low core crush load as well as the much higher transverse modulus of the face sheet compared to the core resulted in the decision to treat the face sheet alone as the target body in the regime prior to core crushing.

Therefore, the local Hertzian indentation, w_h , was calculated as

$$w_h = \left(\frac{3P}{4E^* \sqrt{R}} \right)^{\frac{2}{3}} \quad (9.2)$$

where P is the applied load, R is the indenter radius and E^* is the equivalent transverse modulus of the indenter (i) and face sheet (f) given as

$$\frac{1}{E^*} = \frac{1 - \nu_i^2}{E_i} + \frac{1 - \nu_f^2}{E_f} \quad (9.3)$$

In equation 9.3, ν represents the Poisson's ratio. The value of E_f is the E_{33} value presented in Table 7.2 while ν_f is the ν_{13} value of the face sheet laminate which is approximated to be zero in these calculations. The modulus, E_i , and the Poisson's ratio, ν_i , for the steel indenter were taken as 200 GPa and 0.3 respectively.

9.3.2 Bending Deflection of the Face Sheet, w_o

In the regime prior to core crushing, the bending deflection of the face sheet is also considered. The face sheet is modeled using small deflection plate theory for an infinite circular isotropic plate on an elastic foundation with a reactive pressure, σ_z , represented as

$$\sigma_z = w_o k_F \quad (9.4)$$

In equation 9.4, w_o represents the maximum bending deflection and k_F represents the core foundational stiffness. The core foundational stiffness, k_F , is defined as the core resistive pressure per unit displacement for linear elastic core behaviour which ignores any shear stiffening. The core foundational stiffness is calculated as [61]

$$k_F = \frac{E_{zc}}{h_c^*} \quad (9.5)$$

with

$$h_c^* = \left\{ \begin{array}{l} \frac{h_c}{1.38} \text{ for } h_c \leq h_{cmax} \\ 2h_{cmax} \text{ for } h_c > h_{cmax} \end{array} \right\} \quad (9.6)$$

and

$$h_{cmax} = h_f \frac{32}{27} \left(\frac{4 E_{33}}{3 E_{zc}} \right)^{\frac{1}{3}} \quad (9.7)$$

In the above, h_c is the core thickness, h_c^* is the effective core thickness, E_{zc} is the transverse compressive core modulus, E_{33} is the transverse face sheet modulus and h_f is the face sheet thickness. The values of E_{33} and E_{zc} are presented respectively in Tables 7.2 and 7.3 of

Chapter 7. Table 9.1 presents the core foundational stiffness values that were calculated for the different cores that were used for both the 8 and 16 ply face sheet thicknesses.

Table 9.1. Core foundational stiffness, k_F , values for the different cores.

Core Type	8 Ply k_F (N/m ³)	16 Ply k_F (N/m ³)
C1	2.27 E11	1.14 E11
C2	1.60 E11	8.05 E10
C3	3.77 E11	1.89 E11

Based on the core foundational stiffness values and the effective plate bending stiffness, D_r , the maximum bending deflection, w_o , in the regime prior to core crushing is calculated as [61]

$$w_o = \frac{P}{8\sqrt{D_r k_F}} \quad (9.8)$$

The critical displacement for core crushing, w_{cr} , which is reached first reached right underneath the point of load application, is calculated using the crush strength of the core, p_{cr} , and the core foundational stiffness, k_F as

$$w_{cr} = \frac{p_{cr}}{k_F} \quad (9.9)$$

The value of the critical displacement for core crushing is then used with equation (9.8) to calculate the critical load at which the core crushes. The small deflection plate theory is only used up to this critical core crush load for modeling the sandwich response. Prior to this point, face sheet deformation is elastic and the elastic face sheet deflection is added to the displacements obtained in the subsequent regimes all the way up to the peak load. However, the elastic face sheet deformation does not enter into the crushed or dented region in the subsequent

regimes. Beyond core crushing, the Rayleigh-Ritz method of energy minimization is used to model the sandwich response to indentation loading.

9.4 Governing Equations – Rayleigh-Ritz Method of Energy Minimization

The Rayleigh-Ritz method of energy minimization was used to model the face sheet response subsequent to the onset of core crushing. The total potential energy, Π , of a system can be expressed in the most general form as

$$\Pi = U - V \quad (9.10)$$

where U is the strain energy and V is the total work.⁸⁸ For the plate bending problem, the strain energy, U , may be further decomposed into the bending energy, U_b , and the membrane energy, U_m . The membrane energy reflects that due to face sheet stretching in the case of large deflections.

The evaluation of the different energy constituents of the total potential energy is dependent upon the displacement field and the properties of the plate. With regards to the sandwich indentation problem, an appropriate coordinate system had to be first chosen both for defining the displacement field and the equivalent face sheet properties. The use of rectangular coordinates is advantageous from the viewpoint of easy representation of the orthogonal properties of the plate. However, the displacement field is more difficult to choose and a field with circular or elliptical symmetries will result in complex equations in the system. On the other hand, polar coordinates simplify the choice of displacement field. However, it is slightly disadvantaged because of the need to approximate the plate properties especially when there is increased plate anisotropy such as after the onset of delamination. The experimental results show that the dents are essentially round. This important fact coupled with the overall approach of the

model being dependent upon the combined ideas of Olsson [61] and Turk and Hoo Fatt [57] led to the choice of a polar coordinate system over a rectangular coordinate system for the displacement field and energy representation in this dissertation.

For the definition of the energy equations, a circular isotropic plate will be considered to represent the face sheet. This isotropic plate will be defined in terms of “equivalent properties” or “homogenized properties”. This means that the equivalent face sheet has the same in-plane and bending stiffnesses in every radial direction. For this reason, in the equations for the circular isotropic plates presented subsequently, the equivalent orthogonal properties are denoted by the subscript r .

For a circular isotropic plate, the bending strain energy is given by [88]

$$U_b = \frac{D_r}{2} \iint \left\{ \left(\frac{\partial^2 w}{\partial r^2} + \frac{1}{r} \frac{\partial w}{\partial r} \right)^2 - \frac{2(1 - \nu_r)}{r} \frac{\partial w}{\partial r} \frac{\partial^2 w}{\partial r^2} \right\} r dr d\theta \quad (9.11)$$

where D_r is the plate bending stiffness, ν_r is the Poisson's ratio, w is displacement field as a function of r and r is the distance from the center of the plate. When w is independent of angle, such as for the indentation of a circular plate, equation 9.11 can be integrated from 0 to 2π , which yields

$$U_b = \pi D_r \int \left[r \left(\frac{\partial^2 w}{\partial r^2} \right)^2 + \frac{1}{r} \left(\frac{\partial w}{\partial r} \right)^2 + 2\nu_r \left(\frac{\partial w}{\partial r} \right) \left(\frac{\partial^2 w}{\partial r^2} \right) \right] dr \quad (9.12)$$

Equation (9.12) represents the governing bending energy equation that is used in this dissertation.

For a circular isotropic plate undergoing large deflections, the membrane strain energy is assumed constant for every angle θ and is given by [88]

$$U_m = \frac{\pi E_r h_f}{1 - \nu_r^2} \int (\varepsilon_r^2 + \varepsilon_t^2 + 2\nu_r \varepsilon_r \varepsilon_t) r dr \quad (9.13)$$

where

$$\varepsilon_r = \frac{\partial u}{\partial r} + \frac{1}{2} \left(\frac{\partial w}{\partial r} \right)^2 \quad (9.14)$$

and

$$\varepsilon_t = \frac{u}{r} \quad (9.15)$$

In equations 9.13-9.15, E_r represents the in-plane radial modulus, u represents the in-plane radial displacement, h represents the plate thickness, ε_r represents the strain in the radial direction and ε_t represents the strain in the tangential direction. According to Turk and Hoo-Fatt's assumption [57], the radial displacement u is much smaller than the transverse displacement w . Therefore in modeling the sandwich face sheet as a membrane, this can be ignored. This simplifies the membrane strain energy (equation 9.13) to

$$U_m = \frac{\pi E_r h_f}{4(1 - \nu_r^2)} \int r \left(\frac{\partial w}{\partial r} \right)^4 dr \quad (9.16)$$

Equation (9.16) represents the governing membrane energy equation in this dissertation.

Turk and Hoo Fatt's [57] idea of treating the hemispherical indenter as an equivalent flat-nosed indenter is adopted in the post crushing regime of the model presented in this dissertation. Derivation of the equivalent flat-nosed indenter radius is discussed in Section 9.4.2.

The loading on the face sheet is modeled as a combination of an externally applied load, P and an opposing crushed core resistive pressure, p_{oc} . The idea of a constant core resistive pressure opposing the face sheet deflection is adopted from the idealized honeycomb core behavior proposed by Minakuchi et al. [65] presented in Chapter 7. The crushed core resistance to the face sheet was further divided into two segments – one right underneath the indenter and the other in the region beyond the indenter. Considering an equivalent flat-nosed indenter of radius b , an outer dent radius of a and a constant maximum displacement w_o within the radius b because of the flat-nosed indenter assumption, the total work done on the system can be defined as

$$V = Pw_o - \pi p_{oc} b^2 w_o - 2\pi p_{oc} \int_b^a w(r) r dr \quad (9.17)$$

where $w(r)$ is the displacement field for $b \leq r \leq a$.

Equation (9.17) represents the governing total work equation used in this dissertation.

Figure 9.3 shows a schematic that defines the different geometrical parameters of the flat-nosed indenter radius, b , the maximum face sheet deflection, w_o , and the dent radius, a .

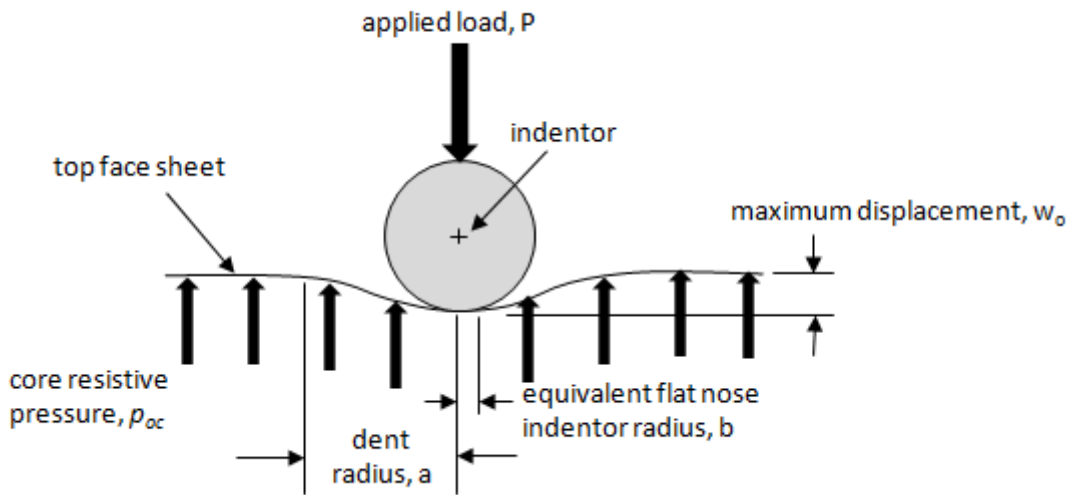


Figure 9.3. Schematic defining the dent radius, equivalent flat-nosed indenter radius and the maximum dent depth during the indentation process.

The different energy constituents, as defined by equations 9.12, 9.16 and 9.17, are dependent upon the assumed displacement field, the equivalent flat-nosed indenter radius, b , and the sheet and core properties where the equivalent face sheet properties of D_r , ν_r and E_r had to be defined. Derivation of the assumed displacement field, the equivalent flat-nosed indenter radius, b , and the face sheet properties are discussed in Sub-sections 9.4.1, 9.4.2 and 9.4.3 respectively.

9.4.1 Assumed Displacement Field

To evaluate the different energy constituents of the total system potential energy so that Rayleigh-Ritz method of potential energy minimization could be used, an appropriate displacement field had to be first chosen. The displacement field had to be kinematically admissible, be complex enough to capture the desired behavior, yet still lend itself to an analytical solution.

As discussed in section 9.2, an equivalent flat-nosed indenter assumption similar to that imposed by Turk and Hoo Fatt [57] appeared to be the most analytically viable assumption for implementing the indenter size effects in the model. This implied that the displacement within the indenter-face sheet contact periphery is constant throughout. The assumed displacement field also had to satisfy certain boundary conditions. These were primarily that the slope and the displacement at the edge of the dented region had to be zero. Due to the assumption of an equivalent flat-nosed indenter, the slope at the indenter-face sheet contact periphery is also taken to be zero. Taking into consideration the different boundary conditions that needed to be satisfied as well as the need to have a displacement field that did not yield itself to analytical complexities especially when solving for the resulting potential energy minimized equations, the following displacement field was chosen.

$$w = w_o \left[1 - 3 \left(\frac{r-b}{a-b} \right)^2 + 2 \left(\frac{r-b}{a-b} \right)^3 \right] \text{ for } b \leq r \leq a$$

$$w = w_o \text{ for } r \leq b$$

(9.18)

The different geometrical parameters w_o , a and b are as defined in Figure 9.3. Section 9.4.2 presents the method for evaluating the equivalent flat-nosed indenter contact radius, b , while the maximum displacement, w_o , and the dent radius, a , are determined through minimization of the total potential energy.

9.4.2 Determination of the Equivalent Flat-nosed Indentor Radius, b

The Hertzian indentation contact theory of a rigid spherical indenter on an elastic half space was used for the determination of the flat-nose indenter contact radius. As discussed in Section 9.3.1, up to the core crush onset load the face sheet alone could be treated as the target body or the elastic half space. Therefore, taking the face sheet as the target body without any contribution of the core up to the core crush load, the indenter contact radius, b , at the core crush onset load, P_{cr} , can be calculated using the standard Hertzian formulation as [91]

$$b = \left(\frac{3P_{cr}R}{4E^*} \right)^{\frac{1}{3}} \quad (9.19)$$

where R is the indenter radius and E^* is as defined by equation (9.3).

As mentioned in Section 9.3.1, prior to core crushing the indenter is treated as spherical. The equivalent flat-nosed indenter assumption therefore is only used subsequent to core crushing in the Rayleigh-Ritz method of energy minimization. The flat-nosed indenter radius is taken as the b value calculated using equation (9.19) at the core crush onset load. The value of b is therefore treated as a constant at load levels higher than the core crush onset load. Figure 9.4 presents a schematic that summarizes the profile of the indenter contact radius with increasing load both prior to core crushing as well as post the onset of core crushing.

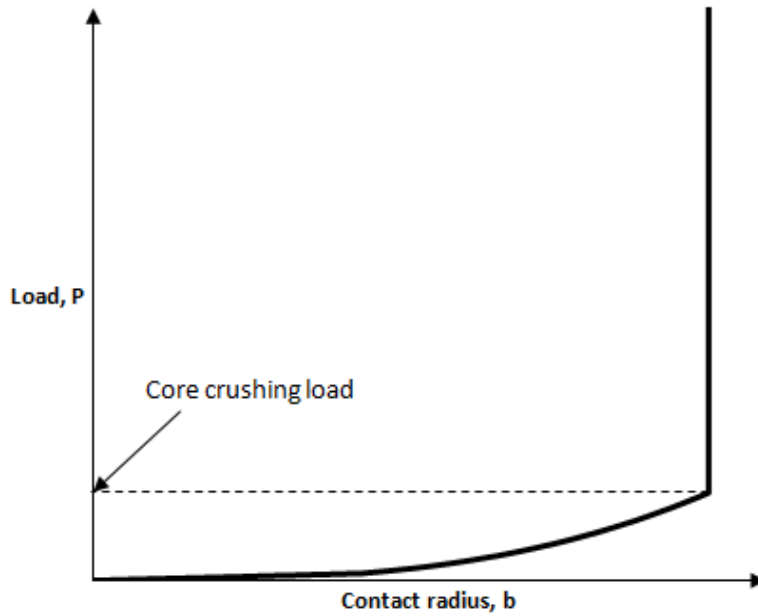


Figure 9.4. Schematic representing the variation of contact radius, b , with increasing load, P .

9.4.3 Effective Face Sheet Properties

In the strain energy equations presented in the previous sub-section, the orthotropic face sheet is being treated as isotropic since it greatly simplifies analysis. Therefore, the strain energy equations use circular isotropic plate properties that are independent of angular direction. Equivalent face sheet properties of the bending stiffness, D_r , the in-plane radial modulus, E_r , and the Poisson's ratio, ν_r were therefore determined using the classical laminate plate theory (CLPT)⁸⁹. This section presents the equations for the calculation of the “intact” face sheet properties. The use of the word “intact” here, and subsequently, refers to face sheet laminate that is without any damage in the form of matrix cracks and delaminations.

The in-plane radial modulus of a quasi-isotropic laminate is independent of angular direction.⁸⁹ Therefore, the in-plane radial modulus for the intact laminate was calculated using CLPT as [89]

$$E_r = E_{11} = \frac{1}{\alpha_{11} h_f} \quad (9.20)$$

where h_f is the face sheet thickness. The resulting value of E_r for both the 8 and 16 ply cases was 5.52×10^{10} Pa.

The Poisson's ratio for the intact face sheet for a quasi-isotropic laminate is also independent of direction.⁸⁹ Therefore, using CLPT, the Poisson's ratio for the intact laminate was calculated as [89]

$$\nu_r = \nu_{12} = -\frac{\alpha_{21}}{\alpha_{11}} \quad (9.21)$$

The radial Poisson's ratio value for all the face sheet layups for both the 8 and 16 ply cases was 0.334.

Finally, the equivalent bending stiffness for the face sheet, D_r , was calculated as

$$D_r = \frac{1}{8} [3D_{11} + 2(D_{12} + 2D_{66}) + 3D_{22}] \quad (9.22)$$

Equation 9.22 is commonly used in literature⁵⁹⁻⁶⁰ for the analysis of an orthotropic face sheet laminate and is obtained from the original orthotropic plate solution for a clamped circular plate under uniformly distributed load derived by Lekhnitskii.⁹² The D_r by Lekhnitskii is found by comparing the displacement to load ratios of an isotropic plate with that of an orthotropic plate. In equation 9.22, D_{ij} is obtained from the flexural stiffness matrix of the face sheet laminate which is calculated using CLPT. The equivalent bending stiffness, D_r , as per equation 9.22 was evaluated to be 5.43 Nm for all the 8 ply layups and 43.4 Nm for all the 16 ply layups.

9.5 Method of Solution

As discussed in Section 9.4, the constituents of the total potential energy, Π , are the face sheet bending energy, the face sheet membrane energy and the total work. Using the Rayleigh-Ritz method, the total potential energy is minimized with respect to the undetermined coefficients, which from the assumed displacement field presented in equation 9.18 are the center point deflection, w_o , and the dent radius, a , i.e., the radius of the region where the core has crushed. The total potential energy minimization equations can therefore be represented as

$$\frac{\partial \Pi}{\partial w_o} = \frac{\partial \Pi}{\partial a} = 0 \quad (9.23)$$

This results in two non-linear equations which when solved gives the solution for the dent center-point displacement, w_o , and the radius or the deformed region, or the dent radius, a . The resulting non-linear equations are solved numerically in MATLAB using built-in *fsolve* command. The *fsolve* command in MATLAB is specifically designed to solve non-linear equations or system of equations and uses a robust math algorithm called the “trust-region-dogleg algorithm” for its method of solution. A simple code based on the Newton-Raphson method was also initially developed to verify the accuracy of the *fsolve* method that Matlab uses and both approaches gave essentially identical results. The *fsolve* command in Matlab was primarily used thereafter due to its relative ease of implementation. In this approach, an initial guess of the solution is provided for the first load level. The first load level is the load level right after the core crush onset load. The initial guess of w_o was taken as the bending deflection value calculated using equation (9.8) at the core crush onset load while the initial value of a was taken as 10 times the flat-nosed indenter radius b expressed up to 1 significant figure. These initial guesses always gave the desired results. Each consecutive load level which was a slightly larger

value than the previous load level and used the w_o and a values obtained from the previous load level. The analysis is therefore run in small increments of load from the core crush onset load to the desired load up to which the regime is being modeled. A general MATLAB code that implements the process of solving the system of non-linear equations is presented in Appendix G.

9.6 Modeling Loading Regime II: Core Crushing Onset Load to Delamination Onset Load

The Rayleigh-Ritz method of energy minimization is first used to model the response of the panel from the core crushing onset load to the delamination onset load. Only the face sheet bending energy and the total work is considered for this analysis. Membrane effects are not considered; the experimental face sheet deflection is still relatively small and less than 20% of the face sheet thickness for all the sandwich configurations.

Prior to using the proposed method to model this regime, a validation exercise was carried out where the displacements obtained by the energy method were compared to the exact solutions for clamped circular isotropic plates presented by Timoshenko and Woinowsky-krieger [88]. Results of this validation exercise are presented in Appendix H. The validation exercise showed good correlation for loadings where exact solutions were available.

As described previously, the total potential energy of the system is minimized with respect to the dent diameter, a , and the dent depth, w_o , and these parameters are solved for numerically from the two resultant equations. The total linear elastic displacement at the core crush onset load, w_{el} , calculated using the method described in Section 9.3, is added as a constant to the maximum displacement obtained using the Rayleigh-Ritz energy minimization. Therefore, the total deflection in this regime is represented as

$$w_T = w_{el} + w_o \quad (9.24)$$

Figures 9.5 to 9.8 present the results of the analysis for this regime for the 8 and 16 ply Q1-C1 specimens indented with the 25.4 mm and 76.2 mm diameter indentors. The procedure for the calculation of the delamination onset load is described in Section 9.8. The results of the analysis for the zero load to the core crush onset load regime, as derived in section 9.3, is also presented in these figures. As can be seen in the Figures, the model predicts the onset of core crushing at relatively low loads. The P-d curve for the regime prior to core crushing is linear, and non-linearity in the curve arises due to the growing dent.

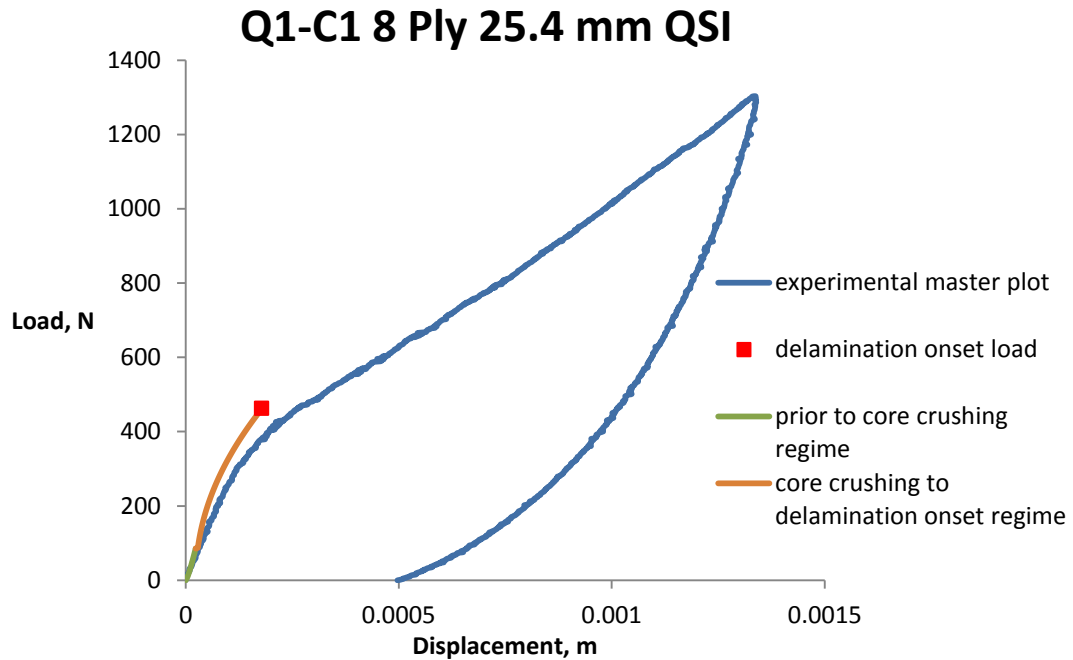


Figure 9.5. Results for the modeling regimes described in sections 9.3 and 9.6 for the 8 ply Q1-C1 specimens indented with the 25.4 mm diameter indentor.

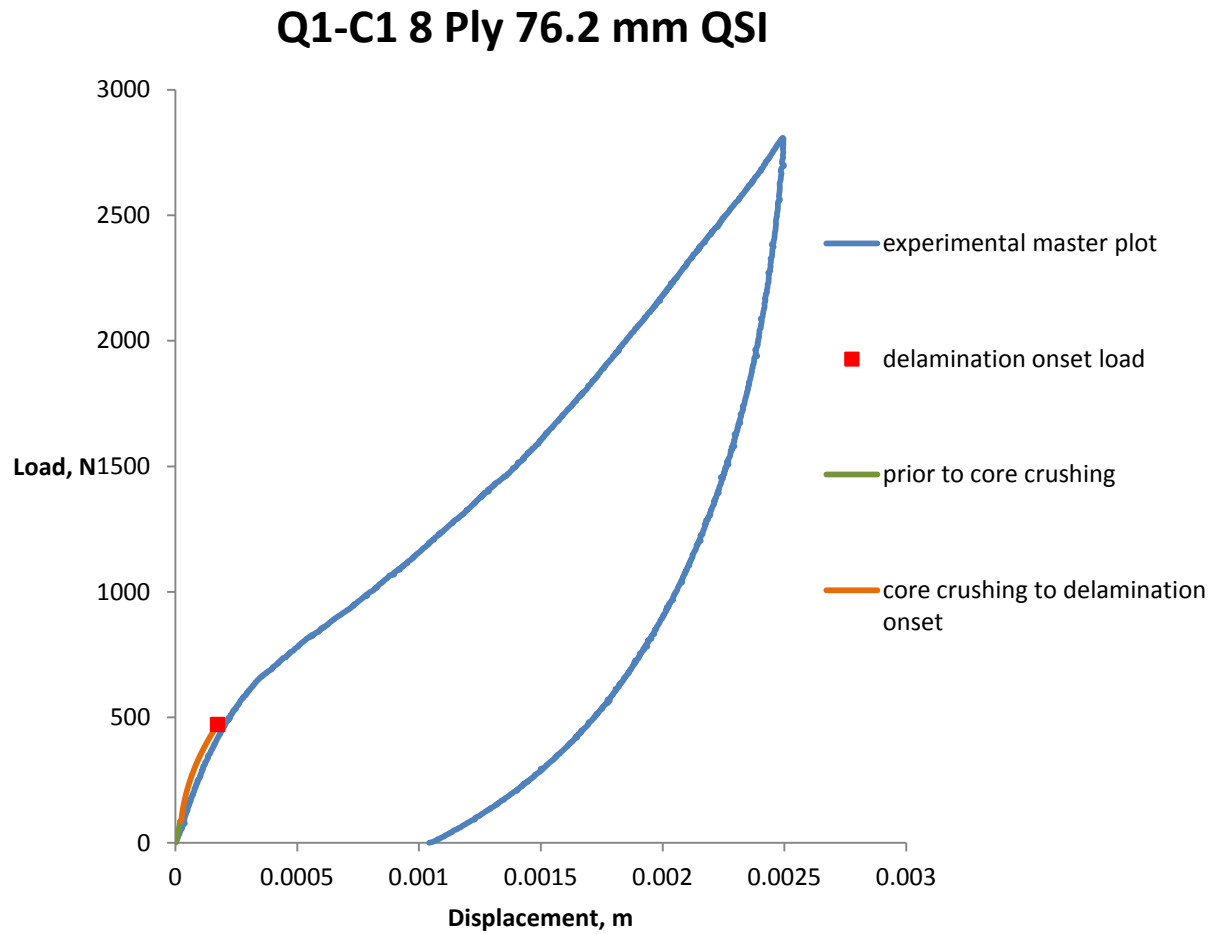


Figure 9.6. Results for the modeling regimes described in sections 9.3 and 9.6 for the 8 ply Q1-C1 specimens indented with the 76.2 mm diameter indenter.

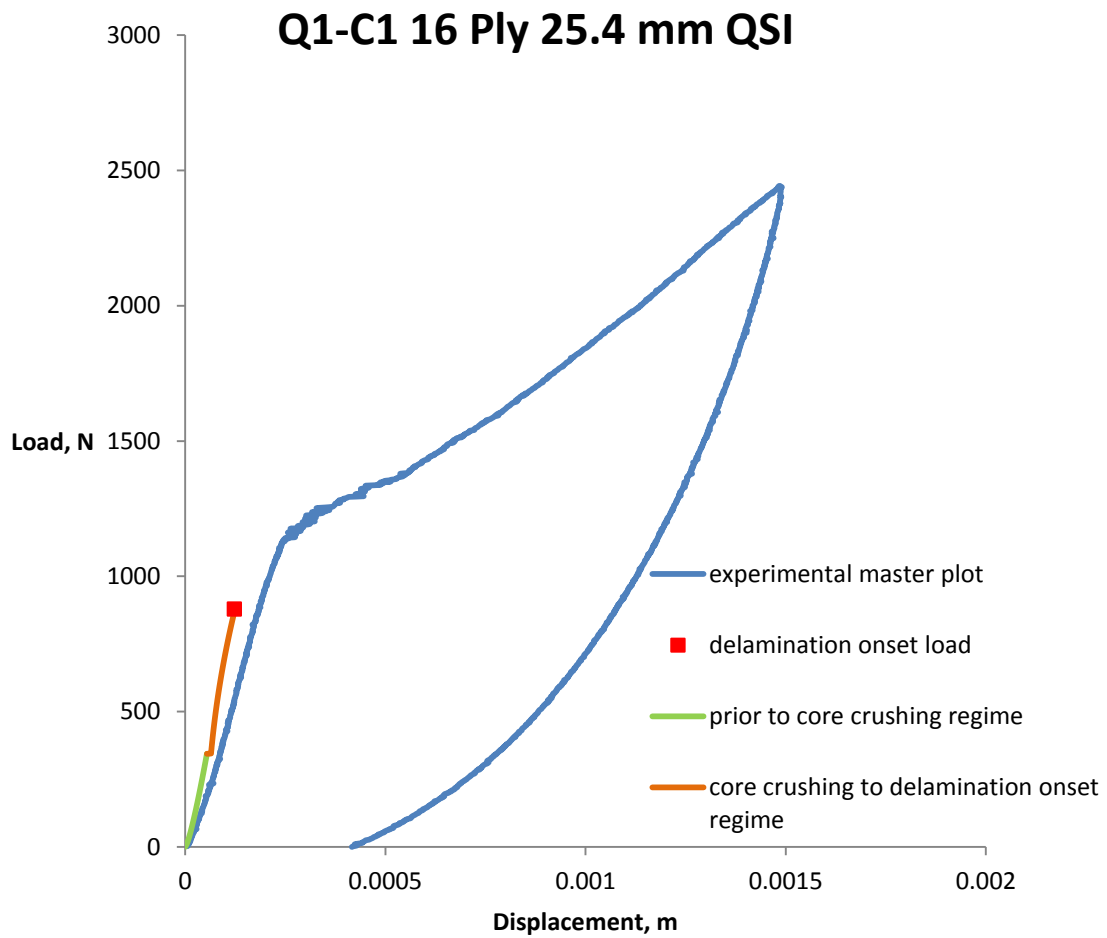


Figure 9.7. Results for the modeling regimes described in sections 9.3 and 9.6 for the 16 ply Q1-C1 specimens indented with the 25.4 mm diameter indenter.

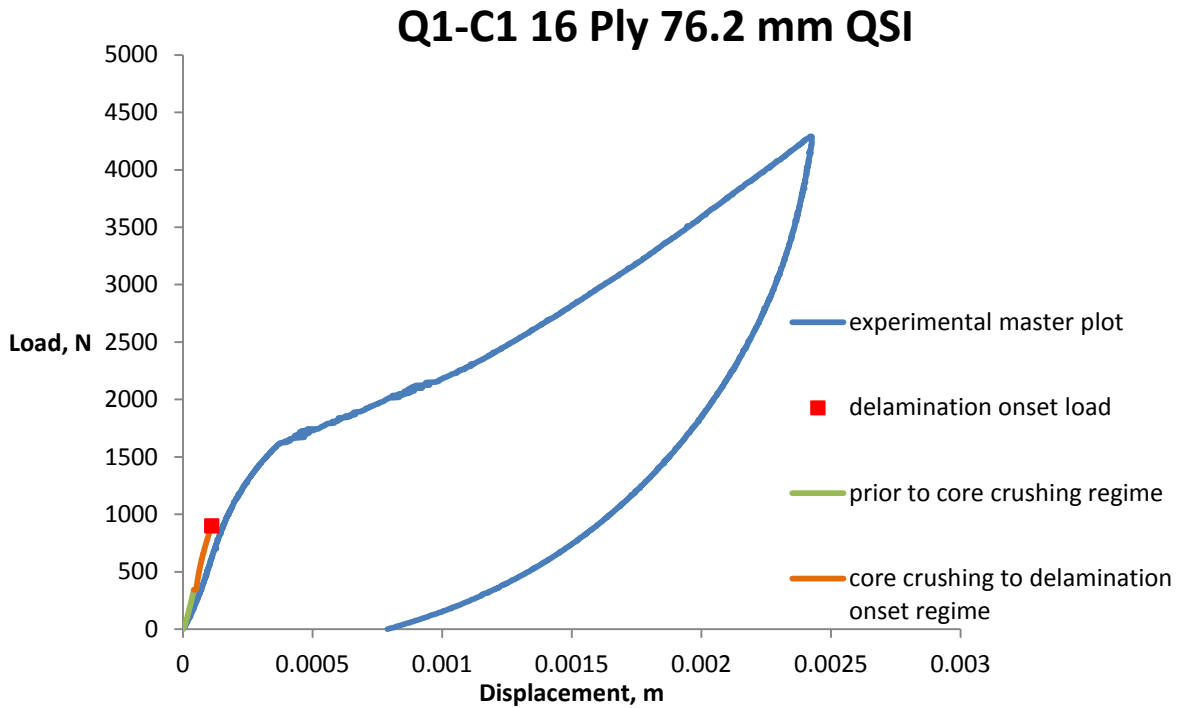


Figure 9.8. Results for the modeling regimes described in sections 9.3 and 9.6 for the 16 ply Q1-C1 specimens indented with the 76.2 mm diameter indenter.

The regime described in this section is used only up to the predicted delamination onset load. Matrix cracks and delaminations are assumed to occur at the delamination onset load which results in the degradation of the face sheet properties. In order to predict the delamination onset load, degraded properties are required since delamination onset is predicted by evaluating the change in energy from an intact to a degraded, delaminated state of the face sheet laminate. Section 9.7 presents the degraded face sheet properties due to matrix cracking and delaminations. The derivation of these properties is presented in Appendix I. Section 9.8 presents the procedure for calculating the delamination onset load. The model for the post delamination onset load to peak load regime is presented in Section 9.9.

9.7. Property Degradation Due to Matrix Cracking and Delaminations

Face sheet properties become degraded, i.e., reduced, due to the onset and presence of matrix cracks and interlaminar delaminations. Matrix cracks degrade the individual lamina properties while delaminations degrade the overall laminate properties.

9.7.1 Degraded Lamina Properties Due to Matrix Cracking

It is assumed and supported by the literature that matrix cracks act as delamination onset sites.^{2,12-15} Material degradation due to matrix cracks is implemented in the model through a reduction of ply level face sheet properties of E_{22} , G_{12} and ν_{12} . These properties are degraded by 80%. In this approach, it is assumed that the matrix cracks have reached “saturation spacing”, i.e. no more matrix cracks develop in the plies with increasing load. The 80% reduction/20% residual stiffness and Poisson’s ratio assumption is based on typical shear-lag analysis for plies with saturated matrix crack spacing within a multidirectional laminate.⁹³

9.7.2 Assumed Delaminating Interfaces

In the context of this dissertation, a “fully delaminated” face sheet is defined as a face sheet laminate where all the interfaces that are assumed to be delaminating have delaminated, and these delaminations are further assumed to cover the entire dent area. The experimental findings of Chapter 5 showed that delaminations occur at all interfaces except interface 1 and the midplane. This is true for both the 8 and 16 ply face sheets. It is therefore also assumed in the model that apart from interfaces 1 and the midplane, all the other interfaces delaminate in both the 8 and 16 ply face sheets. The individual sublaminates that result due to the delamination of these interfaces for the different face sheet layups are presented in Tables 9.2 and 9.3 for the 8 and 16 ply cases respectively.

Table 9.2. Table of resulting sublaminates due to the assumed delaminations at the different interfaces for the 8 ply case.

Sublamine (i)	Q1	Q2	Q3	Q4
1	[45/0]	[45/-45]	[-45/45]	[45/90]
2	[-45]	[0]	[90]	[-45]
3	[90/90]	[90/90]	[0/0]	[0/0]
4	[-45]	[0]	[90]	[-45]
5	[0]	[-45]	[45]	[90]
6	[45]	[45]	[-45]	[45]

Table 9.3. Table of resulting sublaminates due to the assumed delaminations at the different interfaces for the 16 ply case.

Sublaminates (i)	Q1	Q2	Q3	Q4	Q5
1	[45/0]	[45/-45]	[45/-45]	[45/90]	[45/0]
2	[-45]	[0]	[90]	[-45]	[-45]
3	[90]	[90]	[0]	[0]	[90]
4	[-45]	[45]	[45]	[-45]	[90]
5	[0]	[-45]	[-45]	[90]	[-45]
6	[45]	[0]	[90]	[45]	[0]
7	[90/90]	[90/90]	[0/0]	[0/0]	[45/45]
8	[45]	[0]	[90]	[45]	[0]
9	[0]	[-45]	[-45]	[90]	[-45]
10	[-45]	[45]	[45]	[-45]	[90]
11	[90]	[90]	[0]	[0]	[90]
12	[-45]	[0]	[90]	[-45]	[-45]
13	[0]	[-45]	[-45]	[90]	[0]
14	[45]	[45]	[45]	[45]	[45]

9.7.3 Reduced Equivalent Bending Stiffness, D_{res}

In a fully delaminated face sheet, the intact bending stiffness, D_r , is exchanged for the residual bending stiffness, D_{res} , which is calculated as

$$D_{res} = \sum_{i=1}^{n+1} D_i \quad (9.25)$$

In equation (9.25), D_i is the bending stiffness of the individual sublaminates calculated using equation (9.16) and n is the number of interfaces that have supposedly delaminated. For a fully delaminated face sheet laminate, the value of n is taken as 5 for the 8 ply case and 13 for the 16 ply case. The number of sublaminates that result will always be one more than the number of interfaces that delaminate. A derivation of equation (9.25) is presented in Appendix I. Degraded ply properties are used for the calculation of the equivalent bending stiffness since it is assumed that matrix cracks have already occurred. The evaluations show that for the fully delaminated quasi-isotropic face sheet laminates considered in this dissertation, both the intact and the residual bending stiffness values are independent of face sheet layup for both the 8 and 16 ply cases. A summary of intact and residual bending stiffness values for the 8 and 16 ply cases is presented in Table 9.4.

Table 9.4. Table of intact and residual bending stiffness values for both the 8 and 16 ply face sheets.

Laminate Thickness	Intact Bending Stiffness, D_r (Nm)	Residual Bending Stiffness, D_{res} (Nm)
8 Ply	5.43	0.1879
16 Ply	43.4	0.2631

9.7.4 Reduced In-plane Radial Modulus, E_{res}

The presence of delaminations and matrix cracks also degrades the in-plane radial modulus. For a fully delaminated laminate, the intact in-plane radial modulus, E_r , is exchanged for the reduced in-plane radial modulus, E_{res} . The derivation of the homogenized in-plane radial modulus for the delaminated laminate is presented in Appendix I. Tables 9.5 and 9.6 present the reduced in-plane radial modulus values for the different 8 and 16 ply fully delaminated face sheet laminates.

Table 9.5. Table of reduced in-plane bending modulus for the fully delaminated 8 ply face sheet laminates.

Face Sheet Layup – 8 Ply	Reduced In-plane Modulus, E_{res} (N/m ²)
Q1	1.17E10
Q2	1.10E10
Q3	1.10E10
Q4	1.17E10

Table 9.6. Table of reduced in-plane bending modulus for the fully delaminated 16 ply face sheet laminates.

Face Sheet Layup – 16 Ply	Reduced In-plane Modulus, E_{res} (N/m ²)
Q1	1.11E10
Q2	1.07E10
Q3	1.07E10
Q4	1.11E10
Q5	1.11E10

9.7.5 Residual In-plane Poisson's Ratio, ν_{res}

The presence of delaminations and matrix cracks also degrades the in-plane Poisson's ratio. For a fully delaminated face sheet laminate, the intact radial Poisson's ratio, ν_r , is exchanged for the reduced in-plane Poisson's ratio ν_{res} . The derivation for the homogenized radial Poisson's ratio for a fully delaminated laminate is also presented in Appendix I. Tables 9.7 and 9.8 present the reduced in-plane Poisson's Ratio values for the different 8 and 16 ply fully delaminated face sheet laminates.

Table 9.7. Table of reduced in-plane Poisson's ratio for the fully delaminated 8 ply face sheet laminates.

Face Sheet Layup – 8 Ply	Reduced In-plane Poisson's Ratio, ν_{res}
Q1	0.153
Q2	0.272
Q3	0.272
Q4	0.151

Table 9.8. Table of reduced in-plane bending modulus for the fully delaminated 16 ply face sheet laminates.

Face Sheet Layup – 16 Ply	Reduced In-plane Poisson's Ratio, ν_{res}
Q1	0.180
Q2	0.251
Q3	0.251
Q4	0.180
Q5	0.224

9.8 Prediction of Delamination Onset Load

An approach based on the linear elastic fracture mechanics (LEFM) analogous to that proposed by Olsson [61] was used for the prediction of the delamination onset load. Huang et al. [60] proposes a similar approach for the prediction of the delamination onset load for a monolithic laminate, but with differences in how the delamination area is assumed. The approach proposed by Huang et al. [60] considers partial delamination as compared to the overall dent area. Partial delamination is more true to what has been observed experimentally in the sandwich

indentation problem presented in this dissertation. However, solving for the partial area that delaminates within the total dented region is not possible within the present formulation.

While the approach presented for delamination onset load calculation in this dissertation is analogous to that proposed by Olsson, some minor differences between the two approaches exist. These are described as follows:

- i. Olsson uses Timoshenko and Woinowsky-Krieger's⁸⁸ isotropic circular plate displacement field. For the approach used in this dissertation, the displacement field as stated by equation (9.18) is used. This enabled obtaining a solution for the delamination onset load within the construct of the displacement field chosen for the model.
- ii. Olsson reduces the bending stiffness for the delaminated face sheet based on the relationship $D_{res} = \frac{D_o}{(n+1)^2}$, where n is the number of delaminating interfaces. This is based on an isotropic face sheet with D_o being the original (undamaged) bending rigidity. For the delamination onset analysis presented in this dissertation, the reduced bending stiffness is calculated using equation (9.25) with the results presented in Table 9.4.
- iii. Olsson developed his delamination onset load equation based on the growth of multiple delaminations spanning the entire dent area and finally reduces his derived equations for the prediction of the onset load for a single delamination. This he does by assuming that the first delamination occurs at the midplane. In the delamination onset load prediction criteria presented in this dissertation, multiple delaminations are assumed to occur at once and this assumption is retained. Unlike Olsson, no single midplane delamination is assumed in the prediction of the delamination onset loads.

To facilitate the analysis of the delamination onset load, the following assumptions are further made:

- i. The matrix cracks occur “just before” (almost simultaneously) with delamination onset. This is backed by the literature which also suggests that these matrix cracks act as delamination onset sites.^{2,12-15} There is therefore no stiffness loss expected in the face sheet laminate until the matrix cracks and delaminations happen together.
- ii. The delaminations have an idealized circular shape. The actual delamination shapes are more lemniscates with variations from interface to interface. Correct representation of the exact delamination shapes is complex and is not possible within the present formulation.
- iii. The delaminations cover the entire dent or crush area. Even though delaminations occur within a portion of the overall dented region, the exact planar area of delamination over which they occur is not possible within the present formulation. An alternative approach to that pursued here is described in Chapter 12.
- iv. Bending deformation is dominant up to the delamination onset load and there are no membrane effects up to that point.
- v. The composite laminate behaves like a linear elastic material up to the delamination onset load, so that linear elastic fracture mechanics (LEFM) is valid. Inelastic processes have not begun to occur in the face sheet laminate until matrix cracking and delaminations happen almost simultaneously.

Considering the face sheet laminate in pure bending up to the delamination onset load, the onset of delamination causes a change in deflection given as $w_d - w_o$, where w_d is the displacement of the delaminated face sheet and w_o is the displacement of the intact face sheet.

The residual bending stiffness, D_{res} , and the intact bending stiffness, D_r , are used in the

calculation of w_d and w_o respectively. The corresponding change in strain energy, U_d , at the delamination onset load therefore can be described in terms of the delamination onset load, P_d , as

$$U_d = \frac{1}{2} P_d (w_d - w_o) \quad (9.26)$$

The strain energy release rate, G_{II} , for a delaminated area growing in mode II may be obtained following the Griffith energy criterion as

$$G_{II} = \frac{\partial U_d}{\partial A} \quad (9.27)$$

where A is the crack area. For multiple delaminations, n , the total delamination area can be expressed in terms of the delamination radius a (assumed to be same as the dent radius) as

$$A = n\pi a^2 \quad (9.28)$$

Therefore

$$\frac{dA}{da} = 2n\pi a \quad (9.29)$$

or

$$dA = 2n\pi a da \quad (9.30)$$

As discussed in Section 9.7, the value of n is taken to be 5 for the 8 ply case and 13 for the 16 ply case. Replacing equation (9.30) into equation (9.27), the final expression for the calculation of G_{II} is obtained as

$$G_{II} = \frac{1}{2n\pi a} \frac{\partial U_d}{\partial a} \quad (9.31)$$

Based on the value of the precracked mode II interlaminar fracture toughness, G_{IIC} , of 772 J/m^2 as presented and discussed in Chapter 7, the delamination onset load is calculated. Because of the existence of the matrix cracks that supposedly act as delamination onset sites, the precracked value of G_{IIC} is used.

A comparison of the predicted delamination onset loads was made with values that were obtained by direct calculation using the formula derived by Olsson [61] for multiple delaminations. The comparison of results for both the 8 and 16 ply cases are presented in Table 9.9 and 9.10. It was noticed that the values obtained by the above procedure were slightly different from those predicted using Olsson's formula. This was because Olsson used a different displacement field as well as a slightly different residual bending stiffness.

Table 9.9. Predicted delamination onset loads, 8 ply specimens.

8 Ply, 25.4 mm Diameter Indentor Tests			8 Ply, 76.2 mm Diameter Indentor Tests		
Sandwich Geometry	Predicted Onset Load (N)	Prediction by Olsson's Formula (N)	Sandwich Geometry	Predicted Onset Load (N)	Prediction by Olsson's Formula (N)
Q1-C1	465	552	Q1-C1	475	554
Q1-C2	468	554	Q1-C2	481	557
Q1-C3	478	562	Q1-C3	496	565
Q2-C1	465	552	Q2-C1	475	554
Q3-C1	465	552	Q3-C1	475	554
Q4-C2	468	554	Q4-C2	481	557
Q4-C3	478	562	Q4-C3	496	565

Table 9.10. Predicted delamination onset loads, 16 ply specimens.

16 Ply, 25.4 mm Diameter Indentor Tests			16 Ply, 76.2 mm Diameter Indentor Tests		
Sandwich Geometry	Predicted Onset Load (N)	Prediction by Olsson's Formula (N)	Sandwich Geometry	Predicted Onset Load (N)	Prediction by Olsson's Formula (N)
Q1-C1	879	1052	Q1-C1	901	1057
Q1-C2	888	1055	Q1-C2	914	1060
Q1-C3	908	1065	Q1-C3	947	1072
Q2-C1	879	1052	Q2-C1	901	1057
Q3-C1	879	1052	Q3-C1	901	1057
Q4-C1	879	1052	Q4-C1	901	1057
Q4-C3	908	1065	Q4-C3	947	1072
Q5-C1	879	1052	Q5-C1	901	1057

9.9 Loading Regime III: Delamination Onset Load to Peak Load Model

Once matrix cracks and delaminations occur, the bending stiffness of the face sheet laminate is significantly reduced. This results in large deflections which bring about the need to include face sheet stretching (membrane) effects. Therefore both bending and membrane energy were used in the model in the regime from delamination onset to peak load. Similar to that done for the previous regime, a validation exercise was first carried out where the displacements obtained by this energy method approach were compared to exact large deflection solutions for clamped circular isotropic plates [88]. This was done in order to see how the displacements obtained using the energy solutions compared to the exact plate solutions. Results of this validation exercise are presented in Appendix H. The validation exercise showed good

correspondence between the displacements obtained using the energy solutions and the exact solutions for cases of similar loadings, and gave added confidence in the accuracy of the proposed approach.

The initial approach for modeling the post delamination onset regime was to use fully degraded laminate properties consistently at every load higher than the delamination onset load. The fully degraded laminate properties assume that the maximum possible number of delaminations occurs simultaneously at the delamination onset load and that all delaminations cover the entire dent area. Based on these degraded properties, the total potential energy is calculated and minimized with respect to the dent radius, a , and the maximum displacement, w_0 . The model predictions for the post delamination onset regime for the Q1-C1 sandwich configuration for both the 8 and 16 ply cases are presented in Figures 9.9-9.12.

As clearly seen in the Figures 9.9 - 9.12, two major issues arise in the post delamination onset regime in the model's current form. Firstly, the displacements at the peak load are much larger than what the experiments show. This is true for both face sheet thicknesses. Secondly, a large strain jump is seen at the delamination onset load. Within the model, this occurs due to the sudden yet significant stiffness loss of face sheet properties. The model prediction is clearly not supported by experimental data. Another issue that arose in this model was that there was a sudden decrease in the predicted dent radius at the delamination onset load. This is shown by Figure 9.13 where the load versus dent radius results for the 8 ply Q1-C1 sandwich configuration indented with the 25.4 mm diameter indenter is presented. This also occurs due to a sudden degradation of material properties. To correct for these shortcomings in the model, an improved model was developed with the improvement being made in two consecutive stages. The first stage involved the correction of the peak displacement, and the second stage involved the

correction of the strain jump at the delamination onset load. These are described in what follows.

Q1-C1 8 Ply 25.4 mm QSI

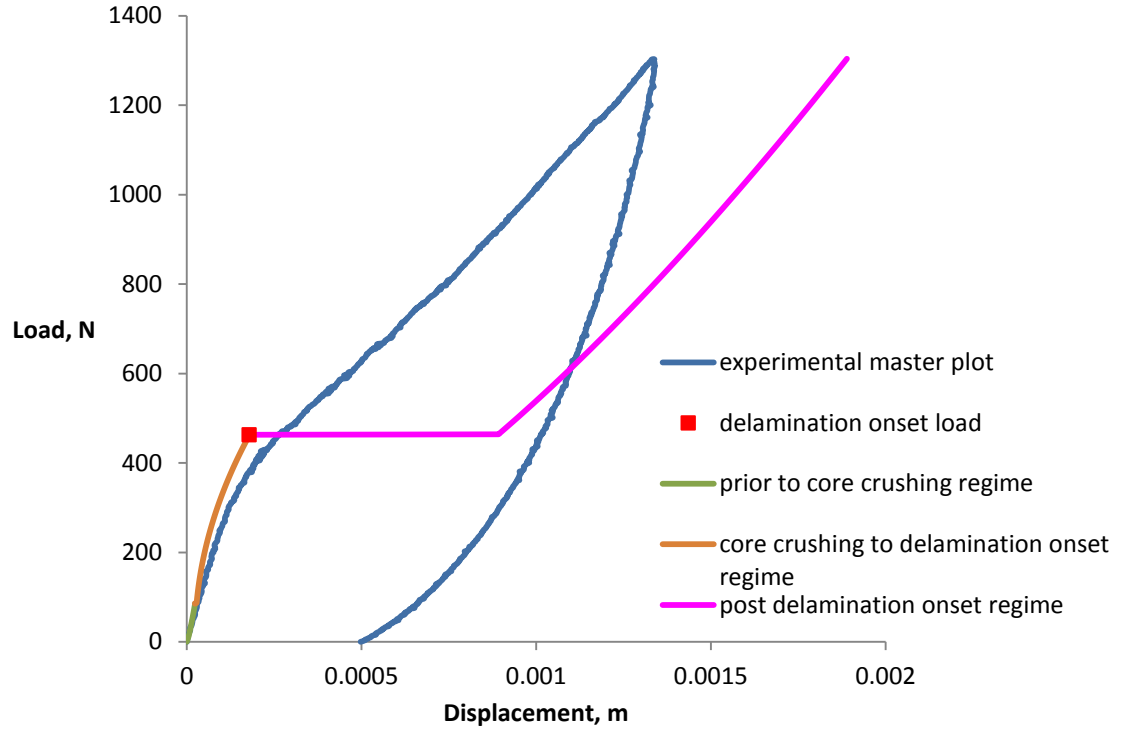


Figure 9.9. Plot showing the loading regime model versus experimental results for the 8 ply Q1-C1 sandwich configuration indented with the 25.4 mm diameter indenter.

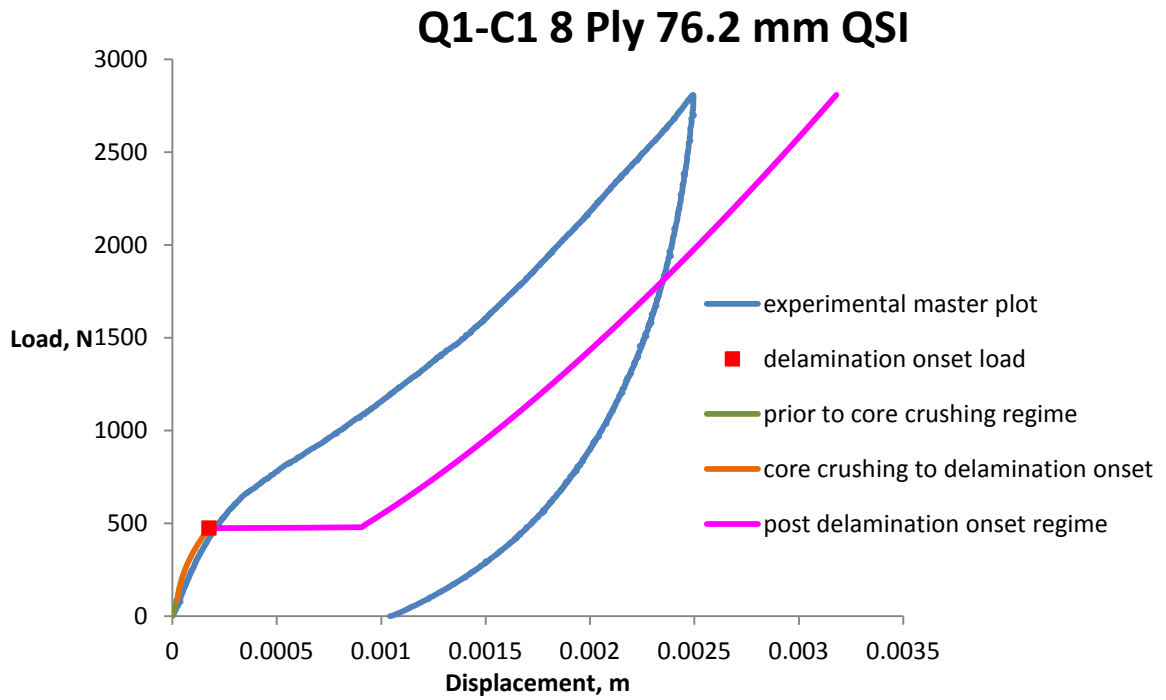


Figure 9.10. Plot showing the loading regime model versus experimental results for the 8 ply Q1-C1 sandwich configuration indented with the 76.2 mm diameter indenter.

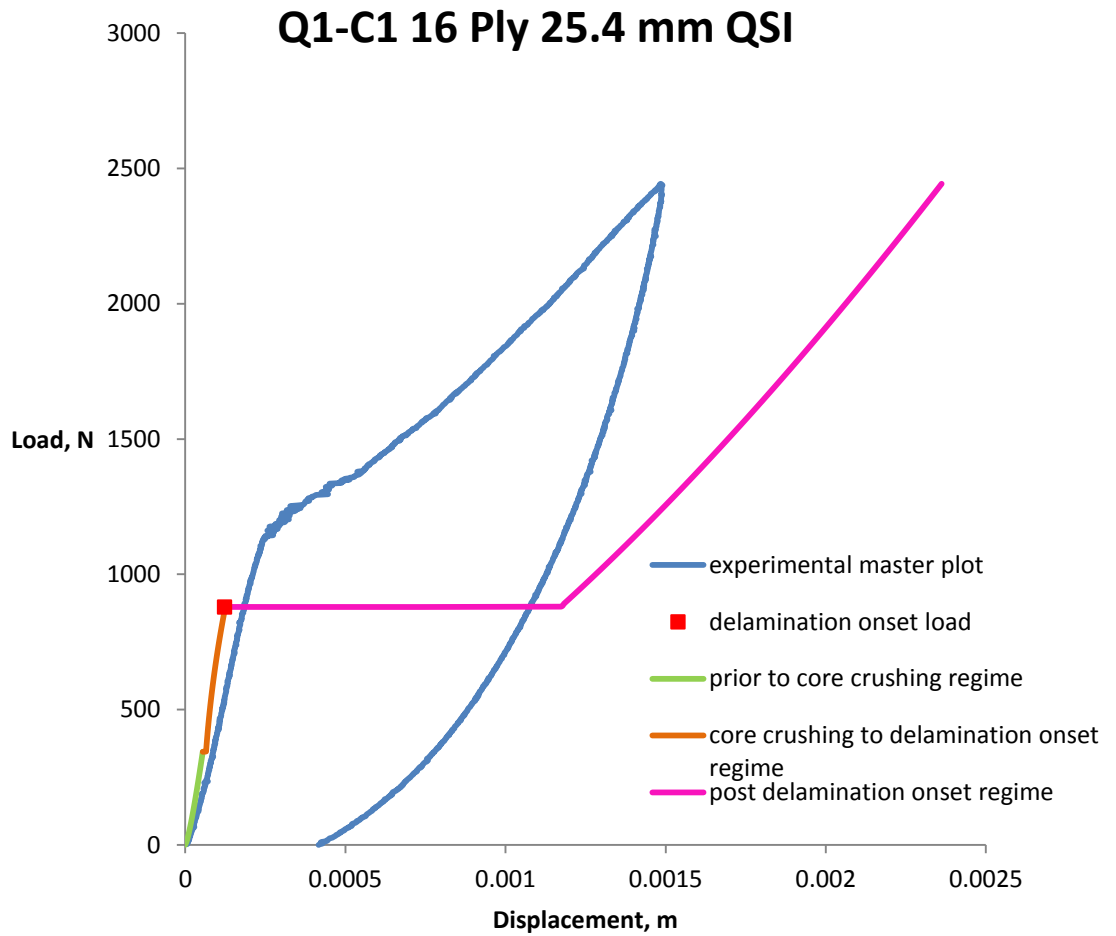


Figure 9.11. Plot showing the loading regime model versus experimental results for the 16 ply Q1-C1 sandwich configuration indented with the 25.4 mm diameter indenter.

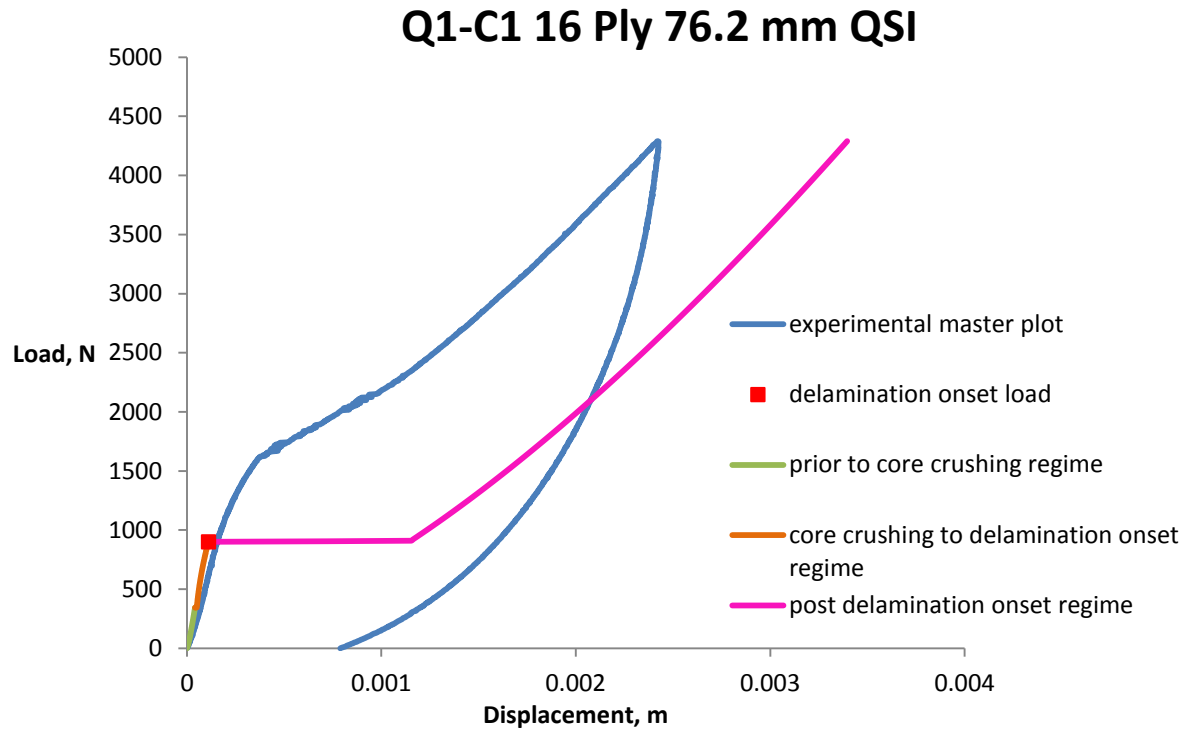


Figure 9.12. Plot showing the loading regime model versus experimental results for the 16 ply Q1-C1 sandwich configuration indented with the 76.2 mm diameter indenter.

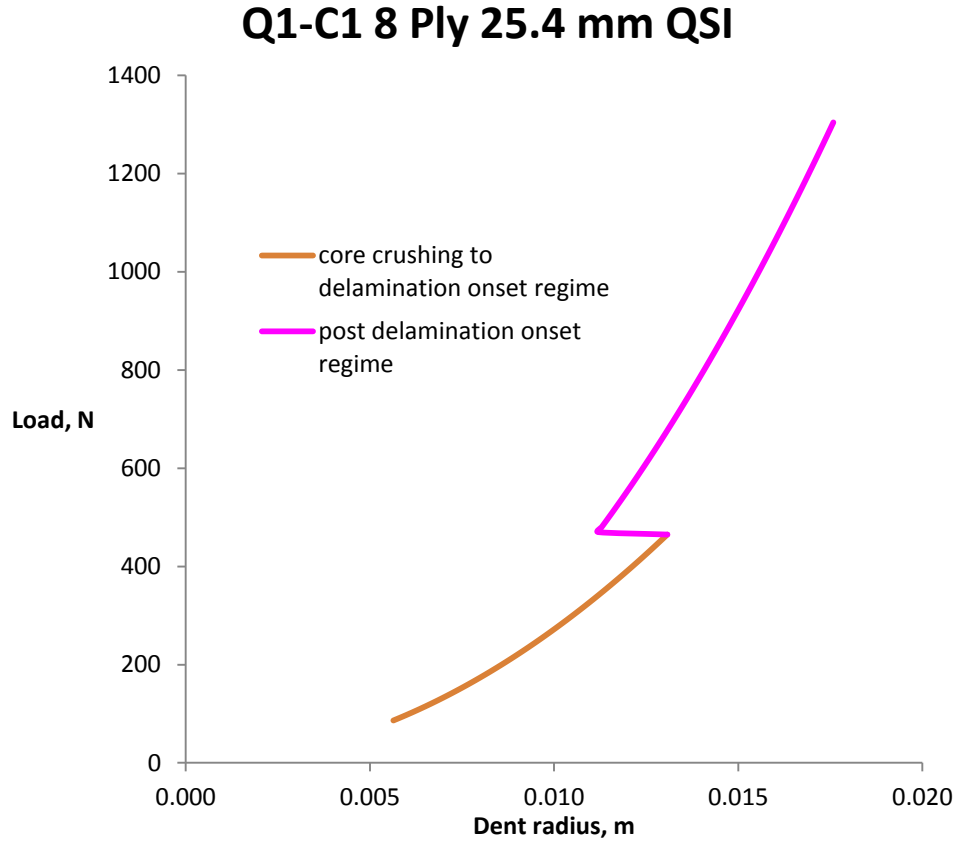


Figure 9.13. Load versus dent radius plot for the different regimes in the loading phase of the model for the 8 ply Q1-C1 sandwich configuration indented with the 25.4 mm diameter indenter.

9.9.1 Correction of Peak Displacement

The experimental evaluations of planar area of delamination and dent area show that the planar area of delamination is always smaller than the dent area, i.e., the delaminations are contained within the dent area and do not cover the entire dent area. These results are presented in Chapter 6 in Figures 6.9 and 6.17 for the 8 and 16 ply cases respectively. However, it was assumed in the predicted results presented in Figures 9.10-9.13 that the size of the delaminations for the individual interfaces was the same as the dent size, i.e, the planar area of delamination was assumed to be the same as the dent area. These assumptions caused a huge degradation in face sheet properties resulting in significantly larger peak displacements than what the

experiments showed. Analytical prediction of the exact ratio of planar area of delamination to dent area is not possible within the current model and is what motivates the proposed two-region plate solution presented in Chapter 12. To correct for the predicted peak displacements, a way had to be found that more correctly implemented the proportion of degraded and intact properties based on the relative amount of planar area of delamination as compared to the dent area.

To accomplish the above, the total dent region is assumed to consist of an inner region that is matrix cracked and fully delaminated, and an outer region that is intact (non-matrix cracked, non-delaminated). The approach chosen is to define homogenized properties of the face sheet that account for both the degraded properties of the inner region and the intact properties of the outer region. This was done in the following manner.

Let Z_p^* represent a homogenized property of the face sheet in the dented region. Also, let Z_d represent that property when fully degraded, corresponding to the inner region, and Z_i represent that property in its intact state, corresponding to the outer region. The fully degraded properties for the different face sheet layups are presented in Section 9.7 while the intact properties are presented in Section 9.4. The homogenized face sheet property of the dented region is represented as

$$Z_p^* = A_d * Z_d + A_i * Z_o$$

where $A_d + A_i = 1$ (9.32)

A_d and A_i may be thought of as the areas of the degraded and intact ratios. However, other choices of A_d and A_i may also be considered to better reflect the overall response of the face sheet. Guided by the experimental planar area of delamination to dent area ratios presented in Chapter 6, different A_d (and A_i) values of 0.3 (0.7), 0.5 (0.5), 0.7 (0.3) and 0.8 (0.2) were initially

evaluated to calculate the homogenized properties as defined by equation 9.32. These homogenized properties were then implemented in the model and the same values were used at every load from the delamination onset load to the peak load. That is, the displacement jump at the delamination onset load described previously was not addressed as part of this process. Figure 9.14 presents the results of this evaluation for the 8 ply Q1-C1 specimen indented with the 25.4 mm diameter indenter. As can be seen in the Figure, the displacement values at peak load varies for the different choices of A_d and A_i and the best results are obtained for values of 0.7 and 0.3, respectively. Similar evaluations were done for other sandwich configurations and it was found that at an A_d value of 0.7 and A_i value of 0.3 best corrects the peak load displacement. Therefore, these values of A_d and A_i were chosen for all model evaluations. However, as seen clearly in Figure 9.14, the issue of strain jump at the delamination onset load remains uncorrected, i.e., there is still a strain jump at the delamination onset load. To correct for this, a linear degradation of properties was justified. This is discussed in the subsequent sub-section.

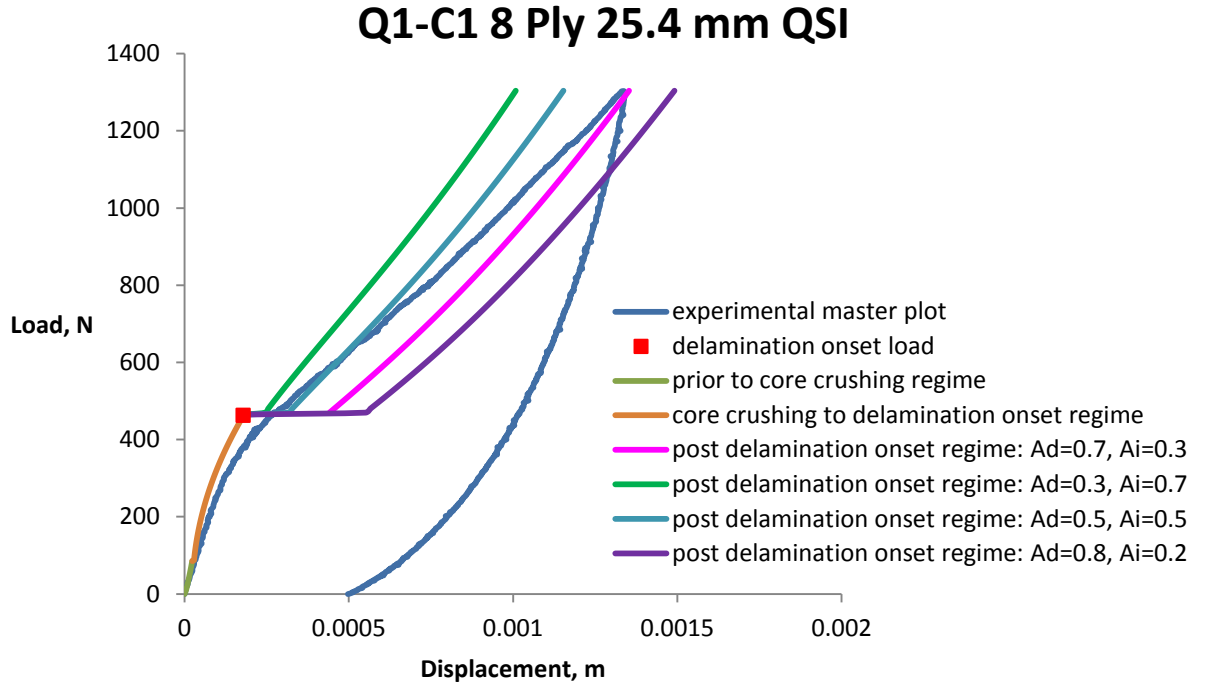


Figure 9.14. Model versus the experimental results for the different A_d and A_i ratios, as defined by equation 9.30, for the 8 ply sandwich configuration indented with the 25.4 mm diameter indenter.

9.9.2 Linear Degradation of Face Sheet Properties

As can be seen in Figure 9.14, there still remained the issue of strain jump at the delamination onset load which needed to be corrected. To correct this, a linear degradation of properties was assumed in the following manner.

Let δ^* represent the displacement value to which the sandwich structure is loaded such that upon subsequent unloading from this displacement value, the resultant residual dent depth in the sandwich structure is the same as the BVID residual dent depth defined in Chapter 3 for the 8 and 16 ply cases. The face sheet properties are therefore linearly degraded from the point of delamination onset to δ^* . The intact values of properties were taken at the delamination onset

load and the values obtained using equation (9.32), with $A_d=0.7$ and $A_i=0.3$, were taken at δ^* . That is, at delamination onset load, Z_p^* was taken equal to Z_i , since $A_d=0$ and $A_i=1$. At δ^* ,

$$Z_p^* = 0.7 * Z_d + 0.3 * Z_o \quad (9.33)$$

The linear degradation of properties from the intact values at the delamination onset load to the degraded values, defined by equation 9.33, at δ^* resulted in decreasing values of the properties being implemented in the model between the delamination onset load and δ^* . Figures 9.15 to 9.18 present the results based on the linear property degradation for the 8 and 16 ply Q1-C1 specimens indented with the 25.4 mm and the 76.2 mm diameter indenter respectively. The linear property degradation also corrected the jump in dent radius seen at the delamination onset load seen in the earlier model. The corrected load versus dent radius results for the Q1-C1 specimen indented with the 25.4 mm diameter indenter is presented in Figure 9.19.

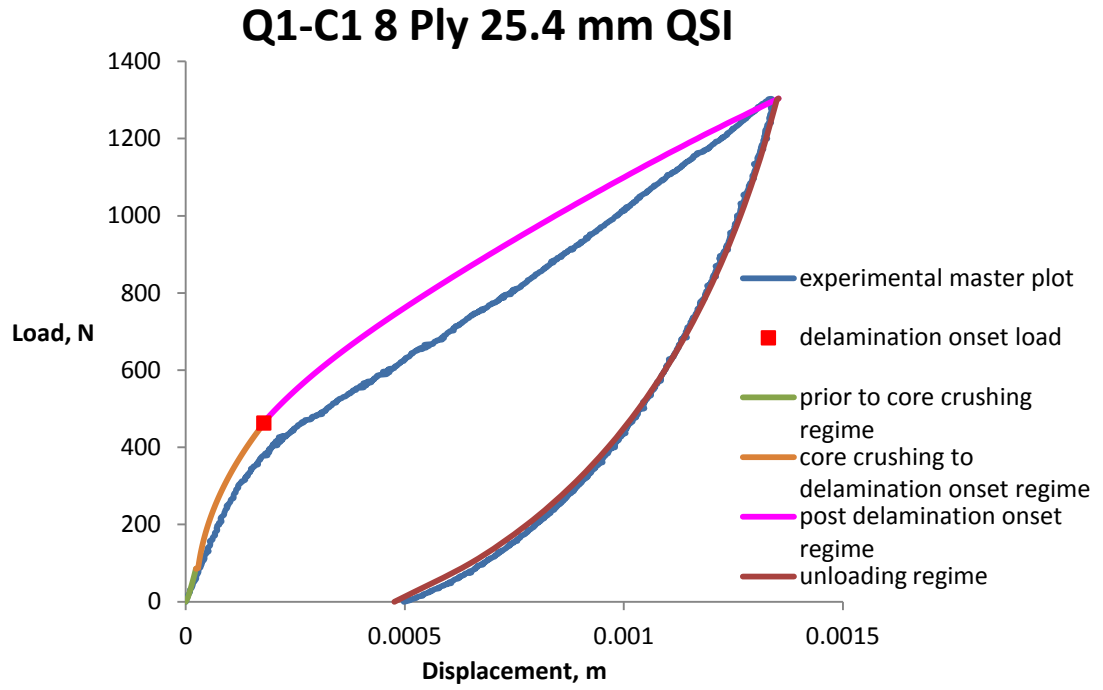


Figure 9.15. Improved (linear degradation) post delamination onset regime model for the 8 ply Q1-C1 sandwich configuration indented with the 25.4 mm diameter indenter.

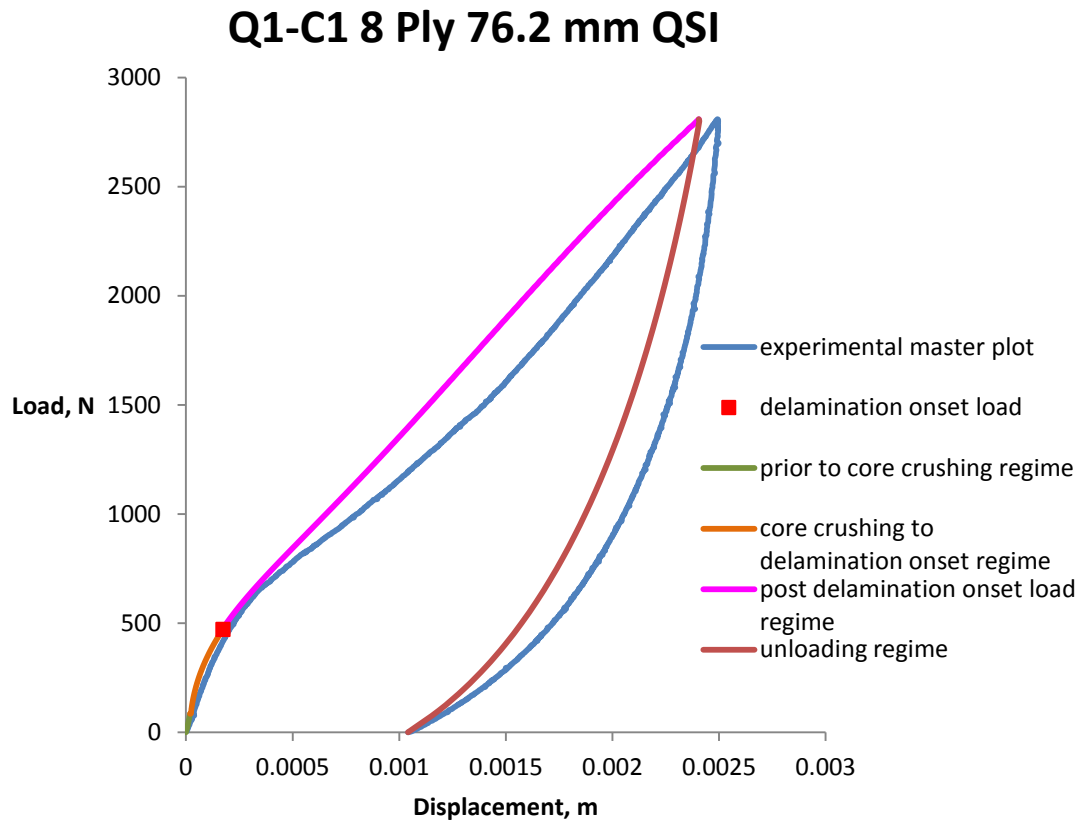


Figure 9.16. Improved (linear degradation) post delamination onset regime model for the 8 ply Q1-C1 sandwich configuration indented with the 76.2 mm diameter indenter.

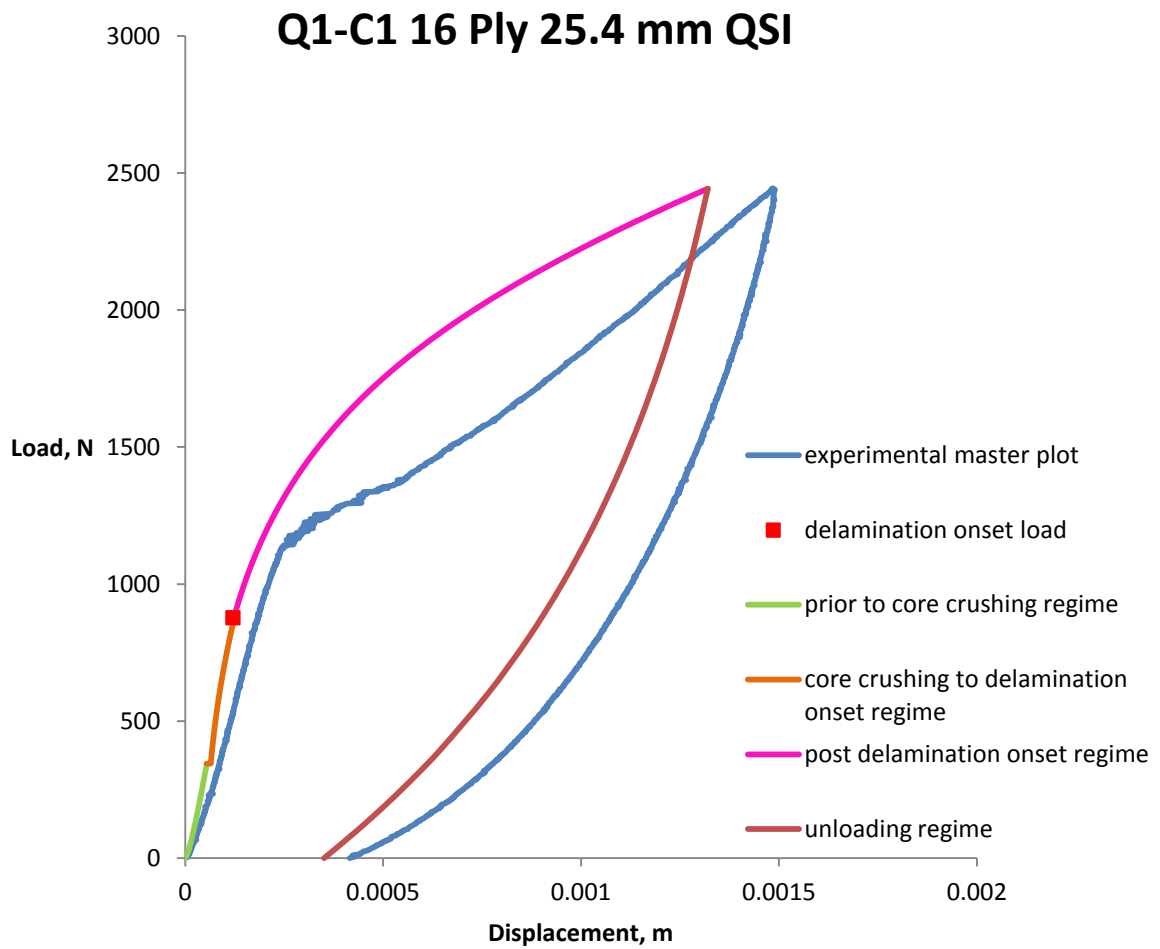


Figure 9.17. Improved (linear degradation) post delamination onset regime model for the 16 ply Q1-C1 sandwich configuration indented with the 25.4 mm diameter indenter.

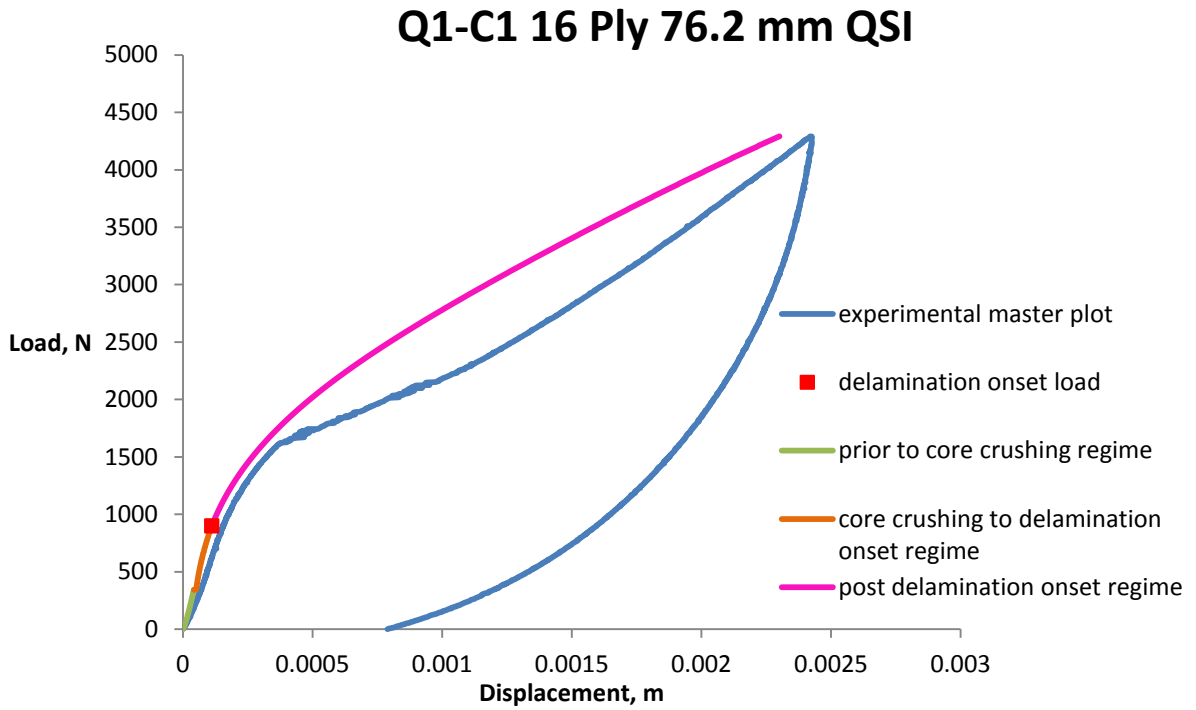


Figure 9.18. Improved (linear degradation) post delamination onset regime model for the 16 ply Q1-C1 sandwich configuration indented with the 76.2 mm diameter indenter.

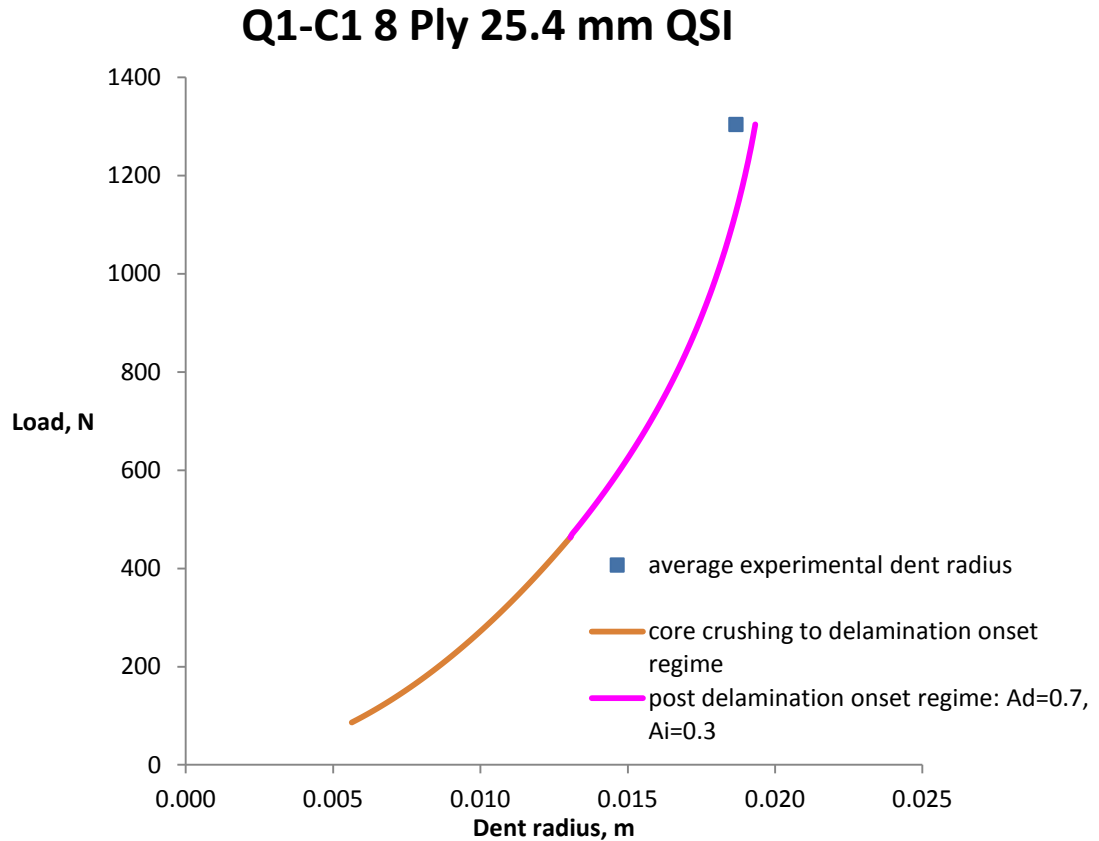


Figure 9.19. Load versus dent radius plot for the 8 ply Q1-C1 sandwich configuration indented with the 25.4 mm diameter indenter assuming linear property degradation.

9.10 The Unloading Regime

The Rayleigh-Ritz method of potential energy minimization was extended to the unloading regime to model the unloading response of the face sheet. The total system potential energy was calculated by considering the face sheet bending and membrane energy as well as the total external work done. The bending and membrane energy for the unloading phase are calculated using equations 9.12 and 9.16 respectively. The face sheet properties, as defined at the peak load using equation 9.33, are used at the same value during the entire unloading regime.

According to Minakuchi et al's idealized core behavior [65], there is an initial elastic zone in the

unloading regime with a constant core tensile modulus, E_{zt} . This is followed by a constant plastic flow stress, p_{ot} . In the model for the unloading regime, the initial elastic behavior is ignored and the core is believed to resist face sheet deflection by pulling against it with a constant core resistive pressure, p_{ot} , right from the time the unloading begins all the way to zero load. Figure 9.20 presents a schematic that shows the core behavior during the unloading regime.

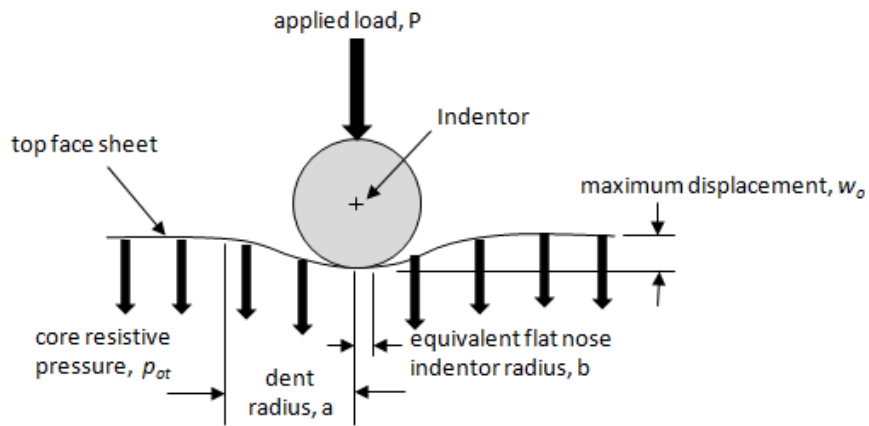


Figure 9.20. Schematic showing core behavior during the unloading regime.

The total work formula that was used in the loading regime therefore gets modified for the unloading regime as

$$V = Pw_o + \pi p_{ot} b^2 w_o + 2\pi p_{ot} \int_b^{a_c} w(r) r dr \quad (9.34)$$

In equation 9.34, a_c is the radius of the crushed core. It was initially assumed that the entire crushed zone starts getting pulled back together as the unloading begins. Here, the crushed zone is assumed to be the size of the dent at peak load determined from the loading model.

Therefore, a_c in equation 9.34 is the same as the dent radius at peak load. The total potential

energy based on the face sheet bending energy, face sheet membrane energy and the total work, as defined by equation 9.34, was determined and the resulting equation was minimized with respect to the maximum displacement. By using the value of peak displacement and the crush radius, a_c , the load, P , was solved for. As expected, there was a sudden drop in load at the peak displacement when the switch was made from the loading to unloading regime. This is shown by the regime marked AB in the Q1-C1, 8 ply 25.4 mm diameter unloading results presented in Figure 9.21. That is, because the direction of the core crush resistance has changed in the unloading regime and it acts in the same direction as the externally applied load, a sudden drop in the external load must occur for the displacement to remain constant. Further unloading using the same maximum crush radius is then computed from the dropped load, P_{new} , to zero load. The maximum displacement, w_o , at every load was solved for using the minimized energy equation. This resulted in an unloading trajectory as shown by path BC in Figure 9.21. While the overall unloading path from A to C was inconsistent with what has been observed experimentally, the residual dent depth value that the model predicted is close to the experimental value. The assumption that at zero load the entire crushed radius gets pulled back gives could correspondence of residual dent depth with the experimental results.

In order to obtain better correlation with the experimental unloading trajectory, it is postulated that initially, i.e., at the peak displacement where the unloading begins, a somewhat smaller central region of the entire crushed zone initially “uncrashes”. Supporting arguments and derivations for this postulate are presented in Appendix J. The evaluation of this smaller crushed zone that initially deflects at the peak load, when the change is made from loading to the unloading regime, was calculated by the minimization of the total system potential energy with respect to the maximum displacement. In this evaluation, the total work is evaluated using

equation (9.34). By keeping the peak displacement and the peak load fixed, the resultant equation is solved for a_i , which at the peak load represents the radius of the inner portion of the crush zone that initially uncrushes during unloading. It is observed that the calculated value of a_i is in the vicinity 80% of a_c for all the sandwich configurations. In solving for the maximum displacement at every load in the unloading regime, the crush zone radius is allowed to increase linearly from a_i to a_c as the unloading progresses. That is at the peak load, a slightly smaller crush zone radius, a_i , is used while at zero load, the maximum crush zone radius, a_c , is used. The maximum displacement at every load level in the unloading regime is solved through the total potential energy minimization with respect to w_o . The correlation between the predicted and the experimental results is excellent as shown in Figure 9.22 for the 8 ply Q1-C1 sandwich configuration indented with the 25.4 mm diameter indenter. The unloading regime therefore is modeled in this manner for all the sandwich configurations. It is pointed out that these assumptions only affect the path from point A to C in Figure 9.21 and are adopted solely to improve the correlation of predicted and observed results along the path. The model's predictions of the peak displacement at point A, the residual displacement at point C, and the residual dent radius, a_c , are not affected.

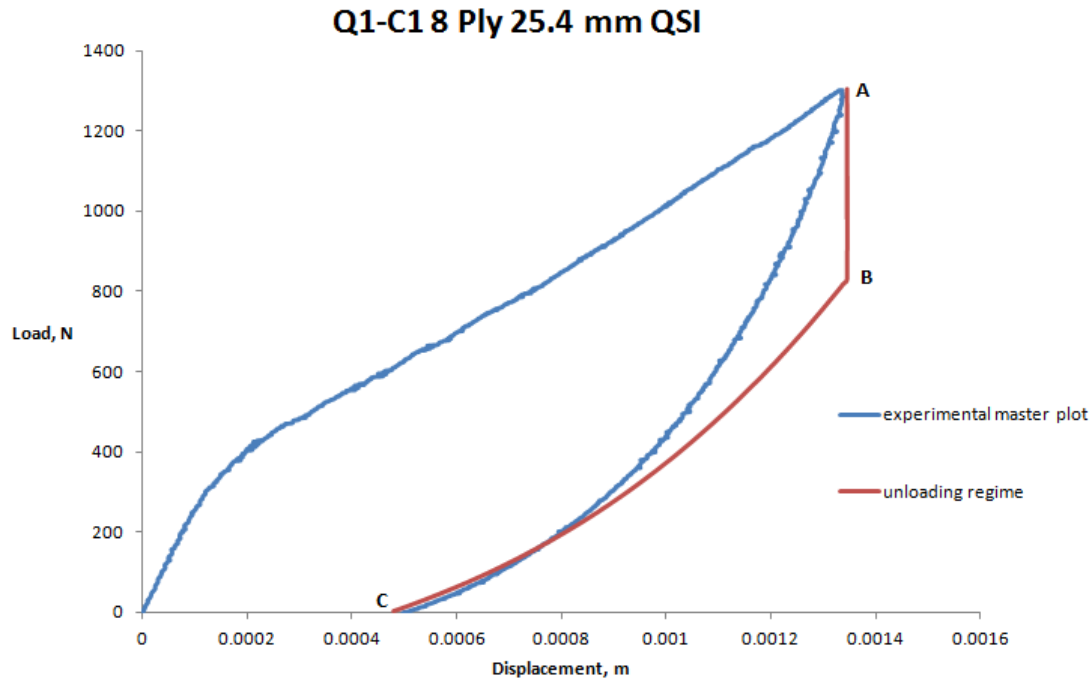


Figure 9.21. Model versus experimental unloading regime results for the 8 ply, Q1-C1 sandwich configuration indented with the 25.4 mm diameter indenter assuming uncrushing of the entire crush zone at every load.

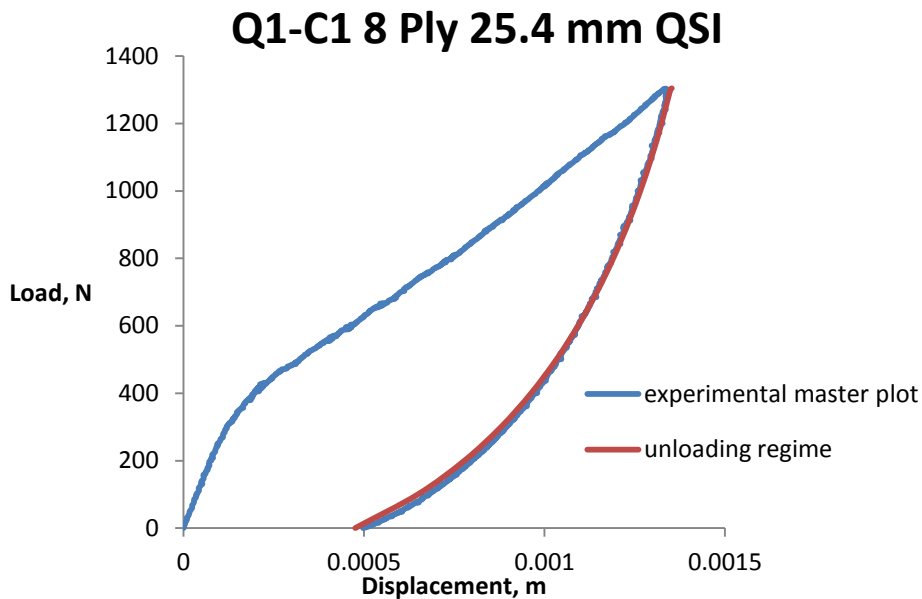


Figure 9.22. Model versus experimental unloading regime results for the 8 ply Q1-C1 sandwich configuration indented with the 25.4 mm diameter indenter assuming linear increase in crush zone radius getting uncrushed from the peak load to zero load.

9.11 Summary

An analytical model has been developed and presented in this chapter for predicting the loading and unloading response of sandwich structures undergoing quasi-static indentation up to damage within the vicinity of BVID. The model is capable of predicting the core crush onset load, the delamination onset load, the maximum displacement versus load, the dent radius versus load, the residual dent depth and the residual dent radius. Up to core crushing, the model uses classical plate theory for small deflections of a plate on an elastic foundation. Beyond this point, a Rayleigh-Ritz method of total potential energy minimization is utilized.

The model can be useful for damage resistance evaluations from the viewpoint of design when dent depth or dent diameter is considered as the damage metric. The residual dent depth and dent diameter prediction capabilities of the model are useful for CAI modeling where these parameters can be implemented as pre-existing damage. An evaluation on the accuracy of the model for the different sandwich configurations considered in this work is presented in Chapter 10. One of the major issues in the model that requires further attention is the prediction of the relative amount of delamination with respect to the size of the external dent so that the properties can be more accurately degraded. To this end, a two-region plate solution has also been proposed and is discussed in Chapter 12 under “Future Work”.

Chapter 10

MODELING RESULTS

Introduction

Two of the key features of the analytical model derived in Chapter 9 are its ability to predict residual dent depths and dent diameters for indentation within the vicinity of BVID. These damage metrics are important for a variety of design uses, such as parametric trade-off studies. They also may be useful for implementation in a compression-after-impact (CAI) model, i.e., as a pre-existing damage state.

This chapter presents a comparison of the model predictions with experimental results for the different 8 and 16 ply sandwich configurations with BVID. The key comparisons include those between the predicted dent depth and dent diameter results versus those determined experimentally using the ultrasonic technique described in Chapter 5. A comparison of the load versus displacement plots between the model predictions and the experimental results are also presented in order to qualitatively analyze the ability of the model to capture the correct mechanics of the sandwich indentation problem.

10.1 Dent Diameter and Dent Depth Results

As described above, one major use of the analytical model derived in this dissertation is the prediction of the residual dent diameters and dent depths. Tables 10.1 and 10.2 present a comparison of the model predictions with the experimental results for damage within the vicinity of BVID. Likewise, Tables 10.3 and 10.4 present a comparison of the model predictions with the experimental dent diameter results for the 8 and 16 ply cases respectively. The predicted residual dent depths are the values obtained by the unloading regime model derived in Chapter 9. The

predicted residual dent diameter values are those obtained at the peak load by the loading model from the delamination onset load to the peak load. That is, the model assumes that the diameter of the crushed radius does not change during unloading. The percentage error of the model is calculated by equation 10.1. These results are also presented in Tables 10.1-10.4 where a negative percentage means the model under-predicts the results compared to the experimental whereas a positive percentage means the model over-predicts the results.

$$\% \text{ error of model} = 100 * \left[\frac{\text{predicted value} - \text{experimental value}}{\text{experimental value}} \right] \quad (10.1)$$

Summaries of the overall range of the percentage errors as well as the average percentage errors are presented in Tables 10.5 and 10.6 respectively. The results are categorized by the face sheet thicknesses and the diameter of the indenter used for testing.

Table 10.1. Comparison of the experimental versus predicted dent depths for the 8 ply case.

sandwich configuration (8 Ply)	test indenter size (mm)	average experimental dent depth (mm)	model predicted dent depth (mm)	% error of model
Q1-C1	25.4	0.50	0.47	-6.00
Q1-C2	25.4	0.47	0.42	-10.64
Q1-C3*	25.4	0.53	0.56	5.66
Q2-C1	25.4	0.46	0.48	4.35
Q3-C1	25.4	0.47	0.47	0.00
Q4-C2	25.4	0.53	0.43	-18.87
Q4-C3*	25.4	0.46	0.51	10.87
Q1-C1	76.2	1.04	1.04	0.00
Q1-C2	76.2	0.99	0.96	-3.03
Q1-C3*	76.2	1.04	0.95	-8.65
Q2-C1	76.2	0.96	1.04	8.33
Q3-C1	76.2	1.10	1.04	-5.45
Q4-C2	76.2	1.02	0.95	-6.86
Q4-C3	76.2	0.91	0.83	-8.79

*The BVID load for these sandwich configurations was higher than the rest of the sandwich configurations for the 8 ply case.

Table 10.2. Comparison of the experimental versus predicted dent depths for the 16 ply case.

sandwich configuration (16 Ply)	test indenter size (mm)	average experimental dent depth (mm)	model predicted dent depth (mm)	% error of model
Q1-C1	25.4	0.43	0.35	-18.60
Q1-C2	25.4	0.42	0.31	-26.19
Q1-C3	25.4	0.30	0.24	-20.00
Q2-C1	25.4	0.39	0.35	-10.26
Q3-C1	25.4	0.40	0.36	-10.00
Q4-C1	25.4	0.45	0.35	-22.22
Q4-C3	25.4	0.28	0.24	-14.29
Q5-C1	25.4	0.42	0.35	-16.67
Q1-C1	76.2	0.80	0.77	-3.75
Q1-C2	76.2	0.82	0.69	-15.85
Q1-C3	76.2	0.64	0.56	-12.50
Q2-C1	76.2	0.74	0.77	4.05
Q3-C1	76.2	0.77	0.77	0.00
Q4-C3	76.2	0.71	0.56	-21.13
Q5-C1	76.2	0.83	0.77	-7.23

Table 10.3. Comparison of the experimental versus predicted dent diameters for the 8 ply case.

sandwich configuration (8 Ply)	test indenter size (mm)	average experimental dent diameter (mm)	model predicted dent diameter (mm)	% error of model
Q1-C1	25.4	37	39	3.59
Q1-C2	25.4	34	36	7.18
Q1-C3*	25.4	32	34	5.75
Q2-C1	25.4	36	39	9.13
Q3-C1	25.4	36	39	7.28
Q4-C2	25.4	37	36	-1.41
Q4-C3*	25.4	33	33	-0.18
Q1-C1	76.2	58	53	-8.14
Q1-C2	76.2	55	50	-9.09
Q1-C3*	76.2	47	45	-5.06
Q2-C1	76.2	56	53	-4.10
Q3-C1	76.2	55	53	-3.02
Q4-C2	76.2	57	50	-11.96
Q4-C3	76.2	42	41	-3.33

*The BVID load for these sandwich configurations was higher than the rest of the sandwich configurations for the 8 ply case.

Table 10.4. Comparison of the experimental versus predicted dent diameters for the 16 ply case.

sandwich configuration (16 Ply)	test indenter size (mm)	average experimental dent diameter (mm)	model predicted dent diameter (mm)	% error of model
Q1-C1	25.4	69	57	-17.53
Q1-C2	25.4	64	54	-16.43
Q1-C3	25.4	51	43	-16.04
Q2-C1	25.4	66	57	-12.82
Q3-C1	25.4	67	57	-14.42
Q4-C1	25.4	63	57	-9.24
Q4-C3	25.4	40	43	7.05
Q5-C1	25.4	69	57	-16.61
Q1-C1	76.2	82	71	-12.67
Q1-C2	76.2	79	67	-14.84
Q1-C3	76.2	62	54	-12.72
Q2-C1	76.2	84	71	-14.66
Q3-C1	76.2	91	71	-21.45
Q4-C3	76.2	56	54	-2.89
Q5-C1	76.2	87	72	-17.34

Table 10.5. Summary of the percentage range of error for the dent depth and dent diameter predictions under the different test conditions.

Percentage Range of Error		
test condition	dent depth predictions	dent diameter predictions
8 ply, 25.4 mm diameter indenter tests	-18.87% to 10.87%	-1.41 % to 9.13%
8 ply, 76.2 mm diameter indenter tests	-8.79% to 8.33%	-11.96% to 3.02%
16 ply, 25.4 mm diameter indenter tests	-26.19% to -10.00%	-17.53% to 7.05%
16 ply, 76.2 mm diameter indenter tests	-21.13% to 4.05%	-21.54% to -2.89%

Table 10.6. Summary of the average percentage error for the dent depth and dent diameter predictions under the different test conditions.

Average Percentage Error		
test condition	dent depth predictions	dent diameter predictions
8 ply, 25.4 mm diameter indenter tests	-2.09%	4.48%
8 ply, 76.2 mm diameter indenter tests	-3.49%	-6.39%
16 ply, 25.4 mm diameter indenter tests	-17.28%	-12.01%
16 ply, 76.2 mm diameter indenter tests	-8.06%	-13.80%

Tables 10.1-10.6 show that the depth and dent diameter predictions are overall better for the 8 ply case as compared to the 16 ply case. The average dent depth and dent diameter errors in the 8 ply case are less than that in the 16 ply case for both the indenter sizes. A close review of the individual sandwich configuration results presented in Table 10.1 shows that the predicted dent depth is overall pretty close to those determined experimentally for the 8 ply face sheets. This is useful from the viewpoint of CAI modeling since dent depth is a primary metric and a

primary driver of CAI strength. From the viewpoint of dent depth and dent diameter predictions, the model's accuracy is likely acceptable for most practical purposes.

10.2 Load versus Displacement Comparisons

This section presents comparisons of the load versus displacement predictions versus the experimental results for the different sandwich configurations for both the 8 and 16 ply cases tested to loads in the vicinity of the BVID threshold. Although the key parameters of interest are the residual dent depth and the dent diameters, the individual plots for the different sandwich configurations are presented to show how well or poorly the model captures the mechanics of the sandwich indentation problem. For discussion purposes, the plots and the comparison of results are considered in terms of the four regimes and the associated different modeling approaches that were described in Chapter 9. The first regime is the regime prior to core crushing, followed by the regime between the core crushing and the delamination onset load. The third regime is between the delamination onset load and the peak load and the last regime is the unloading regime. In most cases, the results are compared with the experimental master plots, the derivation of which are described in Chapter 8. In cases where the model is compared to an individual specimen result because no master plot was available for this sandwich configuration, it is clearly stated. The delamination onset loads, as predicted by the method presented in Chapter 9 are also presented in the plots.

10.2.1 8 Ply Specimens Indented with the 25.4 mm Diameter Indentor

Figures 10.1 to 10.7 compares the load versus displacement predictions with the experimental results for the 8 ply specimens indented with the 25.4 mm diameter indentor. The approximate location of the “knee”, referred to as the “transition regime” as defined in Chapter 4, in the model predictions compares well with the experimental results. It is believed that the

onset of delamination in actual experiments happens in the transition regime. In this regard, the delamination onset load predictions also compare well with the experimental results. In the regime subsequent to the delamination onset, the load versus displacement plot characteristics for the model do not appear to reflect the experimental results. That is, the experiments generally show stiffening after the transition region whereas the model shows softening. This happens because, although the model accurately reflects the total property degradation at peak load, the rate subsequent to the delamination onset load at which this occurs in the actual experiments appears to initially be faster than that which is predicted.

As referred to above, despite the difference in the post transition regime in the model's predictions versus the experimental results, Figures 10.1 – 10.7 show that the peak displacements predicted by the model are generally reasonably accurate. The figures also show that the model captures the mechanics of the unloading process quite well. The model predictions can be made to better agree with the experimental results by altering the way in which the material properties and the structural properties are degraded. That is, the model contains within it the capacity to fully recreate the experimental observations. However, within the construct of the model, there is no clear mechanics-based approach to choose the specific degradation rate such that this occurs. Moreover, making the modifications would not affect the peak predicted displacements nor the results in Tables 10.1-10.6. This observation lends credibility to the assumption that the mechanics of the model are fundamentally correct and reflective of physical behavior, albeit without exactly capturing the details of damage onset and growth.

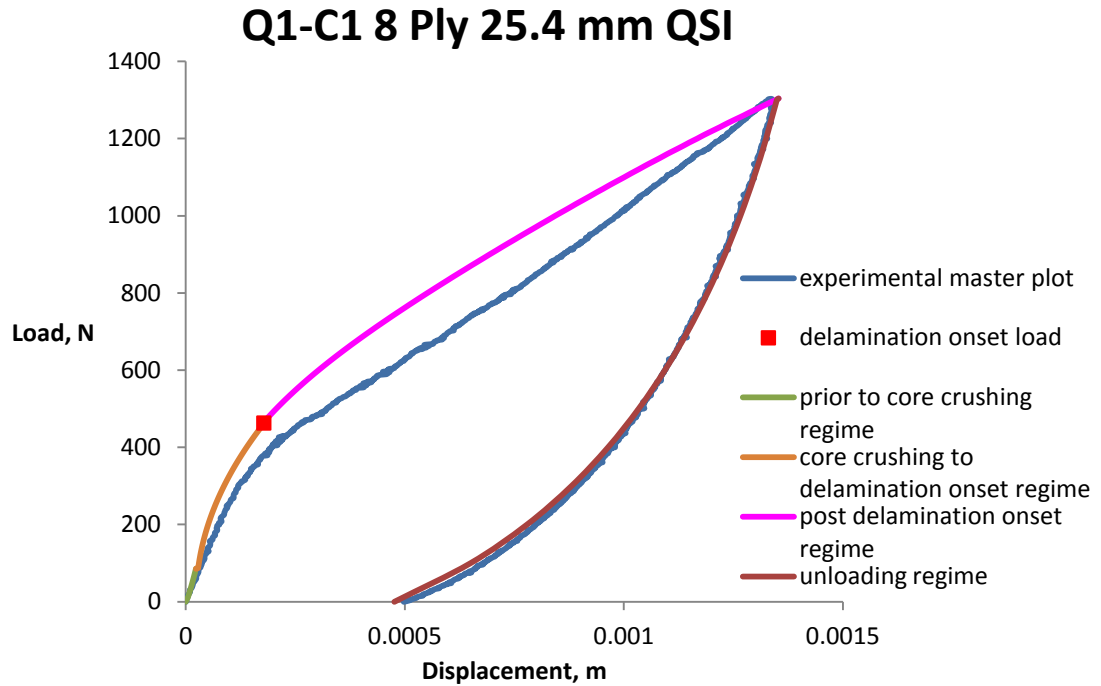


Figure 10.1. Q1-C1 8 ply model versus experimental P-d plot comparisons for specimens indented with the 25.4 mm diameter indenter.

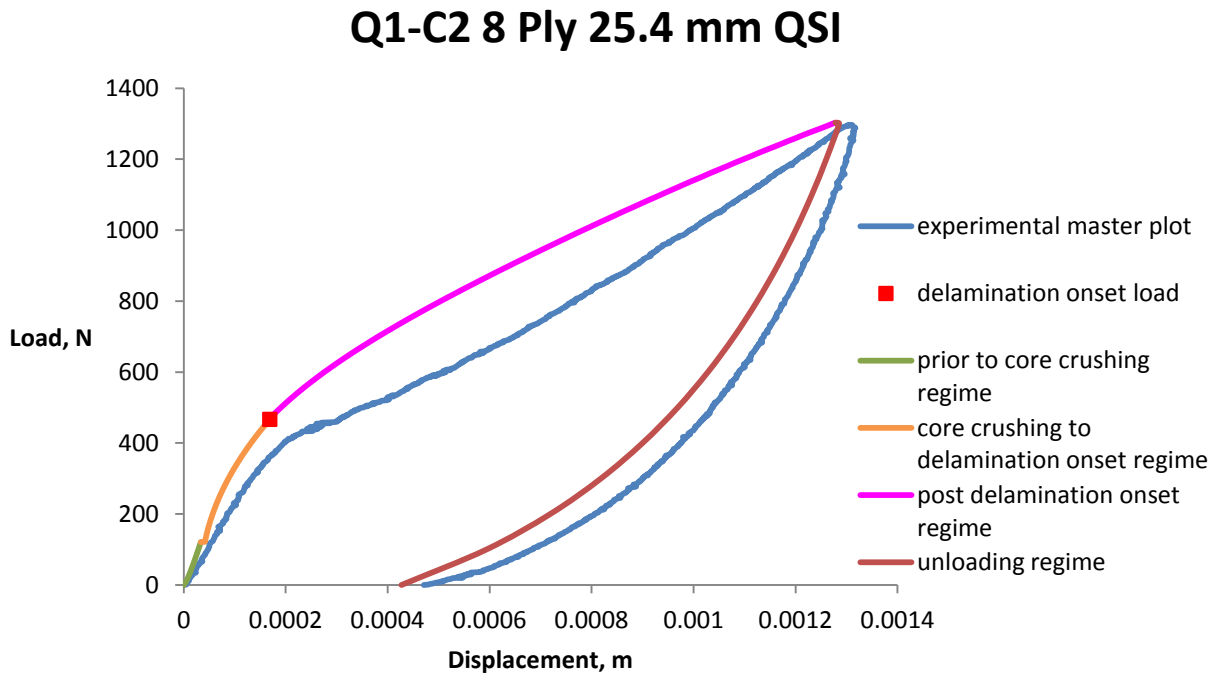
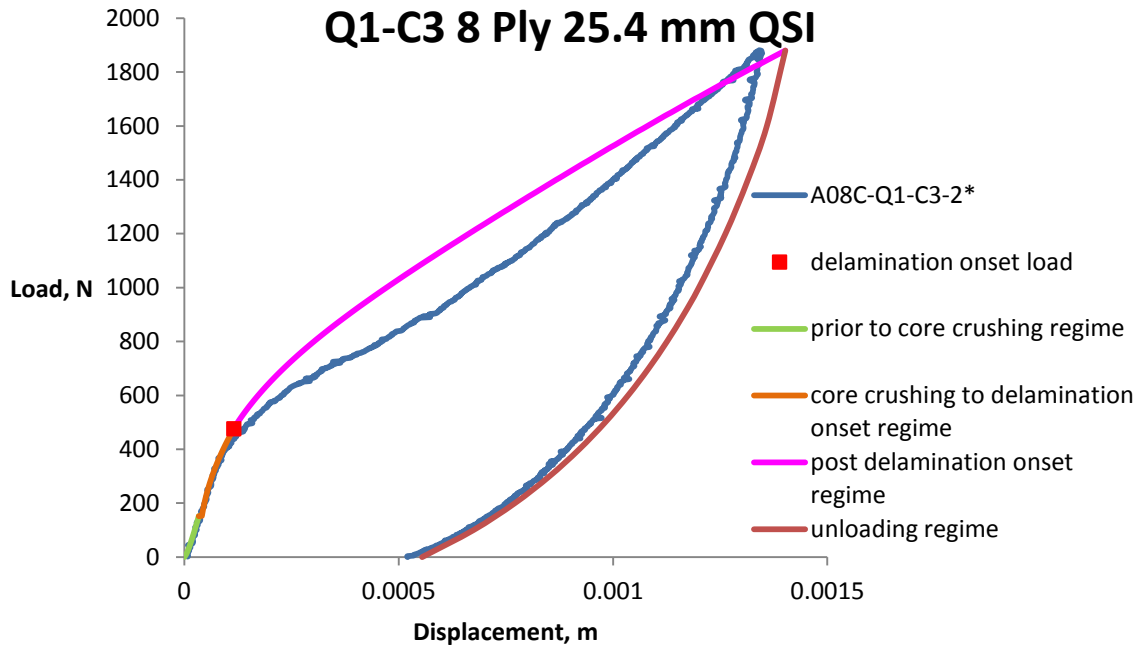


Figure 10.2. Q1-C2 8 ply model versus experimental P-d plot comparisons for specimens indented with the 25.4 mm diameter indenter.



*There was no master plot for this configuration. Specimen A08C-Q1-C3-2 was the only specimen indented to BVID load threshold

Figure 10.3. Q1-C3 8 ply model versus experimental P-d plot comparisons for specimens indented with the 25.4 mm diameter indenter.

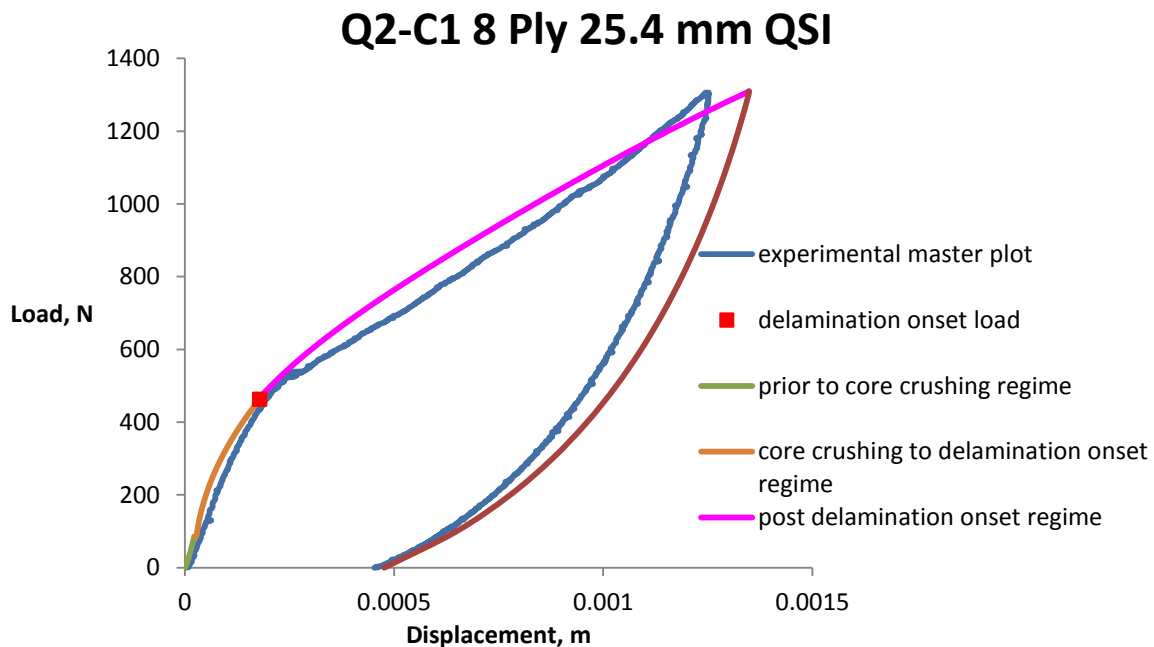


Figure 10.4. Q2-C1 8 ply model versus experimental P-d plot comparisons for specimens indented with the 25.4 mm diameter indenter.

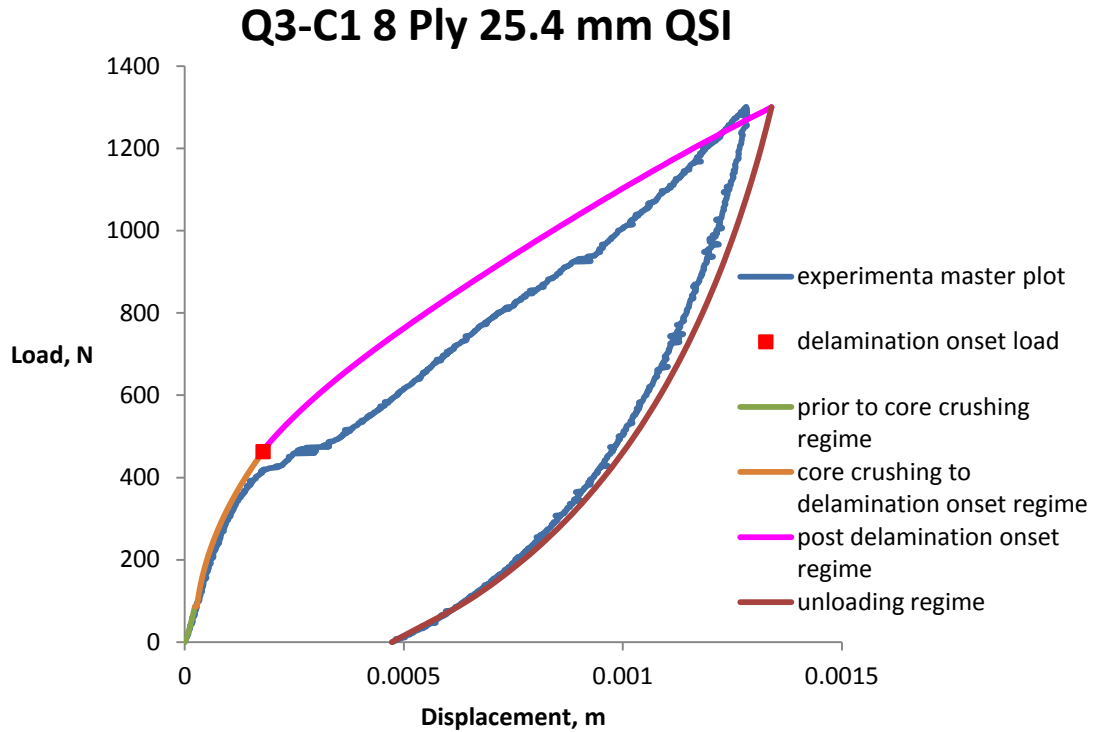


Figure 10.5. Q3-C1 8 ply model versus experimental P-d plot comparisons for specimens indented with the 25.4 mm diameter indenter.

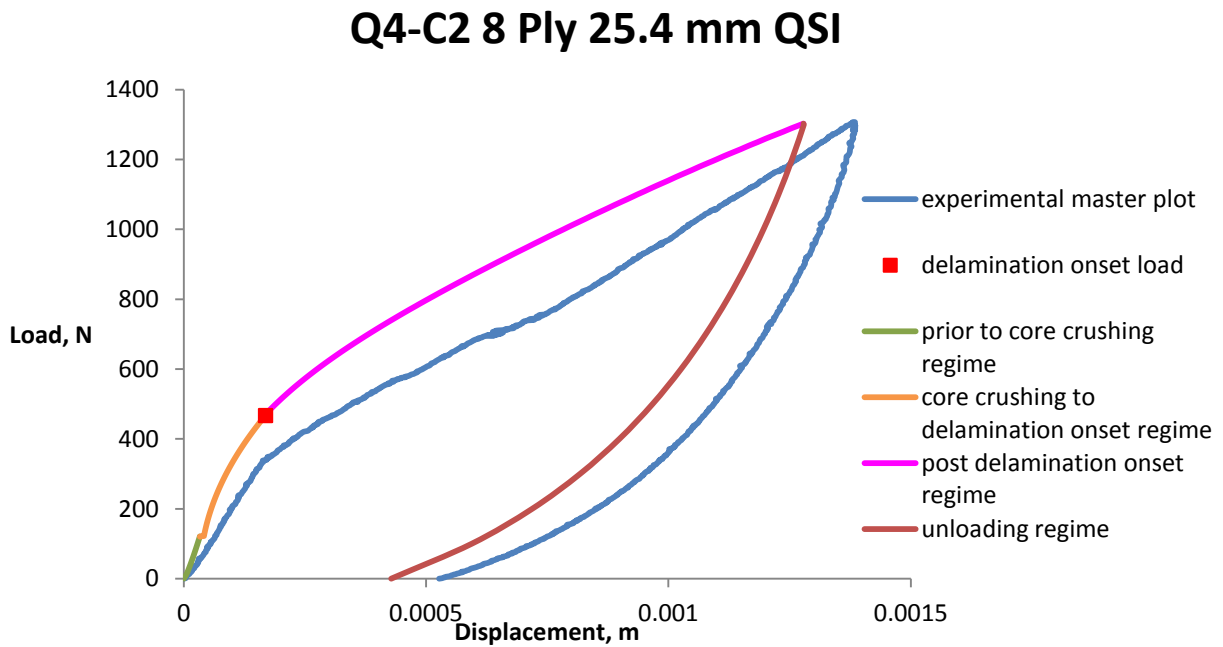


Figure 10.6. Q4-C2 8 ply model versus experimental P-d plot comparisons for specimens indented with the 25.4 mm diameter indenter.

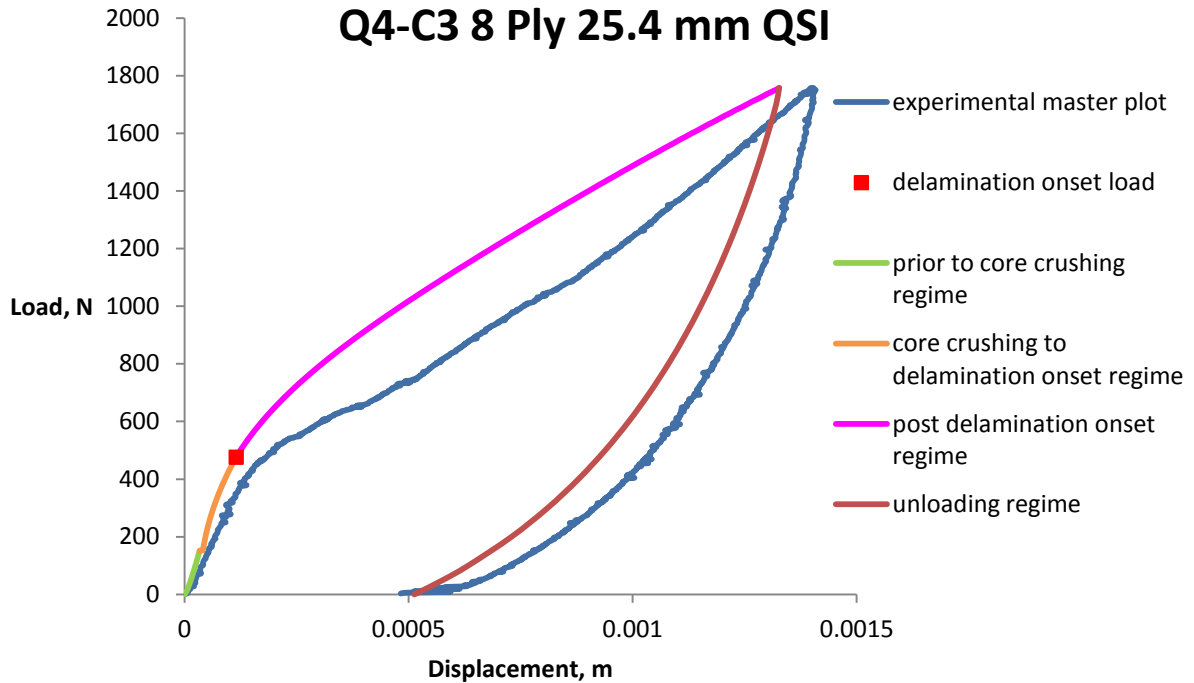


Figure 10.7. Q4-C3 8 ply model versus experimental P-d plot comparisons for specimens indented with the 25.4 mm diameter indenter.

10.2.2 8 Ply Specimens Indented with the 76.2 mm Diameter Indenter

Figures 10.8 to 10.14 compare load versus displacement model predictions with the experimental results for the 8 ply specimens indented with the 76.2 mm diameter indenter. Just as for the 8 ply specimens indented with the 25.4 mm diameter indenter, the prediction for the location of the knee compares well with the experimental results. The delamination onset load predictions also compare well with the experimental results. In the regime subsequent to the delamination onset load, the load versus displacement plot characteristics resemble the experimental results somewhat better than what was seen for the 8 ply specimens indented with the 25.4 mm diameter indenter. This is likely due to a more rapid growth of the area of the damaged region within the model than that which occurs for the 25.4 mm diameter indenter,

which causes the model to predict a more compliant response after the transition regime. In the unloading regime, the model again captures the mechanics of the unloading process quite well.

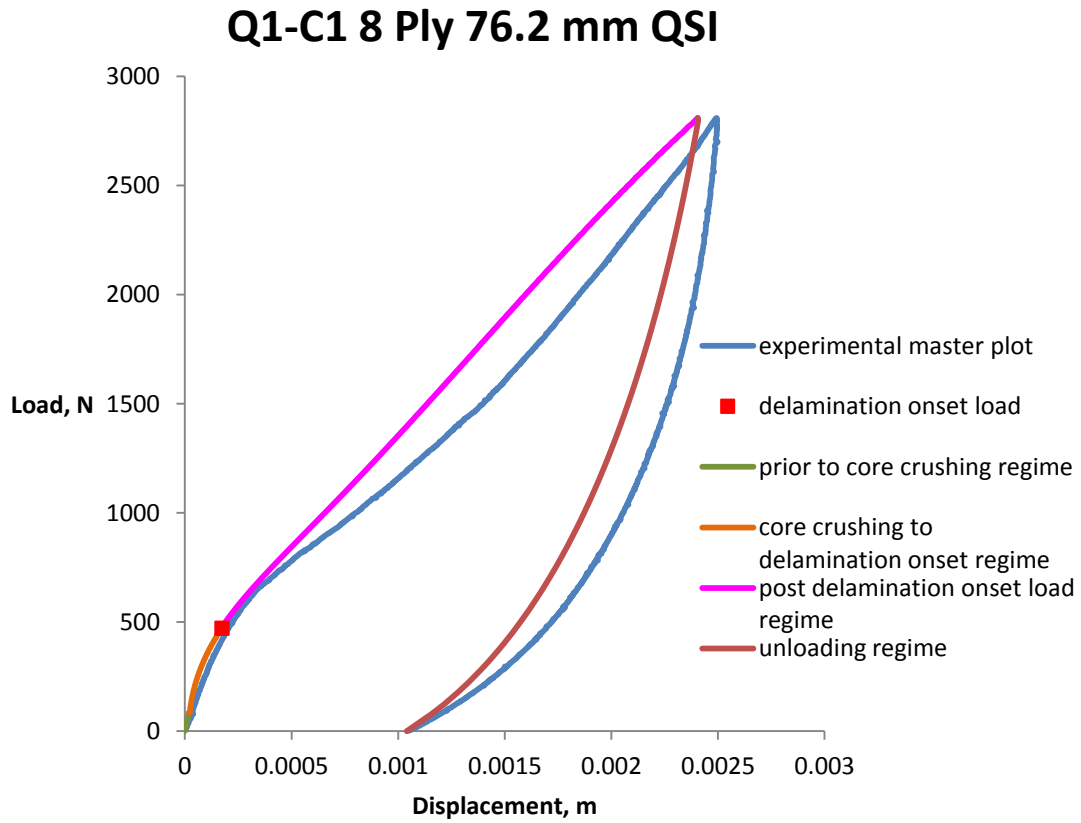


Figure 10.8. Q1-C1 8 ply model versus experimental P-d plot comparisons for specimens indented with the 76.2 mm diameter indenter.

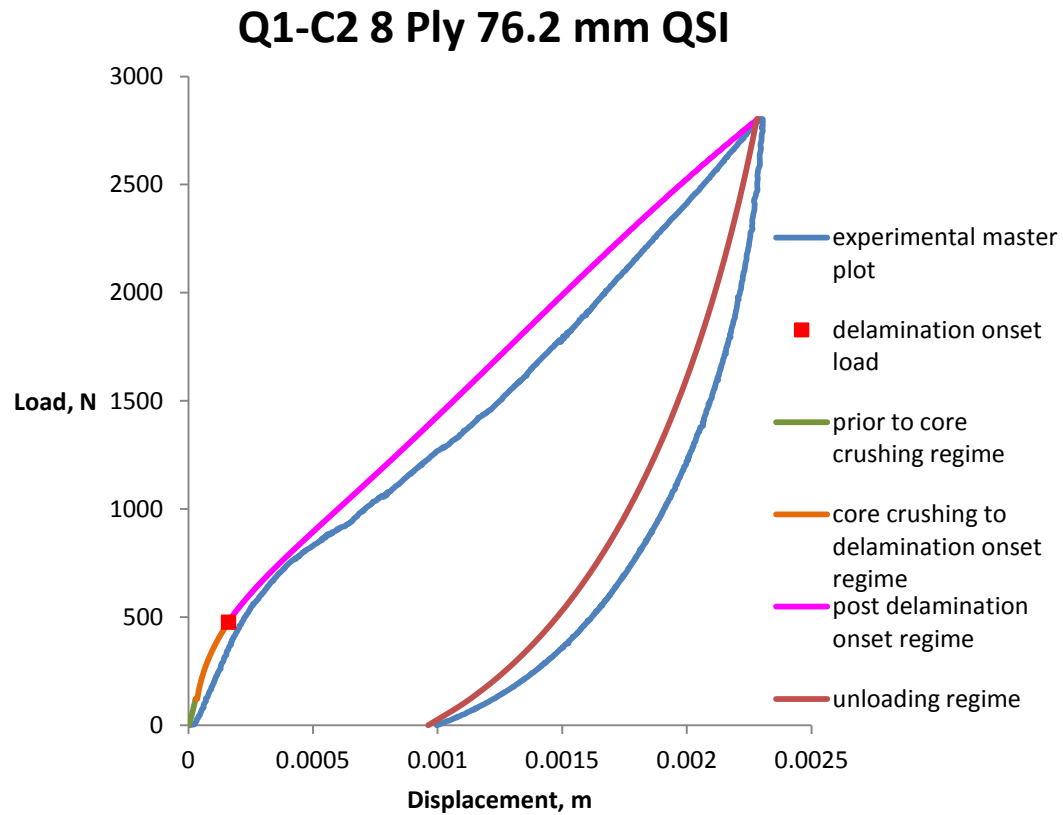


Figure 10.9. Q1-C2 8 ply model versus experimental P-d plot comparisons for specimens indented with the 76.2 mm diameter indenter.

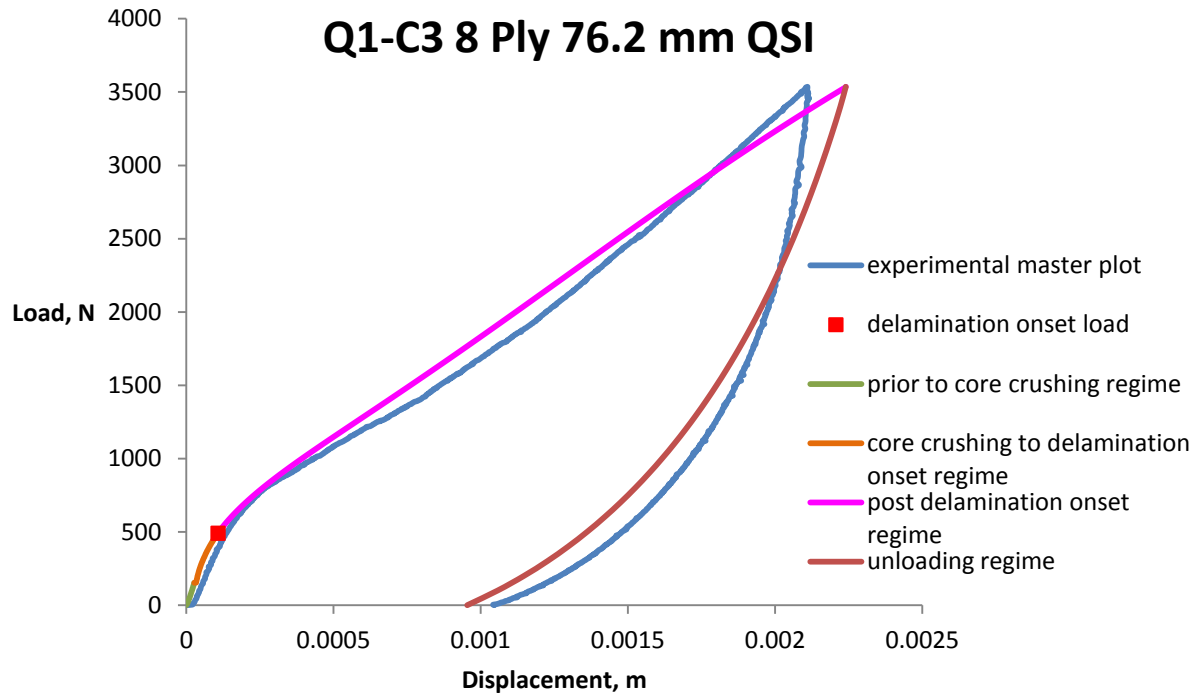


Figure 10.10. Q1-C3 8 ply model versus experimental P-d plot comparisons for specimens indented with the 76.2 mm diameter indenter.

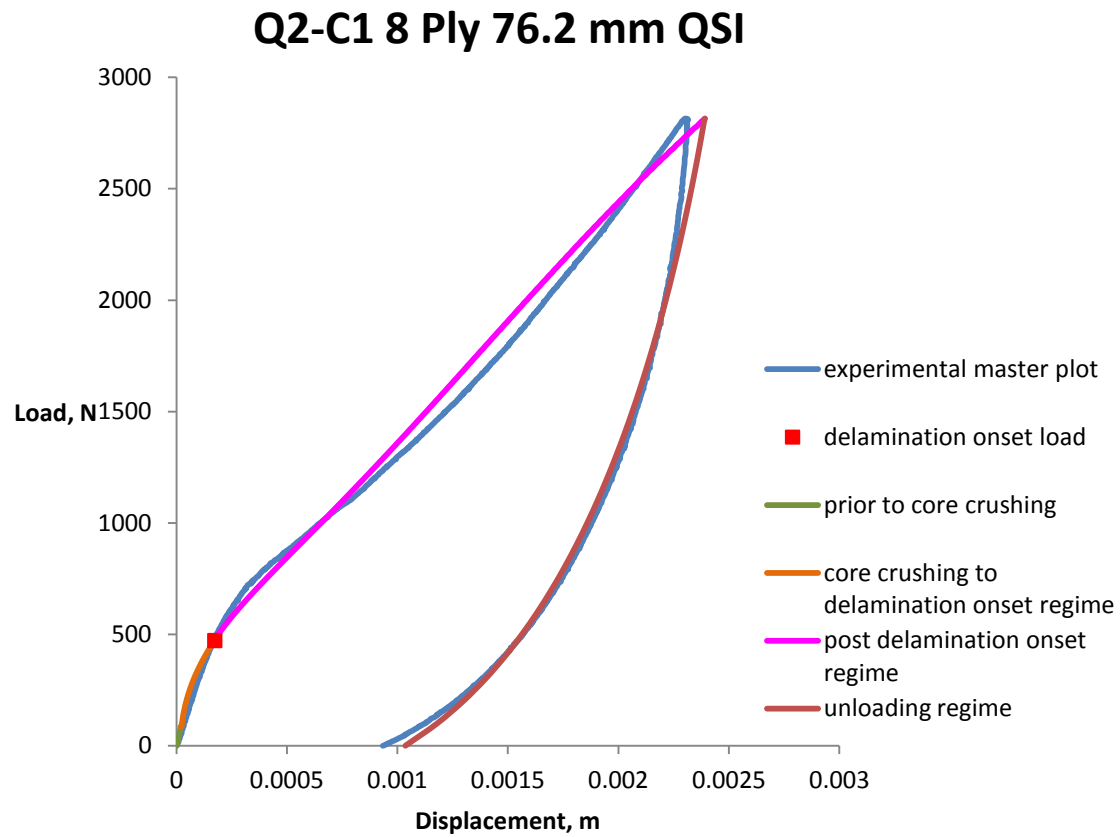


Figure 10.11. Q2-C1 8 ply model versus experimental P-d plot comparisons for specimens indented with the 76.2 mm diameter indenter.

Q3-C1 8 Ply 76.2 mm QSI

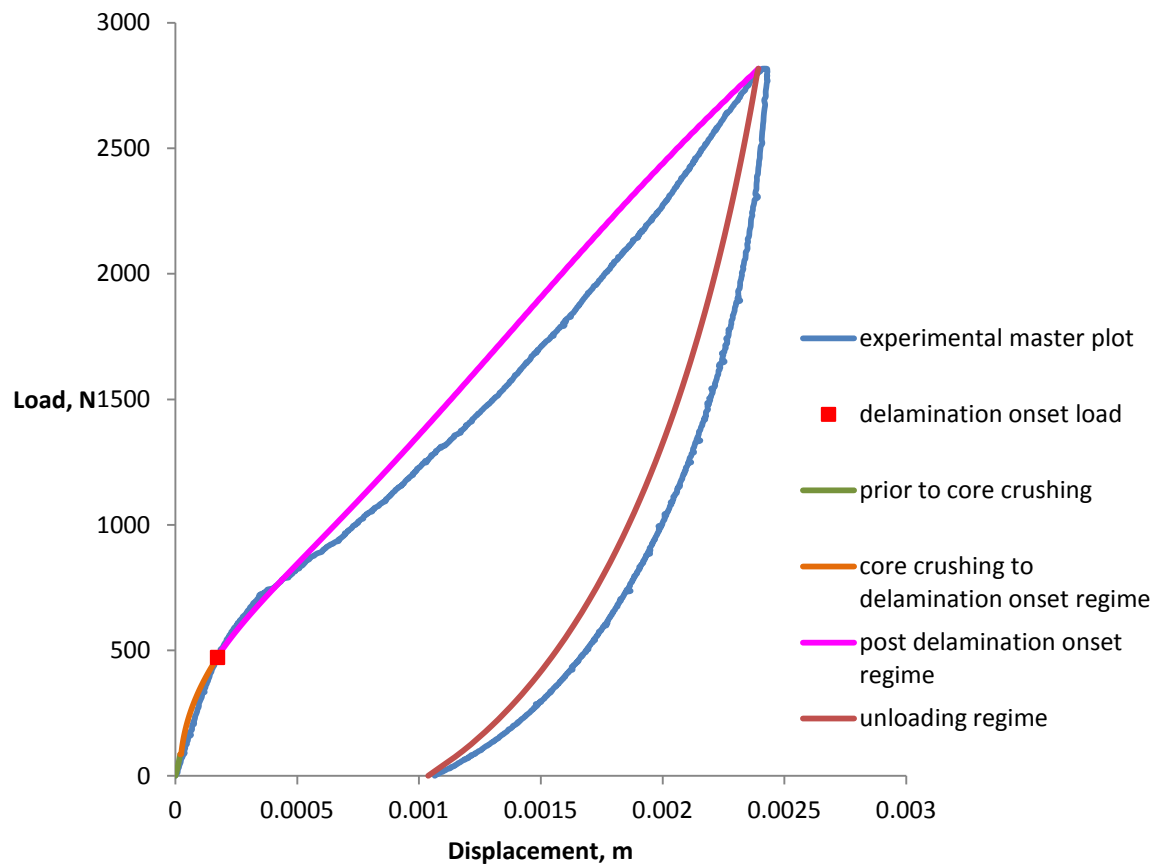


Figure 10.12. Q3-C1 8 ply model versus experimental P-d plot comparisons for specimens indented with the 76.2 mm diameter indenter.

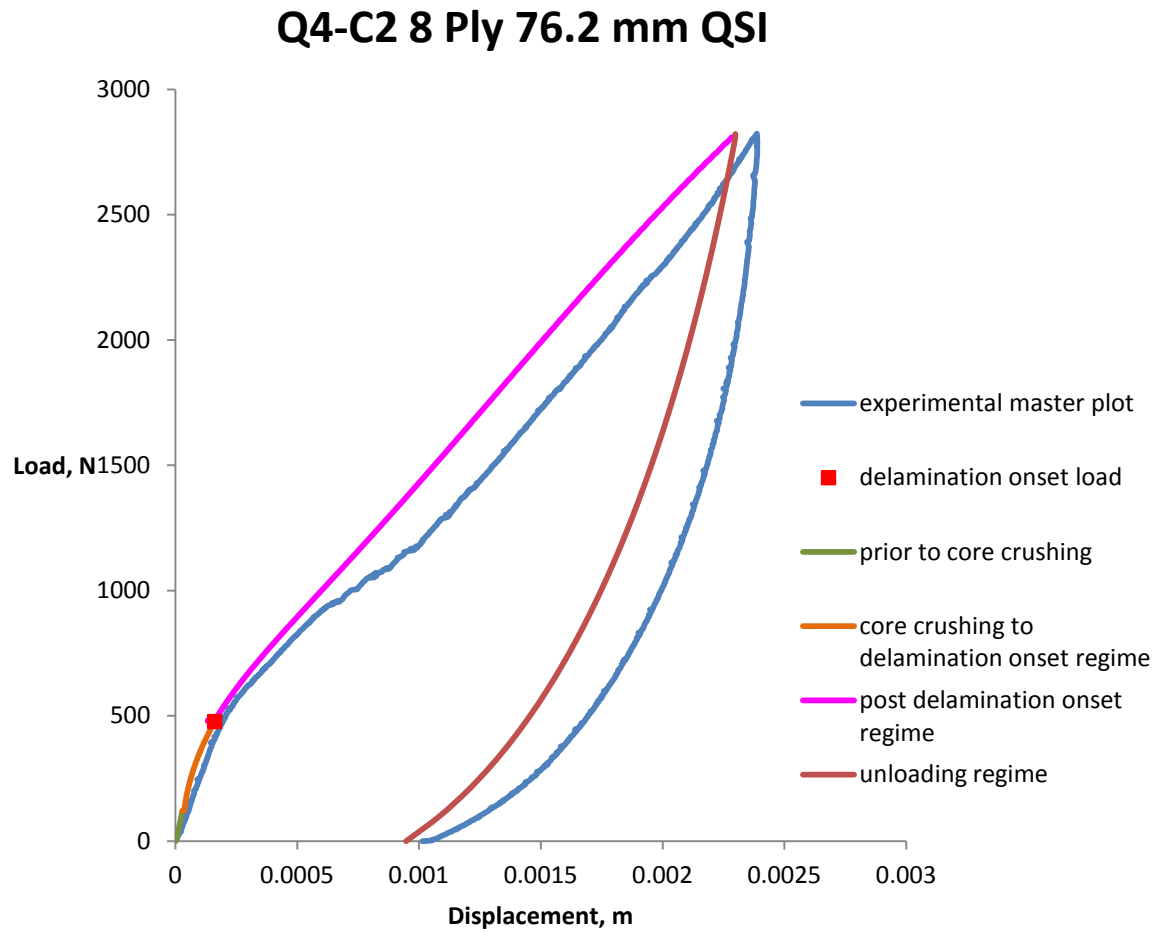


Figure 10.13. Q4-C2 8 ply model versus experimental P-d plot comparisons for specimens indented with the 76.2 mm diameter indenter.

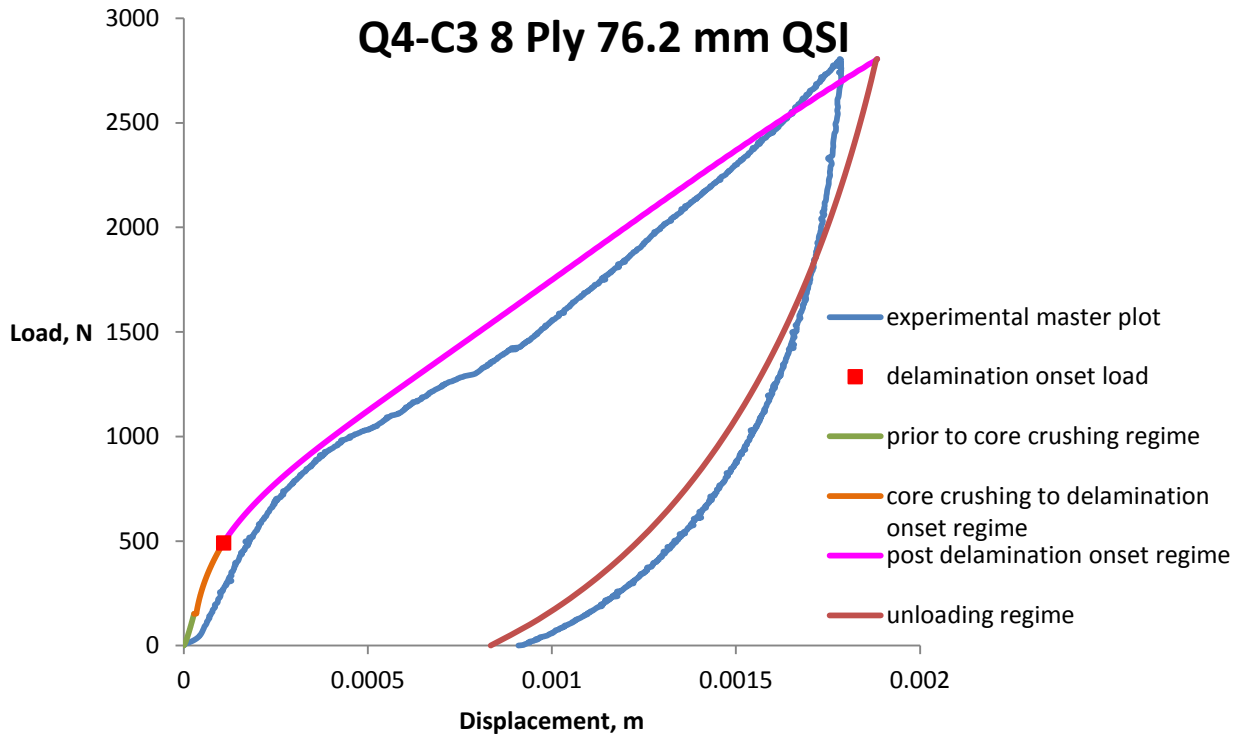


Figure 10.14. Q4-C3 8 ply model versus experimental P-d plot comparisons for specimens indented with the 76.2 mm diameter indenter.

10.2.3 16 Ply Specimens Indented with the 25.4 mm Diameter Indentor

Figures 10.15 to 10.21 compares the load versus displacement model predictions with the experimental results for the 16 ply specimens indented with the 25.4 mm diameter indenter. The model under-predicts the knee as well as the delamination onset load. In the regime subsequent to the delamination onset, the load versus displacement plot characteristics for the model do not appear to reflect the experimental results. That is, the experiments generally show stiffening after the transition region whereas the model shows significant softening. The level of softening appears to be more than what was seen for the 8 ply specimens indented with the 25.4 mm diameter indenter. This likely happens because the model accounts for less property degradation

at the delamination onset load than what happens in the actual experiments. The peak displacements are not predicted as well for these cases as for those described previously. The peak displacement is typically under-predicted. The model also shows less recovery of displacements than the experiments, which tends to improve the accuracy of the residual dent depth predictions.

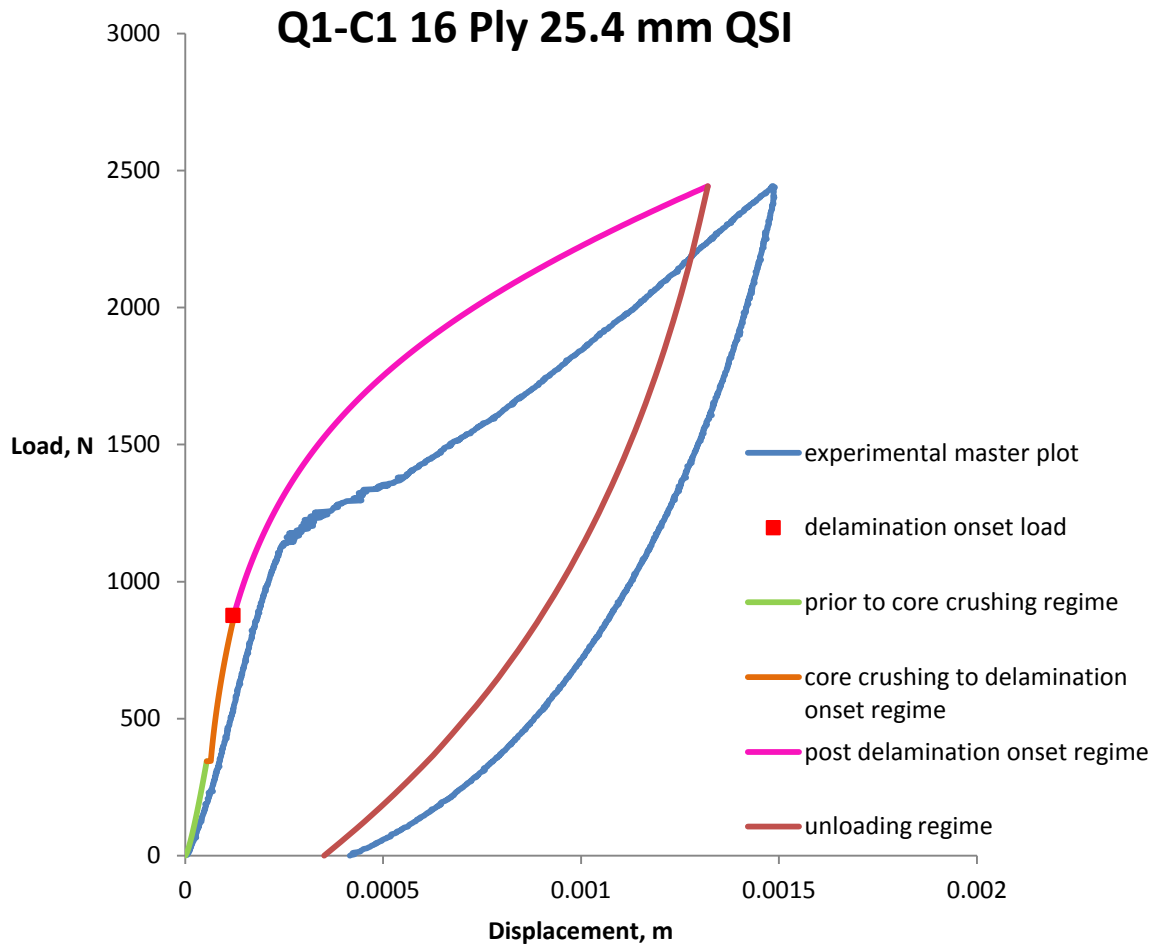


Figure 10.15. Q1-C1 16 ply model versus experimental P-d plot comparisons for specimens indented with the 25.4 mm diameter indenter.

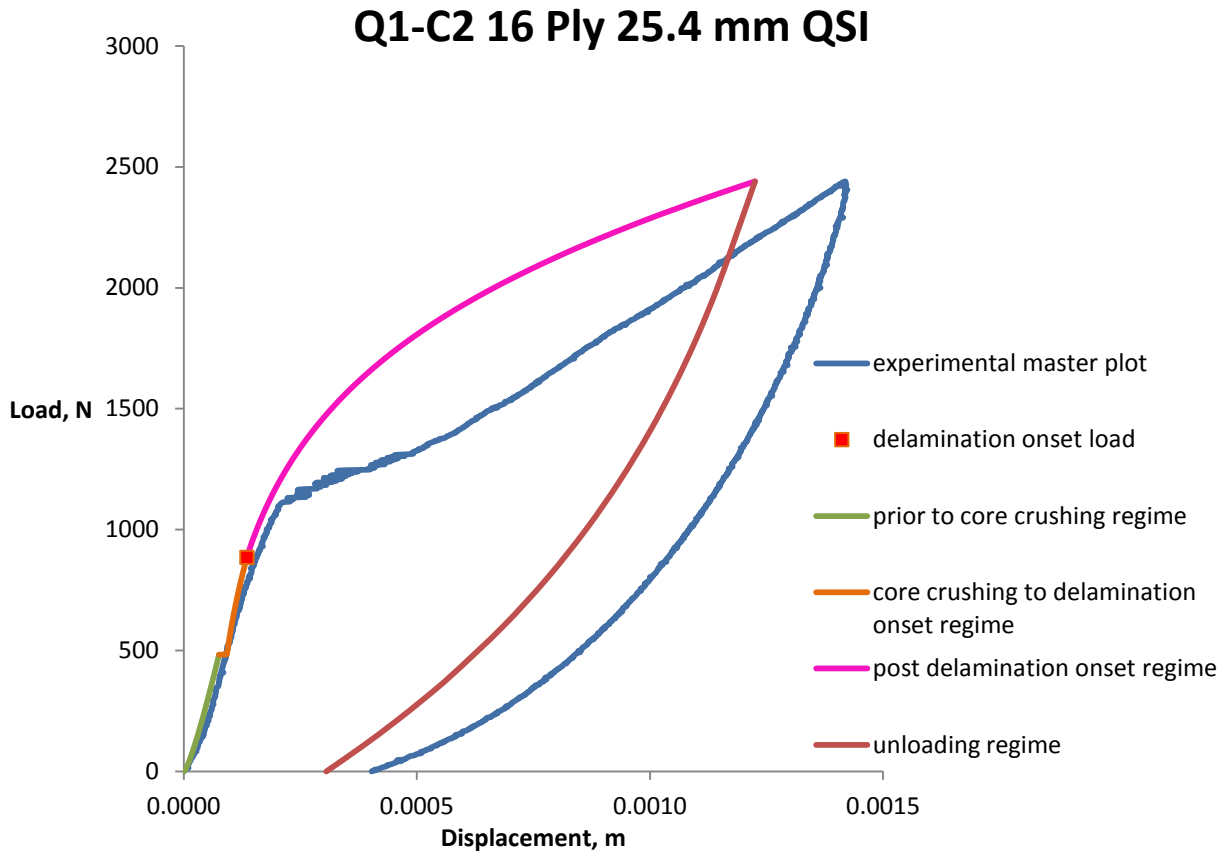


Figure 10.16. Q1-C2 16 ply model versus experimental P-d plot comparisons for specimens indented with the 25.4 mm diameter indenter.

Q1-C3 16 Ply 25.4 mm QSI

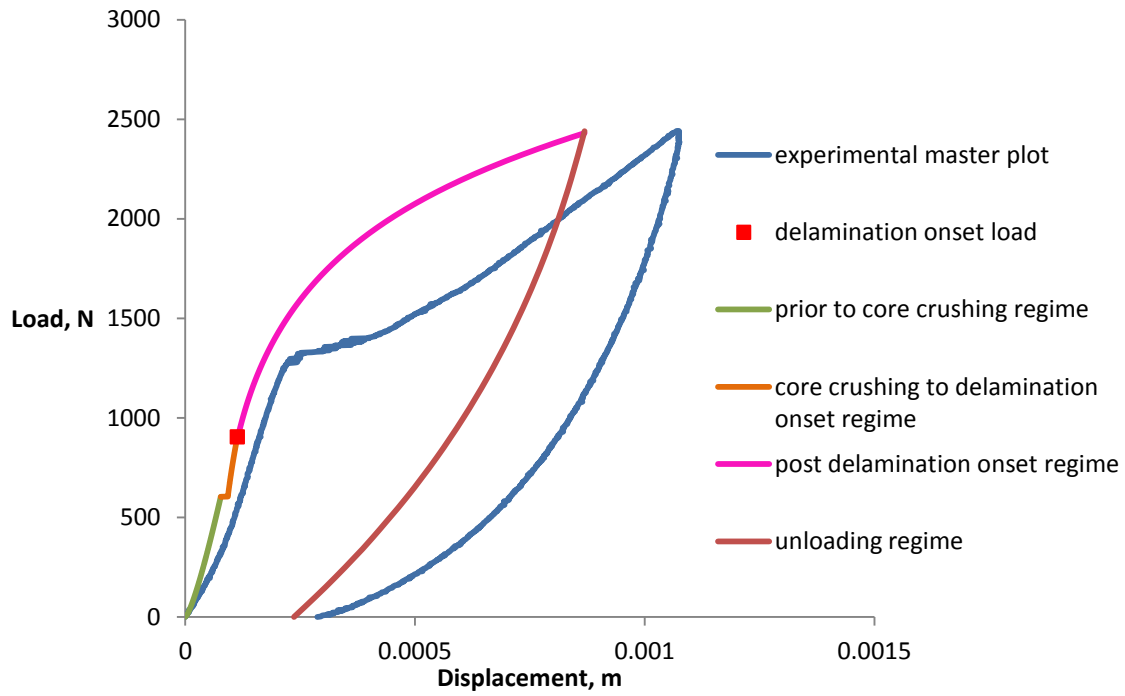


Figure 10.17. Q1-C3 16 ply model versus experimental P-d plot comparisons for specimens indented with the 25.4 mm diameter indenter.

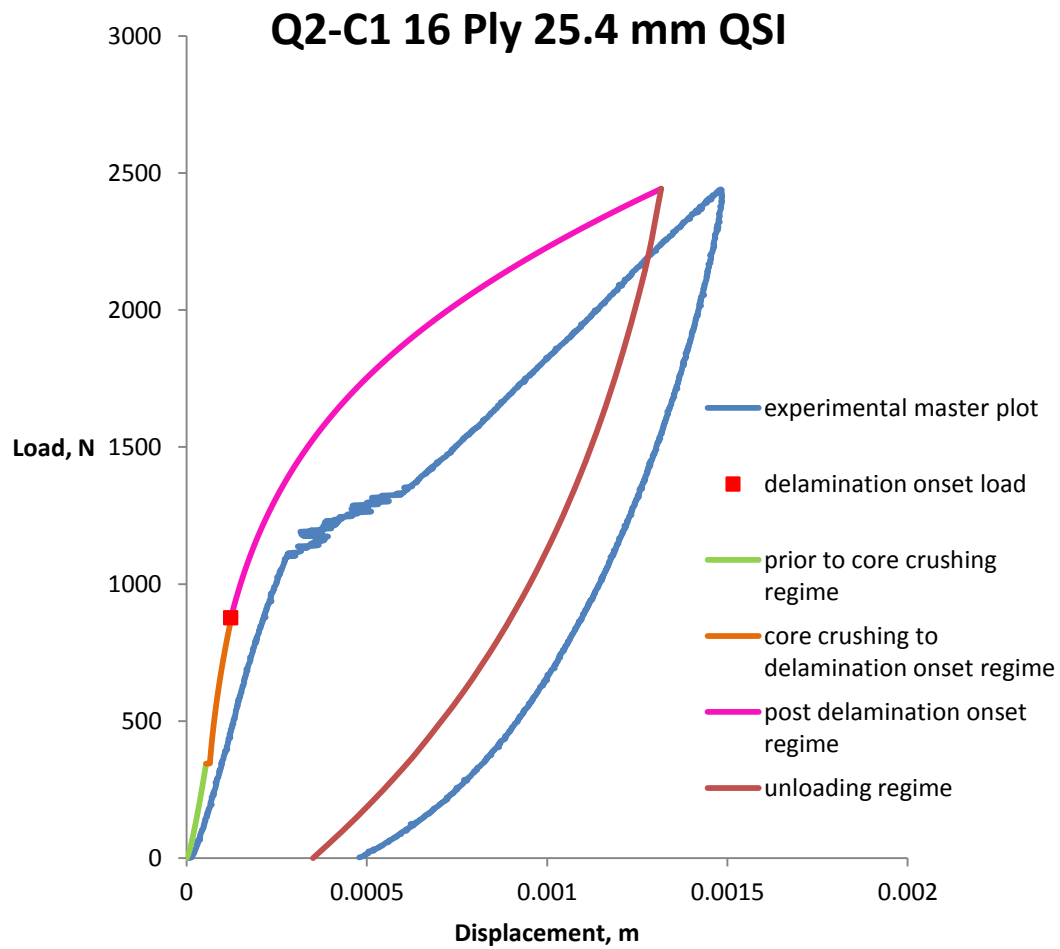


Figure 10.18. Q2-C1 16 ply model versus experimental P-d plot comparisons for specimens indented with the 25.4 mm diameter indenter.

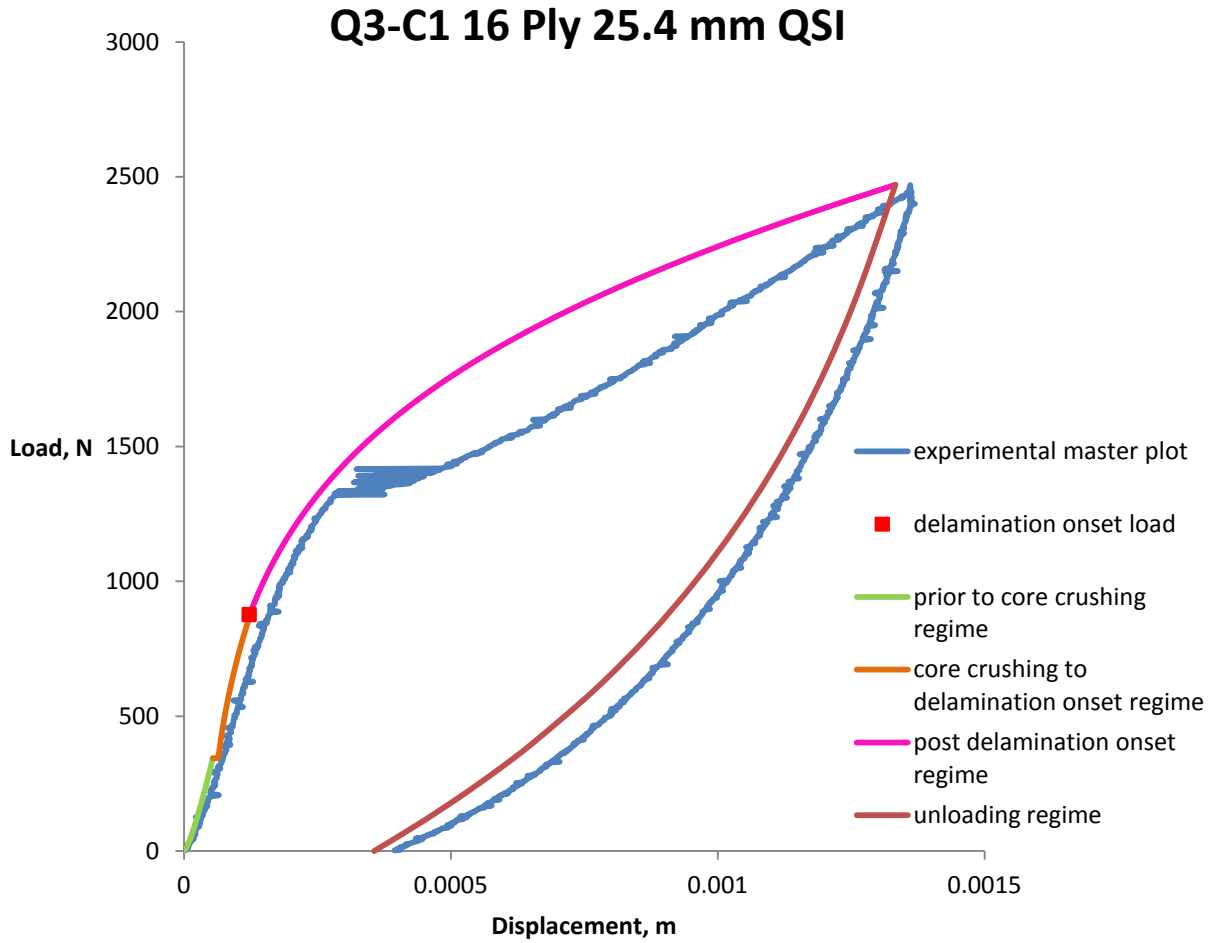


Figure 10.19. Q3-C1 16 ply model versus experimental P-d plot comparisons for specimens indented with the 25.4 mm diameter indenter.

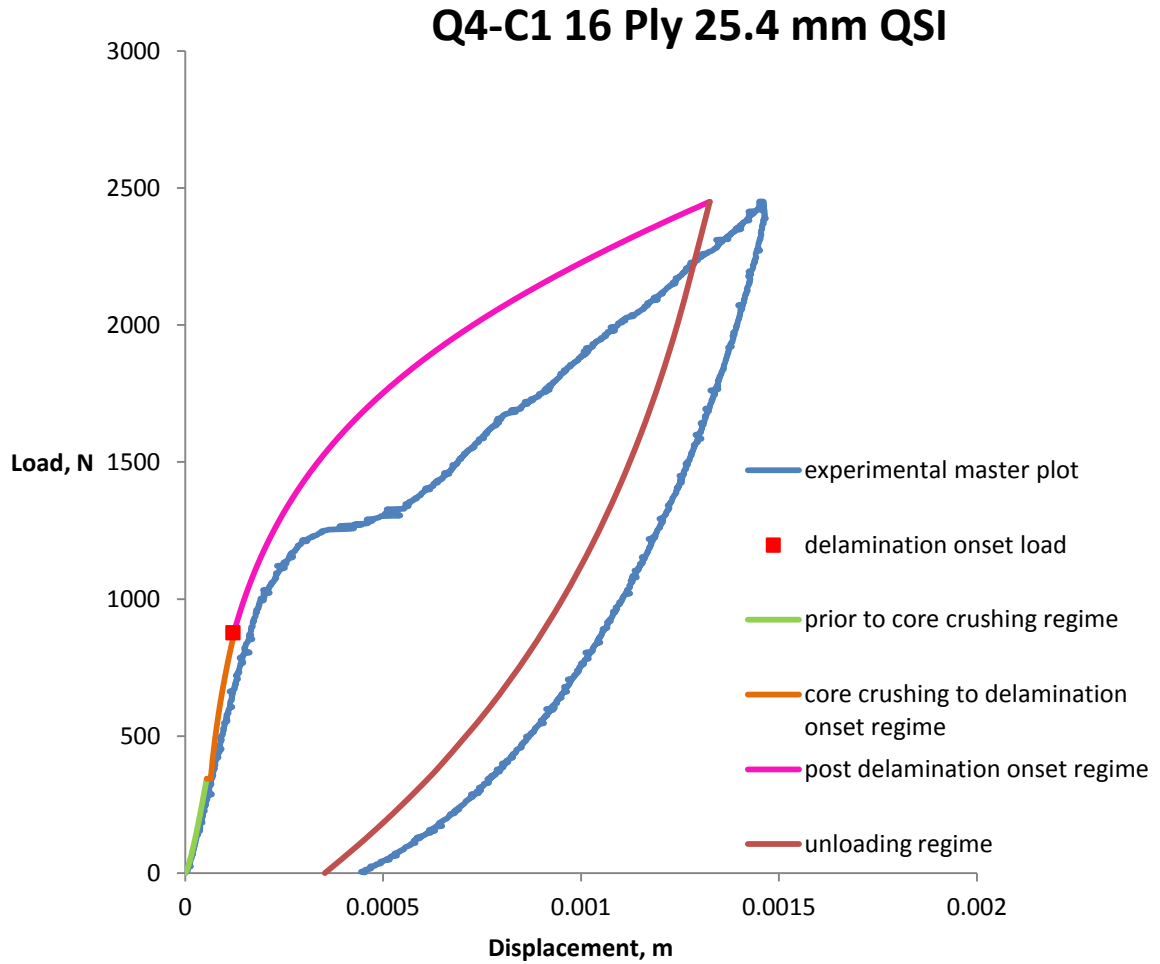


Figure 10.20. Q4-C1 16 ply model versus experimental P-d plot comparisons for specimens indented with the 25.4 mm diameter indenter.

Q5-C1 16 Ply 25.4 mm QSI

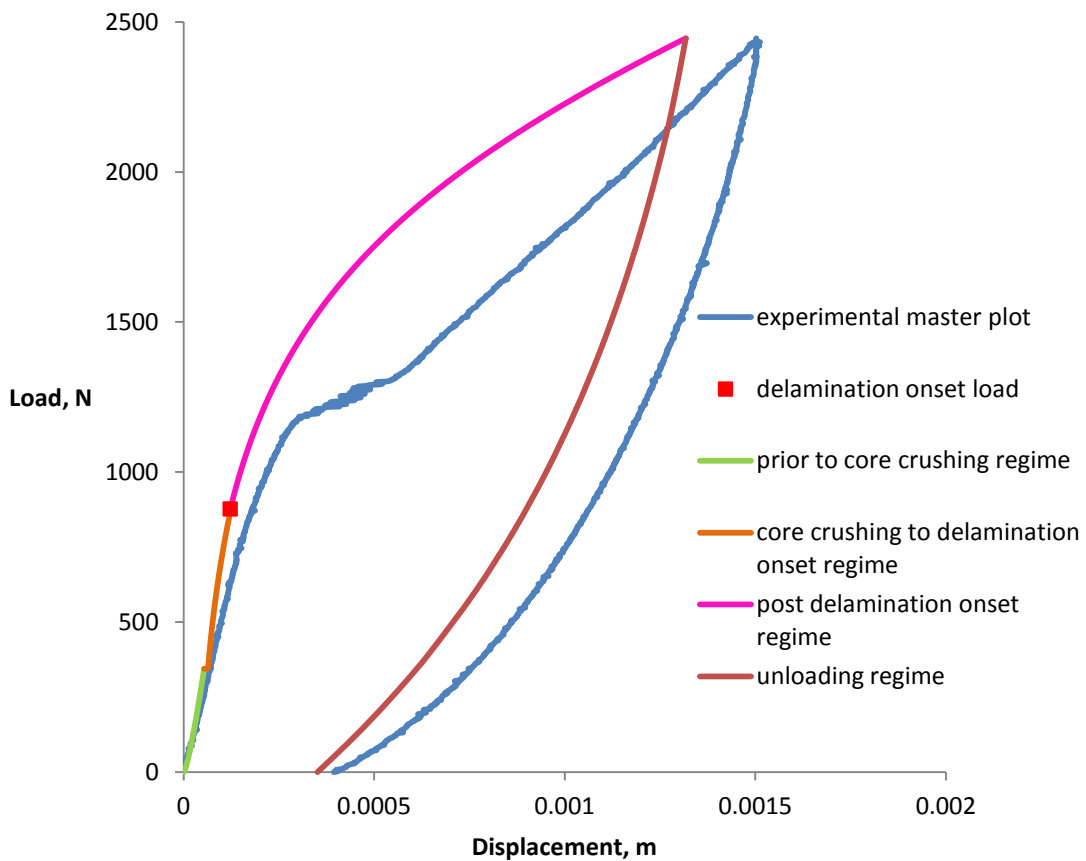


Figure 10.21. Q5-C1 16 ply model versus experimental P-d plot comparisons for specimens indented with the 25.4 mm diameter indenter.

10.2.4 16 Ply Specimens Indented with the 76.2 mm Diameter Indentor

Figures 10.22 to 10.27 compares the load versus displacement model predictions with the experimental results for the 16 ply specimens indented with the 76.2 mm diameter indenter. Just as in the case of the 16 ply specimens indented with the 25.4 mm diameter indenter, the model under-predicts the knee as well as the delamination onset load. By observing the curve characteristics, it is noted that the load versus displacement plot characteristics for the model do

not appear to reflect the experimental results in the regime post the delamination onset load. That is, the experiments once again generally show stiffening after the transition region whereas the model shows softening. As before, this is likely because the model accounts for less property degradation at and just subsequent to the delamination onset load than what happens in the actual experiments. The model however appears to capture the mechanics of the post delamination onset regime better than what was seen for the 16 ply specimens indented with the 25.4 mm diameter indenter. The model appears to capture the physical mechanics of the problem better than what was seen for the 16 ply specimens indented with the 25.4 mm diameter indenter. The prediction of peak displacements are also better than that for the 16 ply specimens indented with the 25.4 mm diameter indenter. The figures show that the model captures the mechanics of the unloading process quite well.

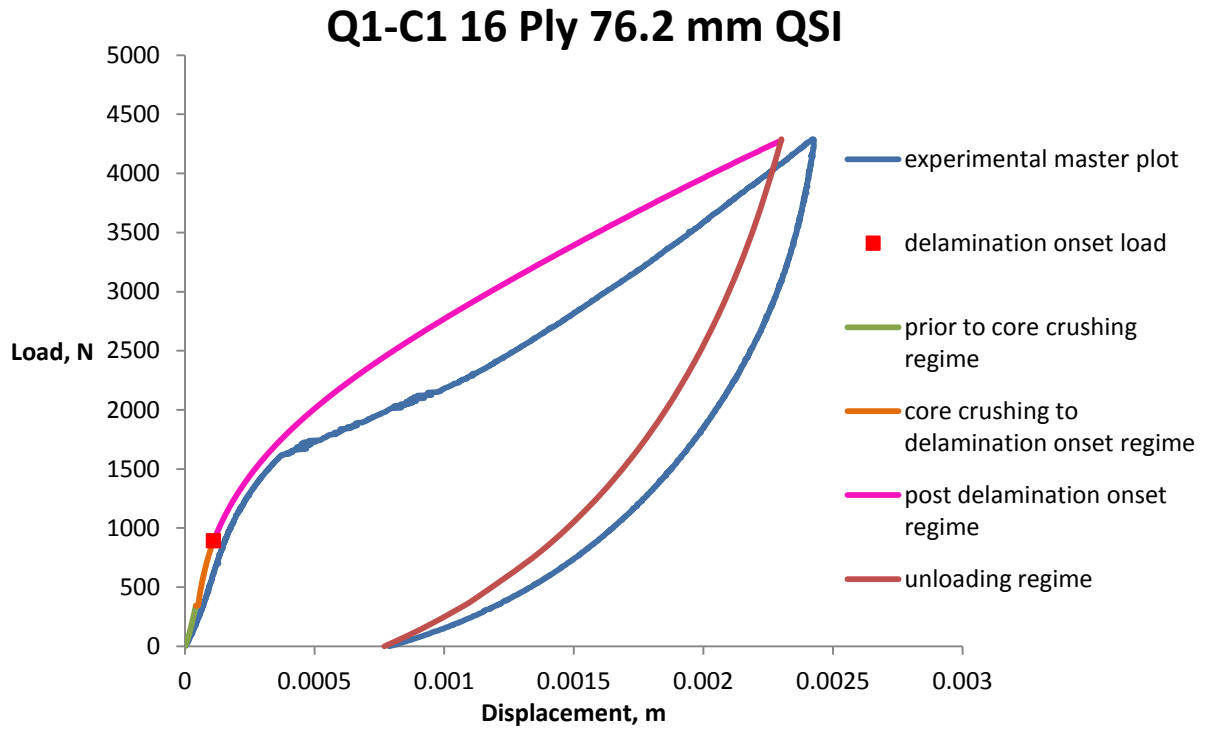


Figure 10.22. Q1-C1 16 ply model versus experimental P-d plot comparisons for specimens indented with the 76.2 mm diameter indenter.

Q1-C2 16 Ply 76.2 mm QSI

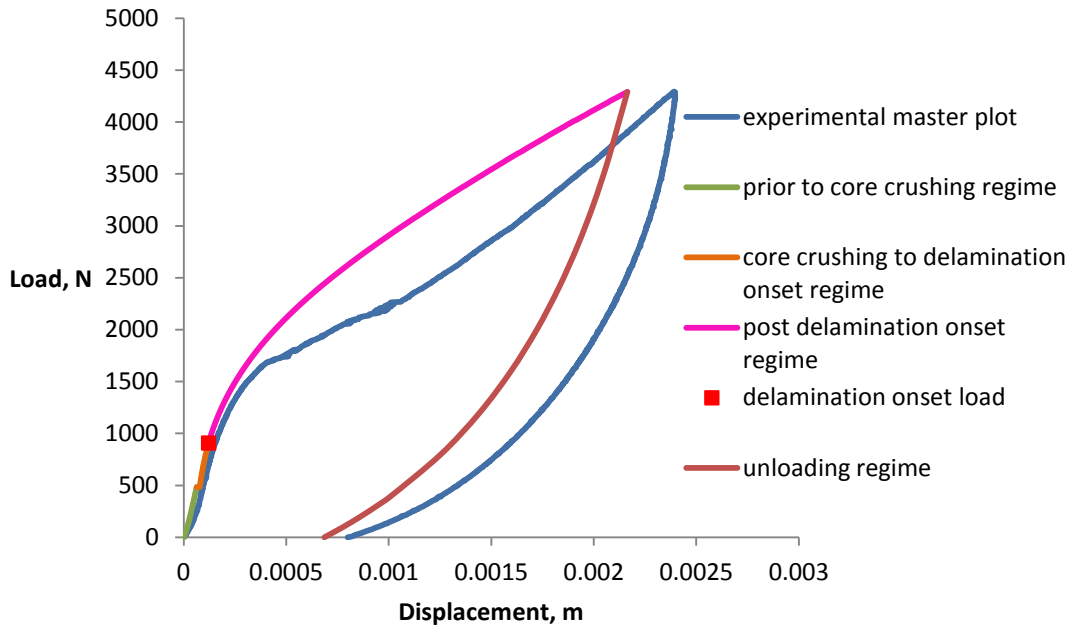


Figure 10.23. Q1-C2 16 ply model versus experimental P-d plot comparisons for specimens indented with the 76.2 mm diameter indenter.

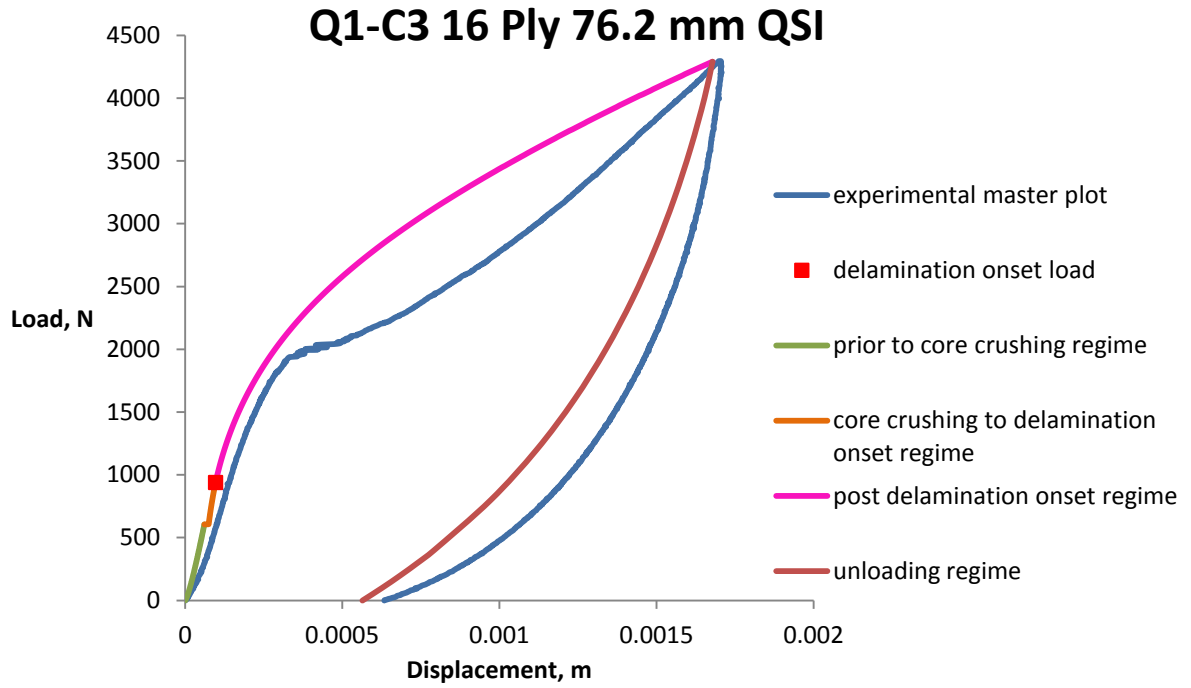


Figure 10.24. Q1-C3 16 ply model versus experimental P-d plot comparisons for specimens indented with the 76.2 mm diameter indenter.

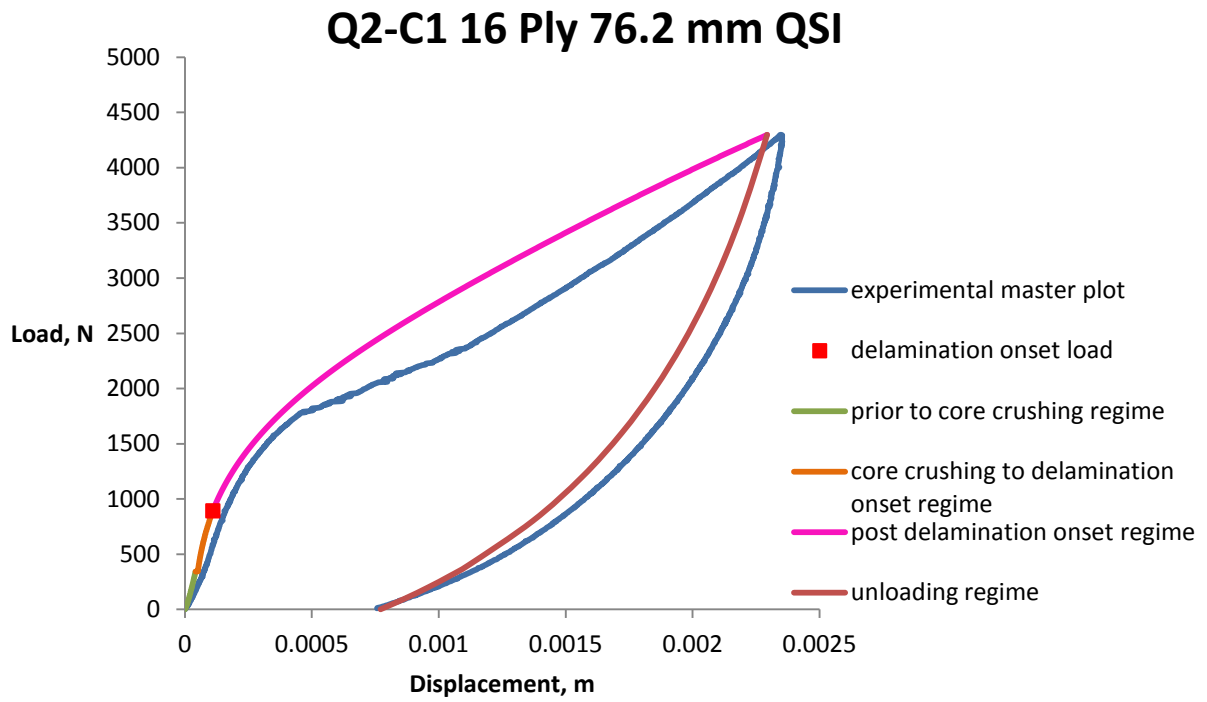


Figure 10.25. Q2-C1 16 ply model versus experimental P-d plot comparisons for specimens indented with the 76.2 mm diameter indenter.

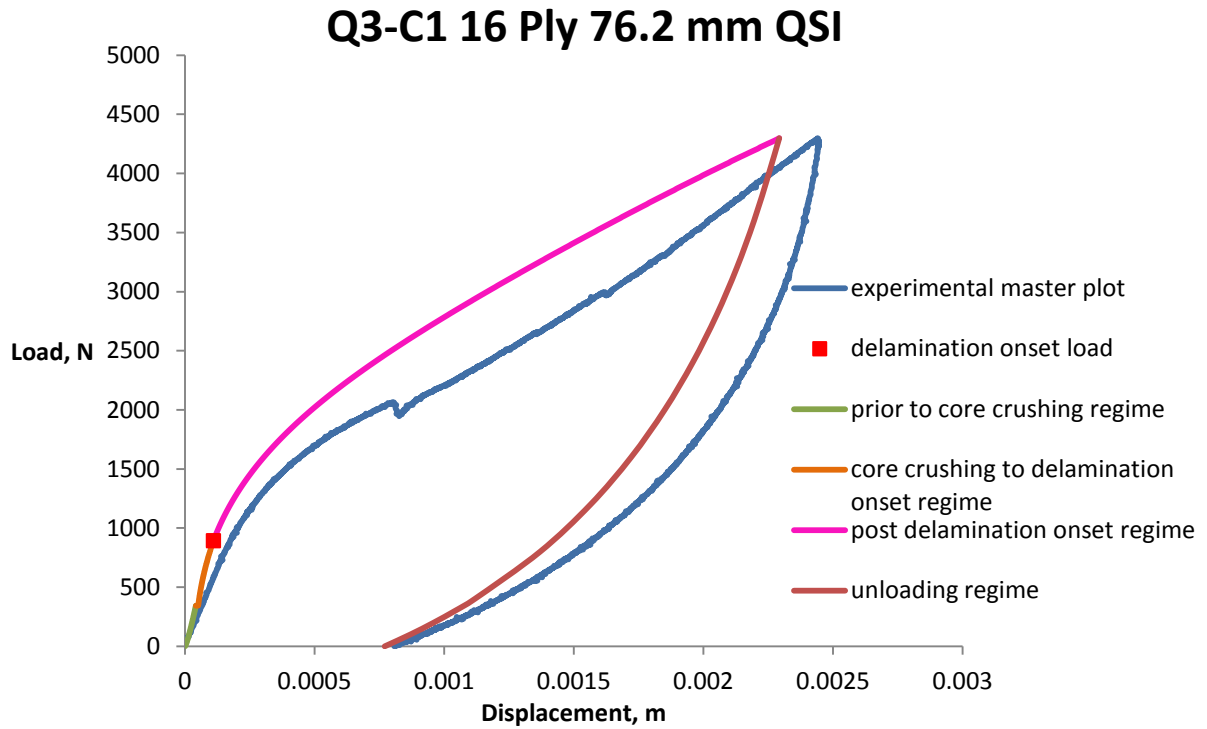


Figure 10.26. Q3-C1 16 ply model versus experimental P-d plot comparisons for specimens indented with the 76.2 mm diameter indenter.

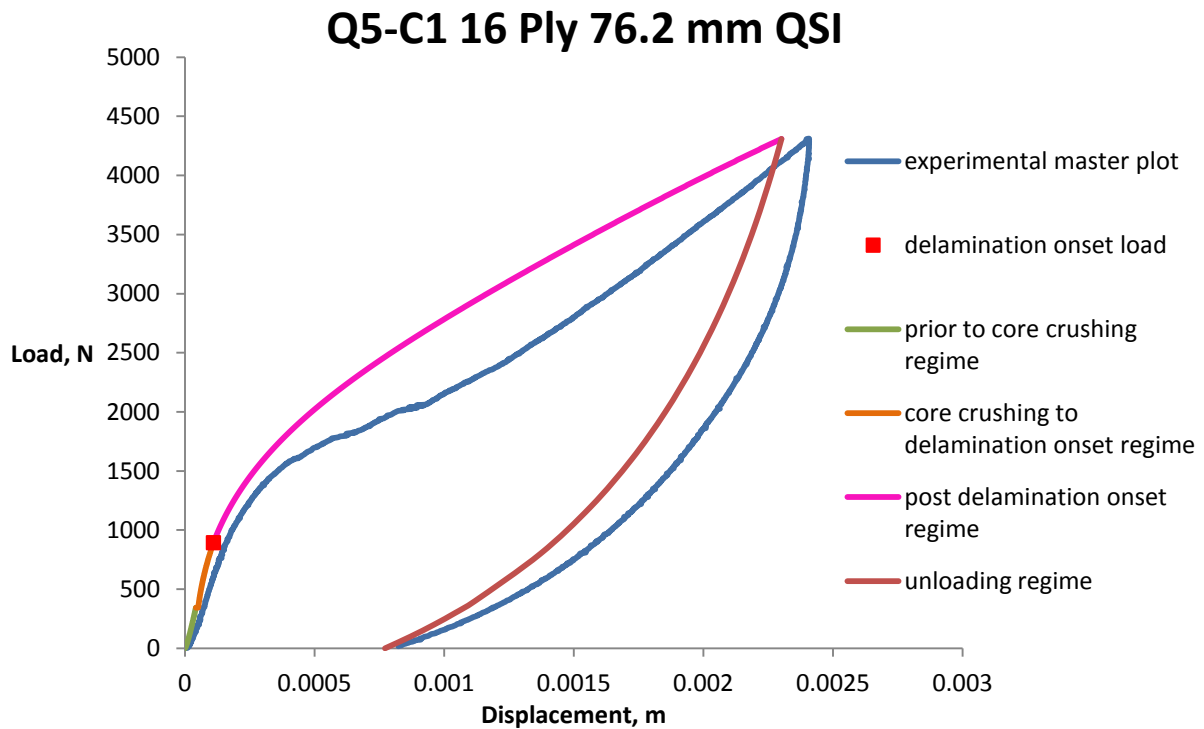


Figure 10.27. Q5-C1 16 ply model versus experimental P-d plot comparisons for specimens indented with the 76.2 mm diameter indenter.

10.3 Summary

The model results presented in this section indicate that the mechanics of the model are essentially correct, and lend confidence to the ability of the model to predict the residual dent depths and dent diameters for sandwich specimens indented quasi-statically and with damage within the vicinity of BVID. These damage metrics are important for a variety of design uses, such as parametric trade-off studies. Also, from the viewpoint of CAI modeling, these damage predictions can be implemented as pre-existing damage. The dent depth and dent diameter predictions are better for the 8 ply specimens as compared to the 16 ply specimens. It is observed that the model does not capture the mechanics of the post delamination onset to peak load regime very well. This is due to the lack of a clear mechanics based approach within the model to adjust

the rate at which the properties degrade between the onset of delamination and the peak load. However, the overall mechanics of the model in this regime is fundamentally correct and reflective of physical behavior, albeit without exactly capturing the details of damage onset and growth. That is, the model contains within it the capacity to fully recreate the experimental results should a more accurate way be implemented within the model for property degradation subsequent to the onset of delamination. However, this issue does not affect the prediction of displacement at peak load or of the key parameters of residual dent depth and dent diameter. For both the face sheet thicknesses tested with both the indenter diameters, the model captures the mechanics of the unloading process well.

Chapter 11

CONCLUSIONS

The study presented in this dissertation focused on the experimental characterization of damage in quasi-statically indented graphite/epoxy-honeycomb core sandwich structures and the development of an analytical model for modeling the sandwich response to indentation loading and subsequent unloading. The level of damage under consideration in this study was barely visible impact damage (BVID).

In the experimental investigations, the 8 ply specimens showed slightly stiffer response for specimens with the higher density core in the initial elastic regime. No significant difference in the stiffness of the response based on either the core type or the face sheet layup was seen for the 16 ply case in the initial elastic regime. In the inelastic regime, specimens with the higher density core showed significantly stiffer response for both the 8 and 16 ply cases. The higher density core also showed smaller residual dent diameter and dent depths for both the 8 and 16 ply cases. Therefore, when dent diameter or dent depth is considered as the damage metric, specimens with the higher density core can be said to be the most damage resistant. For the 8 ply case, the smallest planar areas of delamination are seen for the specimens with the lower density core and smaller ply angle changes. On the contrary, the largest planar areas of delamination in the 16 ply case are seen for the specimens with the lower density core and smaller ply angle changes. It is therefore concluded that when planar area of delamination is considered as the damage metric, the parameters that govern the damage size differ for the different face sheet thicknesses. For the 8 ply case, the combination of a lower density core and smaller ply angle changes is the most damage resistant, while for the 16 ply case it is the least damage resistant.

The analytical model developed in this dissertation is capable of predicting the key damage parameters of residual dent depth and residual dent diameter. Prediction of these damage parameters is useful in the determination of the most damage resistant sandwich structure when these parameters are considered as the damage metric. Also, the predicted dent diameter and dent depth results can be implemented in a compression-after-impact model as pre-existing damage for the prediction of the post-impact compressive strengths of the sandwich structure. Apart from these key damage parameters, the model is also able to predict the core crush onset load, the delamination onset load, the load versus maximum displacement as well as the load versus dent radius. The model contains within it the capacity to fully recreate the experimental results should a more accurate way be implemented within the model for property degradation subsequent to the onset of delamination. Despite this being a major shortcoming of the model in its current form, it does not affect the prediction of key damage parameters of residual dent depths and diameters by the model. A way to address this shortcoming in the model is proposed in Chapter 12 under “Future Work”.

Chapter 12

FUTURE WORK

This chapter presents proposals for future work that will help answer some of the remaining issues that have not been fully addressed in this dissertation. Two of the primary proposals are damage investigation in the transition region, i.e., where the sandwich response changes from elastic to inelastic behavior, and development of a “two-region plate model” for modeling the sandwich response to indentation loading in the post delamination onset regime.

12.1 Damage Evaluation in the Transition Region

The different damage modes that exist in the transition region of the sandwich response to indentation loading are not clearly known. The transition region, as defined in Chapter 4, is the region where the sandwich response changes from linear elastic to inelastic behavior. While core crushing is widely believed to be the dominant damage mode in the transition region, it is not clearly known if matrix cracks and delaminations also occur in the transition region. To investigate this, it is proposed that further QSI tests be done in different sandwich configurations where the unloading should start as soon as the non-linearity in the load versus displacement curve becomes visible. After unloading, the damage in the sandwich structure can be evaluated using a combination of destructive and non-destructive evaluation techniques to see the kind of damage modes that exist in the transition region. This proposed unloading path is presented in Figure 12.1. Further loading and subsequent unloading can be extended all the way to the peak load to track the damage evolution. The knowledge attained from this investigation would be helpful in understanding the progression of damage. A better understanding of damage progression would be highly useful from the viewpoint of modeling the sandwich response to indentation loading.

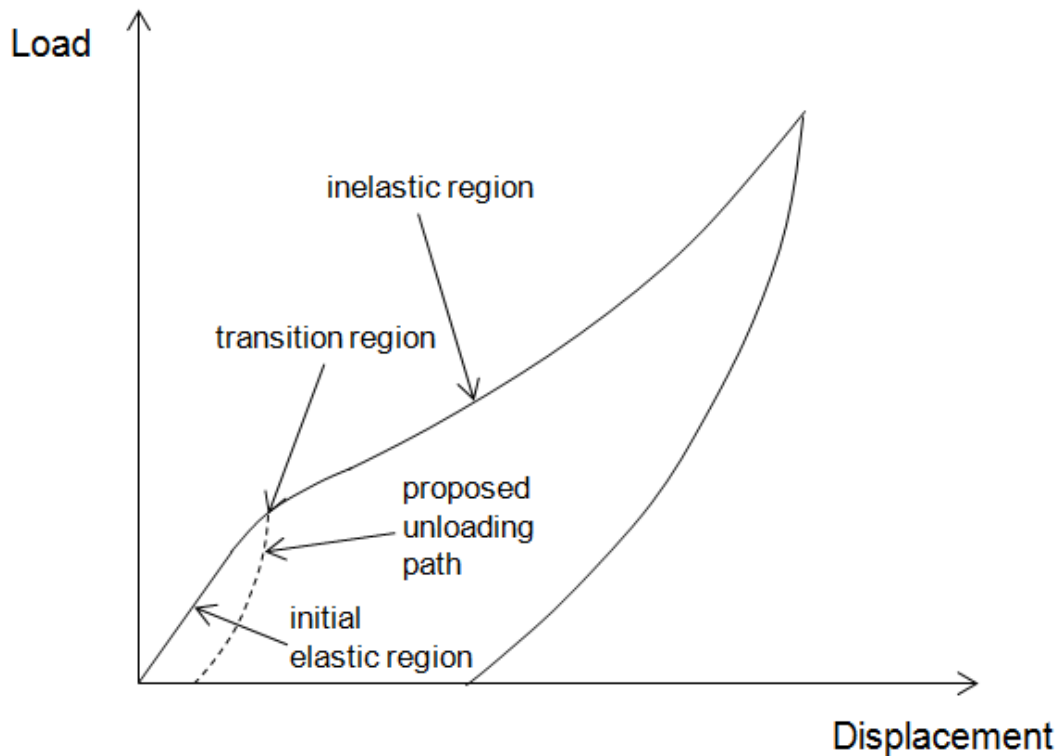


Figure 12.1. Schematic showing the proposed unloading path for further tests to investigate the damage modes in the transition region.

12.2 The Two-region Plate Model

One of the problems encountered in modeling the post delamination onset regime is to account for the size of the delamination area relative to dent area so that this information can be more accurately implemented through property degradation in the model and thereby give more accurate results. Experimental investigations show that the planar area of delamination is always less than the dent area. These results are presented in Figures 6.9 and 6.17 for the 8 and 16 ply cases respectively.

A two-region plate model is proposed that considers the delaminated area to be only a portion of the overall dented area. A schematic of the two-region plate model is presented in

Figure 12.2. In the two-region plate model, an inner plate with radius c represents the matrix cracked, delaminated region while the outer plate of radius a represents the intact region, i.e., the non-matrix cracked, non-delaminated region. The Rayleigh-Ritz method of energy minimization can also be used to solve for the two-region plate model with a single displacement field, $w(r)$, being used for the entire plate. In this model, the inner plate can be treated as a pure membrane or with both membrane and bending characteristics. It is presumed that with increasing load, both the inner plate and the outer plate grow simultaneously at individual rates that are close to the rates of delamination and dent growth in the actual experiments. In the model, the bending and membrane energy equations can be given in terms of the intact properties D_r , E_r and ν_r , the fully degraded properties D_{res} , E_{res} and ν_{res} . The resulting bending and membrane energy equations are presented by equations (12.1) and (12.2) respectively. The total work is calculated using equation 9.17 presented in Chapter 9.

$$\begin{aligned}
 U_b = \pi \left(D_{res} \int_b^c \left[r \left(\frac{\partial^2 w}{\partial r^2} \right)^2 + \frac{1}{r} \left(\frac{\partial w}{\partial r} \right)^2 + 2\nu_{res} \left(\frac{\partial w}{\partial r} \right) \left(\frac{\partial^2 w}{\partial r^2} \right) \right] dr \right. \\
 \left. + D_r \int_c^a \left[r \left(\frac{\partial^2 w}{\partial r^2} \right)^2 + \frac{1}{r} \left(\frac{\partial w}{\partial r} \right)^2 + 2\nu_r \left(\frac{\partial w}{\partial r} \right) \left(\frac{\partial^2 w}{\partial r^2} \right) \right] dr \right)
 \end{aligned}
 \tag{12.1}$$

$$U_m = \frac{\pi E_{res} h_f}{4(1 - \nu_{res}^2)} \int_b^c \int r \left(\frac{\partial w}{\partial r} \right)^4 dr
 \tag{12.2}$$

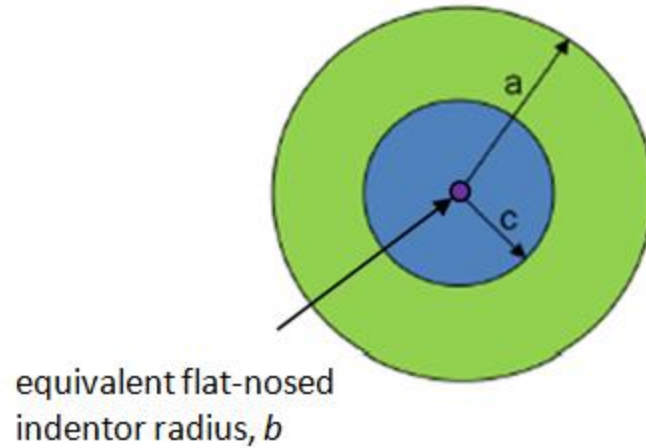


Figure 12.2 Schematic showing the proposed two-region plate assumption for the planar area of delamination and the dent area.

One major issue with the two-region plate model is the determination of the planar radius of delamination, c . The best and the most viable option is to minimize the total potential energy with respect to the maximum displacement, the planar radius of delamination and the dent radius as presented by equation (12.3).

$$\frac{\partial \pi}{\partial w_o} = \frac{\partial \pi}{\partial a} = \frac{\partial \pi}{\partial c} = 0 \quad (12.3)$$

This results in three highly non-linear equations that can be solved to determine a , c and w_o . It is expected that due to the high non-linearity of these equations, solving the equations would not be simple. Should these equations be solved, the model contains within it the ability to predict the planar area of delamination which is another critical damage metric from the viewpoint of CAI modeling.

In order to demonstrate the workability of the idea, different c/a ratios of 0.2, 0.4, 0.5, 0.6 and 0.8 were tried to see how the solution behaves in the post delamination onset regime. The

results based on these ratios for the 8 ply Q1-C1 sandwich configuration tested with the 25.4 mm diameter indenter is presented in Figure 12.2. As can be seen in the figure, the c/a ratio of 0.6 most accurately models the post delamination onset regime. It is however expected that if computationally successful, the value of c will vary in a manner such that it will more closely depict the experimental results. Should the value of c for the different load levels be solved through equation (12.3) or be pre-determined as accurately as possible using some other mechanics based approach, the two-region plate solution shows great promise in modeling the post-delamination onset regime of the sandwich indentation problem.

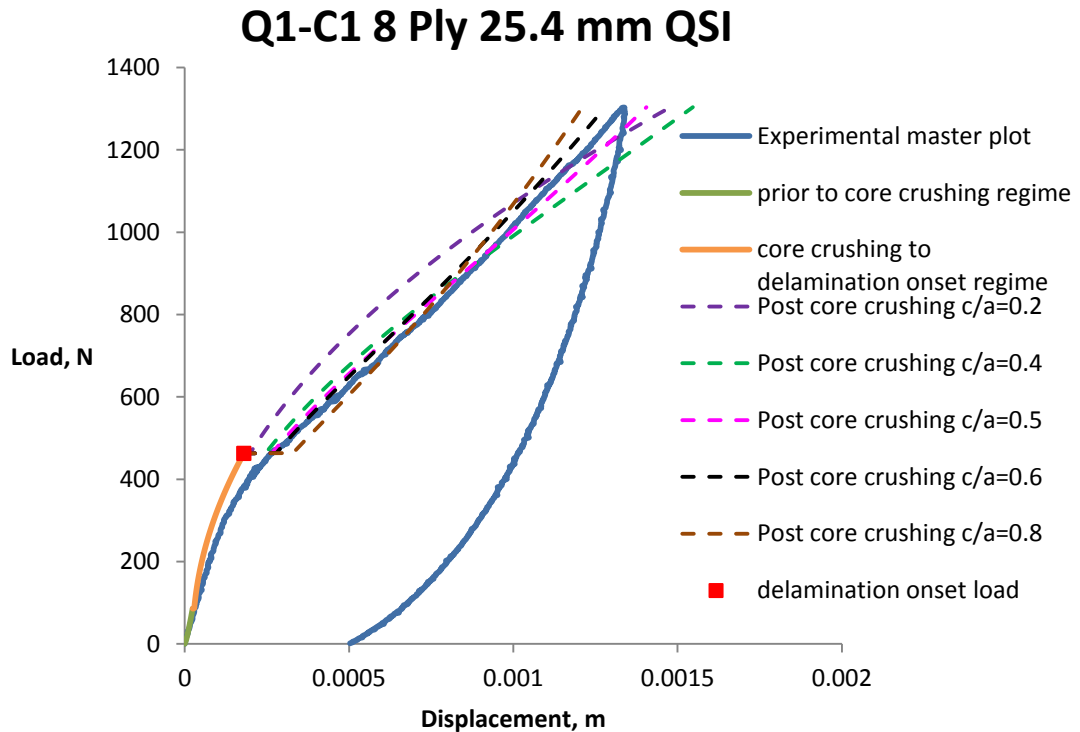


Figure 12.3 The two-region plate solution for the 8 ply Q1-C1 sandwich configuration indented with the 25.4 mm diameter indenter.

APPENDIX A

AUTOCLAVE CYCLE FOR SANDWICH PANEL MANUFACTURE

The face sheets, cut from a prepreg tape, were initially laid by hand and the panels were then fabricated in a single autoclave cure cycle where 3M AF-555 adhesive was used to bond the face sheet with the core. The autoclave cycle used was in accordance to the cure cycle proposed for sandwich panels by Hexcel Corporation, the manufacturers of IM7/8552 which was the material used for the face sheet. Figure A1.1 presents information on the different stages in the autoclave cure cycle.

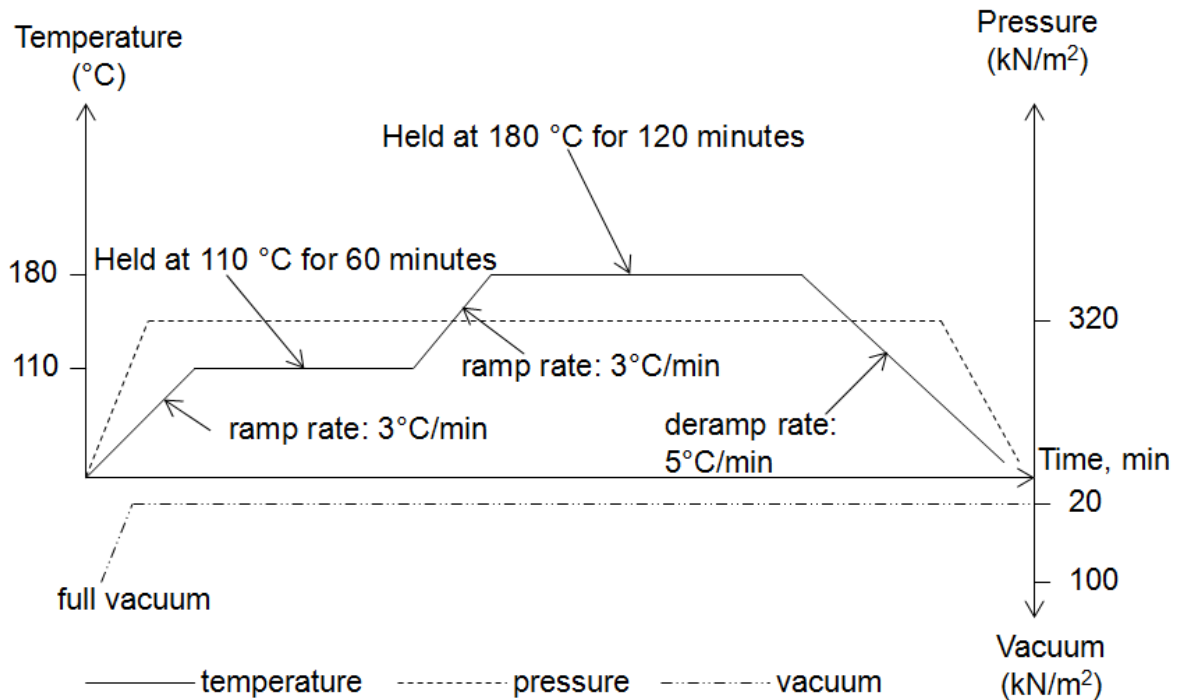


Figure A.1. Autoclave cycle used for sandwich panel curing.

APPENDIX B

DAMAGE AND STRENGTH DATA FOR INDENTOR SIZE DETERMINATION

In the preliminary investigation on the choices of indenter size to be used for quasi-static indentation (QSI), an indenter with a 12.7 mm diameter was also considered. Table B.1 compares the damage and strength data for certain sandwich specimens tested with the 12.7 mm and 25.4 mm diameter indentors. The strength data presented is the residual compressive strength of the damaged structures which was evaluated using the compression-after-impact (CAI) tests. The results show that the size of the damage and the residual strengths are very similar to each other for the specimens tested with both the indenter sizes. This led to excluding the 12.7 mm diameter indenter for the actual QSI tests and using only the 25.4 mm and 76.2 mm diameter indentors for the final test matrix. The specimen nomenclature for the specimens presented in Table B.1 follows exactly the nomenclature described in Chapter 6, except that 'H' instead of 'A' is used in some of the specimen names to refer to those that were initially manufactured using the hot press instead of the autoclave. These were the very first plates that were manufactured after which, the idea of using a hot press was dropped and only the autoclave was used for all future manufacture. Also, the hot press manufactured plates were not included in the final test matrix but were primarily used in the preliminary investigations. Exclusion of the hot press manufactured plates from the final test matrix was done in order to avoid any effects of manufacturing techniques on the final results.

Table B.1. Damage and residual compressive strength data for preliminary tests of certain full-sized specimens tested with 12.7 mm and 25.4 mm diameter indentors.

specimen	indenter diameter, mm	QSI load, N	dent depth, mm	dent diameter, mm	planar area of delamination, mm²	compressive strength, kPa
H08A-Q1-C1-6	12.7	1204	0.41	41	148	356197
H08A-Q1-C1-2	25.4	1305	0.44	39	161	377605
A08A-Q4-C3-3	12.7	1206	0.31	23	271	314022
A08A-Q4-C3-2	25.4	1312	0.30	28	284	317745

APPENDIX C

RESULTS OF PRELIMINARY TESTS ON SMALL QSI SPECIMENS FOR BVID LOAD DETERMINATION

Tables C.1-C.4 presents the results of the preliminary tests done on certain “small QSI specimens”, the sizes of which are presented in Chapter 3. These were done in order to determine the appropriate BVID load levels for the actual tests. Based on primarily the dent depth results and the qualitative evaluation of visible damage for the different load levels to which the different specimens were tested, appropriate BVID load levels were decided upon for the 8 and 16 ply cases by the consensus of the research team.

Table C.1. Test results for the preliminary tests for the 8 ply small QSI specimens indented with the 25.4 mm diameter indenter.

specimen	size (0° x 90°), mm x mm	indenter diameter, mm	QSI load, N	dent depth, mm	dent diameter, mm	planar area of delamination, mm ²
A08A-Q1-C2-d	88 x 56	25.4	1783	0.71	46	293
A08A-Q1-C2-e	107 x 56	25.4	1550	0.65	41	285
A08A-Q1-C2-f	107 x 58	25.4	1303	0.56	39	255
A08B-Q2-C1-a	94 x 61	25.4	1312	0.56	43	316
A08B-Q2-C1-b	88 x 64	25.4	1452	0.59	41	447
A08A-Q2-C1-c	56 x 49	25.4	1463	0.64	38	362
A08A-Q3-C1-d	90 x 99	25.4	1779	1.17	43	487
A08A-Q3-C1-e	90 x 99	25.4	1345	0.63	34	420

Table C.2. Test results for the preliminary tests for the 8 ply small QSI specimens indented with the 76.2 mm diameter indenter.

specimen	size (0° x 90°), mm x mm	indenter diameter, mm	QSI load, N	dent depth, mm	dent diameter, mm	planar area of delamination, mm ²
A08A-Q4-C2-a	100 x 93	76.2	2808	1.10	55	NA
A08B-Q1-C3-a	102 x 102	76.2	3524	1.01	45	NA

Table C.3. Test results for the preliminary tests for the 16 ply small QSI specimens indented with the 25.4 mm diameter indenter.

specimen	size (0° x 90°), mm x mm	indenter diameter, mm	QSI load, N	dent depth, mm	dent diameter, mm	planar area of delamination, mm ²
A16A-Q4-C1-a	64 x 44	25.4	1779	0.25	34	206
A16A-Q4-C1-b	64 x 44	25.4	2224	0.36	39	297
A16A-Q4-C1-c	89 x 44	25.4	1779	0.35	42	252

Table C.4. Test results for the preliminary tests for the 16 ply small QSI specimens indented with the 76.2 mm diameter indenter.

specimen	size (0° x 90°), mm x mm	indenter diameter, mm	QSI load, N	dent depth, mm	dent diameter, mm	planar area of delamination, mm ²
A16A-Q3-C1-d	76 x 57	76.2	3781	0.38	48	606
A16A-Q3-C1-d*	76 x 57	76.2	5338	0.72	inconclusive**	987
A16A-Q3-C1-e	76 x 57	76.2	6672	0.70	inconclusive**	903
A16A-Q3-C1-a	114 x 116	76.2	4448	0.84	83	865

*The other (back) surface of the same specimen was indented.

**The size of the dent spanned the entire specimen so the dent diameter could not be determined. This was due to the relatively small size of the specimen in comparison to the level of load that was applied to the specimen.

APPENDIX D

THE EDGEWISE COMPRESSION TEST SET-UP

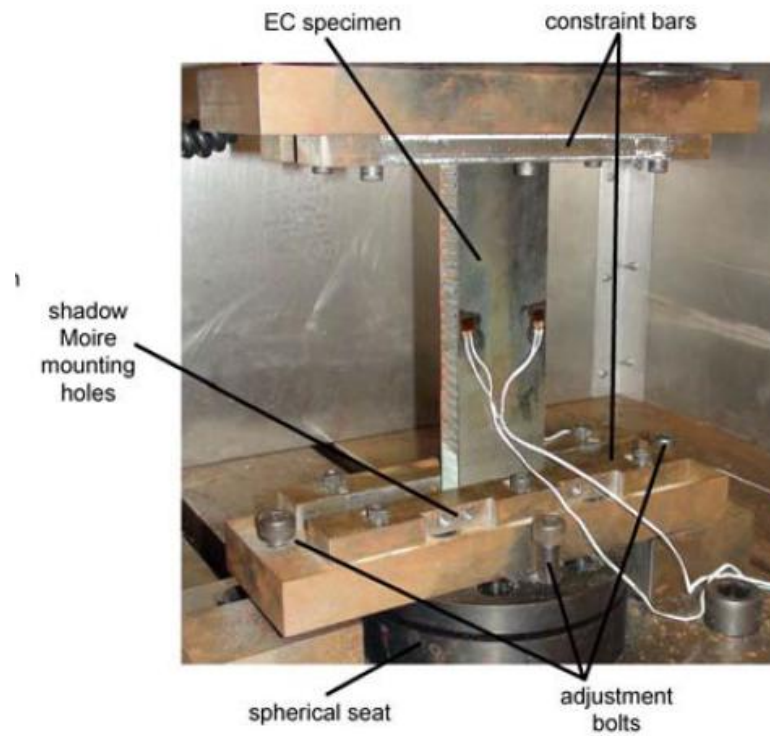


Figure D.1. The edgewise compression test set-up used for the determination of the in-plane compliance, α_{11}

APPENDIX E

THE FOUR POINT BEND TEST SET-UP

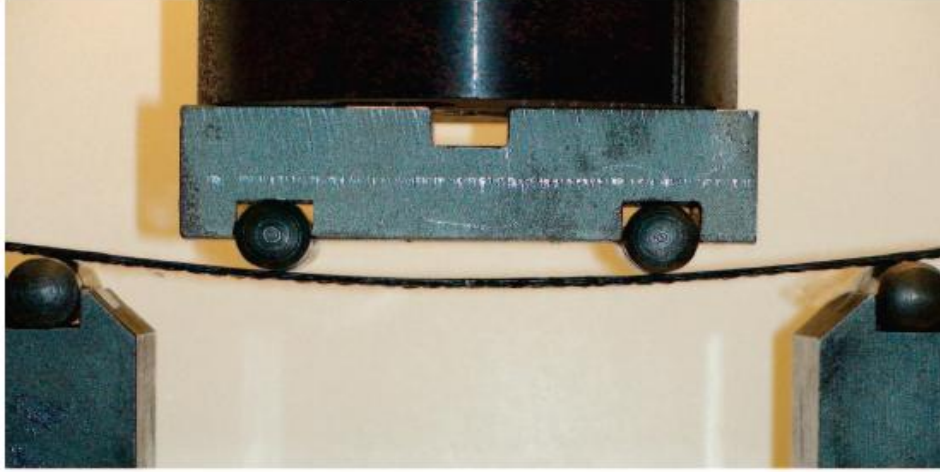


Figure E.1. The four point bend test set-up used for the determination of the flexural compliances, δ_{11} and δ_{12}

APPENDIX F

THE FLAT-WISE COMPRESSION TEST SET-UP



Figure F.1. Flat-wise compression test set-up for the core property determination.

APPENDIX G

GENERAL MATLAB CODE: RAYLEIGH-RITZ ENERGY MINIMIZATION

```
% BENDING + MEMBRANE ENERGY SOLUTION BASED ON ENERGY MINIMIZATION

function final = fsolvecode(const)

k = 0;
L = 0;
final = [];
global c;
global k;
global L;

I = 1;

c = const;
results = [];

format long
for(k=1:length(const(:,1)))

    globalvar(k);

    if(k == 1)

xo = ['define the initial values of a and wo here'];
else
xo = results(length(results(:,1)),:);
end

results = [fsolve(@myfun,xo,optimset('MaxIter', 1000000,'MaxFunEvals',
3000000,'TolFun',1E-6))];
    l = length(results);
    if(l >= L)
        L = l;
        xo = results(length(results(:,1)),:);

    end
    final = [final; results];
    L = 0;
    l = 0;

end

final;
end

function F=myfun(a)
```

```

global k;

i=1;

const = constants(k);

% Provide the values of the parameters P, b, D, E, h, v and poc in respective
columns 1-7 in the Matlab workspace.
% Successive rows of the same data be placed in the workspace for the
different load levels

P=const(1);
b=const(2);
D=const(3);
E=const(4);
h=const(5);
v=const(6);
poc=const(7);

F=['provide the equations for dPi/dwo=0 and dPi/da=0. The equations may be
written as one underneath the other inside these square brackets without a
semi-colon'.];

end

function out = constants(k)

global c;

out = c(k,:);

end

function globalvar(a)

global k;

k = a;

end

```

APPENDIX H

VALIDATION OF MODELING RESULTS WITH EXACT PLATE SOLUTIONS

Before the bending and membrane energy equations were used, a validation exercise was carried out by comparing the displacements obtained using the energy solutions with the exact plate theory solutions [88]. This was done in order to see how the displacement values that were obtained using the energy method compared with the exact plate theory solutions for loadings where the exact solutions were available. Because the exact solutions are based on isotropic plate properties, the assumption of a 1 mm thick isotropic steel plate was used for the comparisons. The Young's modulus of elasticity for steel is taken as 200 GPa and the Poisson's ratio is taken as 0.3.

AH.1 BENDING ONLY SOLUTION

The displacements obtained by the energy solution involving only the bending energy and total work, i.e., no membrane energy was included in the total system energy evaluation, were compared to certain available exact small deflection plate solutions.⁸⁸ The comparisons were made by assuming either the core resistive pressure, p_{oc} , equal to zero or the point load, P , equal to zero.

AH.1.1 Assumption 1: Core Resistive Pressure, $p_{oc}=0$

Assuming the core resistive pressure, $p_{oc}=0$, the displacements were solved for using the energy solution for the different a/b ratios, where a is the dent radius and b is the flat-nosed indenter radius. The results were compared to the exact plate theory solutions for the following cases:

- i. concentric load on a continuous circular plate.
- ii. point load on an annular plate as shown in Figure AH.1.⁸⁸

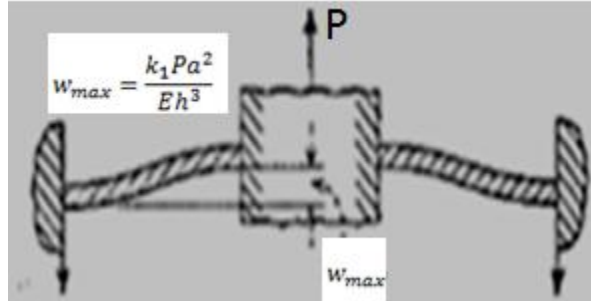


Figure AH.1 Exact annular plate solution for the point load condition. *Source [88]*

The corresponding k_1 values for the equation presented in Figure AH.1 is presented in Table AH.1. In Table AH.1, a represents the outer plate radius and b represents the inner plate radius. As seen in Table AH.1, the exact annular plate solution was only available up to a/b ratios of 5. An effort was made to look for the exact solution at higher a/b ratios but to no avail.

Table AH.1. Values of k_1 for the different cases presented in Figure AH.1. *Source [88]*

a/b	k_1
1.25	0.00129
1.50	0.0064
2.00	0.0237
3.00	0.062
4.00	0.092
5.00	0.114

Figure AH.2 presents the ratios of the displacements obtained using the energy solution to the displacements obtained using the different exact plate theory solutions for certain a/b ratios. The circular plate with concentric load out of all the cases most closely resembles the plate type and the external load form of the face sheet. The exact displacement values for the circular plate with concentric load shows good correlation with displacements obtained using the

energy solution for the higher a/b ratios. In the experiments, the dent radius is significantly larger than the indenter contact radius so an improved correlation for the higher a/b ratios is expected. However, the displacement ratio seems to plateau around 0.8 with increasing a/b . This is because the exact solution, even at higher a/b ratios, predicts slightly larger deflections than the deflections predicted by the energy solution. This happens primarily because in the exact solution for a circular plate with a ring load, the slope at $r=b$ is not being forced to be zero as in the case of the energy solution due to the equivalent flat-nosed indenter assumption. This results in the deflections being a little larger in the exact solution than the predicted deflection by the energy method. The bending energy solution compares well with the annular plate solution up to $a/b=5$. However, there is a slight decrease in displacement ratio with increasing a/b ratio. This is because with increasing a/b ratio, the effect of the differences in the inner slope close to $r=b$ becomes more and more significant which results in the exact solution having larger displacements than that predicted by the energy solution.

Overall, comparisons with both the exact solutions validate the displacements obtained by the energy solution. This is said primarily because the displacement ratios are reasonably high. It is around 0.8 for $a/b =20$ for the concentric load on a circular plate case, and the current trend of the annular plate case hints that it will likely plateau around the same or a little higher value. The small differences in displacements between the values obtained by the energy solution and the exact solution are expected due to the different displacement fields as well as the slope issue at or in the vicinity of $r=b$ as discussed above.

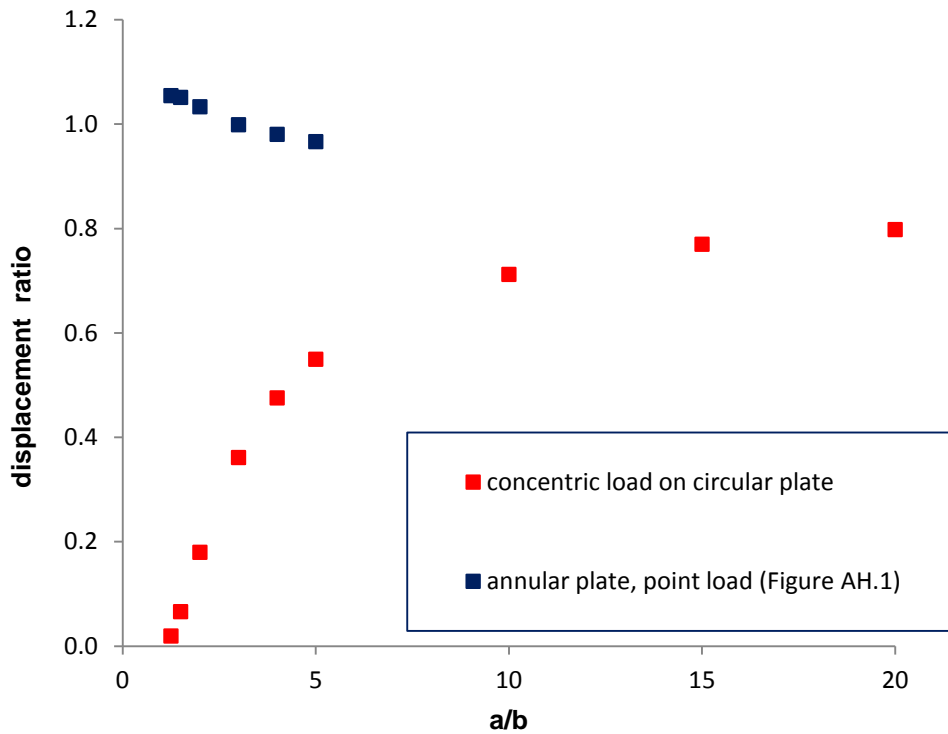


Figure AH.2. Displacement ratio plots for the comparison of the bending energy solution to the exact small deflection plate solution with $p_{oc}=0$.

AH.1.2 Assumption 2: Applied load, $P=0$

The same exercise was repeated as described in section AH.1.1 except in this case, instead of assuming $p_{oc}=0$, the externally applied load, P , was assumed to be zero. The displacements obtained from the bending energy solutions were compared to the exact solution for a uniformly distributed load on a continuous circular plate. The bending energy solution is compared to this particular exact solution because the deflected face sheet in the sandwich structure is like a continuous circular plate with a constant core resistive pressure.

Figure AH.3 presents the displacement ratios obtained from the energy solution to the exact plate solution for certain a/b ratios. Comparison of the displacements obtained by the energy solution to the exact solution shows excellent correlation at higher a/b ratios. In the experiments, the dent radius is significantly larger than the indenter contact radius so an improved correlation for the higher a/b ratios is expected. For the uniformly distributed load on a circular plate, the effect of the slope at $r=b$ is expected to be less than that for the ring load case due to a wider distribution of load in the former compared a greater concentration of load around the ring in the latter. This would imply that the displacement ratios should be better for the uniformly distributed load than the ring load case. This is exactly what is seen by a comparison of the circular plate results presented in Figure AH.3 to the ring load results presented in Figure AH.2. As obvious from the results presented in Figure AH.3, comparison of the displacements obtained by the energy method to the exact plate solution clearly validates the displacements obtained by the energy method.

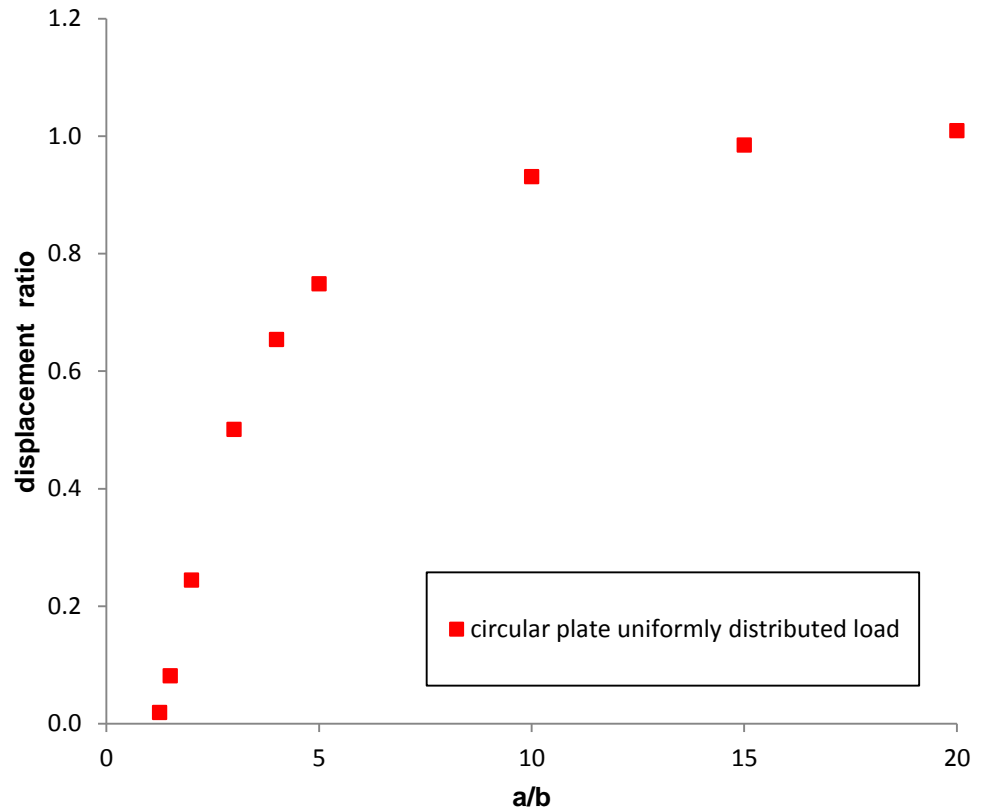


Figure AH.3. Displacement ratio plots for the comparison of the bending energy solution to the exact small deflection solution for $P=0$.

AH.2 BENDING AND MEMBRANE ENERGY COMBINED SOLUTION

The displacement obtained by the energy method involving the bending energy, the membrane energy and the total work were compared to the exact large deflection plate solutions.⁸⁸ These were also done by assuming either the core resistive pressure, p_{oc} , equal to zero or the point load, P , equal to zero.

AH.2.1 Assumption 1: Core resistive pressure, $p_{oc}=0$

Assuming the core resistive pressure, p_{oc} , equal to zero, the maximum displacements at different a/b ratios were obtained using the energy solution for $P=1300$ N. This was the BVID load for the 8 ply Q1-C1 specimens. The displacements were compared to exact large deflection solution for a clamped circular plate with immovable edge.⁸⁸ The results are presented in Figure AH.4 as the ratio of the displacements obtained by the energy solution to the displacement obtained by the exact solution for the different a/b ratios. For the higher a/b ratio, the displacement ratios show good correlation between the displacements obtained by the energy method to those obtained by the exact solution. The displacement ratio plateaus around 0.8 for higher a/b ratios which is significantly good and validates the displacement values obtained by the energy method. The difference in the displacements between the values obtained by the energy method and the exact solution is mostly due to the slope not being forced to zero at $r=b$ in the exact solution which results in slightly higher displacement values.

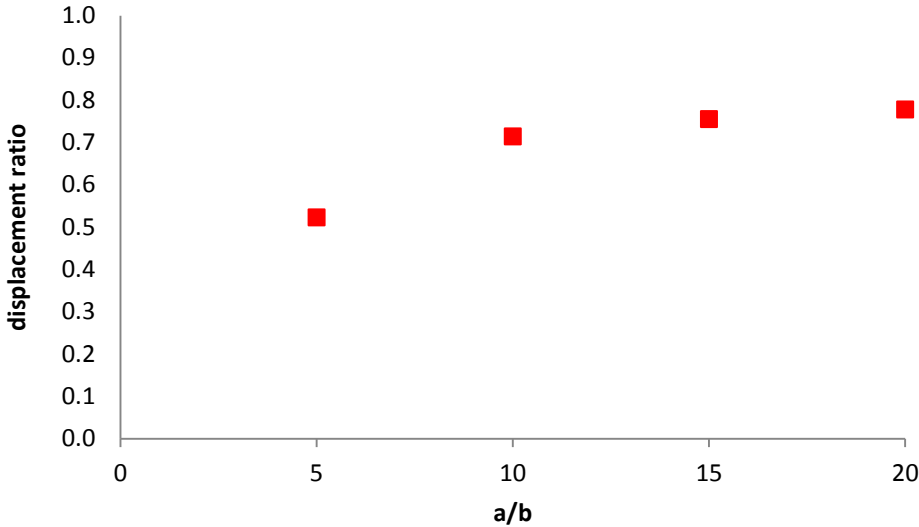


Figure AH.4. Displacement ratio plots for the comparison of bending and membrane energy combined solution to the exact large deflection plate solution with $p_{oc}=0$.

AH.2.2 Assumption 2: Applied load, $P=0$

Assuming the applied load, P , equal to zero, the maximum displacements at the different a/b ratios were obtained using the energy solution for a constant core resistive pressure, p_{oc} , of $9.6E5$ Pa. This pressure value corresponded to the core resistive pressure of the C1 core in the actual indentation problem. The displacements were compared to the exact large deflection solution for a clamped circular plate with immovable edges. The results are presented in Figure AH.5 as the ratio of the displacements obtained by the energy solution to the displacements obtained by the exact solution for the different a/b ratios. For the higher a/b ratio, the displacement ratios show good correlation between the displacements obtained by the energy solution to those obtained by the exact solution. The displacement ratio plateaus around 0.85 for higher a/b ratios which is significantly good and validates the displacement values obtained by the energy method. The difference in the displacements between the values obtained by the energy method and the exact

solution is again mostly due to the slope not being forced to zero at $r=b$ in the exact solution which results in slightly higher displacement values. However, when compared to the results presented in Figure AH.4 for the point load, the results are better in the case of the uniformly distributed load. This also shows that the slope issue at $r=b$ becomes less significant in the uniformly distributed case as compared to the point load case.

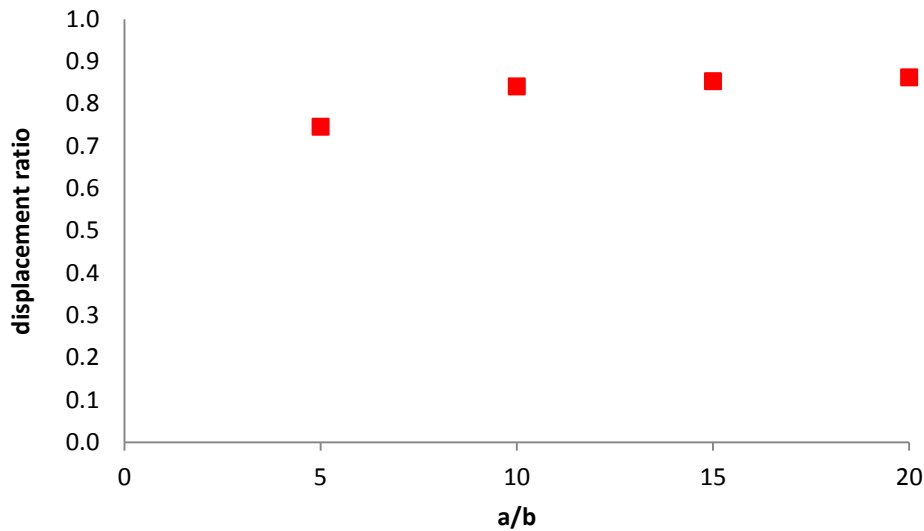


Figure AH.5. Displacement ratio plots for the comparison of bending and membrane energy combined solution to the exact large deflection plate solution with $P=0$.

APPENDIX I

DERIVATION OF EQUIVALENT FACE SHEET PROPERTIES FOR A DELAMINATED LAMINATE

In this appendix, the derivation of equivalent in-plane modulus, in-plane Poisson's ratio and the bending stiffness of a delaminated laminate is presented.

AI.1 Equivalent In-plane Modulus

Consider a delaminated laminate of width b , ply thickness t_i and the total laminate thickness t . Figure AI.1 shows a schematic that describes these geometrical parameters. In the given coordinate system, global in-plane directions are represented by 1 and 2 while the transverse (through-the laminate thickness) direction is represented by 3.

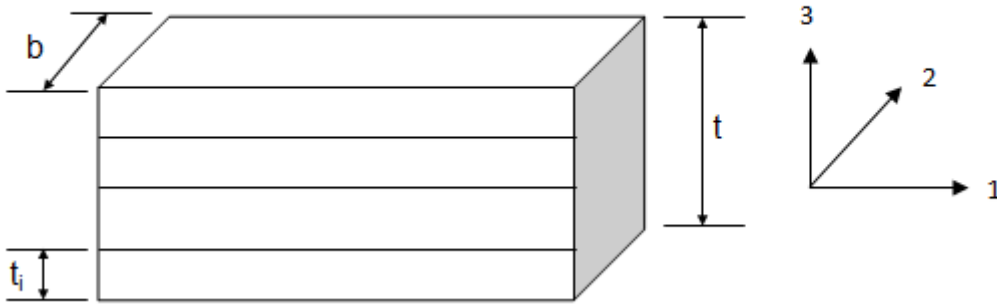


Figure AI.1 Schematic of a delaminated laminate with global coordinate axes directions.

To derive the equivalent in-plane modulus of the delaminated laminate in the 1 direction, E_{11}^* , assume a pure axial load P applied in the global 1 direction. Each of the sublaminates will then carry a fraction of the delaminated load which can be represented as

$$P = \sum_{i=1}^n P_i \quad (\text{AI.1})$$

Here, i represents an individual sublamine and n represents the total number of sublaminates. Since there is pure axial loading, i.e., there is no bending, it can be said that $P = \sigma A$ where σ is the axial stress and A is the cross-sectional area. Equation (AI.1) can therefore be re-written as

$$\sigma_{11} A = \sum_{i=1}^n \sigma_{11i} A_i \quad (\text{AI.2})$$

Assuming the same width b for all the sublaminates and the area $A=bt$, equation (AI.2) can therefore be restated as

$$\sigma_{11} bt = \sum_{i=1}^n \sigma_{11i} b_i t_i \quad (\text{AI.3})$$

Taking $b=b_i$ and replacing σ with $E\epsilon$, where E is the in-plane axial modulus and ϵ is the axial strain, equation (AI.3) can be written in terms of the axial modulus and the axial strain as

$$E_{11}^* \epsilon_{11}^* t = \sum_{i=1}^n E_{11i} \epsilon_{11i} t_i \quad (\text{AI.4})$$

In equation AI.4, ϵ_{11}^* represents the midplane strain in the 1 direction of the delaminated laminate. E_{11i} can be stated in terms of the in-plane compliance, α_{11i} , and the sublamine thickness, t_i as $E_{11i} = \frac{1}{\alpha_{11i} t_i}$. Assuming the same value of strain in the 1 direction for all the sublaminates, the equivalent in-plane modulus, E_{11}^* , can therefore be stated as

$$E_{11}^* = \frac{1}{t} \sum_{i=1}^n \frac{1}{\alpha_{11i}} \quad (\text{AI.5})$$

The equivalent in-plane modulus in the 2 direction, E_{22}^* , is derived in exactly the same way and as E_{11}^* and stated as

$$E_{22}^* = \frac{1}{t} \sum_{i=1}^n \frac{1}{\alpha_{22i}} \quad (\text{AI.6})$$

Likewise, the equivalent in-plane modulus, E_{rr}^* , in any direction θ can be stated as

$$E_{rr}^* = \frac{1}{t} \sum_{i=1}^n \frac{1}{\alpha_{rri}} = \frac{1}{t} \sum_{i=1}^n E_{rri} t_i \quad (\text{AI.7})$$

The E_{rri} value for the individual sublaminates represents the varying equivalent in-plane modulus of the individual sublaminate in any direction θ . Equation AI.7 therefore gives the equivalent in-plane modulus, E_{rr}^* , for the delaminated laminate in any direction θ . The value of E_{rr}^* is expected to vary with changing angle θ . In order to determine E_{rr}^* , the E_{rri} value for the individual sublaminate has to be determined first. The E_{rri} value for the individual sublaminate is determined using the classical laminate plate theory (CLPT) in the following manner.

The classical laminate plate theory (CLPT)⁸⁹ relates the in-plane compliance, α , the coupling compliance, β and the flexural compliance, δ , of a laminate with the extensional stiffness, A , the coupling stiffness, B , and the bending stiffness, D , as

$$\begin{bmatrix} \alpha & \beta \\ \beta^T & \delta \end{bmatrix} = \begin{bmatrix} A & B \\ B & D \end{bmatrix}^{-1} \quad (\text{AI.8})$$

The extensional stiffnesses, A_{ij} , the coupling stiffness, B_{ij} , and the bending stiffness, D_{ij} , are calculated using the reduced stiffness Q_{ij} as

$$A_{ij} = \sum_{p=1}^n Q_{ij}^p (z_{p+1} - z_p)$$

$$B_{ij} = \frac{1}{2} \sum_{p=1}^n Q_{ij}^p (z_{p+1}^2 - z_p^2)$$

$$D_{ij} = \frac{1}{3} \sum_{p=1}^n Q_{ij}^p (z_{p+1}^3 - z_p^3)$$

(AI.9)

where z and p defined according to Figure AI.2 which shows the cross-sectional view of a sublaminate with n plies.

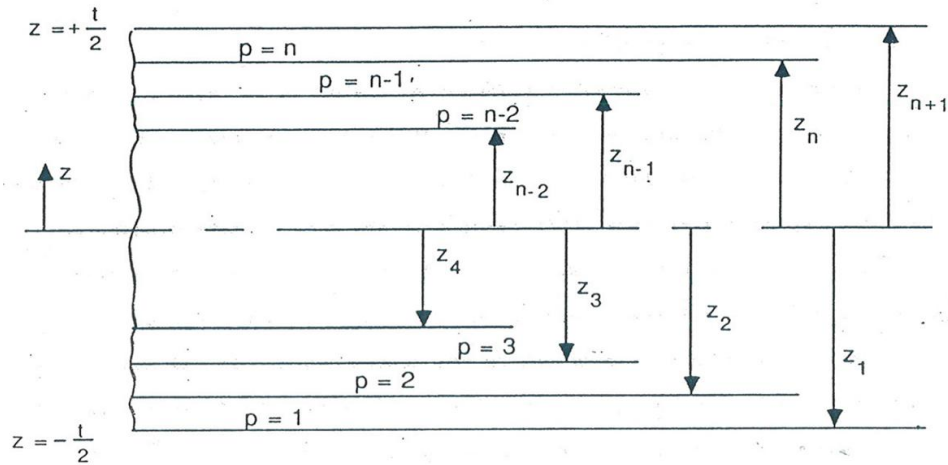


Figure AI.2 Cross-sectional view of a laminated plate with n layers

Let us first determine E_{rri} for each of the sublaminates when the global 1 direction is taken to be the same as the 0° direction. When the material axis of a ply (lamina) in a particular sublaminate does not coincide with the global axis, the reduced stiffnesses, Q_{ij} , must be transformed to the global axis using the CLPT transformation relations⁸⁹. The transformed reduced stiffness values for each ply in a particular sublaminate is then used in equation AI.9 to calculate the A, B and D matrix of every sublaminate. The inverse relation represented by equation AI.8 is then used to find the in-plane compliances for each of the sublaminates. Using

CLPT,⁸⁹ the in-plane modulus, E_{rri} , is calculated using the in-plane compliance values, α_{11i} , for the individual sublaminates as

$$E_{rri} = \frac{1}{\alpha_{11i}t_i}$$

(AI.10)

Using equation AI.7, the equivalent in-plane modulus, E_{rr}^* is then calculated in the 0° direction. The value E_{rr}^* is same as E_{11}^* for $\theta=0^\circ$. This exercise is repeated by changing the direction of the global axis in increments of 5° from 0° to 360° . For each of these directions, E_{rri} , for the individual sublaminates and the corresponding E_{rr}^* is calculated in the same manner as described for the 0° case above.

The plots for the variation of the in-plane modulus E_{rr} with θ for the individual sublaminates for an 8 ply Q1 delaminated laminate is shown in Figure AI.3. The rapid drop-off of E_{rr} with θ from the fiber direction for any unidirectional ply is consistent with what is expected since the modulus is the highest in the fiber direction of a single ply and the drop-off is rapid at small angular changes with the smallest values in the transverse direction. For the $[45^\circ/0^\circ]$ sublaminates, an almost constant modulus is seen between 0° to 45° . When going from the 0° direction to the 45° direction for this sublaminates, the 0° ply modulus rapidly decreases while the 45° ply modulus rapidly increases. Upon superposing, the decrease in the modulus of the 0° ply is compensated by the increase in the modulus of the 45° ply. Therefore, the modulus remains constant between 0° and 45° .

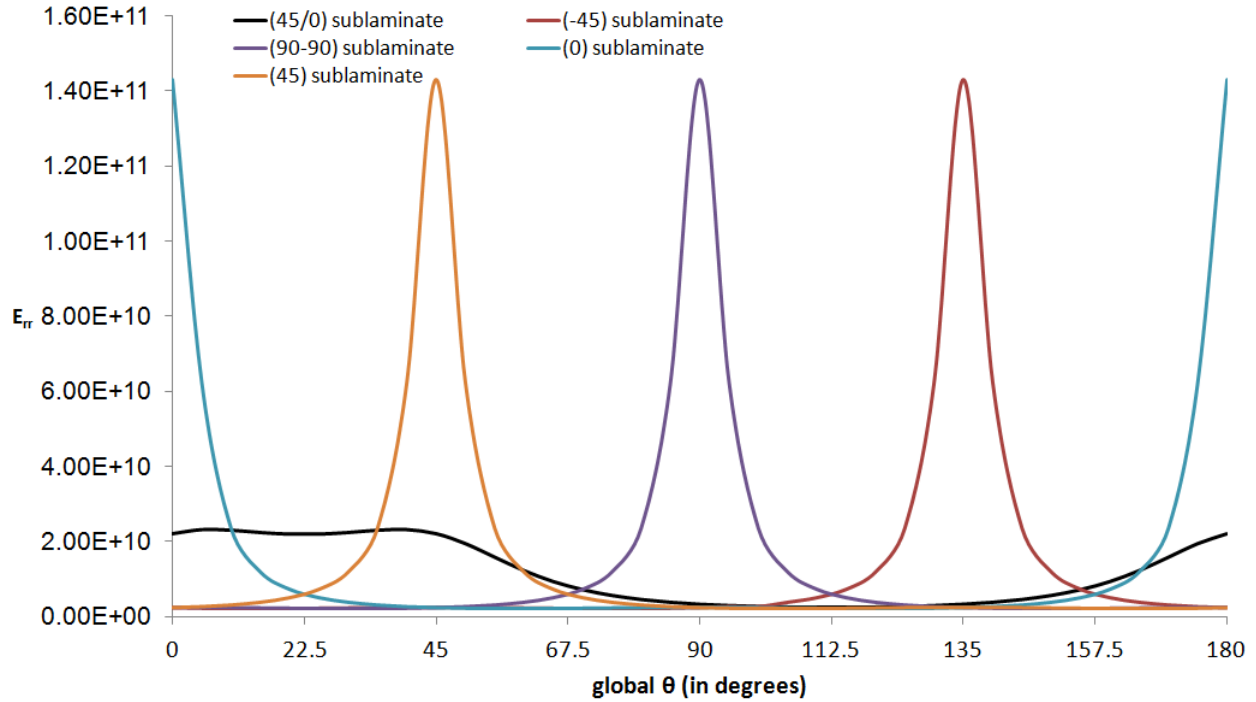


Figure AI.3 Plot of E_{rr} with θ of the individual sublaminates for the 8 ply Q1 delaminated laminate.

The plot of the variation of the equivalent in-plane modulus, E_r^* with θ for the 8 ply Q1 delaminated laminate is shown in Figure AI.4. As seen in the plot, the value of E_r^* changes with θ . To be consistent with the equivalent circular isotropic plate assumption used in the model, a single average value of E_r^* for all angles θ needed to be determined. The average value of E_r^* for the delaminated laminate is evaluated by taking the area under the curve and dividing it by the length of the x-axis. The average value is presented in Figure AI.4. The intact value of E_r is also presented in the figure.

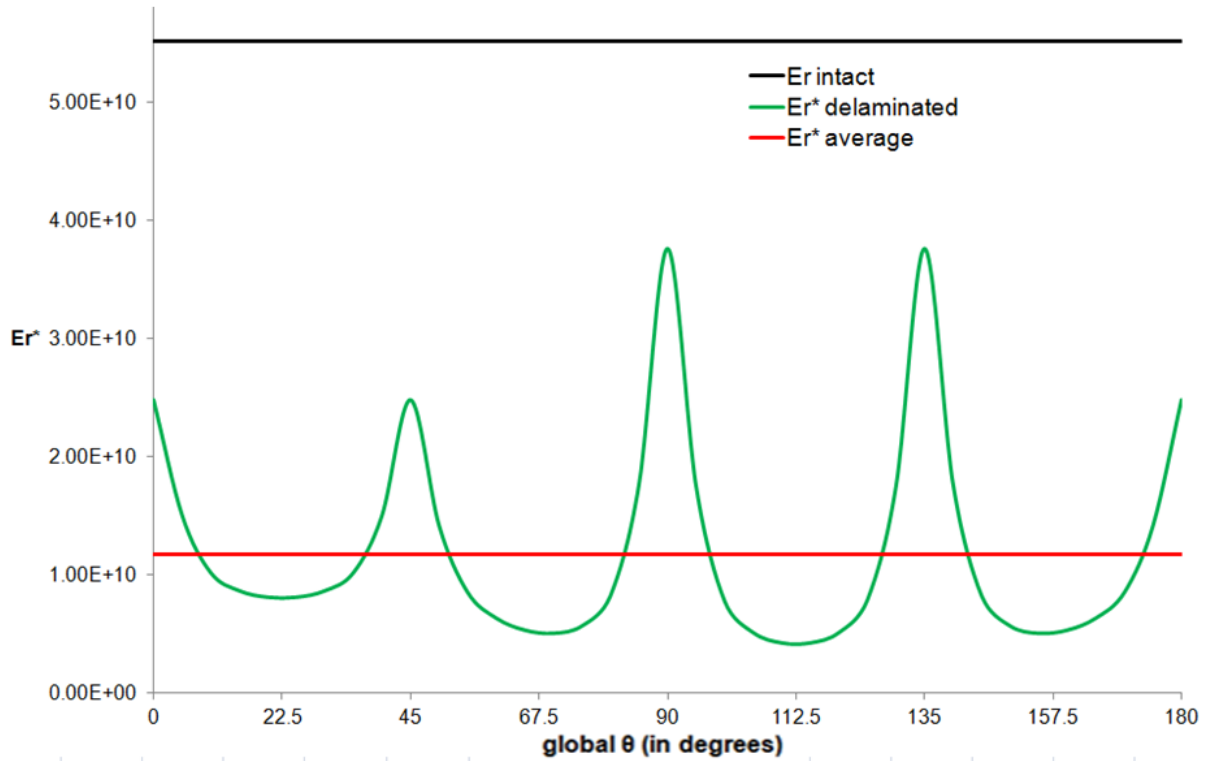


Figure AI.4 Plot of E_r^* with θ for the individual sublaminates for the 8 ply Q1 delaminated laminate.

AI.2 Equivalent Poisson's Ratio

Consider again the delaminated laminate in Figure AI.1 and assume a uniaxial midplane strain, ϵ_0 , applied in the 1 direction. The amount each ply will strain in the 2 direction can be determined using a three step superposition procedure in the following manner.

- i. With the application of the strain in the 1 direction, first allow the free deformation of each of the plies in the 2 direction. The strains in the individual plies, i , in the 2 direction can therefore be stated as ϵ_2^i . The strain in the 2 direction is defined in terms of the individual sublaminate Poisson's ratio, ν_{12}^i , and the midplane strain, ϵ_0 , as

$$\epsilon_{2i} = v_{12}^i \epsilon_o \quad (\text{AI.11})$$

- ii. Determine the total force per unit width required in the 2 direction to return each ply in the delaminated laminate to its undeformed state. To evaluate this, the stress required to return each ply to its undeformed configuration is first determined as

$$\sigma_2^i = E_{22i} v_{12}^i \epsilon_o \quad (\text{AI.12})$$

The force required per unit width for each ply can therefore be stated as

$$N_2^i = E_{22i} v_{12}^i \epsilon_o t_i \quad (\text{AI.13})$$

The in-plane sublaminar modulus in the 2-direction, E_{22i} , is defined as

$$E_{22i} = \frac{1}{\alpha_{22i} t_i} \quad (\text{AI.14})$$

Therefore, equation (AI.13) can be re-written as

$$N_2^i = \frac{1}{\alpha_{22i}} v_{12}^i \epsilon_o \quad (\text{AI.15})$$

The total force per unit width required to return the laminate to its original state can then be stated as

$$N_2 = \sum_{i=1}^n \frac{1}{\alpha_{22i}} v_{12}^i \epsilon_o$$

(AI.16)

- iii. Since the laminate is traction free, an equal and opposite total force is applied to the laminate to keep it traction free. The resultant strain in the 2 direction, ϵ_2 , can therefore be stated as

$$\epsilon_2 = \frac{N_2}{E_{22}^* t} = \frac{1}{E_{22}^* t} \sum_{i=1}^n \frac{1}{\alpha_{22i}} v_{12}^i \epsilon_o$$

(AI.17)

To determine the equivalent Poisson's ratio, v_{12}^* , it is assumed that the same amount of deformation happens in the 1 direction for each of the plies which is the same as the midplane strain ϵ_o . The equivalent Poisson's ratio, v_{12}^* , can finally be stated as

$$v_{12}^* = -\frac{\epsilon_2}{\epsilon_o} = \frac{1}{E_{22}^* t} \sum_{i=1}^n \frac{v_{12i}}{\alpha_{22i}}$$

(AI.18)

Equation (AI.18) is used to calculate the equivalent Poisson's ratio of the delaminated laminate based on the global axes in the 1 and 2 directions in Figure AI.1. The equivalent Poisson's ratio can be determined for the different global axes directions defined in increments of 5° from 0° to 360° in exactly the same way as described in this section.

The variation of equivalent Poisson's ratio with θ for the 8 ply Q1 delaminated laminate

is shown in Figure AI.4. The average Poisson's ratio is determined in the same manner as described for the in-plane modulus, where the area under the plot is divided by the length of the x-axis for its determination. The average Poisson's ratio value is also plotted in Figure AI.4.

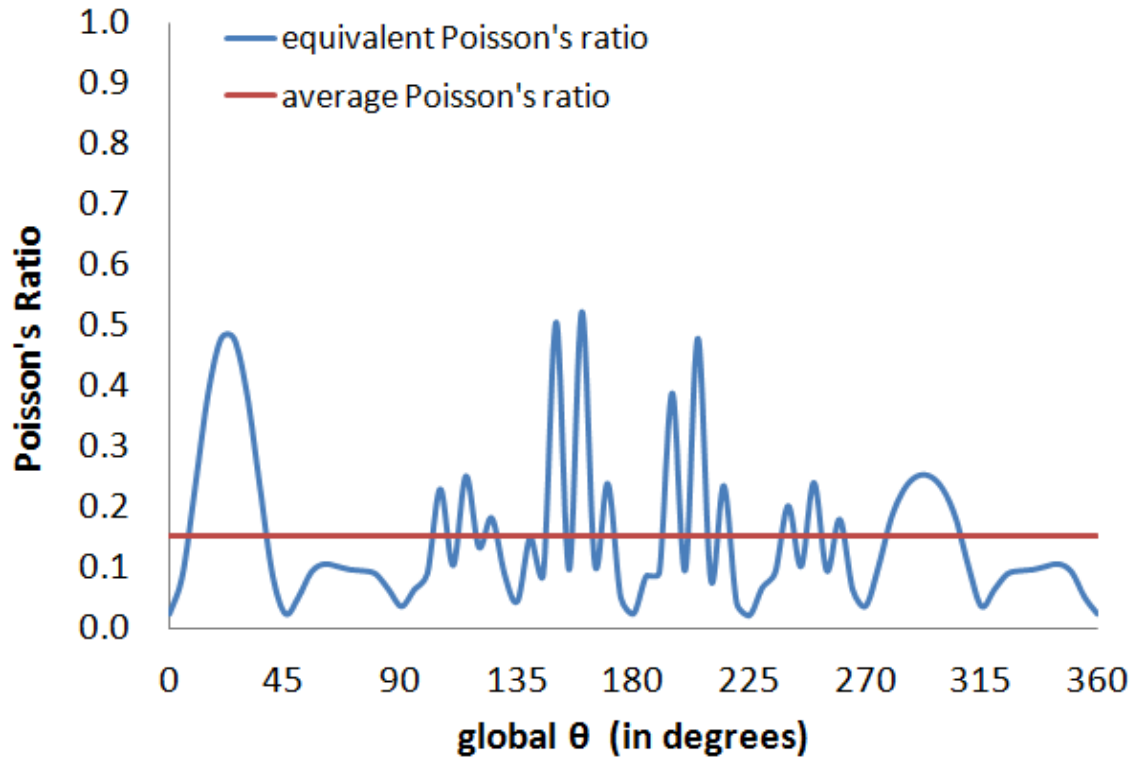


Figure AI.4. Plot of equivalent Poisson's ratio values for the delaminated 8 ply Q1 laminate in the different angular directions.

AI.3 Equivalent Bending Stiffness

Consider a bending moment applied to a circular delaminated laminate as shown in Figure AI.5.

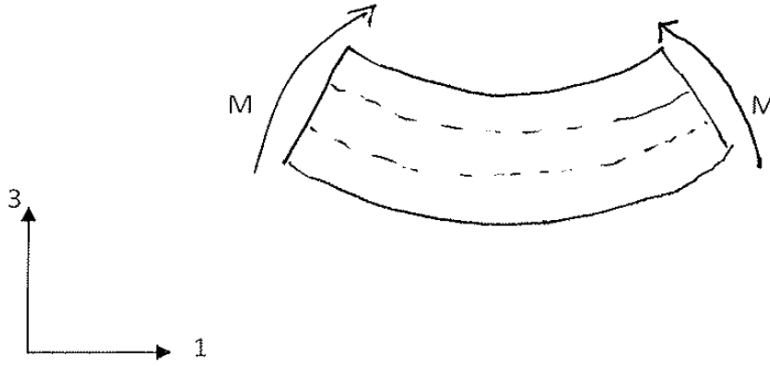


Figure AI.5 Schematic showing assumed applied bending moment in a delaminated laminate.

It can therefore be said that the total moment is divided in the individual sub-laminates which can be represented as

$$M = \sum_{i=1}^n M_i \quad (\text{AI.19})$$

The moment-curvature equation for the symmetrical bending of a circular isotropic plate [88] can also be stated for the delaminated laminate using homogenized bending stiffness, D_r and homogenized Poisson's ratio, ν_r as

$$M_r = -D_r \left(\frac{d^2 w}{dr^2} + \frac{\nu_r}{r} \frac{dw}{dr} \right) \quad (\text{AI.20})$$

where w is the transverse deflection. Assuming the same transverse deflection, w , at every sublaminar in the delaminated laminate, equation AI.20 can be substituted into equation AI.19.

The resultant equation can be represented as

$$-D_r \left(\frac{d^2 w}{dr^2} + \frac{v_r}{r} \frac{dw}{dr} \right) = \sum_{i=1}^n \left(-D_{ri} \left(\frac{d^2 w}{dr^2} + \frac{v_{ri}}{r} \frac{dw}{dr} \right) \right) \quad (\text{AI.21})$$

By comparison of the left hand side of equation AI.21 with the right hand side and assuming the same transverse deflection in all the individual sub-laminates, it can be said that

$$D_r = \sum_{i=1}^n D_{ri} \quad (\text{AI.22})$$

and

$$D_r v_r = \sum_{i=1}^n (D_{ri} v_{ri}) \quad (\text{AI.23})$$

Only equation AI.22 is used in the model for the determination of the equivalent bending stiffness of a delaminated laminate. The D_{ri} for the individual sublaminates is determined using equation (9.22) presented in the dissertation. While equation AI.23 is not used in the dissertation, it is mentioned here that the definition of Poisson's ratio, v_{ri} , for the in-plane response is also used for the bending response.

APPENDIX J

MOMENT DISTRIBUTION IN EXACT CLAMPED CIRCULAR PLATE SOLUTION

This Appendix presents the moment distributed in clamped circular plates under point and uniform load. This appendix is presented in support of the postulate in the unloading regime of the model presented in Chapter 9 which stated that a smaller portion of the crushed region uncrushes initially when the switch is made from loading to unloading.

AJ.1 Point Load

Figure AJ.1 presents a schematic that shows a point load acting on the midspan of a clamped circular plate of radius a .

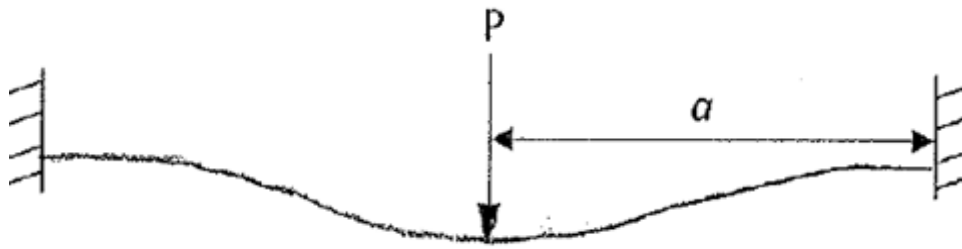


Figure AJ.1 Schematic presenting a clamped circular plate under a point load.

The distribution of moment in a clamped circular plate with a point load at the midspan is given by the exact plate theory equation as [88]

$$M_r = \frac{P}{4\pi} \left[(1 + \nu) \ln \left(\frac{a}{r} \right) - 1 \right] \quad (\text{AJ.1})$$

where r is the distance away from the plate center and ν is the Poisson's ratio.

The distribution of moment for any load P assuming a Poisson's ratio of 0.3 is shown in Figure AJ.2. There is a region from $r/a = 0$ to $r/a = 0.463$ where the moment is positive. This is the region in the circular plate with the point load where the stresses in the lower surface of the plate would be tensile. Beyond $r/a = 0.463$ to $r/a = 1$, the moment is negative with the stresses in the lower surface compressive. The highest compressive stresses are therefore seen at the outer edge with the largest negative moments and compressive stresses. Physically, during unloading, plate deflection is rapid in the inner region than the edge region. Based on the exact plate solutions for the moment distribution, it is therefore postulated that initial uncrushing would be more rapid in the regions in the lower surface of the plate where the moment is primarily positive as the face sheet tries pull away faster. Thus, a smaller portion of the core from the dent center to a certain distance r is expected to be pulled back initially rather than the entire crush zone. This is also supported by a similar analysis on distributed load in the subsequent section.

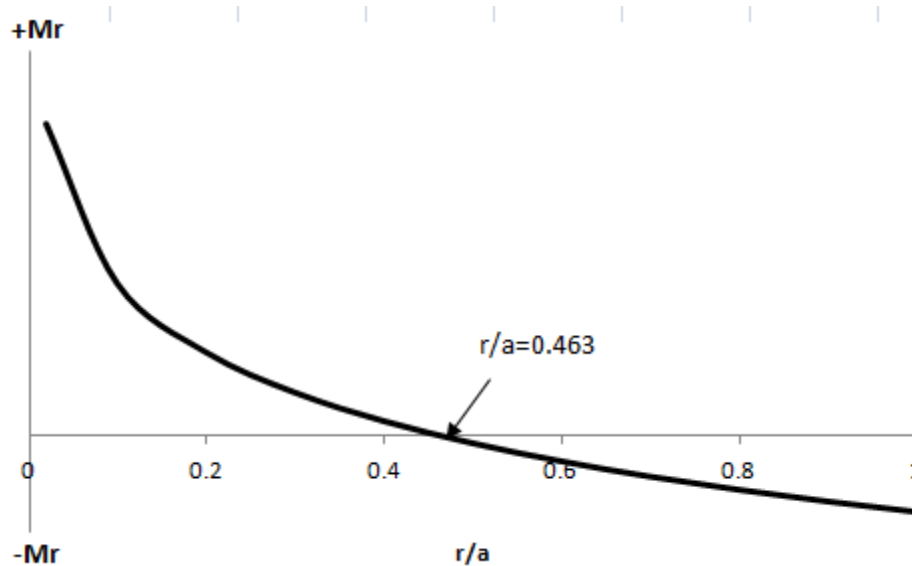


Figure AJ.2 Distribution of moment for a point load on a circular plate.

AJ.2 Uniformly Distributed Load

Replacing the load in Figure AJ.1 with a uniformly distributed load, q , that spans the entire plate from $r = 0$ to $r = a$ and points in the same direction as load P, the exact equation for the distribution of moment can be stated as [88]

$$M_r = \frac{q}{16} [a^2(1 + \nu) - r^2(3 + \nu)] \quad (\text{AJ.2})$$

The distribution of moment for the uniformly distributed load assuming a Poisson's ratio of 0.3 is shown in Figure AJ.3. There is a region from $r/a = 0$ to $r/a = 0.628$ where the moment is positive. This is the region in the circular plate with the uniformly distributed load where the stresses in the lower surface of the plate would be tensile. Beyond $r/a = 0.628$ to $r/a = 1$, the moment is negative with the stresses in the lower surface compressive. Therefore for the uniformly distributed case also, the highest compressive stresses are therefore seen at the outer edge with the largest negative moments and compressive stresses. There is an inner region of the plate where the moment is positive and the stresses in the lower surface of the plate tensile. The distribution of moment in the uniformly distributed case also supports the postulate that initial uncrushing would be more rapid in the regions in the lower surface of the plate where the moment is primarily positive as the face sheet tries pull away faster. Thus, a smaller portion of the core from the dent center to a certain distance r is expected to be pulled back initially rather than the entire crush zone.

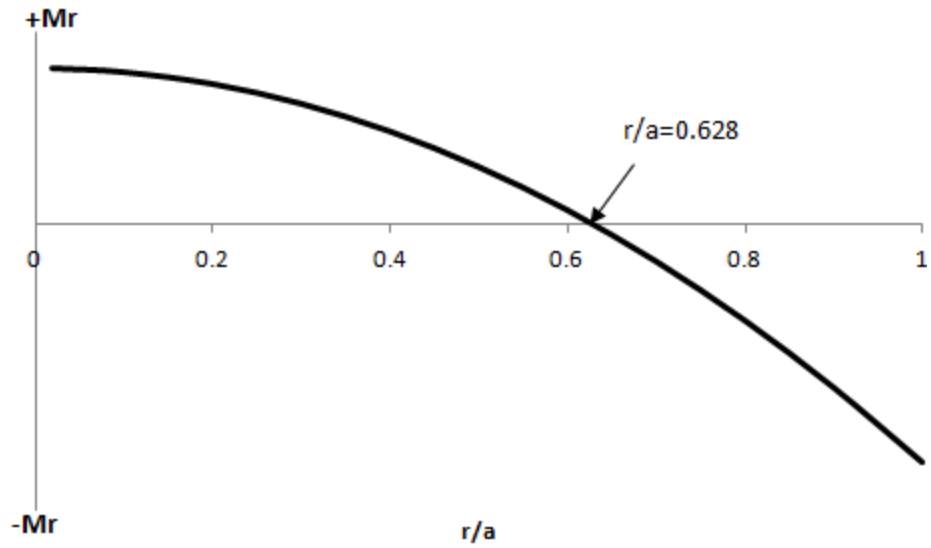


Figure AJ.3 Distribution of moment for a uniformly distributed load on a circular plate.

References

1. Davis GAO and Zhang X. Impact damage prediction in carbon composite structures. *International Journal of Impact Engineering* 1995; 16 (1): 149-170.
2. Schoeppner GA and Abrate S. Delamination threshold loads for low velocity impact on composite laminates. *Composites Part A* 2000; 31: 903-915.
3. Olsson R. Mass criterion for wave controlled impact response of composite plates. *Composites Part A: 2000; 31: 879-887.*
4. Swanson SR. Limits of quasi-static solutions in impact of composite structures. *Composites Engineering* 1992; 2 (4): 261-267.
5. Williamson JE and Lagace PA. Response mechanisms in the impact of graphite/epoxy honeycomb sandwich panels. Proceedings of the American Society for Composites Eighth Technical Conference on Composite Materials; 1993; Cleveland, OH.
6. Herup EJ, and Palazotto AN. Low-velocity impact damage initiation in graphite/epoxy/nomex honeycomb-sandwich plates. *Composites Science and Technology* 1997; 57: 1581 – 1598.
7. Li Y, Xuefang A and Xiaosu Y. Comparison with low-velocity impact and quasi-static indentation testing of foam core sandwich composites. *International Journal of Applied Physics and Mathematics* 2012; 2 (1); 58-62.
8. Ferri R and Sankar BV. A comparative study on the impact resistance of composite laminates and sandwich panels. *Journal of Thermoplastic Composite Materials* 1997; 10 (4): 304-315.

9. Tomblin JS, Lacy TE, Smith B, Hooper S, Vizzini A and Lee S. Review of damage tolerance for composite sandwich airframe structures. Final report, Federal Aviation Administration Report, DOT/FAA/AR-99/49.
10. Shyprykevich P, Tomblin JS, Ilcewicz L, Vizzini AJ, Lacy TE and Hwang Y. Guidelines for analysis, testing, and non-destructive inspection of impact damaged composite sandwich structures. Final Report, Federal Aviation Administration Report 1999; DOT/FAA/AR-02/121.
11. Abrate S. Localized impact on sandwich structures with laminated facings. *Applied Mechanics Review* 1997; 50 (2): 69-82.
12. Kim CG and Jun E. Impact resistance of composite laminated sandwich plates. *Journal of Composite Materials* 1992; 26:2247–2261.
13. Sjoblom PO, Hartness JT and Cordell TM. On low-velocity impact testing of composite materials. *Journal of Composite Materials* 1988; 22 (1): 30-52.
14. Abrate S. Impact on laminated composite materials. *Applied Mechanics Reviews* 1991; 44 (4): 155 – 190.
15. Liu S and Chang F. Matrix cracking effect on delamination growth in composite laminates induced by a spherical indenter. *Journal of Composite Materials* 1994; 28 (10): 940-977.
16. Renault M. Compression après impact d'une plaque stratifiée carbone époxyde – Etude expérimentale et modélisation éléments finis associée. Rapport interne EADS CCR 1994.
17. Choi HU and Chang F. A model for predicting damage in graphite/epoxy laminated composites resulting from low velocity point impact. *Journal of Composite Materials* 1992; 26 (14): 2134-2169.

18. Liu D. Impact-Induced delamination – A view of bending stiffness mismatching. *Journal of Composite Materials* 1988; 22 (7): 674-692.
19. Davidson BD, Michaels JE, Sundararaman V and Michaels TE. Ultrasonic imaging of impact damaged composite panels. *Acoustical Imaging* 1992; 19: 589-594.
20. Michaels TE and Davidson BD. Ultrasonic inspection detects hidden damage in composite materials,” *Advanced Materials and Processes* 1993; 143 (3): 34-38.
21. Park JH, Ha SK, Kang KW, Kim CW and Kim HS. Impact damage resistance of sandwich structure subjected to low velocity impact. *Journal of Materials Processing Technology* 2008; 201: 425-430.
22. Xue Z, Hutchinson JW. A comparative study of impulse-resistant metallic sandwich plates. *International Journal of Impact Engineering* 2004; 30:1283 –1305.
23. Fleck NA, Deshpande VS. The resistance of clamped sandwich beams to shock loading. *Journal of Applied Mechanics* 2004; 71:386–401.
24. Gibson LJ and Ashby MF. Cellular solids: structure & properties. Oxford: Pergamon Press 1988.
25. Daniel IM, Gdoutos EE, Wang KA and Abot JL. Failure modes of composite sandwich beams. *International Journal of Damage Mechanics* 2002; 11: 309-334.
26. Saha MC, Kabir E and Jeelani S. Study of debond fracture toughness of sandwich composites with nanophased core. *Materials Letters* 2008; 62: 567-570.
27. Zhou G, Hill M, Loughlan J and Hookham N. Damage characteristics of composite honeycomb sandwich panels in bending under quasi-static loading. *Journal of Sandwich Structures and Materials* 2006; 8 (1): 55-90.

28. Flores-Johnson EA and Li QM. Experimental study of indentation of sandwich panels with carbon fibre-reinforced polymer face sheets and polymeric foam core. *Composites: Part B* 2011; 42: 1212-1219.
29. Zhou G, Hill M and Hookman N. Investigation of parameters governing the damage and energy absorption characteristics of honeycomb sandwich panels. *Journal of Sandwich Structures and Materials* 2007; 8: 309-342.
30. Shyprykevich P, Tomblin J, Ilcewicz L, Vizzini AJ, Lacy TE and Hwang Y. Guidelines for analysis, testing, and non-destructive inspection of impact damaged composite sandwich structures. Federal Aviation Administration Report Number DOT/FAA/AR-02/121.
31. Raju KS, Smith BL, Tomblin JS, Liew KH and Guarddon JC. Impact damage resistance and tolerance of honeycomb core sandwich plates. *Journal of Composite Materials* 2008; 42: 385-412.
32. Tsotsis TK and Lee SM. Characterisation of localized failure modes in honeycomb sandwich panels using indentation. *Composite Materials: Testing and Design 1996*; ASTM STP; 1274: 139—165.
33. Anderson T and Madenci E. Experimental investigation of low-velocity impact characteristics of sandwich composites. *Composite Structures* 2000; 50: 239-247.
34. Hoo Fatt MS and Park KS. Dynamic models for low-velocity impact damage of composite sandwich panels – Part A: Deformation. *Composite Structures* 2001; 52: 335-351.
35. Hong S and Liu D. On the relationship between impact energy and delamination area. *Experimental Mechanics* 1989; 115-120.

36. Finn SR, He Y and Springer GS. Delaminations in composite plates under transverse impact loads – experimental results. *Composite Structures* 1993; 23:191-204.
37. Palm TE. Impact resistance and residual compression strength of composite sandwich panels. Proceedings of the 8th International Conference on Composite Materials (ICCM/8); 1991 July; Honolulu, HI.
38. Meo M, Vignjevic R and Marengo G. The response of honeycomb sandwich panels under low-velocity impact loading. *International Journal of Mechanical Sciences* 2005; 47: 1301-1325.
39. Lacy TE, Samarah IK and Tomblin JS. Damage Resistance Characterization of Sandwich Composites Using Response Surfaces. Federal Aviation Administration Report Number DOT/FAA/AR-01/71; 2002; 1-67.
40. Bernard ML and Lagace PA. Impact resistance of composite sandwich plates. *Journal of Reinforced Plastics and Composites* 1989; 8:432-445.
41. Nettles AT and Jackson JR. Compression after impact testing of sandwich composites for usage on expendable launch vehicles. *Journal of Composite Materials* 2010 ; 44: 707–738.
42. Schubel PM, Luo J and Daniel IM. Low velocity impact behavior of composite sandwich panels. *Composites: Part A* 2005; 2005 (36): 1389-1396.
43. Feraboli P and Kedward KT. Enhanced evaluation of the low velocity impact response of composite plates. *AIAA Journal* 2004; 42 (10): 2143-2152.
44. Scott IG and Scala CM. A review of non-destructive testing of composite materials. *NDT International* 1982; 75-86.

45. Nettles AT and Jackson JR. Compression after impact testing of sandwich composites for usage on expendable launch vehicles. *Journal of Composite Materials* 2010; 44: 707–738.
46. Tomblin JS, Raju KS, Walker T and Acosta JF. Damage tolerance of composite sandwich airframe structures – additional results. Final Report 2005; Federal Aviation Administration Report, DOT/FAA/AR-05/33.
47. Minguet PJ. A model for predicting the behavior of impact damaged minimum gage sandwich panels under compression. Proceedings of the 32nd AIAA/ASME/ASCE/AHS/ASC Structures, Structural Dynamics and Materials Conference; 1991; Baltimore, MD.
48. Ratcliffe JG, Jackson WC and Schaff J. Predicting the compression strength of impact-damaged sandwich panels. Proceedings of the 60th American Helicopter Society 60th Annual Forum 2004; Baltimore, MD.
49. Ratcliffe JG and Jackson WC. A finite element analysis for predicting the residual compressive strength of impact-damaged sandwich panels. NASA Technical Memorandum, NASA/TM-2008-215341.
50. Abrate S. Modeling of impacts on composite structures. *Composite Structures* 2001; 51:129–138, 2001.
51. Caprino G and Teti R. Impact and post-impact behavior of foam core sandwich structures. *Journal of Composite Structures* 1994; 29:47–55.
52. Feraboli P. Modified SDOF models for improved representation of the impact response of composite plates. *Journal of Composite Materials* 2006; 40 (24):2235-2255.

53. Anderson TA. An investigation of SDOF models for large mass impact on sandwich composites. *Composites: Part B* 2005; 36 : 135-142.
54. Shivakumar KN, Elber W and Illg W. Prediction of Impact force and duration due to low-velocity Impact on circular composite laminates. *Journal of Applied Mechanics* 1985; 52: 674-680.
55. Gong SW and Lam KY. Effects of structural damping and stiffness on impact response of layered structures. *AIAA Journal* 2000; 38(9):1730–1735.
56. Malekzadeh K, Khalili MR and Mittal RK. Response of composite sandwich panels with transversely flexible core to low velocity transverse impact: A new dynamic model. *International Journal of Impact Engineering* 2007; 34: 522-543.
57. Türk MH and Hoo Fatt MS. Localized damage response of composite sandwich plates. *Composites: Part B* 1999; 30:157–165.
58. Zhou D and Stronge W. Low velocity impact denting of HSSA lightweight sandwich panel. *International Journal of Mechanical Sciences* 2006; 48:1031–1045.
59. Foo CC, Seah LK and Chai GB. A modified energy-balance to predict low-velocity impact response for sandwich composites. *Composite Structures* 2011; 93: 1385-1393.
60. Huang AY, Boer A and Akkerman R. Analytical modeling of impact resistance and damage tolerance of laminated composite plates. *AIAA Journal* 2008; 46 (11): 2760-2772.
61. Olsson R. Engineering method for prediction of impact response and damage in sandwich panels. *Journal of Sandwich Structures and Materials* 2002; 4: 3-29.

62. Sun C and Wu C. Low velocity impact response of composite sandwich panels. Proceedings of the 32nd AIAA/ASME/ASCE/AHS/ASC Structures, Structural Dynamics, and Materials Conference; 1991 April; Baltimore, MD.
63. Olsson R. Simplified theory for contact indentation of sandwich panels. SM Thesis, Aero.and Astro. Dept., MIT, 1994.
64. Zenkert D, Shipsha A and Persson K. Static indentation and unloading response of sandwich beams. *Composites Part B: Engineering* 2004; 35:511–522.
65. Minakuchi S, Okabe Y and Takeda J. “Segment-wise model” for theoretical simulation of barely visible indentation damage in composite sandwich beams: Part I-Formulation. *Composites Part A: applied science and manufacturing* 2008; 39; 133-144.
66. Chai GB and Zhu S. A review of low velocity impact on sandwich structures. *Proceedings of the Institution of Mechanical Engineers, Part L, Journal of Materials: Design and Applications* 2011; 207-230.
67. Luo RK, Green ER and Morrison C J. Impact damage analysis of composite plates. *International Journal of Impact Engineering* 1999; 22: 435–447.
68. Nguyen M Q, Elder D J and Bayandor J. A review of explicit finite element software for composite impact analysis. *Journal of Composite Materials* 2005; 39(4): 375–386.
69. Tita V, Carvalho JD and Vandepitte D. Failure analysis of low velocity impact on thin composite laminates: Experimental and numerical approaches. *Composite Structures* 2008; 83(4): 413–428.
70. Meo M, Morris AJ, Vignjevic R and Marengo G. Numerical simulation of low velocity impact on an aircraft sandwich panel. *Composite Structures* 2003; 62: 353–360.

71. Besant T, Davies GAO and Hitchings D. Finite element modeling of low velocity impact of composite sandwich panels. *Composites: Part A* 2001; 32: 1189–1196.
72. Aktay L, Johnson AF and Holzapfel M. Prediction of impact damage on sandwich composite panels. *Computational Materials Science* 2005; 32(3–4): 252–260.
73. Aktay L, Johnson AF and Kroplin BH. Numerical modelling of honeycomb crush behaviour. *Engineering Fracture Mechanics* 2008; 75(9): 2616–2630.
74. Jiang D and Shu D. Local displacement of core in two-layer sandwich structures subjected to low-velocity impact. *Composite Structures* 2005; 71: 53–60.
75. Zhang J and Ashby MF. The out-of-plane properties of honeycombs. *International Journal of Mechanical Sciences* 1992; 34(6): 475–489.
76. Meraghni F, Desrumaux F and Benzeggagh ML. Mechanical behavior of cellular core for structural sandwich panels. *Composites: Part A* 1999; 30: 767–779.
77. Hohe J and Becker WA. Mechanical model for two-dimensional cellular sandwich cores with general geometry. *Computational Material Science* 2000; 19: 108–115.
78. Burton WS and Noor AK. Assessment of continuum models for sandwich panel honeycomb cores. *Computational Methods Applied Mechanical Engineering* 1997; 145: 341–360.
79. Gornet L Marguet S and Marckmann G. Numerical modelling of Nomex honeycomb cores: Failure and effective elastic properties. Proceedings of the 3rd European Conference on Computational Mechanics: Solids, Structure and Coupled Problems in Engineering 2006, Lisbon, Portugal.

80. Horrigan DPW, Aitken RR and Moltschaniwskyj G. Modelling of crushing due to impact in honeycomb sandwiches. *Journal of Sandwich Structures and Materials* 2000; 2: 131–151.
81. Nguyen MQ, Jacombs SS, Thomson RS, Hachenberg, D and Scott ML. Simulation of impact on sandwich structures. *Composite Structures* 2005; 67(2): 217–227.
82. Czabaj MW, Zehnder AT, Davidson BD, Singh AK and Eisenberg DP. Compression after impact of sandwich composite structures: experiments and modeling. Proceedings of the 51st AIAA/ASME/ASCE/AHS/ASC Structures, Structural Dynamics, and Materials Conference; 2010 April; Orlando, FL.
83. ASTM Standard C364, 2007, “Standard test method for edgewise compressive strength of sandwich constructions,” ASTM International, West Conshohocken, PA, 2007, DOI: 10.1520/C0364_C0364M-07, www.astm.org.
84. Michaels TE, Krafchak TM and Davidson BD. Ultrasonic inspection of thin walled composite tubes. *Review of Progress in Quantitative Nondestructive Evaluation* 1992; 12; Thompson DO and Chimenti DE, eds.
85. <http://www.hexcel.com>; HexPly® 8552 Product Data Sheet 2007; Hexcel Corporation.
86. Czabaj MW. Damage and damage tolerance of high temperature composites and sandwich composite structures. PhD Thesis; Department of Theoretical and Applied Mechanics, Cornell University 2010.
87. O’Brien TK, Johnston W and Toland G. Mode II interlaminar fracture toughness and fatigue characterization of a graphite epoxy composite material. NASA/TM-2010 216838, 2010.

88. Timoshenko S and Woinowsky-krieger. Theory of Plates and Shells. Second Edition. McGraw-Hill Book Company.
89. Jones RM. Mechanics of composite materials. Mc-Graw Hill Company 1975; Washington DC.
90. Olsson R and McManus HL. Improved Theory for Contact Indentation of Sandwich Panels. *AIAA Journal* 1996; 34 (6): 1238-1244.
91. Ugural AC and Fenster SK. Advanced strength and applied elasticity. Fourth edition; Prentice Hall 2003; NJ 07548.
92. Lekhnitskii, Tsai and Cheron. Anisotropic plates. Gordon and Breach Science Publishers 1968; New York, NY 10011.
93. Highsmith AL and Reifsnider KL. Stiffness-reduction mechanisms in composite laminates. In: Damage in composite materials 1982; ASTM STP 775: 103-117.

VITA

- Name of Author:** Abhendra K. Singh
- Place of Birth:** Kavanagasau, Sigatoka, Fiji Islands.
- Date of Birth:** March 30, 1979
- Schools Attended:** Indian Institute of Technology (IIT) – Roorkee, India
Syracuse University, NY, USA.
- Degrees Awarded:** Bachelor of Technology in Mechanical Engineering (2002), Indian Institute of Technology, Roorkee, India.
Master of Science in Mechanical Engineering (2009), Syracuse University, NY, USA.